



University  
of Glasgow

Nelson, David Martin (2012) Chromatin modification contributes to senescence associated proliferation arrest. PhD thesis

<http://theses.gla.ac.uk/4220/>

Copyright and moral rights for this thesis are retained by the author

A copy can be downloaded for personal non-commercial research or study, without prior permission or charge

This thesis cannot be reproduced or quoted extensively from without first obtaining permission in writing from the Author

The content must not be changed in any way or sold commercially in any format or medium without the formal permission of the Author

When referring to this work, full bibliographic details including the author, title, awarding institution and date of the thesis must be given.

**Chromatin Modification Contributes to Senescence  
Associated Proliferation Arrest**

David Martin Nelson

Submitted in fulfillment of the requirements  
for the degree of Doctor of Philosophy

The Beatson Institute for Cancer Research  
College of Medical, Veterinary & Life Sciences  
University of Glasgow  
September 2012

## Abstract

Senescence is a state of permanent proliferation arrest that normal cells undergo in response to shortened telomeres, oncogenic activation and other sources of cellular stress, thus restricting the replicative capacity of impaired or damaged cells. As such, senescence provides a potent mechanism of tumor suppression, but has also been implicated in organismal aging. Senescence is accompanied by profound chromatin remodeling, which reinforces several important features of the senescence program. Consequently, there is considerable interest in elucidating precisely how chromatin structure influences senescence.

In the present work, I set out to investigate the role of the H4K20me3 histone modification in senescence, as the mark has been implicated in aging and is commonly lost in human cancers. I first showed that although senescent cells undergo a progressive loss of bulk histone content, the H4K20me3 modification is selectively retained during senescence. I next demonstrated that while the net abundance of H4K20me3 remains unaltered, senescent cells display a nuclear redistribution of the mark that coincides with SAHF. Utilizing ChIP coupled with next-generation sequencing, I mapped the genome-wide distribution of H4K20me3 in proliferating and senescent cells and found that H4K20me3 is highly enriched at several classes of DNA repeats and ZNF genes in senescent cells. Although H4K20me3 is associated with transcriptional repression, presence of the mark did not correlate with gene expression changes in senescence.

In order to investigate the mark functionally, I established cells overexpressing SUV420H2, a histone methyltransferase that catalyzes trimethylation of H4K20. Ectopic expression of SUV420H2 increased levels of the mark robustly, but produced no overt phenotype. When subjected to long-term culturing, SUV420H2 overexpression produced a moderate acceleration of senescence compared to control cells. Following infection with oncogenic H-RASG12V, SUV420H2 cells displayed an enhanced degree of senescence compared to H-RASG12V-infected control cells, based on multiple molecular readouts. Most remarkably, SUV420H2 overexpression blocked senescence escape following H-RASG12V infection, which occurred at a much higher frequency in H-RASG12V-infected control cells. Therefore, the data suggest that high levels of SUV420H2 and the H4K20me3 mark are beneficial to the

senescence program and serve to reinforce the permanent proliferation arrest. Although the molecular basis for this effect is presently unclear, the findings provide convincing evidence that chromatin structure is indeed an important contributor to the senescence program.

## Table of Contents

Abstract.....	1
Table of Contents.....	3
List of Figures.....	7
List of Tables .....	9
Author’s Declaration.....	10
Acknowledgements.....	11
List of Abbreviations .....	12
Chapter 1. Introduction.....	14
1.1 Cell Senescence.....	14
1.1.1 Overview of Cell Senescence .....	14
1.1.2 Triggers of Senescence .....	14
1.1.2.1 Telomere Shortening .....	14
1.1.2.2 Activated Oncogenes.....	16
1.1.2.3 Loss of Tumor Suppressors .....	17
1.1.2.4 Cellular Stress.....	18
1.1.3 Effectors of Senescence .....	19
1.1.3.1 The p53 and pRB Pathways.....	19
1.1.3.2 DNA Damage Response.....	22
1.1.3.3 Senescence-Associated Secretory Phenotype.....	23
1.1.3.4 Autophagy.....	24
1.1.4 Functions and Consequences of Senescence .....	26
1.1.4.1 Tumor Suppression.....	26
1.1.4.2 Wound Healing.....	28
1.1.4.3 Aging and Cancer .....	29
1.2 Chromatin.....	31
1.2.1 Chromatin Structure and Organization .....	31
1.2.2 Histone Variants.....	32
1.2.3 Histone Posttranslational Modifications .....	34
1.2.4 Histone Binding Proteins .....	36
1.2.5 Nucleosome Positioning .....	38
1.2.6 DNA Methylation .....	39
1.2.7 Non-Coding RNA .....	40

1.2.8 Lamins .....	42
1.3 Chromatin Dynamics in Cell Senescence.....	43
1.3.1 Senescence-Associated Heterochromatic Foci .....	43
1.3.2 Histone Modifications and Senescence.....	46
1.3.3 Histone Loss and Senescence .....	48
1.3.4 DNA Methylation and Senescence .....	49
1.3.5 Lamins and Senescence .....	50
1.4 Aim of the Study .....	52
<b>Chapter 2. Materials and Methods.....</b>	<b>55</b>
2.1 Expression and shRNA Vectors .....	55
2.1.1 Expression Vectors .....	55
2.1.2 Generation of SUV420H1 and SUV420H2 Vectors .....	55
2.1.3 Short Hairpin RNA (shRNA) Vectors .....	56
2.2 Cell Culture .....	56
2.2.1 IMR90 Cells.....	56
2.2.2 Phoenix-Ampho Cells.....	56
2.2.3 HEK-293T Cells .....	57
2.2.4 Transfection of Phoenix-Ampho Retroviral Packaging Cells.....	57
2.2.5 Retroviral Production and Infection.....	57
2.2.6 Transfection of HEK-293T Lentiviral Packaging Cells .....	58
2.2.7 Lentiviral Production and Infection .....	58
2.3. Induction of Cell Senescence and Quiescence .....	59
2.3.1 Induction of Replicative Senescence .....	59
2.3.2 Induction of Oncogene-Induced Senescence .....	60
2.3.3 Induction of Quiescence.....	60
2.4 Senescence Assays .....	61
2.4.1 Senescence-Associated $\beta$ -Galactosidase Assay .....	61
2.5 Gene Expression Analysis.....	61
2.5.1 RNA Isolation .....	61
2.5.2 Qualitative Assessment of RNA .....	62
2.5.3 Affymetrix Microarray Analysis.....	63
2.5.4 Microarray Data Analysis .....	64
2.6 Protein Analysis .....	65
2.6.1 Protein Isolation .....	65
2.6.2 Protein Quantification .....	66
2.6.3 Polyacrylamide Gel Electrophoresis (SDS-PAGE) .....	66

2.6.4 Immobilization of Protein .....	68
2.6.5 Western Blotting .....	68
2.7 Chromatin Analysis .....	70
2.7.1 Chromatin Immunoprecipitation .....	70
2.7.2 Preparation of ChIP-Seq Libraries .....	72
2.7.3 Qualitative Assessment of ChIP-Seq Libraries .....	73
2.7.4 ChIP-Sequencing .....	73
2.7.5 ChIP-Seq Data Analysis .....	74
2.8. Immunological Methods .....	77
2.8.1. Immunofluorescence .....	77
2.8.2 Epifluorescence Microscopy and Imaging .....	78
2.8.3 MODified Histone Peptide Array .....	78
Chapter 3. Establishing Model Systems of Cell Senescence .....	80
3.1 Rationale .....	80
3.2 Results .....	80
3.2.1 Establishing Experimental Models of Cell Senescence .....	80
3.2.2 Identifying Gene Expression Changes in RS .....	88
3.2.3 Identifying Gene Expression Changes in OIS .....	92
3.2.4 Defining a Transcriptional Profile of Cell Senescence .....	98
3.3 Discussion .....	105
Chapter 4. Characterization of H4K20me3 in Senescence .....	108
4.1 Rationale .....	108
4.2 Results .....	108
4.2.1 Evaluation of H4K20me3 Antibody Specificity .....	108
4.2.2 H4K20me3 is Selectively Retained in Senescent Cells .....	111
4.2.3 Assessment of H4K20me3 Localization in Senescent Cells .....	116
4.2.4 SUV420H2 Expression is Modestly Altered in Senescent Cells .....	122
4.3 Discussion .....	126
Chapter 5. Mapping H4K20me3 Distribution in Senescence .....	130
5.1 Rationale .....	130
5.2 Results .....	130
5.2.1 Optimization of ChIP-Seq Conditions .....	130
5.2.2 ChIP-Seq of H4K20me3 in Proliferating and Senescent Cells .....	137
5.2.3 Senescent Cells Contain Regions of H4K20me3 Enrichment .....	141
5.2.4 H4K20me3 Does Not Correlate with Transcriptional Changes .....	156
5.2.5 H4K20me3 is Enriched at ZNF Genes in Senescent Cells .....	160

5.3 Discussion .....	163
Chapter 6. Functional Dissection of H4K20me3 .....	167
6.1 Rationale.....	167
6.2 Results .....	167
6.2.1 Technical Approaches for Depleting H4K20me3.....	167
6.2.2 MYC-SUV420H2 Cells Proliferate Despite Elevated H4K20me3 .....	176
6.2.3 SUV420H2 Overexpression Accelerates Senescence Onset .....	181
6.2.4 SUV420H2 Protects Against Senescence Escape.....	187
6.3 Discussion .....	189
Chapter 7. Discussion .....	193
7.1 Summary of Findings .....	193
7.2 Limitations of the Study .....	196
7.2.1 Loss-of-Function Experiments.....	196
7.2.2 H4K20me3 and Senescence <i>In Vivo</i> .....	198
7.3 Implications of the Study .....	200
7.3.1 Regulation of H4K20me3 .....	200
7.3.2 H4K20me3 and Cancer .....	202
References.....	208

## List of Figures

Figure 1.1 The triggers, effectors, phenotype and impact of senescence .....	15
Figure 1.2 p53 and pRB are the master regulators of senescence .....	21
Figure 1.3 Histones undergo extensive posttranslational modification.....	35
Figure 1.4 Senescence-associated heterochromatic foci (SAHF).....	44
Figure 3.1 Characterizing an <i>in vitro</i> model of RS.....	82
Figure 3.2 Characterizing an <i>in vitro</i> model of OIS .....	85
Figure 3.3 Characterizing an <i>in vitro</i> model of quiescence .....	87
Figure 3.4 Global assessment of RS gene expression changes.....	89
Figure 3.5 Global assessment of OIS gene expression changes .....	94
Figure 3.6 Comparison of RS and OIS gene expression changes .....	99
Figure 3.7 IPA of genes upregulated in RS and OIS .....	101
Figure 3.8 IPA of genes downregulated in RS and OIS .....	103
Figure 3.9 IPA of genes that changed in common in RS and OIS .....	104
Figure 4.1 Evaluation of H4K20me3 antibody specificity .....	110
Figure 4.2 Determination of H4K20me3 levels in RS and OIS .....	113
Figure 4.3 H4K20me3 levels remain stable during RS .....	115
Figure 4.4 Senescent cells exhibit punctate nuclear H4K20me3 staining.....	117
Figure 4.5 H4K20me3 does not co-localize with PML, 53BP1 or $\gamma$ -H2AX.....	119
Figure 4.6 H4K20me3 co-localizes with SAHF in senescent cells .....	121
Figure 4.7 Validation of the SUV420H2 antibody .....	125
Figure 4.8 SUV420H2 expression is modestly altered in RS and OIS.....	127
Figure 5.1 Optimization of chromatin fragmentation.....	132
Figure 5.2 Evaluation of antibody binding by ChIP .....	134
Figure 5.3 Optimization of ChIP stringency conditions .....	136
Figure 5.4 Identification of H4K20me3 differentially enriched domains .....	144

Figure 5.5 H4K20me3 is enriched at defined genomic features.....	146
Figure 5.6 H4K20me3 is enriched at features of heterochromatin.....	150
Figure 5.7 Distribution of H4K20me3 across chromosome 19.....	151
Figure 5.8 H4K20me3 is enriched at discrete regions of chromosome 19.....	154
Figure 5.9 H4K20me3 is enriched at ZNF genes on chromosome 19.....	155
Figure 5.10 H4K20me3 does not correlate with gene expression changes .....	157
Figure 5.11 H4K20me3 is specifically enriched at ZNF genes in RS.....	161
Figure 5.12 H4K20me3 is highly enriched at ZNF genes .....	164
Figure 6.1 shRNA-mediated knockdown of SUV420H2 .....	169
Figure 6.2 SUV420H2 knockdown cells are not viable .....	171
Figure 6.3 SUV420H2 281-462 expression is insufficient to deplete H4K20me3 .	173
Figure 6.4 SUV420H2 281-462 expression is insufficient to reduce H4K20me3 levels.....	175
Figure 6.5 MYC-SUV420H1 and MYC-SUV420H2 increase H4K20me3 but do not induce cell cycle arrest.....	177
Figure 6.6 MYC-SUV420H1 and MYC-SUV420H2 exhibit distinct nuclear staining patterns.....	180
Figure 6.7 MYC-SUV420H2 accelerates the onset of senescence.....	182
Figure 6.8 H-RASG12V-infected MYC-SUV420H2 cells exhibit enhanced senescence.....	184
Figure 6.9 MYC-SUV420H2 enhances H-RASG12V-induced senescence .....	186
Figure 6.10 MYC-SUV420H2 prevents escape from H-RASG12V-induced senescence.....	188
Figure 6.11 MYC-SUV420H2 promotes stable proliferation arrest.....	190
Figure 7.1 Model of H4K20me3 function in senescence .....	207

## List of Tables

Table 2.1 Separating gel recipes .....	67
Table 2.2 Summary of antibodies that were used in this study .....	69
Table 3.1 Gene sets enriched in RS cells .....	91
Table 3.2 Gene sets enriched in proliferating cells.....	93
Table 3.3 Gene sets enriched in H-RASG12V cells.....	96
Table 3.4 Gene sets enriched in control cells .....	97
Table 4.1 Evaluating SUV420H2 gene expression in RS and OIS .....	123
Table 5.1 H4K20me3 ChIP-Seq experiment 1 summary statistics .....	139
Table 5.2 H4K20me3 ChIP-Seq experiment 2 summary statistics .....	142

## **Author's Declaration**

I am the sole author of this thesis and all work presented is entirely my own unless stated otherwise. No part of this work has been submitted for consideration as part of any other degree or award.

## **Acknowledgements**

First, I would like to thank my parents for providing me with unconditional love, support and encouragement as I endeavored to complete these studies. Their constant and genuine belief in my abilities provided me with the confidence and drive that I needed to make it through the challenging days and nights in the laboratory. I would also like to thank my sister Catherine for her support and for encouraging me to explore a new locale.

I would like to express my sincerest gratitude to Jiyeon for her relentless encouragement and cheerful optimism. Her continual patience and willingness to listen enabled me to stay focused and keep things in perspective. I am truly honored to have such a remarkable friend!

I would like to thank my supervisor, Dr. Peter Adams, for providing me with the opportunity to pursue a PhD in his laboratory. I am extremely grateful for the years of mentorship and thoughtful discussion that he has provided. I would also like to thank Peter for providing exceptional training when I was a young impressionable scientist.

Finally, I would like to acknowledge the generosity of Cancer Research UK for providing me with the financial resources necessary for completion of this work.

## List of Abbreviations

BH-FDR	Benjamini–Hochberg false discovery rate
BrdU	5-bromo-2'-deoxyuridine
BSA	bovine serum albumin
CAR	chromatin-associated ribonucleic acid
cDNA	complementary deoxyribonucleic acid
ChIP	chromatin immunoprecipitation
ChIP-Seq	chromatin immunoprecipitation sequencing
DAPI	4',6-diamidino-2-phenylindole
DDR	deoxyribonucleic acid damage response
DMEM	Dulbecco's modified Eagle medium
DMSO	dimethyl sulfoxide
DNA	deoxyribonucleic acid
dsDNA	double-stranded deoxyribonucleic acid
DTT	dithiothreitol
ECL	enhanced chemiluminescence
EDTA	ethylenediaminetetraacetic acid
EGTA	ethylene glycol tetraacetic acid
GAIx	Genome Analyzer Ix
GCOS	GeneChip Operating Software
GCRMA	GC robust multi-array average
GSEA	gene set enrichment analysis
HDF	human diploid fibroblast
IF	immunofluorescence
IgG	immunoglobulin G
IP	immunoprecipitation
IPA	Ingenuity Pathway Analysis
IPDB	immunoprecipitation dilution buffer
lncRNA	long non-coding ribonucleic acid
$\mu\text{M}$	micromolar
mM	millimolar
mNLB	modified nuclear lysis buffer

mRNA	messenger ribonucleic acid
ncRNA	non-coding ribonucleic acid
nM	nanomolar
OIS	oncogene-induced senescence
PAGE	polyacrylamide gel electrophoresis
PBS	phosphate buffered saline
PCR	polymerase chain reaction
PD	population doubling
pM	picomolar
PMSF	phenylmethylsulfonyl fluoride
PTM	post-translational modification
PVDF	polyvinylidene fluoride
RNA	ribonucleic acid
ROS	reactive oxygen species
RS	replicative senescence
SA $\beta$ -gal	senescence-associated beta-galactosidase
SAHF	senescence-associated heterochromatic foci
SASP	senescence-associated secretory phenotype
SDS	sodium dodecyl sulfate
shRNA	short hairpin ribonucleic acid
TBS	tris-buffered saline
TES	transcription end site
TSS	transcription start site
WB	Western blot
X-gal	5-bromo-4-chloro-3-indolyl- $\beta$ -d-galactopyranoside

# **Chapter 1. Introduction**

## **1.1 Cell Senescence**

### **1.1.1 Overview of Cell Senescence**

Cell senescence is a state of permanent proliferation arrest that normal cells can undergo in response to a variety of detrimental stimuli. In this manner, senescence restricts the proliferative capacity of impaired or damaged cells. Several well-characterized triggers of senescence have been identified including short telomeres, oncogenic signalling, loss of tumor suppressors and general cell stress. Upon exposure to these triggers, cells exhibit a characteristic set of morphological, transcriptional and biochemical changes, the culmination of which is a permanent proliferation arrest. In order to establish senescence, cells engage a coordinated network of effector pathways. The p53 and pRB pathways are the master regulators of senescence and interact extensively with additional effector processes including DNA damage signalling, altered secretion and autophagy. Importantly, senescence is accompanied by profound changes to chromatin structure, which is thought to reinforce aspects of the senescence program. Functionally, senescence serves as a potent tumor suppression mechanism and facilitates wound healing. However, senescence has also been implicated in aging and tumorigenesis. Thus, senescence is a complex but important biological process that undoubtedly requires further study (Figure 1.1).

### **1.1.2 Triggers of Senescence**

#### **1.1.2.1 Telomere Shortening**

In 1961, Leonard Hayflick and Paul Moorhead described a phenomenon that they termed “Phase III,” in which primary human diploid cell strains exhibited a reduced proliferative capacity and underwent striking morphological changes following extended periods in culture (Hayflick & Moorhead, 1961). Four years later, Hayflick reported the seminal finding that primary human diploid cells indeed have a finite lifespan in culture and described the Phase III phenomenon as a form of

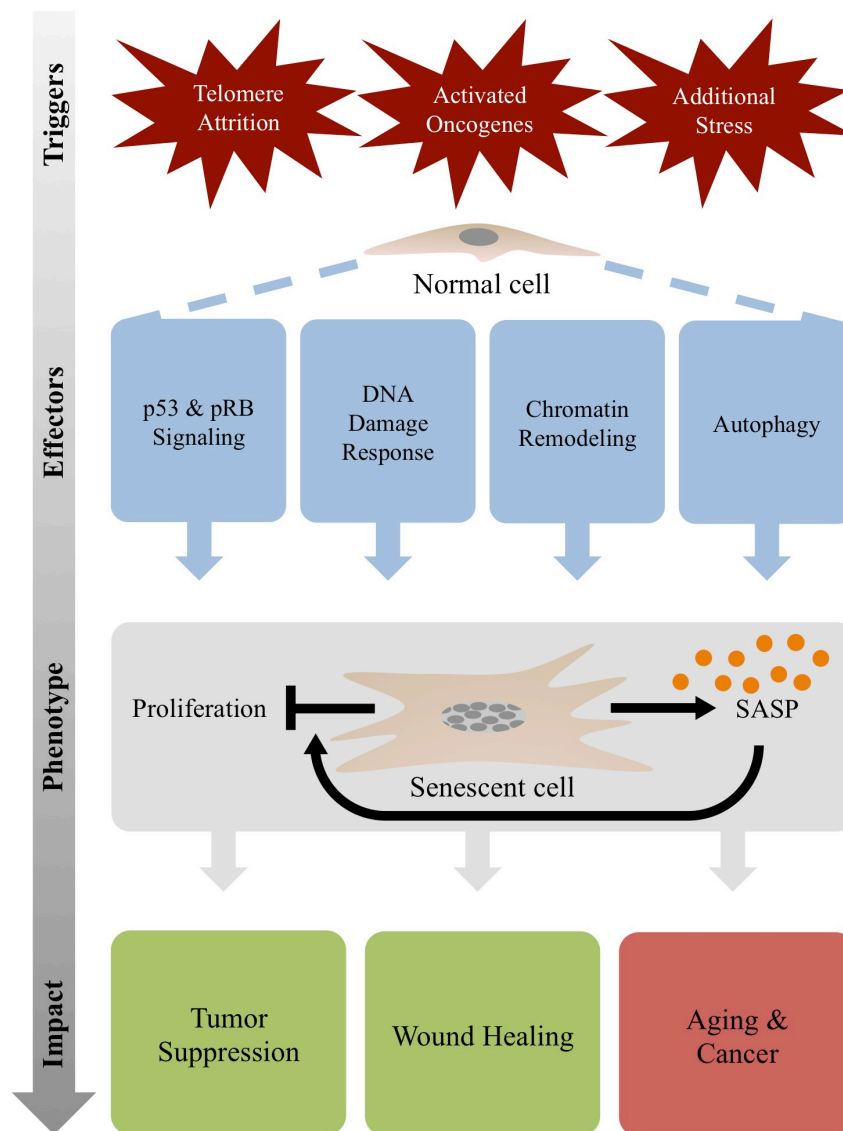


**Figure 1.1 The triggers, effectors, phenotype and impact of senescence.** Several well-characterized triggers of senescence have been identified, including telomere attrition, activated oncogenes and oxidative stress. Upon exposure to these triggers, normal cells initiate the senescence program, a network of effector pathways which cooperate to establish a stable proliferation arrest. Establishment of the proliferation arrest is accompanied by an altered pattern of secretion termed the SASP, which in turn reinforces senescence. Functionally, senescence serves to suppress tumorigenesis and facilitates the wound healing process. However, in certain contexts senescence is thought to have a deleterious impact by promoting tissue aging and cancer.

“senescence” at the cellular level (Hayflick, 1965). As a result, the point at which normal cells cease to proliferate is commonly referred to as the “Hayflick limit.”

It is now recognized that after an extended period in culture, primary cells undergo a form of senescence called replicative senescence (RS) that results from the shortening of telomeres. Telomeres are the regions of repetitive DNA sequence (5'-TTAGGG-3') and associated proteins that protect the linear ends of chromosomes (Shay & Wright, 2005). However, due to the properties of DNA polymerase, a short 50-200 base pair segment of the lagging strand is lost with each sequential round of DNA replication, which is referred to as the end-replication problem (Harley et al., 1990). Thus, following repeated rounds of replication, telomeres become critically short and dysfunctional, which activates the DNA damage response (DDR) and initiates senescence (d'Adda di Fagagna et al., 2003; Herbig et al., 2004). Precisely how the DDR engages senescence will be discussed in detail in a subsequent section.

Because the rate of telomere loss is not identical for every chromosome in the cell, some chromosomes develop critically short telomeres faster than others. Consequently, the presence of only a few short telomeres is capable of inducing senescence (Martens et al., 2000). Remarkably, ectopic expression of telomerase, a ribonucleoprotein enzyme that can synthesize telomeric DNA but is not ordinarily expressed sufficiently in human somatic cells, is sufficient to extend lifespan and delay senescence in primary human cells (Bodnar et al., 1998). Importantly, this confirmed that telomere attrition is a molecular trigger of senescence.

### **1.1.2.2 Activated Oncogenes**

Subsequent to the discovery that telomere shortening limits the replicative lifespan of normal cells, it was reported that activated oncogenes are also sufficient to induce senescence in primary cells. Previous studies had established that expression of oncogenic H-RAS is capable of transforming most immortal rodent cell lines (Newbold & Overell, 1983). In contrast, Scott Lowe and colleagues noted that introduction of an oncogenic form of H-RAS into primary human and rodent cells resulted in a stable G1 cell cycle arrest and the acquisition of morphological features reminiscent of replicative senescent cells (Serrano et al., 1997). Lowe and colleagues further confirmed senescence in the mutant H-RAS-expressing cells by showing induction of the tumor suppressors p53 and p16INK4a and pH-dependent senescence-associated  $\beta$ -galactosidase activity. Importantly, co-expression of viral

E1A, a protein that binds and inactivates pRB, prevented H-RAS-induced senescence in the human cells. These data convincingly established that oncogene activation is indeed capable of inducing premature senescence in primary cells.

Since the time of these initial findings, numerous oncogenes have been reported to induce senescence *in vitro*. For example, the activation of additional members of the RAS-RAF-MEK signaling pathway, including RAF, BRAF, MEK and MOS, has been shown to drive senescence (Zhu et al., 1998; Michaloglou et al., 2005; Narita et al., 2003; Lin et al., 1998; Bartkova et al., 2006). Likewise, countless other oncogenic proteins (e.g., MYC, TGF $\beta$ , RUNX1) have also been implicated in the induction of senescence (Grandori et al., 2003; Katakura et al., 1999; Wolynec et al., 2009). Importantly, oncogene-induced senescence (OIS) is not strictly an *in vitro* phenomenon and has been described in variety of *in vivo* contexts. In fact, various oncogenic mutations have been associated with the accumulation of senescent cells in premalignant lesions (Collado et al., 2005). To this end, oncogenic forms of BRAF, KRAS and NRAS appear to induce senescence in the contexts of benign melanocytic nevi, lung adenomas and lymphoproliferative disorders, respectively (Michaloglou et al., 2005; Collado et al., 2005; Braig et al., 2005).

Although oncogene-induced senescent cells resemble replicative senescent cells phenotypically, oncogenic activity appears to drive senescence independently of telomere shortening. As such, expression of telomerase, which is sufficient to delay replicative senescence, does not prevent OIS, indicating that oncogenes do not induce senescence via telomere shortening (Wei et al., 1999). Instead, oncogenic activation is thought to induce senescence by driving hyper-replication, resulting in stalled replication forks and DNA double-strand breaks, which in turn activates the DDR (Di Micco et al., 2006). Thus, oncogene activation represents a distinct trigger of cell senescence.

### **1.1.2.3 Loss of Tumor Suppressors**

The loss or inactivation of tumor suppressor proteins is also capable of inducing cell senescence *in vitro* and *in vivo*. Illustrating this, Pier Paolo Pandolfi and colleagues reported that while targeted deletion of both alleles of the tumor suppressor *Pten* in mouse embryonic fibroblasts (MEFs) induces senescence, *Pten/Trp53* double-null MEFs continue to proliferate (Chen et al., 2005). Intriguingly, MEFs in which only a single *Pten* allele is deleted fail to senesce and

proliferate more than wild-type cells. In the same study, the authors investigated the effect of tumor suppressor loss *in vivo* and found that prostate-specific deletion of both *Pten* alleles in mouse results in the initial development of pre-malignant prostatic intraepithelial neoplasia and senescence.

In a separate study, Karen Cichowski and colleagues demonstrated that depletion of the neurofibromin (NF1) tumor suppressor from primary human fibroblasts results in p53/pRB-mediated senescence (Courtois-Cox et al., 2006). The authors also showed that knockdown of NF1 results in a transient activation of the RAS pathway that is quickly attenuated. Importantly, inactivation of the RAS pathway after NF1 knockdown precedes senescence, suggesting that a negative feedback loop might be responsible for triggering senescence upon loss of NF1. Finally, Cichowski and colleagues showed that dermal neurofibromas, small benign tumors that arise from somatic mutation of NF1, contain SA  $\beta$ -gal and p16INK4a-positive senescent cells.

In addition, William Kaelin, Jr and colleagues reported that targeted deletion of the von Hippel–Lindau tumor suppressor gene *Vhl* in MEFs results in a p53-independent senescence proliferation arrest (Young et al., 2008). Specifically, *Vhl* deletion results in loss of the SWI2/SNF2 complex member p400, which leads to elevated p27 levels and subsequent activation of pRB. The authors also reported high levels of SA  $\beta$ -gal in the kidneys of *Vhl*<sup>fl/fl</sup> mice, indicating that loss of *Vhl* is also sufficient to induce senescence *in vivo*. Therefore, collective these studies provide compelling evidence that loss of tumor suppressors can trigger cell senescence.

#### **1.1.2.4 Cellular Stress**

It has also been noted that in culture, cells can undergo senescence in response to various forms of stress. To this end, suboptimal culturing conditions and the stress incurred by maintaining cells in an artificial environment can undoubtedly contribute to premature senescence *in vitro* (Sherr & DePinho, 2000). In addition to the inevitable detriments of growing cells in culture, several other factors have been reported to induce a form of senescence that is occasionally referred to as stress-induced senescence (SIPS) (Toussaint et al., 2000).

As discussed in the sections on telomere shortening and oncogene activation, DNA damage appears to be a common molecular driver of cell senescence. Consequently, other sources of DNA damage are equally effective at inducing

senescence. For example, exposure to ultraviolet (UV) light has been reported to produce stable proliferation arrest and senescence in primary human melanocytes and fibroblasts (Medrano et al., 1995; Helenius et al., 1999). In a similar manner, ionizing radiation has been used extensively to induce senescence in human and mouse fibroblasts (Di Leonardo et al., 1994; Coppé et al., 2008; Rodier et al., 2009).

Drug treatment is widely acknowledged as another source of cellular stress capable of inducing senescence. DNA damaging agents including hydroxyurea, etoposide and doxorubicin are routinely used to trigger senescence in primary cells (Yeo et al., 2000; Kosar et al., 2011). Likewise, treatment of cells with the histone deacetylase (HDAC) inhibitors sodium butyrate and trichostatin A (TSA) has been shown to confer senescence in primary human fibroblasts (Ogryzko et al., 1996; Place et al., 2005). Remarkably, treatment with chemotherapeutic agents has even been reported to induce senescence in certain tumor cells *in vitro* and *in vivo* (te Poele et al., 2002; Zheng et al., 2004; Roberson et al., 2005).

Finally, oxidative stress also limits cellular lifespan in culture through the induction of senescence. First, exposure of primary human fibroblasts to sub-lethal concentrations of H<sub>2</sub>O<sub>2</sub> has been shown to promote proliferation arrest and senescence (Chen et al., 1998a; Dumont et al., 2000). Likewise, culturing cells under hyperoxic conditions accelerates the onset of senescence (von Zglinicki et al., 1995; Klimova et al., 2009). In contrast, maintaining primary human cells under low oxygen conditions extends lifespan in culture (Parker et al., 1977; Saito et al., 1995). Intriguingly, oxidative stress even promotes senescence in response to other triggers, as elevated RAS expression increases intracellular levels of reactive oxygen species (ROS) (Lee et al., 1999). High levels of ROS have also been reported in replicative senescent cells (Furumoto et al., 1998). Thus, it is evident that various sources of cellular stress can serve as triggers of senescence.

### **1.1.3 Effectors of Senescence**

#### **1.1.3.1 The p53 and pRB Pathways**

The establishment and reinforcement of a stable proliferation arrest is one of the defining features of cell senescence. In order to facilitate this critical process, stressed cells engage a coordinated network of effector pathways. To this end, the establishment of senescence is primarily contingent upon the activities of the p53 and

pRB tumor suppressor pathways. Underscoring the significance of p53 and pRB to senescence induction, the simultaneous inactivation of both pathways is required in order to abolish senescence in primary human cells (Shay et al., 1991; Bond et al., 1999; Hahn et al., 2002). However, in mice, individual inactivation of either the p53 pathway or pRB (plus p107 and p130) is sufficient to prevent senescence (Harvey et al., 1993; Dannenberg et al., 2000; Sage et al., 2000). Regardless, the p53 and pRB pathways both serve as the master regulators of the senescence program (Figure 1.2).

The p53 pathway is ordinarily activated upon exposure to a variety of cellular stressors, including DNA damage. DNA damage results in the activation of ATM and ATR, which subsequently phosphorylate and activate the CHK2 and CHK1 kinases, respectively (Kurz & Lees-Miller, 2004). Upon activation, CHK2/CHK1 phosphorylate and stabilize p53, which enables the transcriptional activation of specific p53 target genes (He et al., 2005). One critical p53 target gene is the cyclin-dependent kinase inhibitor p21CIP1 (CDKN1A). Once expressed, p21CIP1 binds and inhibits cyclin-CDK2 complexes, thus blocking cell cycle progression and arresting cells in G1 phase (Sherr & Roberts, 1999). In this manner, activation of the p53 pathway blocks proliferation.

The pRB pathway is a second critical effector mechanism through which senescence is established. In the unphosphorylated state, pRB restricts cell cycle progression by binding to and inhibiting the E2F family of transcription factors. As the cell approaches S phase, pRB is phosphorylated by cyclin D/CDK4/CDK6, which releases E2F and frees the transcription factor to activate a series of target genes required for progression through S phase (Nevins, 2001). Cellular stress, including oncogenic activation, induces the expression of the cyclin-dependent kinase inhibitor p16INK4a (CDKN2A) (Ohtani et al., 2001). Upon induction, p16INK4a inhibits the activity of cyclin D/CDK4/CDK6 complexes, which in turn prevents the phosphorylation of pRB. Dephosphorylation of pRB restores binding with E2F, prevents the transcription of proliferation genes and blocks cell cycle progression (Lowe & Sherr, 2003). Thus, induction of the p16INK4a-pRB pathway provides another important mechanism of restricting proliferation following exposure to stress signals.

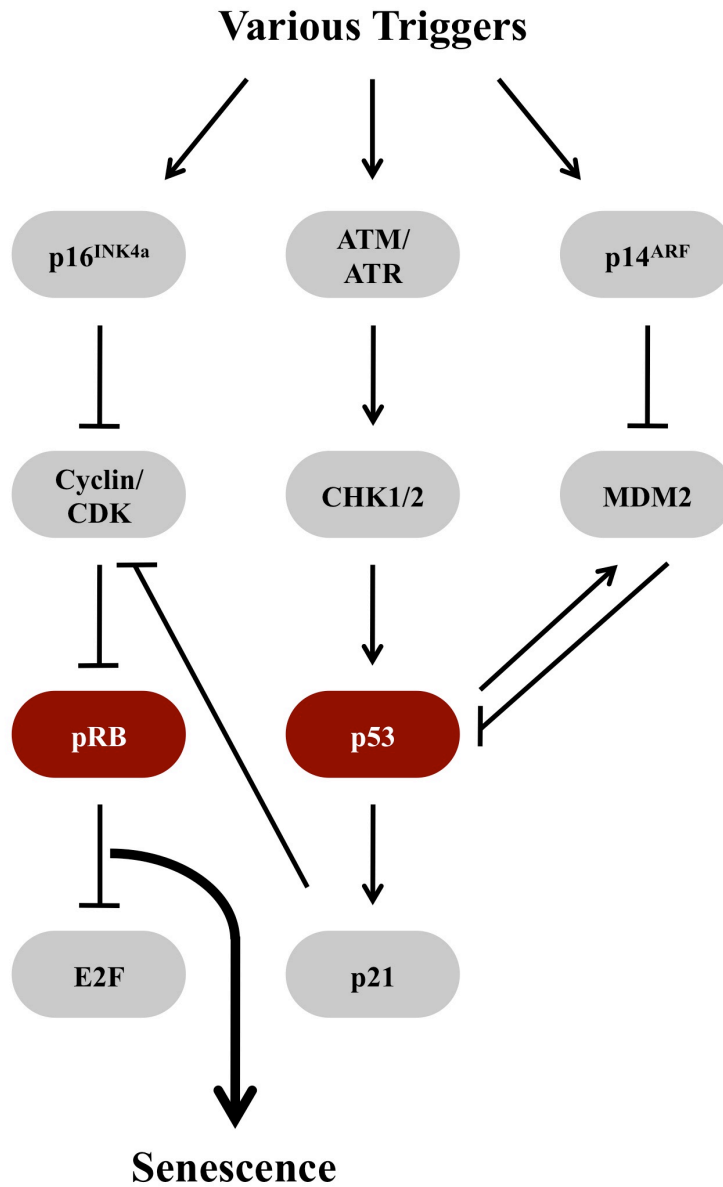


**Figure 1.2 p53 and pRB are the master regulators of senescence.** DNA damage in the form of telomere dysfunction, aberrant replication or oxidative damage is a common upstream trigger of the p53 and/or pRB pathways. As such, activation of the p53 and pRB tumor suppressor pathways is required for the establishment of cell senescence.

### 1.1.3.2 DNA Damage Response

Given the ability of DNA damage to engage the p53 and pRB pathways, it is not surprising that the DNA damage response (DDR) is another important effector pathway through which senescence is established. Although senescence can occur independently of DNA damage, many of the aforementioned triggers of senescence elicit the DDR. In fact, telomere shortening, activated oncogenes, ionizing radiation and genotoxic agents all induce senescence through activation of the DDR (d'Adda di Fagagna et al., 2003; Di Micco et al., 2006; Fumagalli et al., 2012; Ben-Porath & Weinberg, 2005).

The progressive telomere shortening that results from repeated rounds of DNA replication is a well-documented trigger of the DNA damage response. In one of the first demonstrations that telomere attrition could produce a DNA damage signal, Stephen Jackson and colleagues reported that replicative senescent cells accumulate several markers of DNA damage including phosphorylated  $\gamma$ -H2AX, SMC1, RAD17, CHK1 and CHK2 (d'Adda di Fagagna et al., 2003). The study further revealed that  $\gamma$ -H2AX was enriched at subset of subtelomeric regions of chromosomes that have been shown to have particularly short telomeres. Intriguingly, inactivation of the DNA response through expression of dominant negative forms of ATM, ATR, CHK1 and CHK2 enabled replicative senescent cells to resume DNA replication. Expanding on this work, Fabrizio d'Adda di Fagagna and colleagues showed that DNA damage occurring at telomeres cannot be effectively repaired, which results in the presence of chronic DNA damage foci, a persistent DDR and establishment of senescence (Fumagalli et al., 2012).

Activated oncogenes have also been reported to induce senescence through engagement of the DDR. Work from the laboratories of Jiri Bartek and Fabrizio d'Adda di Fagagna demonstrated that oncogenic activation indeed produces a DDR by causing hyper-replication that results in DNA double-strand breaks and improperly terminated replication forks (Bartkova et al., 2006; Di Micco et al., 2006). Significantly, inactivation of CHK2 not only abolishes H-RAS-induced senescence but also results in cell transformation, highlighting the importance of an intact DDR for establishment of OIS (Di Micco et al., 2006).

Finally, the DDR is not only important for the induction of a permanent proliferation arrest, but is also critically important to the generation of the SASP. To this end, Judith Campisi and colleagues reported that inactivation of critical DDR

mediators including NBS1, ATM and CHK2 prevents the SASP in response to radiation-induced senescence (Rodier et al., 2009). In addition, SASP factors including the chemokine IL8 and ligands of CXCR2 provide a feedback loop that enhances the DDR (Acosta et al., 2008). Therefore, the DDR is not an independent process, but rather a fully integrated branch of the other effector pathways that establish senescence.

### **1.1.3.3 Senescence-Associated Secretory Phenotype**

Several early transcriptional profiling studies of senescence revealed that compared to proliferating cells, senescent cells exhibit a discrete pattern of altered gene expression (Shelton et al., 1999; Zhang et al., 2003; Yoon et al., 2004). As anticipated, these studies invariably revealed a significant downregulation of proliferation and cell cycle genes in senescent cells. Unexpectedly, the profiling studies also indicated that numerous genes encoding pro-inflammatory cytokines, chemokines, growth factors and extracellular matrix remodeling enzymes are consistently upregulated in senescent cells. Remarkably, many of these proteins are actively secreted into the extracellular environment (Campisi, 2005). Thus, while initially surprising, it is now evident that these secreted proteins, collectively termed the senescence-associated secretory phenotype (SASP), comprise an important feature of the senescence program (Coppé et al., 2008; Rodier et al., 2009).

Although considered a phenotypic hallmark of cell senescence, the SASP also represents an important effector mechanism involved in the establishment of senescence. To this end, some of the components of SASP have been reported to reinforce the senescence proliferation arrest through an autocrine feedback mechanism. Work by Jinsong Liu and colleagues revealed that ectopic expression of RAS in ovarian epithelial cells induces the expression and secretion of GRO-1, which when applied to stromal fibroblasts in conditioned medium, induces senescence (Yang et al., 2006). Similarly, René Bernards and colleagues determined that expression of the SASP factor PAI-1 is both necessary and sufficient to induce senescence in human BJ fibroblasts and MEFs (Kortlever et al., 2006). Likewise, expression of oncogenic BRAFV600E in primary human cells results in the expression and secretion of IGFB7, which subsequently induces senescence through inhibition of the RAF-MEK-ERK pathway (Wajapeyee et al., 2008). Finally, work from the laboratories of Daniel Peeper and Jesus Gil revealed that the cytokine IL6

and chemokine IL8 help to establish and reinforce senescence by mediating expression of a C/EBP $\beta$ - and NF- $\kappa$ B-dependent network of inflammatory factors (Kuilman et al., 2008; Acosta et al., 2008).

In light of the fact that several SASP factors actively reinforce senescence, considerable attention has been directed toward understanding how the SASP is regulated. As mentioned above, the expression of several SASP factors is regulated through the transcription factors C/EBP $\beta$  and NF- $\kappa$ B. In fact, depletion of C/EBP $\beta$  from cells infected with oncogenic BRAFV600E not only inhibits the expression of IL6 and IL8, but also allows the cells to bypass senescence and continue proliferating (Kuilman et al., 2008). Likewise, pharmacologic inhibition of NF- $\kappa$ B prevents the expression of numerous SASP factors in primary cells overexpressing mutant MEK (Acosta et al., 2008). The DDR appears to play an integral role in facilitating the SASP, as silencing of several DDR components attenuates the expression of several SASP factors (Rodier et al., 2009). It is important to note that although SASP expression typically accompanies several forms of senescence induction (e.g., RS, OIS, stress), senescence and SASP expression are separable processes. For example, ectopic expression of p16INK4a induces senescence in primary cells without eliciting the DDR or the SASP (Coppé et al., 2011). There is also evidence to support roles for p38MAPK signalling and microRNAs in the regulation of the SASP (Freund et al., 2011; Bhaumik et al., 2009). Thus, SASP regulation is undoubtedly a complex process that warrants additional investigation.

While the SASP is certainly a critical effector of the senescence program, it is also a downstream phenotype of senescence. In this capacity, the SASP likely helps to facilitate the physiological function(s) of senescence *in vivo*. Alternatively, the SASP might also contribute to some potentially detrimental aspects of senescence. Indeed, both of these topics will be addressed in a subsequent discussion of the functional relevance of senescence.

#### **1.1.3.4 Autophagy**

More recently, autophagy has been identified as another key effector of the senescence program. Autophagy is an evolutionarily conserved process that facilitates the sequestration, degradation and turnover of intracellular proteins and organelles (Mizushima, 2007; Yang & Klionsky, 2010). It has been reported that as cells age they accumulate oxidatively damaged and misfolded proteins that cannot

undergo efficient degradation and turnover (Ryazanov & Nefsky, 2002; Breusing & Grune, 2008). Indeed, the accumulation of oxidized protein with age has been shown to impair various aspects of cellular function (Squier, 2001). Consequently, autophagy has been proposed as a potential mechanism for limiting the amount of damage protein that increases with age (Levine & Kroemer, 2008).

In view of the concept that replicative senescence represents a form of aging at the cellular level, an interest in investigating the link between senescence and autophagy has emerged. To this end, Christian Behl and colleagues reported that autophagy increases in late passage, replicative senescent IMR90 cells (Gamerding et al., 2009). The study further revealed that induction of autophagy in replicatively aged cells occurs through a switch in the ratio of BAG3 to BAG1, two members of the BCL-2-associated athanogene protein family, and involves the LC3-binding protein SQSTM1. Thus, the authors suggested that autophagy induction in aged cells might mitigate the accumulation of damaged proteins.

Work from Masashi Narita's laboratory revealed that in human diploid fibroblasts, autophagic activity increases during the transition phase of OIS (Young et al., 2009). Activation of autophagy during the transition phase also correlates with the concurrent suppression of mTORC1 and mTORC2 activities. In the same study, shRNA-mediated depletion of ATG5 or ATG7, two genes required for autophagy, attenuated SA  $\beta$ -galactosidase activity and delayed the production of IL6 and IL8, two cytokines that contribute functionally to the senescence program. Importantly, reduction of ATG5 or ATG7 also resulted in a bypass of H-RAS-induced proliferation arrest suggesting that autophagy is an important effector mechanism in the establishment of OIS.

Senescent cells often undergo a significant increase in size and contain more protein per cell than proliferating cells (Young et al., 2009). In order to accommodate this considerable energetic demand, senescent cells must maintain effective protein turnover and synthesis. Another recent study from Masashi Narita's group revealed that protein turnover during OIS is mediated through the co-localization of autophagic and protein synthesis machinery to a sub-cellular space termed the TOR-autophagy spatial coupling compartment (TASCC) (Narita et al., 2011). The authors demonstrated that recruitment of the mTOR complex to the TASCC is dependent on amino acids and Rag GTPase function. Likewise, expression of a Rag GTPase dominant negative disrupts mTOR recruitment to the TASCC and restricts the

expression of IL6 and IL8 during OIS. This indicated that the production of some SASP proteins during senescence is dependent upon the spatial overlap of mTOR-autophagy and protein synthesis organelles. Importantly, all three of these studies support the concept that autophagy is an integral effector pathway of the senescence program.

#### **1.1.4 Functions and Consequences of Senescence**

##### **1.1.4.1 Tumor Suppression**

It has been widely proposed that the primary physiological function of senescence is to suppress tumorigenesis. Indeed, there are several lines of evidence that strongly support a prominent role for senescence in preventing cancer. As addressed in the discussion of OIS, oncogenic activation is one of the key triggers of senescence in a variety of cell types. To this end, well-characterized oncogenic proteins including H-RASG12V and B-RAFV600E are potent inducers of cell senescence *in vitro* and *in vivo* (Serrano et al., 1997; Michaloglou et al., 2005; Sarkisian et al., 2007). In addition, senescent cells are frequently present in various premalignant neoplastic lesions. Senescent cells have been reported in benign melanocytic nevi, early-stage lymphomas, prostate intraepithelial neoplasia, dermal neurofibroma, colon adenoma, pancreatic intraepithelial neoplasia and early-stage thyroid tumors (Michaloglou et al., 2005; Gray-Schopfer et al., 2006; Braig et al., 2005; Collado et al., 2005; Chen et al., 2005; Courtois-Cox et al., 2006; Bartkova et al., 2006; Kuilman et al., 2008; Acosta et al., 2008; Fujita et al., 2009; Morton et al., 2010; Caldwell et al., 2012; Vizioli et al., 2011).

Further supporting a role for senescence in tumor suppression, inactivation of key pathways that drive the senescence program enables the progression from early-stage pre-malignant lesions to more advanced tumors. In fact, targeted disruption of p53 and Ink4a/Arf has been reported to accelerate tumorigenesis in multiple murine models of cancer (Chin et al., 1997; Bardeesy et al., 2002; Chen et al., 2005; Braig et al., 2005). Additionally, reactivation of p53 within tumors results in regression of the tumor and is associated with senescence induction. Tyler Jacks and colleagues reported that reactivation of p53 within established sarcomas in mice results in profound tumor regression and the presence of senescence markers (Ventura et al., 2007). Similarly, Scott Lowe and colleagues elegantly showed that reactivation of

p53 within Hras-induced hepatocarcinomas in mice causes senescence, tumor regression and immune-mediated clearance of the tumors (Xue et al., 2007).

Although these findings provide compelling evidence that senescence provides a barrier to tumorigenesis, it is also important to examine how senescence might accomplish this. Undoubtedly, the anti-proliferative property of senescence restricts damaged cells from expanding clonally, thus preventing tumor formation. For example, benign melanocytic nevi are comprised of non-proliferating senescent melanocytes, and despite frequently harboring oncogenic BRAF mutations, rarely progress to melanoma (Michaloglou et al., 2005; Pollock et al., 2003; Gray-Schopfer et al., 2007). In addition, because senescent cells cease proliferation and DNA replication, there is a reduced likelihood of the cells acquiring additional mutations that might enable bypass of senescence and promote tumorigenesis.

Finally, there is data emerging to suggest that senescence suppresses tumor formation by promoting immune-mediated clearance of damaged cells. As mentioned above, Scott Lowe's laboratory first reported that senescent cells are subject to immune clearance *in vivo* (Xue et al., 2007). In the study, Lowe and colleagues demonstrated that reactivation of p53 in mouse liver tumors induces senescence and causes tumor regression. Remarkably, the authors showed tumor regression was facilitated by the active clearance of senescent cells by natural killer (NK) cells, as antibody depletion of NK cells prevented regression. Subsequent work from Lowe and colleagues revealed that NK cells preferentially kill senescent cells *in vitro* (Krizhanovsky et al., 2008).

Expanding on this concept, recent work from Lars Zender's laboratory showed that in mice, RAS-induced senescent hepatocytes are cleared from the liver through a CD4<sup>+</sup> T-cell-mediated adaptive immune response (Kang et al., 2011). Clearance of senescent hepatocytes also requires an intact monocyte/macrophage response. Importantly, the authors proposed that secretion of cytokines and chemokines by senescent cells mediates recruitment of innate and adaptive immune cells. Likewise, work by Lowe and colleagues revealed that factors secreted by senescent cells are important for attracting NK and other immune cells (Xue et al., 2007). Senescent cells indeed secrete a wide array of chemokines, cytokines and other immune modulating factors as part of the SASP (Kuilman et al., 2008; Acosta et al., 2008). It is now evident that the SASP can promote immune-mediated clearance of senescent cells *in vivo*. Thus, two important features of senescence,

permanent proliferation arrest and the SASP, likely collaborate to provide a barrier to tumorigenesis.

#### **1.1.4.2 Wound Healing**

Cell senescence also contributes functionally to the process of wound repair. Wound repair is the complex but coordinated process through which tissue integrity is restored following injury or damage. The process of wound repair involves a diverse array of cellular components and pathways, but typically involves sequential progression through three distinct phases: inflammation, proliferation/new tissue formation and remodelling (Gurtner et al., 2008b). In adults, the wound repair process inevitably produces a localized region of non-functional fibrotic tissue called a scar. Recent findings suggest that senescent cells accumulate at the sites of healing wounds and restrict the formation of fibrotic tissue through the secretion of extracellular matrix remodelling enzymes.

Utilizing a mouse model of chemical-induced liver fibrosis, Scott Lowe's laboratory demonstrated that in response to carbon tetrachloride (CCl<sub>4</sub>) treatment, hepatic stellate cells (HSCs) undergo an initial proliferative expansion and produce extracellular matrix (ECM) components that comprise the fibrotic scar (Krizhanovsky et al., 2008). The activated HSCs subsequently senesce, downregulate ECM production and induce the expression of ECM degrading enzymes and immune modulators. Following termination of CCl<sub>4</sub> treatment, a significant reversion of hepatic fibrosis accompanied by the elimination of activated HSCs was observed. In contrast, livers from CCl<sub>4</sub>-treated, *p53*<sup>-/-</sup>;*INK4a/ARF*<sup>-/-</sup> senescence-defective mice continued to display marked hepatic fibrosis and numerous activated HSCs, after CCl<sub>4</sub> withdrawal. Consequently, the authors concluded that cell senescence limits the extent of chemical-induced hepatic fibrosis through the secretion of ECM degrading enzymes and by modulating the immune clearance of activated HSCs.

In a separate study utilizing a mouse model of cutaneous wound healing, it was reported that senescent fibroblasts accumulate within granulation tissue during the proliferative phase of the wound repair process (Jun & Lau, 2010). Through the use of transgenic mice, the authors showed that CCN1, a matricellular protein highly expressed in granulation tissue, is required for the accumulation of senescent cells during cutaneous wound healing. CCN1 promotes senescence in fibroblasts by inducing DNA damage, resulting in p53 and RAC-NOX1-dependent production of

reactive oxygen species (ROS) and subsequent activation of the p16INK4a/pRB pathway. Following CCN1-mediated induction of senescence, fibroblasts upregulate the expression of the ECM-degrading enzymes MMP1 and MMP3, and downregulate type I collagen, a component of the ECM. Thus, senescent cells restrict the formation of fibrotic tissue during cutaneous wound healing. Together, these studies both demonstrate a role for cell senescence in the process of normal wound repair.

#### **1.1.4.3 Aging and Cancer**

Despite the proposed beneficial roles of senescence to tumor suppression and wound healing, there is evidence to suggest that senescence might also facilitate some pathophysiological processes. This has led some researchers in the field to view senescence as a form of antagonistic pleiotropy, in which features of senescence might be beneficial early in life, but detrimental to the aged organism (Campisi & d'Adda di Fagagna, 2007). To this end, cell senescence has been implicated as a contributor to both organismal aging and cancer.

Organismal aging is associated with a variety of pathologies that are collectively characterized by a decline of normal tissue function. Indeed, there are several lines of evidence that suggest cell senescence contributes to age-associated tissue dysfunction. First, it has been reported that senescent cells accumulate with age in various tissues in humans, baboons and rodents (Dimri et al., 1995; Paradis et al., 2001; Herbig et al., 2006; Jeyapalan et al., 2007; Wang et al., 2009). To this end, many of the molecular markers of cell senescence increase with age, including SA  $\beta$ -galactosidase activity, p16INK4a induction, the presence of shortened telomeres and DNA damage signals (Dimri et al., 1995; Krishnamurthy et al., 2004; Hastie et al., 1990; Sedelnikova et al., 2004).

Several key functional studies also strongly suggest that senescence contributes to aging. Most somatic mouse tissues express sufficient levels of telomerase to maintain telomere length (Kipling, 1997). Consequently, genetic disruption of the telomerase holoenzyme (*mTR*<sup>-/-</sup>) in mouse accelerates various aging phenotypes, impairs wound healing and shortens lifespan (Rudolph et al., 1999). Inactivation of p16INK4a, a key regulator of senescence, abrogates senescence, prevents loss of tissue integrity and extends lifespan in a mouse model of premature aging (Baker et al., 2008). Utilizing the same prematurely aged mouse model, van

Deursen and colleagues subsequently generated a transgenic strain that enables drug-inducible clearance of p16INK4a-positive cells (Baker et al., 2011). Remarkably, the authors showed that drug-induced clearance of p16INK4a-positive senescent cells delays the premature adipose tissue, skeletal muscle and eye degeneration typically observed in these mice. Moreover, the clearance of p16INK4a-positive cells from tissues in which degeneration is already initiated, blocks further progression. Thus, these data confirm that senescence can promote organismal aging.

Mechanistically, senescence might promote aged-associated tissue degeneration several ways. First, senescence might restrict normal tissue regeneration by blocking the proliferative capacity of progenitor cells. To this end, several groups have reported that the abundance and proliferative capacity of progenitor cells decreases with age in a variety of tissues (Nishimura et al., 2005; Krishnamurthy et al., 2006). Second, because senescent cells secrete an array of chemokines and cytokines as part of the SASP, senescence might promote a state of chronic inflammation. In fact, chronic inflammation is a common hallmark of and contributor to numerous age-associated pathologies (Chung et al., 2009). Senescent cells also secrete a variety of extracellular matrix remodeling enzymes (e.g., MMPs) that can modify the tissue stroma (Page-McCaw et al., 2007). Thus, elevated expression of MMPs and other proteases might irrevocably alter the extracellular environment and potentiate tissue dysfunction (Burrage et al., 2006).

In addition, there is evidence that in certain contexts senescence can actually promote another age-associated disease: cancer. Work by Judith Campisi and colleagues revealed that senescent fibroblasts stimulate the proliferation of premalignant and malignant epithelial cells in culture, but have no effect on normal epithelial cells (Krtolica et al., 2001). Likewise, the authors reported that co-injection of senescent fibroblasts with pre-malignant or malignant epithelial cells into mice promotes tumorigenesis, whereas co-injection with pre-senescent fibroblasts has no effect. Campisi and colleagues subsequently demonstrated that the SASP produced by senescent fibroblasts promotes epithelial–mesenchymal transition (EMT) and enhances the invasiveness of epithelial cells *in vitro* (Coppé et al., 2008). Significantly, both EMT and invasiveness are defining characteristics of malignancy. Finally, cells depleted of IL-1a, an upstream regulator of IL6 and IL8, inhibits secretion of IL6 and IL8 by senescent cells and reduces the pro-malignant properties

of the SASP (Orjalo et al., 2009). Thus, senescent cells, and specifically the SASP, have the ability to promote cancer through a paracrine mechanism.

In light of this, it is reasonable to view senescence as an antagonistically pleiotropic response. To this end, permanent proliferation arrest and SASP are important features of senescence that undoubtedly promote tumor suppression and wound healing early in life, but ultimately become detrimental later in life.

## **1.2 Chromatin**

### **1.2.1 Chromatin Structure and Organization**

Each human cell contains approximately two meters of genetic information in the form of DNA that must be effectively packaged and organized within the nucleus. To accomplish this, DNA is subjected to a series of folds and protein interactions, forming a higher-order structure called chromatin. The basic structural unit of chromatin is the nucleosome, an octameric core of highly conserved proteins called histones, around which approximately 147 basepairs of DNA is wrapped (Richmond et al., 1984). Structural studies have revealed that the nucleosome core consists of a tripartite structure that features one tetramer comprised of two copies each of histones H3 and H4 and two histone H2A/H2B dimers (Arents et al., 1991). Each of the core histones contains two distinct structural domains, a central globular fold domain through which the histone-histone and histone-DNA interactions occur and an unstructured amino-terminal tail domain that extends from the nucleosome core (Luger et al., 1997). In addition to the histone octamer and 1.75 turns of folded DNA, each complete nucleosome contains linker DNA, which connects one nucleosome to the next (Simpson, 1978).

Based on this nucleosome/DNA interaction, if a single chromosome were to be stretched out into a linear arrangement, it would likely assume a “beads-on-a-string” conformation (Hansen, 2002). However, chromatin inevitably forms several additional higher-order structures that exhibit increasing levels of compaction culminating in the mitotic chromosome. Consequently, this raises important questions as to how this is accomplished. To this end, several *in vitro* studies demonstrated that under optimal conditions, the 10-nm “beads-on-a-string” conformation assembles into a densely packed 30-nm chromatin fiber (Gall, 1966). Since this finding, numerous attempts have been made to visualize the 30-nm fiber *in*

*situ* utilizing a variety of sensitive microscopic techniques, but have largely ended unsuccessfully (Grigoryev & Woodcock, 2012).

In recent years, several experimental models have succeeded in producing chromatin fibers approaching the 30-nm structure utilizing folded and zig-zag oriented arrays of reconstituted nucleosomes (Routh et al., 2008). However, an even more recent finding, calls into question whether the assumed 30-nm fiber really even exists as the fundamental unit of higher-order chromatin structure. Using cryo-electron microscopy and synchrotron X-ray scattering, Kazuhiro Maeshima and colleagues demonstrated that mitotic chromosomes from HeLa cells are devoid of 30-nm sized structures, but are actually comprised of approximately 11-nm fibers that are folded in an irregular fashion (Nishino et al., 2012). Thus, it is formally possible that chromosomes and other intermediate chromatin structures arise from the ~11-nm “beads-on-a-string” unit of chromatin.

Despite these unresolved controversies, what is evident is that chromatin exists in the cell in two distinct forms: gene-rich, transcriptionally active euchromatin and gene-poor, transcriptionally silent heterochromatin (Huisinga et al., 2006). This fascinating dichotomy is predominantly mediated through specific epigenetic modifications and associated proteins and dictates much of the nuclear function of the cell. Therefore, it is worth considering each of these structural and regulatory components of chromatin in greater detail.

### **1.2.2 Histone Variants**

An additional level of chromatin regulation is provided by the nucleosome through the incorporation of histone variants. Whereas the expression of most canonical histones is coupled to DNA replication and tightly regulated through the cell cycle, histone variants represent a distinct set of nonallelic histone isoforms that are not necessarily regulated in the same manner (Malik & Henikoff, 2003). Most histone variants are stably incorporated into nucleosomes and impact process ranging from transcription to replication and DNA repair (Sarma & Reinberg, 2005). Numerous histone variants have been identified, including the well-documented histone H2A variants H2AX, H2AZ, macroH2A and H2ABBD and the H3 variants H3.3 and CENP-A (Paull et al., 2000, Popescu et al., 1994; Pehrson & Fried, 1992; Gautier et al., 2004; Ahmad & Henikoff, 2002; Palmer et al., 1987). Some histone variants are expressed in a cell and tissue-dependent manner, suggesting specific

regulatory roles for the variants (Garcia et al., 2008). For example, the histone H1, H2B and H3 variants, H1T, TSH2B and H3T, respectively, are expressed solely in the testis and likely contribute to the unique regulatory requirements of that chromatin environment (Sarg et al., 2009; Zalensky et al., 2002; Tachiwana et al., 2010).

To date, variants of histone H3 have been investigated the most extensively. Several isoforms of histone H3 have been identified, including the structurally similar H3.1, H3.2 and H3.3 forms, the centromeric CENP-A variant and testis-specific H3T. Expression of canonical histone H3.1 is replication-dependent and is restricted to S phase where it is incorporated into newly synthesized DNA (Tagami et al., 2004). In contrast, the H3.3 variant is expressed throughout the cell cycle and is deposited in both replication-dependent and independent contexts (Dunleavy et al., 2011; Drané et al., 2010). Importantly, H3.3 deposition is associated with transcriptional activation, as it is typically enriched around the transcription start sites of active genes and frequently contains activating post-translational modifications (Mito et al., 2005; McKittrick et al., 2004). H3.3 is also deposited at centromeres during DNA replication, but is exchanged for another H3 variant, CENP-A, during G1 phase of the cell cycle (Dunleavy et al., 2011). Finally, deposition of the H3 variants is largely contingent upon the activity of specific histone chaperones. Whereas replication-coupled H3.1 deposition is carried out by CAF-1, H3.3 is deposited by the chaperones HIRA, ATRX and DAXX (Tagami et al., 2004; Goldberg et al., 2010).

Significant attention has also been directed toward understanding the histone H2A variants. The variant H2AX is thought to play an important role in mediating the DNA damage response. H2AX contains an extended C-terminal domain that becomes phosphorylated by ATM and DNA-PK in response to double-strand breaks, which in turn is required for the formation of DNA damage repair foci (Stiff et al., 2004; Celeste et al., 2002). H2AZ is an essential gene in mammals and is reportedly involved in transcriptional activation (Faast et al., 2001; Santisteban et al., 2000). MacroH2A contains a large C-terminal domain and its incorporation into chromatin is enriched at heterochromatic regions including inactive X chromosomes and senescence-associated heterochromatic foci (SAHF) (Costanzi & Pehrson, 1998; Zhang et al., 2005). Less is known about the H2ABBD variant, although reports indicate that it is excluded from inactive X chromosomes and its incorporation into

nucleosomes makes them less stable (Chadwick & Willard, 2001; Gautier et al., 2004). Little has been reported regarding histone H2A variant-specific chaperones, with the exception of H2AZ, which in yeast has been found in a complex that contains the SWI/SNF family member Swr1 (Mizuguchi et al., 2004; Kobor et al., 2004). Thus, additional work is required in order to determine whether individual histone variants require unique chaperone complexes for deposition and eviction.

### **1.2.3 Histone Posttranslational Modifications**

Histones provide far more than just structural support for the genome and have been implicated in nuclear processes including transcriptional regulation, DNA replication and DNA repair (Bannister & Kouzarides, 2011). In order to facilitate these processes, histones are subject to an extensive array of post-translational modifications (PTMs) (Figure 1.3a). The majority of histone modifications occur at the N-terminal tails, which as revealed by the high-resolution crystal structure of the nucleosome, protrude from the nucleosome core (Luger et al., 1997). More than sixty individual histone PTMs have been identified, including acetylation, methylation, phosphorylation, ubiquitylation, sumoylation, ADP ribosylation, deimination and proline isomerization modifications (Kouzarides, 2007). As proposed by Thomas Jenuwein and David Allis in the “histone code” hypothesis over a decade ago, combinations of these histone PTMs likely provide an important layer of regulation to the genome (Jenuwein & David Allis, 2001).

Although numerous histone PTMs have been reported, considerable emphasis has been placed on understanding one modification in particular: histone methylation. Histone methylation primarily occurs on lysine and arginine residues, but has also been reported to occur on histidine residues (Borun et al., 1972). Methylation of lysine residues occurs at the  $\epsilon$ -amino group and can exist in one of three different states: monomethylation, dimethylation or trimethylation (Murray, 1964; Paik & Kim, 1967; Hempel et al., 1968). Arginine methylation takes place on the guanidinyll group of the residue and can occur in a monomethylated, asymmetrically dimethylated or symmetrically dimethylated state (Byvoet et al., 1972; Borun et al., 1972). Histone histidine methylation has not been studied extensively.

Lysine methylation is one of the most abundant histone PTMs in the cell. As such, histone lysine methylation impacts chromatin in a variety of ways. First,

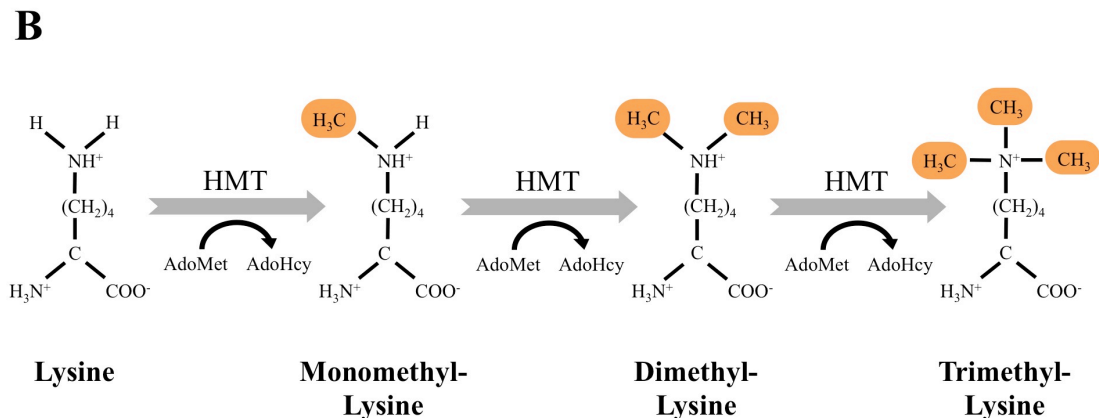
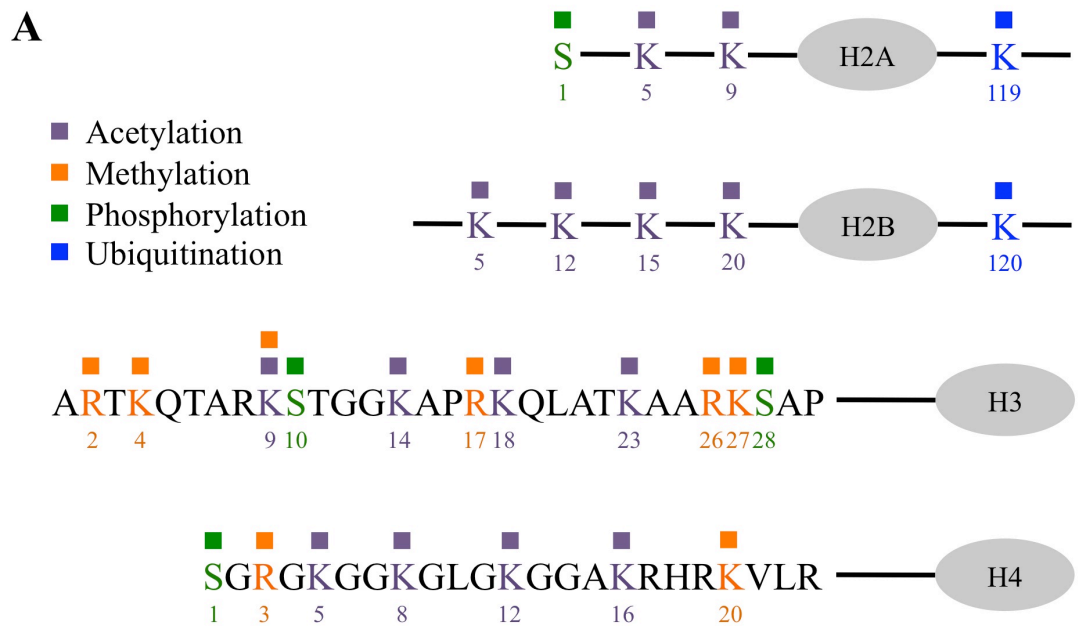


**Figure 1.3 Histones undergo extensive posttranslational modification.** (A) The core histones H2A, H2B, H3 and H4 are subject to a variety of posttranslational modifications including acetylation, methylation, phosphorylation and ubiquitination. The majority of histone modifications occur at the amino acid residues of the N-terminal tail. (B) Histones are frequently methylated on lysine and arginine residues. Histone lysine side-chains may be unmethylated or mono-, di-, or trimethylated. Lysine methylation is typically catalyzed by the enzymatic activity of SET domain-containing and non-SET domain-containing histone methyltransferases utilizing methyl groups from S-adenosyl methionine (AdoMet). Adapted from Zhang & Reinberg (2001).

several methyl-lysine marks, including methylated H3K4, H3K36 and H3K79, are commonly found at transcriptionally active genes (Bernstein et al., 2002; Santos-Rosa et al., 2002; Vakoc et al., 2006). In addition, it has been reported that methylated H3K4 and H3K36 physically interact with RNA polymerase II, suggesting that these marks indeed promote transcription (Ng et al., 2003; Krogan et al., 2003). In contrast, several well-characterized methyl-lysine marks, including H3K9me<sub>3</sub>, H3K27me<sub>3</sub> and H4K20me<sub>3</sub>, are associated with transcriptional repression and heterochromatin (Schotta et al., 2004; Pauler et al., 2009). Further exemplifying the functional diversity of histone lysine methylation, both the H3K79me<sub>2</sub> and H4K20me<sub>2</sub> marks have been reported to have roles in mediating the DNA damage response (Wakeman et al., 2012; Sanders et al., 2010). Thus, histone lysine methylation is a multifaceted and critical component of the chromatin landscape.

The methylation of histone lysine residues is catalyzed by a group of enzymes called the histone methyltransferases (HMTs), which transfer a methyl group from S-adenosyl methionine to the amino group of the lysine (Figure 1.3b). HMTs fall under one of two subcategories: SET domain-containing and non-SET domain-containing methyltransferases (Greer and Shi, 2012). SET domain proteins contain a conserved 130 amino acid catalytic domain that was first identified in the *Drosophila melanogaster* proteins *suppressor of variegation 3-9*, *enhancer of zeste* and *trithorax* (Dillon et al., 2005). Well-characterized SET domain-containing HMTs include MLL, SUV39H1, EZH2 and SUV420H2, which catalyze H3K4, H3K9, H3K27 and H4K20 methylation, respectively (Dou et al., 2006; Ait-Si-Ali et al., 2004; Pasini et al., 2004; Schotta et al., 2008). In addition, the non-SET domain containing methyltransferase DOT1L also catalyzes methylation of histone H3 lysine residues (Min et al., 2003). Finally, in recent years several histone lysine demethylating enzymes have been identified including LSD1 and the JmjC domain containing proteins, thus providing an additional level of regulation (Shi et al., 2004; Tsukada et al., 2006; Whetstine et al., 2006).

#### **1.2.4 Histone Binding Proteins**

Although the histones collectively comprise a major fraction of the total protein content of chromatin, additional non-histone effector proteins also physically associate with and modify chromatin. Importantly, many of these interactions are

mediated by the ability of the effectors to recognize specific chemical moieties in the form of histone PTMs (Taverna et al., 2007). To accomplish this, the effector proteins contain specialized domains or modules that bind specific motifs with high affinity. Although numerous histone binding proteins have been identified, they can be reduced to a few distinct categories based on their binding modules. To this end, the most prominent binding modules include bromodomains, chromodomains, Tudor domains and PHD fingers (Taverna et al., 2007).

Bromodomains (BRDs) are highly conserved 120-amino acid domains that recognize acetylated lysine residues with high selectivity (Filippakopoulos et al., 2012). In humans there are over 40 BRD-containing proteins, including several histone acetyltransferases (HATs) and the HAT co-activator p300/CBP-associated factor (PCAF) (Dhalluin et al., 1999; Filippakopoulos & Knapp, 2012). Despite the highly conserved structure of BRDs, individual BRD-containing proteins exhibit selectivity for different acetylated lysines. For example, whereas the BRD-containing transcription factor FALZ recognizes H4K5ac, the yeast HAT Gcn5p preferentially binds H4K16ac (Filippakopoulos et al., 2012; Owen et al., 2000). This variable selectivity likely enables the effectors to modulate highly specific targets.

In contrast, several distinct protein interaction modules specifically bind methyl-lysine marks, including chromodomains, Tudor domains and PHD fingers. Chromodomains are 40-50-amino acid long motifs present in several chromatin remodelling enzymes that bind di- and trimethylated histone lysine residues (Taverna et al., 2007). For example, the SET domain-containing histone methyltransferase SUV39H1 also contains a chromodomain. Remarkably, deletion of the SUV39H1 chromodomain impairs enzymatic activity demonstrating the interdependence of the binding and catalytic domains (Chin et al., 2006). The Tudor domain is another 50-amino acid module that specifically binds histone methyl-lysines. The double Tudor domain-containing histone demethylase, JMJD2A, binds H4K20me<sub>2</sub> with high affinity, H3K9me<sub>3</sub> with low affinity and actively demethylates H3K9me<sub>3</sub>, revealing one mechanism of histone crosstalk (Ozboyaci et al., 2011). PHD domains represent a third class of histone methyl-lysine binding modules comprised of a Cys<sub>4</sub>-His-Cys<sub>4</sub> structural motif that frequently associate with H3K4me<sub>2</sub>/me<sub>3</sub>. Prominent examples of PHD-containing chromatin effectors include the histone methyltransferase MLL, the nucleosomal remodelling factor BPTF and the DNA methyltransferase accessory protein DNMT3L (Fair et al., 2001; Li et al., 2006; Aapola et al., 2002). Importantly,

the aforementioned binding modules provide important mechanistic links between seemingly autonomous chromatin remodelling processes including histone lysine methylation, demethylation and acetylation, nucleosome remodelling and transcription.

### **1.2.5 Nucleosome Positioning**

Nucleosome density can profoundly affect the structure and function of chromatin. Consequently, nucleosome positioning reflects another important mechanism through which chromatin structure can contribute to the regulation of gene expression. Studies of nucleosome positioning in a variety of species have revealed that nucleosomes are not even distributed across the genome (Yuan et al., 2005; Johnson et al., 2006; Lee et al., 2007; Dennis et al., 2007). For example, the transcribed regions of genes usually exhibit a higher density of nucleosomes than promoters or regulatory elements (Bai & Morozov, 2010). Several groups have reported that while nucleosomes are typically present at the transcription start sites (TSS) of most unexpressed genes, expressed genes and genes containing transcriptional pre-initiation complexes at their promoters are largely devoid of nucleosomes at the TSS (Ozsolak et al., 2007; Schones et al., 2008). In addition, the nucleosome-poor regions around the TSS of active genes also exhibited high levels of transcription factor and RNA polymerase II binding. Thus, nucleosome-free regions likely permit transcription binding and gene expression.

A body of data suggests that nucleosome positioning is governed in a variety of ways. First, the underlying DNA sequence appears to dictate nucleosome positioning to a certain degree. Indeed, nucleosomes have higher affinities for specific DNA sequences and in yeast nearly 50% of nucleosome positions are likely determined by the genomic sequence (Sekinger et al., 2005; Segal et al., 2006). Second, nucleosomes positioning is also regulated by ATP-dependent histone chaperones, which deposit and evict nucleosomes at promoters for the purposes of transcriptional repression and activation, respectively (Williams & Tyler, 2007). For example, in yeast, Asf1-mediated eviction of histones is required for the transcriptional activation of certain promoters (Korber et al., 2006). Similarly, the histone chaperone Spt6 is required for histone deposition and subsequent repression of several yeast promoters (Adkins & Tyler, 2006).

Finally, there is evidence emerging that insulators, including the enhancer-blocker protein CTCF, are involved in determining nucleosome position. Integrative analysis of several genome-wide datasets revealed that nucleosome positioning is relatively variable across the genome, except at gene the TSS of genes and adjacent to CTCF binding sites (Fu et al., 2008). In fact, nucleosome positioning at CTCF sites is even less variable than that of the TSS. To this end, nucleosome positioning might play an important role in maintaining genomic boundaries as well.

### 1.2.6 DNA Methylation

DNA is also subject to chemical modification in the form of DNA methylation, an important structural and regulatory feature of chromatin. The process of DNA methylation involves the transfer of a methyl group from S-adenosyl methionine to the 5 position of the carbon ring of cytosine residues and typically occurs within the context of CpG dinucleotides (Bird, 2002). Approximately 1% of all nucleotides in the human genome are comprised of 5-methylcytosine (5mC) in somatic cells (Ehrlich et al., 1982). Likewise, approximately 70% of all CpG dinucleotides in the human genome contain the 5mC mark (Strichman-Almashanu et al., 2002).

Short regions of high CpG dinucleotide density called CpG islands are present at more than 50% of all genes in the human genome (Gardiner-Garden & Frommer, 1987). However, individual CpGs are also dispersed throughout the genome and tend to account for the majority of 5mC (Gama-Sosa et al., 1983; Bird et al., 1995). As a result, the cytosine residues within the CpG islands of genes are largely unmethylated. Despite this trend, methylation of CpG islands has been reported in the contexts of imprinted genes and the X chromosome inactivation (Ferguson-Smith et al., 1993; Yen et al., 1984).

The process of DNA methylation is catalyzed by the enzymatic activities of a family of enzymes called the DNA methyltransferases (DNMTs). To date, three DNMT family members have been identified: DNMT1, DNMT3a and DNMT3b. DNMT1, functioning as the maintenance DNA methyltransferase, preferentially catalyzes the methylation of hemimethylated CpGs during DNA replication and repair, likely through interactions with PCNA and Np95/Uhrf1, respectively (Chuang et al., 1997; Sharif et al., 2007; Arita et al., 2008; Avvakumov et al., 2008). In contrast, the *de novo* DNA methyltransferases DNMT3a and DNMT3b are capable

of methylating CpG DNA irrespective of the initial methylation status (Hsieh, 1999; Gowher et al., 2005). Although no bona fide DNA demethylase has been confirmed, several demethylase candidates and mechanisms are currently being investigated (Cortázar et al., 2011; Iqbal et al., 2011; Cortellino et al., 2011).

Functionally, DNA methylation has been implicated in a variety of processes including gene regulation, X chromosome inactivation, genomic imprinting and development. DNA methylation is present infrequently at the CpG islands of genes, and targeted methylation is not thought to contribute causally to gene silencing. However, data indicate that some genes indeed gain DNA methylation, but that gene silencing precedes acquisition of the 5mC mark, suggesting that methylation might serve to reinforce long-term gene inactivation (Ohm et al., 2007; Schlesinger et al., 2007). In a similar manner, DNA methylation contributes to long-term gene silencing in the context of X chromosome inactivation (Panning & Jaenisch, 1998; Sharp et al., 2011). An important role for DNA methylation in the control of genomic imprinting, in which genes are either expressed or silenced in a parent-of-origin-specific manner, has also been demonstrated (Li et al., 1993; Ferguson-Smith & Surani, 2001). Finally, DNA methylation is critically important to normal development, as targeted disruption of *Dnmt1* causes a global reduction of 5mC that is embryonically lethal in mice (Li et al., 1992). Thus, DNA methylation is an important epigenetic contributor to diverse aspects of chromatin regulation and function.

### **1.2.7 Non-Coding RNA**

In addition to DNA and protein, recent studies reveal a critical role for RNA as both a structural and regulatory component of eukaryotic chromatin. A considerable fraction of chromatin is comprised of RNA. For example, analysis of chromatin purified from chicken liver revealed RNA to constitute approximately 2-5% of the total nucleic acid content (Rodriguez-Campos & Azorin, 2007). Not surprisingly, as many as 93% of all nucleotides in the human genome have been identified as being present in primary transcripts (Birney et al., 2007). Although the genome is highly transcribed, approximately only 1.5% of the genome is comprised of protein coding genes (Venter et al., 2001; International Human Genome Sequencing Consortium, 2004). Consequently, a large proportion of transcripts represent non-coding RNA (ncRNA).

In humans, ncRNA constitutes a considerable fraction of total chromatin-associated RNA (CAR). One study characterizing the RNA content of chromatin in human fibroblasts indicated that 71% of total CAR was derived from intergenic and intronic regions, whereas only 29% corresponded to exons (Mondal et al., 2010). Given the sheer abundance of ncRNAs, considerable effort is now being directed toward deciphering the functional significance of these transcripts. Indeed, a growing body of data now supports a role for long ncRNA (lncRNA) in the regulation of chromatin structure and gene expression (Saxena & Carninci, 2011). In particular, significant regulatory roles have been revealed for four of the best-characterized lncRNAs: *Kcnq1ot1*, *Airn*, *Xist* and *HOTAIR*.

*Kcnq1ot1* is a 91 kilobase-long lncRNA that is involved in the lineage-specific transcriptional silencing of multiple genes within the imprinted *Kcnq1* domain (Pandey et al., 2008). Specifically, *Kcnq1ot1* promotes the formation of long stretches of H3K9me3 and H3K27me3 enriched silent chromatin, by recruiting the histone methyltransferases G9a and PRC2, respectively. Targeted disruption of the *Kcnq1ot1* transcript in mice restores expression of multiple genes within the *Kcnq1* locus that are ordinarily paternally repressed (Mancini-Dinardo et al., 2006). Similarly, *Airn*, an ncRNA expressed in human and mouse, regulates the imprinted expression of the *Slc22a3*, *Slc22a2* and *Igf2r* genes (Sleutels et al., 2002; Yotova et al., 2008). *Airn* recruits G9a to the promoters of these genes, resulting in H3K9me3-mediated silencing (Nagano et al., 2008). Thus, *Kcnq1ot1* and *Airn* actively mediate epigenetic imprinting control.

In female mammals, epigenetic inactivation of a single X chromosome occurs during embryonic development and differentiation as a form of dosage compensation, and is regulated in part by the ncRNA *Xist* (Brown et al., 1991; Penny et al., 1996). Encoded within the 1 megabase-long chromosome X inactivation center, *Xist* determines which X chromosome will become inactive and facilitates the spreading of epigenetic silencing marks across the chromosome (Marks et al., 2009). Importantly, *Xist* is negatively regulated by another ncRNA, *Tsix*, which is concomitantly repressed during X-inactivation (Marks et al., 2009). This illustrates an important role for ncRNAs in wide-scale chromatin regulation.

Finally, there is also evidence that lncRNAs can mediate long-range regulation of defined genomic loci. The lncRNA *HOTAIR*, encoded within the *HOXC* locus of human chromosome 12, represses the transcription of a 40 kilobase-

long domain of the *HOXD* locus of chromosome 2 (Rinn et al., 2007). Mechanistically, *HOTAIR* silences the *HOXD* locus through the recruitment of the Polycomb Repressive Complex 2 (PRC2) and the LSD1/CoREST/REST complex, thus facilitating methylation of histone H3K27 and demethylation of H3K4 (Tsai et al., 2010). Remarkably, lncRNAs can serve as structural scaffolds capable of targeting chromatin modifiers to distant genomic loci. Collectively, these data illustrate the varied functions that ncRNAs serve in the regulation of chromatin.

### 1.2.8 Lamins

The nuclear lamina is a dense meshwork of filamentous structural proteins that lines the inner surface of the nuclear envelope (Bridger et al., 2007). As such, the nuclear lamina plays a crucial role in maintaining the size, shape and integrity of the nucleus. Structurally, the lamina is comprised of the A- and B-type nuclear lamins, which include lamin A, lamin C, lamin B1 and lamin B2 (Dechat et al., 2008). Lamins A and C are both encoded by the *LMNA* gene and result from alternative splicing (Lin & Worman, 1993). The Lamin B1 and B2 proteins are encoded by two separate genes: *LMNB1* and *LMNB2*, respectively (Lin & Worman, 1995; Höger et al., 1990; Biamonti et al., 1992).

In addition to providing structural integrity to the nucleus, lamins contribute to a variety of nuclear functions including chromatin organization, gene transcription and DNA replication (Shimi et al., 2008). First, in flies, mice and humans, it has been reported that chromatin physically interacts with the nuclear lamina through a series of domains termed lamina-associated domains (LADs) (Pickersgill et al., 2006; Guelen et al., 2008; Peric-Hupkes et al., 2010). Remarkably, most of the genes contained within LADs are transcriptionally inactive. In contrast, lamins also appear to play a role in promoting gene expression, as silencing or inactivation of lamins A and B1 impairs RNA polymerase II-dependent transcription (Spann et al., 2002; Tang et al., 2008; Shimi et al., 2008). Finally, lamins reportedly contribute to DNA replication. To this end, lamins co-localize with PCNA at replication foci as well as at sites of BrdU incorporation (Moir et al., 1994; Kennedy et al., 2000). In addition, DNA replication is blocked by the expression of lamin B dominant negative mutants (Spann et al., 1997; Moir et al., 2000).

Lamin mutations are associated with numerous human diseases, including Hutchinson–Gilford Progeria Syndrome (HGPS) (Dittmer & Misteli, 2011). Caused

by mutation of the *LMNA* gene that results in expression of an abnormal form of lamin A called progerin, HGPS is characterized by an accelerating aging phenotype in children and premature death (Uitto, 2002). Further underscoring the role of lamins in maintaining genomic integrity, cells isolated from HGPS patients exhibit an array of chromatin abnormalities. First, it was reported that in female HGPS fibroblasts, the H3K27me3 histone mark is lost from the inactive X chromosome and is accompanied by reduced expression of the H3K27 histone methyltransferase EZH2 (Shumaker et al., 2006). In addition, HGPS cells contain lower levels of H3K9me3 and exhibit an altered pattern of localization between the mark and heterochromatin protein 1 (HP1) and CREST, suggesting that constitutive heterochromatin is disrupted in the cells. Intriguingly, levels of H4K20me3, another constitutive heterochromatin mark, were markedly elevated in HGPS cells. Collectively, the data illustrate how lamin dysfunction can influence chromatin structure.

### **1.3 Chromatin Dynamics in Cell Senescence**

#### **1.3.1 Senescence-Associated Heterochromatic Foci**

As cells undergo senescence, they typically exhibit profound changes to chromatin structure. Probably the most striking and widely documented manifestation of chromatin reorganization in senescent cells is the formation of senescence-associated heterochromatic foci (SAHF) (Figure 1.4). First reported by Scott Lowe's laboratory, SAHF represent distinct structures of facultative heterochromatin that appear as punctate foci following staining of senescent cells with the DNA dye 4',6-diamidino-2-phenylindole (DAPI) (Narita et al., 2003). The number of visible SAHF foci per cell varies, but typically ranges from approximately 30-50, with each focus arising from compaction of an individual chromosome (Funayama et al., 2006; Zhang et al., 2007). Although SAHF is reflective of a heterochromatic state, domains of constitutive heterochromatin including telomeres and pericentromeres largely localize to the periphery of SAHF (Narita et al., 2003; Funayama et al., 2006; Zhang et al., 2007, Chandra et al., 2012).

Initial molecular analysis of SAHF composition revealed that the foci contain the heterochromatic histone modification H3K9me, but largely exclude the euchromatic H3K9ac and H3K4me marks (Narita et al., 2003; Narita et al., 2006).

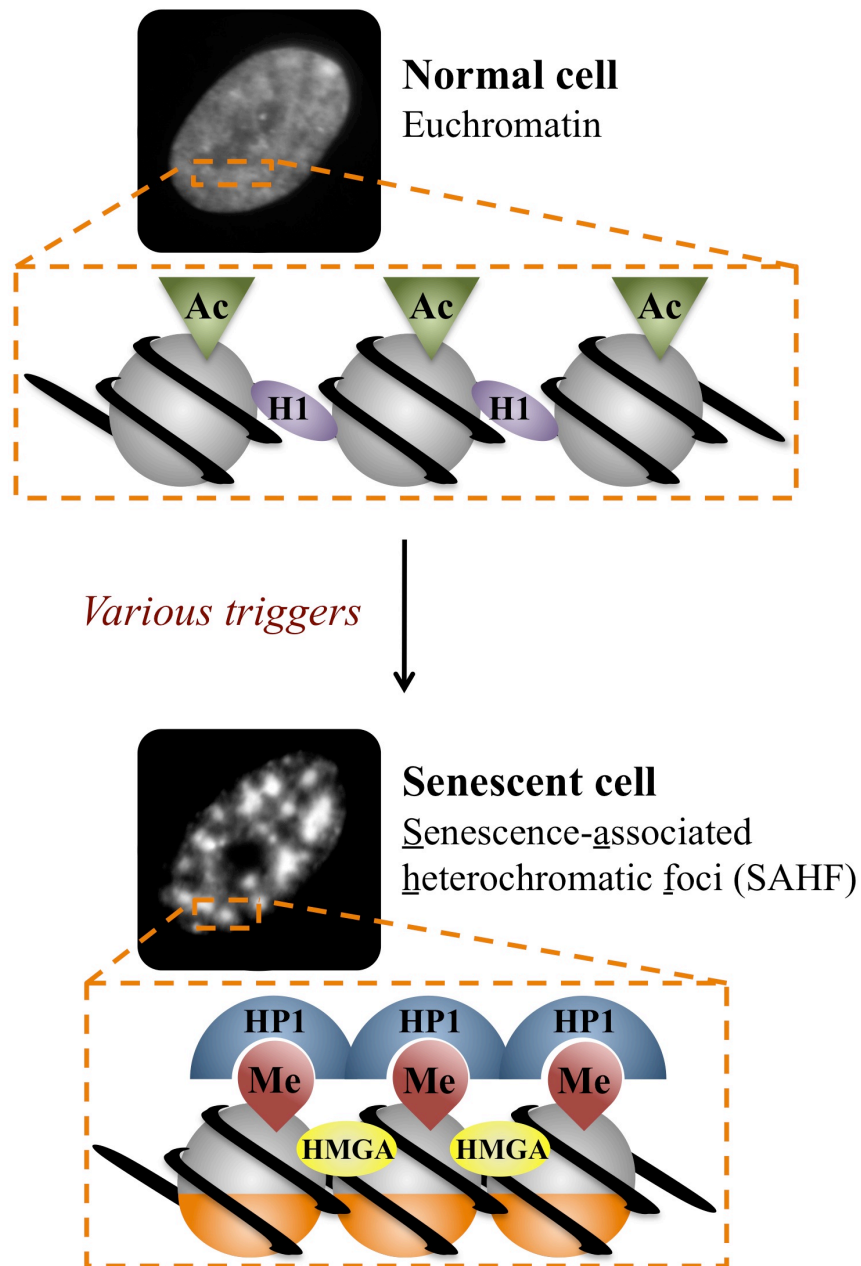


**Figure 1.4 Senescence-associated heterochromatic foci (SAHF).** Senescent cells exhibit profound chromatin remodeling which can be visualized in cells through DAPI staining and epifluorescence microscopy. Whereas proliferating cells typically display a diffuse nuclear DAPI staining pattern, senescent cells display the presence of prominent DAPI-rich foci called SAHF. SAHF reflect a compact chromatin structure and are enriched for repressive histone modifications, the histone variant macro-H2A, HP1 proteins and HMGA proteins.

More recent work from Masashi Narita's lab indicates that SAHF do not form through the spreading of repressive histone modifications, but rather through the spatial reorganization of existing domains of repressive marks into focal structures (Chandra et al., 2012). This work also elegantly showed that H3K9me3 localizes solely to the SAHF core and is surrounded by a ring of H3K27me3, while H3K9me2 is present across the entire SAHF focus. Additional components of SAHF include the histone H2A variant, macroH2A, heterochromatin protein 1 (HP1) and the high-mobility group A (HMGA) proteins (Narita et al., 2003; Narita et al., 2006; Zhang et al., 2005).

Some progress has been made in deciphering the molecular mechanisms by which SAHF is regulated. Several reports indicate that SAHF formation is at least partially, if not fully dependent on the activities of the p16INK4a-pRB and p53 pathways (Narita et al., 2003; Chan et al., 2005; Ye et al., 2007a). To this end, in IMR90 cells, knockdown of either p16INK4a or pRB is insufficient to prevent RAS-induced proliferation arrest but does abolish SAHF formation (Narita et al., 2003). Although correlative, BJ fibroblasts induced to senescence by either replicative exhaustion or exposure to DNA-damaging agents fail to induce p16INK4a and do not form SAHF, providing additional evidence of a critical role for p16INK4a in the formation of SAHF (Kosar et al., 2011).

The chromatin regulators HIRA and ASF1a also appear to play an important role in mediating SAHF formation (Zhang et al., 2005). Upon downregulation of the Wnt ligand, Wnt2, in presenescent primary human fibroblasts, GSK3 $\beta$  phosphorylates the histone chaperone HIRA, resulting in translocation of HIRA to promyelocytic leukemia (PML) nuclear bodies (Ye et al., 2007b). HIRA translocation to PML bodies subsequently promotes SAHF formation, potentially through an interaction with HP1 (Zhang et al., 2007). Also consistent with the putative role for HIRA in the formation of SAHF, in senescent mouse embryonic fibroblasts (MEFs), HIRA does not translocate to PML bodies and the cells fail to form discrete SAHF foci (Kennedy et al., 2010). Alternatively, some other difference between the mouse and human senescence programs might account for the inability of MEFs to form proper SAHF.

Regardless of the precise mechanism, it is clear that the formation of SAHF in senescent cells reflects a profound reorganization of chromatin structure and likely mediates important functions of the senescence program. It was initially suggested

that SAHF might reinforce the senescence proliferation arrest, by suppressing the expression of proliferation genes. Supporting this concept, the cyclin A2 gene acquires the repressive H3K9me histone mark and co-localizes with SAHF foci in senescent cells (Narita et al., 2003; Zhang et al., 2007). Likewise, sites of active transcription are predominantly excluded from SAHF (Narita et al., 2003; Funayama et al., 2006).

However, Fabrizio d'Adda di Fagagna and colleagues recently postulated a different functional role for SAHF, arguing that formation of SAHF serves to dampen the DNA damage response (DDR) following oncogene-induced replication stress (Di Micco et al., 2011). In the study, the authors showed that two distinct forms of heterochromatin exist in senescent cells, one that acts locally to suppress gene expression and another large-scale form, SAHF, which serves to blunt the DDR. The authors also demonstrated that the local heterochromatin formation is mediated through ATM, whereas the formation of SAHF is mediated by ATR. Intriguingly, inactivation of ATM or p53 in RAS-induced cells allowed cells to continue to proliferate, even in the presence of prominent SAHF, indicating that SAHF is not responsible for the silencing of proliferation genes.

### **1.3.2 Histone Modifications and Senescence**

Posttranslational histone modifications play a critical role in the regulation of chromatin structure and function. As such, histone modifications can influence diverse processes ranging from control of gene transcription to the maintenance of higher order chromatin structure. Consequently, the altered pattern of gene expression and profound structural changes to chromatin exhibited by senescent cells are likely mediated at least in part by histone marks. In fact, there is considerable evidence accumulating to suggest this is the case.

As discussed above, work from Scott Lowe's laboratory provided some of the first data implicating histone modifications in the formation of facultative heterochromatin (e.g. SAHF) in senescent cells (Narita et al., 2003). As discussed above, Lowe and colleagues demonstrated that SAHF contain enrichment of the H3K9me modification, but are largely devoid of the euchromatic histone marks H3K9ac and H3K4me. Importantly, the authors also found that in senescent cells, levels of the repressive H3K9me modification increased at the promoters of CCNA2 and PCNA, two E2F target genes that are downregulated during senescence.

Expanding on these earlier observations, Masashi Narita's laboratory subsequently reported that SAHF reflect a spatial rearrangement of regions of chromatin containing pre-existing histone modifications rather than local changes to histone marks (Chandra et al., 2012). Using confocal microscopy, Narita and colleagues elegantly showed that SAHF are comprised of discrete layers of chromatin containing the H3K9me3, H3K9me2 and H3K27me3 modifications, respectively. The SAHF core primarily contains H3K9me3-enriched regions of chromatin and is surrounded by layers of H3K9me2 and H3K27me3. In contrast, the active mark H3K36me3 is largely excluded from SAHF. These findings suggest that histone modifications contribute to higher-order chromatin structure in senescent cells.

Recently, Scott Lowe's laboratory utilized quantitative mass spectrometry in order to screen for global histone modification changes during RAS-induced senescence (Chicas et al., 2012). Consistent with the formation of heterochromatin, the abundances of several repressive histone modifications increase in senescent cells including H3K9me3, H3K27me3 and H4K20me3. In contrast, the RAS-induced senescent cells exhibit a profound loss of H3K4me3, a mark that typically coincides with transcriptional activation. A marked reduction of H3K4me3 levels was also observed in senescent cells induced by either prolonged passage in culture (RS) or etoposide treatment. ChIP-seq of H3K4me3 in proliferating and senescent cells revealed that the mark is predominantly lost at E2F target genes, which are required for proliferation. The authors subsequently showed that pRB mediates H3K4me3 removal at E2F target genes during senescence via recruitment of the histone demethylases Jarid1a and Jarid1b. Importantly, this study illustrates how specific histone modification changes can regulate gene expression during senescence.

Finally, there is evidence to suggest that histone modification changes also contribute to another important feature of senescence: p16INK4a induction. The *INK4a* gene is located within the *INK4b-ARF-INK4a* locus and is controlled by tightly regulated epigenetic mechanisms (Gil & Peters, 2006). Work from Kristian Helin's laboratory showed that in normal proliferating human fibroblasts, the oncoprotein BMI1 directly binds and represses *INK4a* through a mechanism that involves H3K27me3 and the EZH2 and SUZ12-containing Polycomb-Repressive Complex 2 (PRC2) (Bracken et al., 2007). As cells approach senescence, EZH2 expression decreases, which results in a reduction of H3K27me3 at the *INK4a*

promoter, loss of BMI1 binding at the locus and activation of *INK4a* transcription. Similarly, depletion of EZH2 or SUZ12 is sufficient to alleviate BMI1 binding, activate *INK4a* expression and induce senescence. Thus, these data confirm that local histone modification changes can mediate important aspects of the senescence program.

### **1.3.3 Histone Loss and Senescence**

The profound chromatin remodelling that occurs as cells undergo senescence is likely at least partially mediated through changes in histone dynamics. Histone gene expression is a tightly controlled process regulated by both transcriptional and post-transcriptional mechanisms (Ma et al., 2000, Zhao et al., 2000). The expression of most canonical histone genes is tightly coupled to DNA replication and cell cycle progression, culminating in a robust upregulation of histone proteins specifically during S phase (Osley, 1991). Consequently, the expression of replication-dependent histones is largely suppressed in non-proliferating cells. For example, a significant repression of histone gene expression has been observed in quiescent human and murine fibroblasts (Coppock et al., 1993, Zahradka et al., 1993). Likewise, during terminal differentiation, histone gene expression is inhibited at the level of transcription as cells differentiate and exit the cell cycle (Stein et al., 1989). Not surprisingly, the expression of replication-dependent histone genes is also repressed in senescent human diploid fibroblasts (Pang & Chen, 1994).

Although de novo histone synthesis is attenuated in the quiescent and terminally differentiated states, levels of chromatin-bound histones appear to remain unperturbed in these cells. For example, while mRNA levels of HIST1H1D, a gene that encodes the linker histone H1, become undetectable in quiescent human WI-38 fibroblasts, the chromatin-bound levels of histone H1 remain identical to that of proliferating WI-38 cells (Funayama et al., 2006). In contrast, evidence is emerging that chromatin-bound histones are actually lost from senescent cells. To this end, Fuyuki Ishikawa and colleagues reported that the linker histone H1 is lost in senescent primary human fibroblasts induced by either oncogenic activation, prolonged culturing or activation of stress-induced p38 MAP kinase signalling (Funayama et al., 2006). The authors also showed that histone H1 loss occurs through a post-transcriptional mechanism and contributes to the formation of SAHF.

Several additional groups have subsequently reported that aging yeast and senescent human cells contain reduced protein levels of the core histones. Work from Shelley Berger's laboratory revealed that compared to young cells, old *Saccharomyces cerevisiae* exhibit profound histone loss at several subtelomeric loci and moderate histone loss at numerous other regions (Dang et al., 2009). Similarly, Jessica Tyler's laboratory reported a marked reduction of global histone levels in aged *Saccharomyces cerevisiae* (Feser et al., 2010). Remarkably, the authors also found that overexpression of histones H3 and H4 significantly extended lifespan in wild-type yeast. Finally, Jan Karlseder and colleagues reported that core histone protein levels decrease in IMR90 cells during replicative aging or after bleomycin-induced DNA damage (O'Sullivan et al., 2010). Based on their findings, the authors proposed that the stress of progressive telomere shortening during replicative aging inhibits DNA synthesis and destabilizes histone chaperones, which in turn alters the chromatin landscape, resulting in degradation of the core histones. Taken together, these studies confirm that global histone levels indeed decrease during replicative aging and likely during senescence.

#### **1.3.4 DNA Methylation and Senescence**

Methylation of DNA on cytosine residues within the CpG dinucleotide context is an important and stable epigenetic modification that contributes to transcriptional repression. Consequently, DNA methylation plays an important role in maintaining genomic integrity and function (Lengauer et al., 1997; Chen et al., 1998b). In light of the profound chromatin changes that occur during senescence, it is not surprising that DNA methylation patterns are also altered in senescent cells. Seminal work from Peter Jones' laboratory demonstrated that the aging of normal human diploid fibroblasts in culture is accompanied by a prominent reduction of global 5-methylcytosine content (Wilson & Jones, 1983). While this work was not conducted explicitly in senescent cells, it implicated DNA methylation changes in the replicative aging process.

Subsequent studies confirmed that genome-wide 5-methylcytosine patterns are indeed altered in senescent cells. One group reported reductions of both 5-methylcytosine and the expression of the DNA methyltransferase DNMT1 in replicative senescent and oxidative stress-induced senescent human embryonic lung fibroblasts (Zhang et al., 2008). Recent work from Peter Adams' laboratory also

revealed that replicative senescent IMR90 cells exhibit a marked reduction of DNA methylation at late-replicating regions of the genome and lamina-associated domains and increased methylation at some CpG islands (Cruickshanks et al., submitted). DNA methylation profiling conducted on a panel of early passage and senescent mesenchymal stem cells (MSC) identified numerous CpG sites that consistently become either differentially hypomethylated or hypermethylated during senescence (Schellenberg et al., 2011). Importantly, the authors also found that CpG sites that become hypomethylated in senescence are associated with enrichment of the H3K4me3 histone mark, whereas the CpG sites that become hypermethylated are associated with the repressive histone marks H3K27me3 and H3K9me3. Building on this work, the same group recently identified a senescence DNA methylation signature, which based on the methylation levels of six CpG sites, can accurately predict the replicative age and state of senescence of cells in culture (Koch et al., 2012).

Finally, there is emerging evidence that the expression of some genes and non-coding transcripts is regulated at least in part through changes in DNA methylation during replicative aging and senescence. To this end, several genes involved in cell cycle progression, including CDK2, CDK4 and PCNA, or DNA replication, including POLD4, POLE and RFC2, become differentially hypermethylated in late passage MSCs relative to early passage cells, and possibly contribute to the onset of senescence (Choi et al., 2011). Methylation changes have also been described at non-genic loci in senescent cells. Demethylation of the pericentromeric human satellite 3 (HS3) repeats of chromosome 1 has been reported in replicative senescent MRC5 cells, and is associated within increased transcription of the locus (Erukashvily et al., 2007). These data collectively support a functional role for DNA methylation in transcriptional regulation during senescence. It is important to note that to date, the majority of work focused on defining the senescent DNA methylome has been conducted in replicative senescent cells, and altered patterns of DNA methylation have not yet been described for oncogene-induced senescent cells.

### **1.3.5 Lamins and Senescence**

Given the important contribution of the nuclear lamins to the regulation of chromatin structure and function, it is important to consider how dysregulation of

lamins might influence the chromatin state of senescent cells. To this end, a considerable body of data has accumulated implicating lamin dysregulation as a driver of premature senescence in a variety of cellular contexts. First, it has been widely reported that primary cells isolated from Hutchinson-Gilford Progeria Syndrome (HGPS) patients harboring variety of lamin A defects, undergo accelerated senescence in culture (McClintock et al. 2006; Taimen et al. 2009). Importantly, various lamin A mutations have been shown to promote an accelerated senescence phenotype in non-HGPS contexts as well. For example, primary myoblasts isolated from a patient with a lamin A arginine 545 to cysteine point mutation displayed an abnormal nuclear morphology, nuclear accumulation of p21 and a higher percentage of SA  $\beta$ -gal-positive cells, when compared to myoblasts expressing WT lamin A (Kandert et al., 2009). Similarly, the overexpression of lamin A mutants in 82-6pBlox human diploid fibroblasts resulted in abnormal nuclear morphology, accelerated rates of telomere loss and the premature onset of senescence (Huang et al., 2008).

Premature senescence has also been reported in cells lacking sufficient levels of the mature processed forms of lamin A/C. Depletion of lamin A/C from IMR90 cells results in conversion to a large flattened cellular morphology, induction of a p53-mediated cell cycle arrest and concomitant expression of multiple senescence markers (Moiseeva et al., 2011). Similarly, compared to normal human dermal fibroblasts, fibroblasts null for lamin A/C expression accumulate excessive ROS and undergo accelerated senescence following exposure to mild oxidative stress (Pekovic et al., 2011). Finally, accumulation of unprocessed pre-lamin A, either through direct overexpression or through knockdown of the pre-lamin A processing enzyme Zmpste24/FACE1, results in mitotic defects, impaired nuclear integrity and accelerated senescence in vascular smooth muscle cells (Ragnauth et al., 2010).

In addition to the role that dysregulation of the nuclear lamina plays in initiating the onset of senescence, lamin perturbations also occur as a downstream consequence of senescence. Recent work from Robert Goldman's laboratory revealed that in replicative senescent WI-38 human dermal fibroblasts, lamin B1 protein levels decrease by 80-90%, yet remain unaffected in quiescent WI-38 cells (Shimi et al., 2011). The authors also observed a comparable reduction of lamin B1 in senescent WI-38 cells resulting from expression of oncogenic H-RASG12V.

Research conducted by Judith Campisi's laboratory similarly demonstrated that lamin B1 levels decrease in multiple human diploid fibroblast cell lines following induction of senescence by exposure to ionizing radiation, repeated passage in culture, expression of H-RASG12V or continuous p38 MAP kinase activity (Freund et al., 2012). The authors also showed that lamin B1 loss during senescence occurs after activation of either the pRB or p53 pathways, but is independent of the NF- $\kappa$ B, p38 MAPK, ATM and ROS signalling pathways. Importantly, both of these studies suggest that lamin B1 loss is a novel marker of senescence.

#### **1.4 Aim of the Study**

Chromatin structure undoubtedly plays an integral part in the establishment and reinforcement of cell senescence. As discussed above, chromatin undergoes extensive remodeling upon induction of senescence and contributes functionally to important processes including the maintenance of a permanent proliferation arrest and dampening of the DDR. Indeed, the formation of facultative heterochromatin domains, either locally or in the form of SAHF, appears to contribute significantly to both of these processes. Thus, chromatin structure has the potential to influence essential biological processes ranging from tumor suppression to wound healing.

Since the histone code was first proposed, considerable effort has been directed toward understanding how specific histone modifications impact various aspects of chromatin including gene regulation and higher-order chromatin structure. In light of the overt chromatin changes that accompany senescence, several laboratories have investigated the relationship between histone marks and chromatin structure in senescent cells. To this end, elegant work from the laboratories of Scott Lowe, Masashi Narita and others has provided critical insight into the epigenetic underpinnings of senescence-specific chromatin changes.

Despite the current progress, there is much to learn with regards to how individual histone marks might influence the chromatin landscape of senescent cells. More specifically, are specific histone modifications individually capable of regulating features of the senescence program such as gene expression or proliferation arrest? In order to address this question, I first wanted to identify a histone mark that might be of relevance to cell senescence. Therefore, after a thorough review of the literature and given the putative importance of

heterochromatin to senescence, I selected the histone H4 lysine 20 trimethyl (H4K20me3) modification for further investigation.

Histone H4 lysine 20 trimethylation is an evolutionarily conserved histone modification that is found in *S. pombe*, *D. melanogaster* and mammals (Schotta et al., 2004; Sanders et al., 2004). The H4K20me3 mark is typically present at a relatively low abundance in the cell and occupies only 5% of all histone H4 molecules in HeLa S3 cells (Pesavento et al., 2008). Unlike numerous other histone modifications, H4K20me3 levels remain stable and fluctuate very little throughout the cell cycle (Pesavento et al., 2008). In humans, the SET domain-containing HMTs SUV420H1 and SUV420H2 are both capable of methylating histone H4 at lysine 20, although SUV420H2 preferentially deposits the H4K20me3 mark (Schotta et al., 2004; Yang et al., 2008). Subsequent loss-of-function studies confirmed that Suv4-20h2 is indeed responsible for the majority of H4K20me3 deposition in mice, while SUV420H2 confers the mark in human cells (Schotta et al., 2008; Kapoor-Vazirani et al., 2011).

An increasing body of literature indicates that H4K20me3 localizes to domains of constitutive heterochromatin and likely contributes to the transcriptional silencing of these regions. As reported by Thomas Jenuwein and colleagues, the H4K20me3 modification is highly enriched at pericentric heterochromatin in *Drosophila*, mouse embryonic fibroblasts (MEFs) and HeLa cells (Schotta et al., 2004). This study additionally revealed that in MEFs, deposition of the H4K20me3 mark at pericentric heterochromatin is dependent on the H3K9 methyltransferase Suv39h1/2 and the H3K9me3 binding protein HP1. A subsequent study from Maria Blasco's laboratory demonstrated that in MEFs, the RB1 family proteins are required for proper heterochromatin formation and facilitate H4K20 trimethylation at pericentric and telomeric chromatin through recruitment of the HMTs Suv4-20h1 and Suv4-20h2 (Gonzalo et al., 2005).

H4K20me3 enrichment has also been reported at other domains of transcriptionally silent chromatin, including imprinted regions and several classes of repetitive DNA. A study by Denise Barlow and colleagues found that in MEFs, H4K20me3 is present along with H3K9me3 and HP1 $\alpha$ , - $\beta$  and - $\gamma$  at the silent maternal promoter of the *Air* ncRNA, within the *Igf2r* imprinted cluster (Regha et al., 2007). A separate report showed that H4K20me3, H3K4me3 and H3K9me3 together comprise an epigenetic signature that is present at all imprinting control regions in

mice and humans (McEwen & Ferguson-Smith, 2010). Utilizing next-generation sequencing, several groups have observed marked enrichment of H4K20me3 at multiple classes of repetitive elements including satellite repeats, simple repeats and ERVL repeats, as well as at ZNF genes in human CD4<sup>+</sup> T cells (Barski et al., 2007; Ernst & Kellis, 2010). Several lines of evidence support a functional role for H4K20me3 in the maintenance of transcriptional silencing and genomic integrity at regions of repetitive DNA. For example, in *Drosophila* H4K20me3 cooperates with DNMT2 to reinforce the silencing of retrotransposons (Phalke et al., 2009). In addition, H4K20me3 protects against telomere elongation and prevents telomeric recombination in MEFs (Benetti et al., 2007). Collectively, these data demonstrate that H4K20me3 is enriched at domains of constitutive heterochromatin and repetitive DNA and plays a critical role in the maintenance of these genomic regions.

Several key findings from the literature suggest that H4K20me3 might be relevant to senescence. First, as discussed above, H4K20me3 is a marker of heterochromatin and is highly enriched at transcriptionally silent domains including telomeres, pericentromeres, imprinted regions and the inactive X chromosome (Schotta et al., 2004; Henckel et al., 2009; McEwen & Ferguson-Smith, 2010; Chadwick & Willard, 2004). This is potentially significant as senescent cells undergo extensive chromatin changes that ultimately manifest in the formation senescence-associated heterochromatic foci (SAHF). Second, elevated levels of the H4K20me3 mark have been reported in the livers of aged rats and in cells isolated from Hutchinson–Gilford Progeria Syndrome (HGPS) patients (Sarg et al., 2002; Shumaker et al., 2006). Intriguingly, these data suggested a potential link between H4K20me3, aging and senescence. Senescent cells have been reported to accumulate with age in various tissues, including rodent liver (Wang et al., 2009). Likewise, HGPS is premature-aging syndrome and primary cells isolated from HGPS patients senesce at an accelerated rate in culture (McClintock et al., 2006).

Finally, H4K20me3 is frequently lost from human cancers (Fraga et al., 2005). Because senescence provides a barrier to tumorigenesis, I wanted to investigate whether H4K20me3 contributes to the tumor suppressive properties of senescence. Therefore, in the present study I set out to address the following critical questions. (1) What happens to the H4K20me3 modification in senescent cells? (2) Is H4K20me3 required for senescence? (3) What is the function of H4K20me3 in senescent cells?

## Chapter 2. Materials and Methods

### 2.1 Expression and shRNA Vectors

#### 2.1.1 Expression Vectors

The pBABE-puro and pBABE-puro-H-RAS-V12 (H-RASG12V) retroviral expression vectors were obtained as gifts from Robert Weinberg (Massachusetts Institute of Technology). pC1-HA-SUV420H1\_i1 and pC1-HA-SUV420H2 were obtained as gifts from D. Alan Underhill (University of Alberta). pCMV-VSVG was purchased from Clontech Laboratories. psPAX2 was obtained from Addgene (plasmid 12260).

#### 2.1.2 Generation of SUV420H1 and SUV420H2 Vectors

The pBABE-puro-MYC-SUV420H1 and pBABE-puro-MYC-SUV420H2 vectors were generated using conventional molecular biology methods as follows. The full length SUV420H1 ORF was PCR amplified from pC1-HA-SUV420H1\_i1 using the following primers: Forward: 5'-GCG CGG ATC CGC CAC CAT GAA GTG GTT GGG AGA ATC C-3'; Reverse: 5'-GCG CGT CGA CTT AGG CAT TAA GCC TTA AAG A-3'. The PCR product was digested with BamHI and Sall and ligated into pBABE-puro-MYC digested with the same enzymes. The full length SUV420H2 ORF was PCR amplified from pC1-HA-SUV420H2 using the following primers: Forward: 5'-GCG CGG ATC CGC CAC CAT GGG GCC CGA CAG AGT GAC A-3'; Reverse: 5'-GCG CGT CGA CTC ACA GCT CTT CAC CGC CGA C-3'. The PCR product was digested with BamHI and Sall and ligated into pBABE-puro-MYC digested with the same enzymes.

The pBABE-puro-MYC-SUV420H2-281-462 vector was generated using conventional molecular biology methods as follows. A fragment of SUV420H2 corresponding to amino acid residues 281-462 was PCR amplified from pBABE-puro-MYC-SUV420H2 using the following primers: Forward 5'-GCG CGG ATC CCT GGG CCC TCG GGC CTG CGT G-3'; Reverse: 5'-GCG CGT CGA CTC ACA GCT CTT CAC CGC CGA C-3'. The PCR product was digested with BamHI and Sall and ligated into pBABE-puro-MYC digested with the same enzymes. All of

the expression vectors were verified through restriction digestion and direct sequencing.

### **2.1.3 Short Hairpin RNA (shRNA) Vectors**

A set of five human SUV420H2 lentiviral shRNA constructs was purchased from Open Biosystems (RHS4533). The set contains five unique short hairpins (TRCN0000142036, TRCN0000141493, TRCN0000141258, TRCN0000143766, TRCN0000141926) targeted against human SUV420H2, contained within the pLKO.1 lentiviral vector. An additional set of four human SUV420H2 retroviral shRNA constructs was purchased from OriGene Technologies (TR307397). The constructs feature four unique 29-mer hairpins targeted against human SUV420H2, contained within the pRS retroviral vector.

## **2.2 Cell Culture**

### **2.2.1 IMR90 Cells**

IMR90 primary human diploid fibroblasts were obtained from the Coriell Institute (Camden, New Jersey, USA). The cells were cultured in Dulbecco's Modified Eagle Medium (DMEM) supplemented with 20% fetal bovine serum, 2 mM L-glutamine, 25 U/ml penicillin and 25 µg/ml streptomycin. Cells were maintained in a humidified incubator under the following conditions: 37° C, 5% CO<sub>2</sub> and 3% O<sub>2</sub>. The IMR90 cells were subjected to serial passage approximately every two to three days.

### **2.2.2 Phoenix-Ampho Cells**

Phoenix–Ampho embryonic kidney cells (SD-3443) were obtained from the American Type Culture Collection (Manassas, Virginia, USA). The cells were cultured in Dulbecco's Modified Eagle Medium (DMEM) supplemented with 10% fetal bovine serum, 2 mM L-glutamine, 25 U/ml penicillin and 25 µg/ml streptomycin. Cells were maintained in a humidified incubator under the following conditions: 37° C and 5% CO<sub>2</sub>.

### **2.2.3 HEK-293T Cells**

HEK 293T/17 embryonic kidney cells (CRL-11268) were obtained from the American Type Culture Collection (Manassas, Virginia, USA). The cells were cultured in Dulbecco's Modified Eagle Medium (DMEM) supplemented with 10% fetal bovine serum, 2 mM L-glutamine, 25 U/ml penicillin and 25 µg/ml streptomycin. Cells were maintained in a humidified incubator under the following conditions: 37° C and 5% CO<sub>2</sub>.

### **2.2.4 Transfection of Phoenix-Ampho Retroviral Packaging Cells**

Working with 70% confluent 100 mm dishes of Phoenix-Ampho cells, the growth medium was removed, replaced with 9 ml of fresh medium and returned to the incubator four hours prior to transfection. 2.5 M CaCl<sub>2</sub> was diluted to a final concentration of 250 mM with Milli-Q dH<sub>2</sub>O and 0.5 ml of the diluted CaCl<sub>2</sub> was aliquotted into one sterile 15 ml centrifuge tube per transfection. Twenty-five µg of purified plasmid DNA was added to each tube of CaCl<sub>2</sub> and mixed by flicking gently. To each tube of CaCl<sub>2</sub>/DNA, 0.5 ml 2X BBS (50 mM BES, 280 mM NaCl, 1.5 mM Na<sub>2</sub>HPO<sub>4</sub>, pH 6.95) was added slowly, drop-wise. The tubes were incubated for 15 minutes at room temperature, mixed by gently bubbling air through the mixture and distributed drop-wise to the plates of Phoenix-Ampho cells. The plates were rocked gently and placed into a humidified 37° C, 5% CO<sub>2</sub> incubator overnight.

### **2.2.5 Retroviral Production and Infection**

Approximately 12-16 hours after transfection, the medium was removed from the Phoenix-Ampho cells, replaced with 6 ml of complete growth medium and the plates returned to a 32° C, 5% CO<sub>2</sub> incubator for 24 hours. Twenty-four hours after the medium change, viral supernatants were collected from the transfected Phoenix-Ampho cells and passed through 0.45 mm syringe filters. Fresh growth medium was again applied to the plates of Phoenix-Ampho cells and the plates were returned to the 32° C, 5% CO<sub>2</sub> incubator for an additional 24 hours.

Working with 100 mm dishes of target IMR90 cells, the growth medium was removed and replaced with 3 ml of fresh growth medium supplemented with 8 µg/ml polybrene. The target cells were then pre-incubated for 2 hours in a 32° C, 5% CO<sub>2</sub> incubator. After 2 hours, 3 ml of the filtered viral supernatant was applied to the pre-incubated IMR90 cells. The IMR90 cells were returned to the incubator for 24 hours.

After 24 hours, the viral supernatant was removed from the IMR90 cells and replaced with 3 ml fresh viral supernatant and 3 ml growth medium supplemented with 8  $\mu\text{g/ml}$  polybrene. The IMR90 cells were again returned to the 37° C, 5% CO<sub>2</sub>, 3% O<sub>2</sub> incubator for an additional 24 hours. Following the second 24-hour incubation, the viral supernatant was removed from the IMR90 cells and replaced with growth medium containing an appropriate selection drug. Infected IMR90 cells were typically selected as appropriate with either 1  $\mu\text{g/ml}$  puromycin or 500  $\mu\text{g/ml}$  neomycin (G418).

### **2.2.6 Transfection of HEK-293T Lentiviral Packaging Cells**

Working with HEK-293T cells, 11-12 million cells in 15 ml of normal growth medium were seeded onto T175 flasks and allowed to adhere for 24 hours. Approximately 24 hours after seeding, the transfection reactions were prepared. The following plasmids were added to sterile 15 ml centrifuge tubes containing 1.5 ml DMEM: 5  $\mu\text{g}$  pCMV-VSVG, 14  $\mu\text{g}$  psPAX2, 19  $\mu\text{g}$  shRNA-containing plasmid. In a separate set of sterile 15 ml centrifuge tubes, 100  $\mu\text{l}$  Lipofectamine 2000 (Life Technologies) was mixed with 1.5 ml DMEM and incubated for 5 minutes at room temperature. The contents of the DMEM/DNA and DMEM/Lipofectamine 2000 tubes were then combined, mixed gently and incubated for 20 minutes at room temperature. After 20 minutes, the DNA/Lipofectamine 2000 solutions were mixed by gentle bubbling with a pipette and distributed evenly to the flasks of HEK-293T cells. The HEK-293T flasks were then placed into a 37° C, 5% CO<sub>2</sub> incubator. Six hours later, the transfection medium was carefully removed from each flask, replaced with 15 ml of normal growth medium and the flasks returned to the incubator.

### **2.2.7 Lentiviral Production and Infection**

Approximately 12-16 hours after transfection, the medium was removed from the HEK-293T cells, replaced with 15 ml of normal growth medium and the flasks returned to a 37° C, 5% CO<sub>2</sub> incubator for 24 hours. Twenty-four hours after the medium change, the lentiviral supernatants were collected from the HEK-293T cells, placed into sterile 50 ml centrifuge tubes and stored at 4° C overnight. The HEK-293T cells were then covered with a fresh 15 ml of normal growth medium and the flasks were returned to a 37° C, 5% CO<sub>2</sub> incubator for an additional 24 hours. After 24 hours, the second 15 ml batches of lentiviral supernatant were collected and

pooled with the first batches for a total volume of 30 ml. In order to clear cellular debris, the lentiviral supernatants were then subjected to centrifugation for 10 minutes at 3000 rpm. The supernatants were passed through 0.45  $\mu\text{m}$  PVDF low protein-binding filters and transferred to sterile 25 x 89 mm polyallomer centrifuge tubes (Beckman, 326823). The tubes were weighed in a sterile laminar flow hood and balanced by the precise addition of sterile PBS. The tubes were then placed into an SW-28 rotor and subjected to centrifugation for 2 hours at 47,000 x g (23,000 rpm) and 10° C in a Beckman-Coulter ultracentrifuge. Upon completion of the spin, the supernatants were removed by gentle inversion and placed inside sterile 50 ml centrifuge tubes. One hundred  $\mu\text{l}$  of sterile PBS was added to each lentiviral pellet, the tubes were capped and incubated overnight (12-16 hours) at 4° C on an orbital rocking platform. The following day, the purified lentiviruses were aliquotted as small volumes into sterile 1.5 ml microcentrifuge tubes and stored in the -80° C freezer.

Working with 6-well dishes of IMR90 cells, the growth medium was removed and replaced with 2 ml of fresh growth medium supplemented with 8  $\mu\text{g/ml}$  polybrene. The IMR90 cells were then pre-incubated for 2 hours in a 37° C, 5% CO<sub>2</sub>, 3% O<sub>2</sub> incubator. After 2 hours, 0, 4, 8, 12 or 16  $\mu\text{l}$  of purified shControl or shSUV420H2 lentivirus was applied to the wells of the pre-incubated IMR90 cells. The IMR90 cells were then returned to the incubator for 24 hours. After 24 hours, the infection medium was removed from each well, replaced with 2 ml of fresh growth medium supplemented with 1  $\mu\text{g/ml}$  puromycin and cultured until all of the uninfected cells were dead. The minimum volume of shControl or shSUV420H2 lentivirus that yielded 100% cell survival following puromycin selection was utilized for all subsequent infections. For each experiment, the lentiviral-infected IMR90 cells were maintained under puromycin selection for the full duration of the experiment.

## **2.3. Induction of Cell Senescence and Quiescence**

### **2.3.1 Induction of Replicative Senescence**

Low passage IMR90 cells were initially thawed and cultured in normal growth medium (DMEM + 20% fetal bovine serum, 2 mM L-glutamine, 25 U/ml penicillin, 25  $\mu\text{g/ml}$  streptomycin) under standard conditions (37° C, 5% CO<sub>2</sub>, 3%

O<sub>2</sub>). The cells were subjected to prolonged serial passage in culture under these conditions and counted at every split. Cumulative population doublings were calculated using the following equation ( $[\log(\text{number of cells counted}) - \log(\text{number of cells plated})] / \log(2)$ ) and the resulting growth curves were plotted graphically. Once the growth curves began to exhibit a plateau, the cells were assayed routinely for markers of senescence (e.g., SA  $\beta$ -gal activity, decreased BrdU incorporation, p16INK4a induction, SAHF formation). The cells were considered replicative senescent when no proliferation was observed for a two week period following the final passage and the cells displayed the senescence hallmarks listed above.

### **2.3.2 Induction of Oncogene-Induced Senescence**

Low passage IMR90 cells were initially thawed and cultured in normal growth medium (DMEM + 20% fetal bovine serum, 2 mM L-glutamine, 25 U/ml penicillin, 25  $\mu$ g/ml streptomycin) under standard conditions (37° C, 5% CO<sub>2</sub>, 3% O<sub>2</sub>). Control (pBABE-puro) or H-RASG12V (pBABE-puro-H-RASG12V) retroviruses were produced following transfection of Phoenix-Ampho cells by standard procedures. IMR90 cells were subsequently infected with either control or H-RASG12V retroviruses and subjected to drug selection in normal growth medium supplemented with 1  $\mu$ g/ml puromycin. The cells were maintained in culture under puromycin selection for the remainder of each experiment and passaged as necessary. Control and H-RASG12V-infected cells were typically harvested 12-14 days after infection. The H-RASG12V-infected cells were considered senescent when no proliferation was observed and the cells displayed the senescence hallmarks (e.g., SA  $\beta$ -gal activity, decreased BrdU incorporation, p16INK4a induction, SAHF formation).

### **2.3.3 Induction of Quiescence**

Low passage IMR90 cells were initially thawed and cultured in normal growth medium (DMEM + 20% fetal bovine serum, 2 mM L-glutamine, 25 U/ml penicillin, 25  $\mu$ g/ml streptomycin) under standard conditions (37° C, 5% CO<sub>2</sub>, 3% O<sub>2</sub>). Once the cells reached confluence, they were subjected to a 1:2 split in growth medium containing reduced serum (DMEM + 0.1% fetal bovine serum, 2 mM L-glutamine, 25 U/ml penicillin, 25  $\mu$ g/ml streptomycin). Seventy-two hours after splitting, the cells were harvested and assayed for hallmarks of proliferation arrest

and senescence. The cells were considered quiescent if they no longer proliferated, but also did not exhibit markers of senescence (e.g., SA  $\beta$ -gal activity, p16INK4a induction).

## **2.4 Senescence Assays**

### **2.4.1 Senescence-Associated $\beta$ -Galactosidase Assay**

Prior to the onset of senescence, cells were seeded onto sterile glass coverslips, allowed to adhere and transferred to 6-well tissue culture dishes. At the time of harvest, cells were rinsed once briefly with 1X PBS. The PBS was aspirated and the cells were covered with 2 ml of freshly prepared fixative solution (1X PBS containing 2% formaldehyde, 0.2% glutaraldehyde) and subjected to fixation for 5 minutes at room temperature. The cells were washed twice with 1X PBS. After the second wash, the PBS was aspirated and cells were covered with 2 ml of freshly prepared staining solution (40mM Na<sub>2</sub>HPO<sub>4</sub> pH 6, 150mM NaCl, 2mM MgCl<sub>2</sub>, 5mM K<sub>3</sub>Fe(CN)<sub>6</sub>, 5mM K<sub>4</sub>Fe(CN)<sub>6</sub>, 1mg/mL X-gal (in DMSO)) and incubated 12-16 hours at 37° C in a non-CO<sub>2</sub> incubator. Following incubation, the cells were washed twice with 1X PBS and twice with dH<sub>2</sub>O to remove residual salt. The coverslips were allowed to air dry at room temperature, mounted on glass microscope slides and visualized using conventional bright field microscopy.

## **2.5 Gene Expression Analysis**

### **2.5.1 RNA Isolation**

Isolation of total RNA was performed using the RNeasy Mini Kit (Qiagen, 74104). Working with 1-5 million IMR90 cells per 100 mm dish, the dishes were immediately transferred from the incubator to an ice tray. The growth medium was removed by aspiration and replaced with 10 ml of ice cold 1X PBS. The 1X PBS was removed and the cells were scraped into 350  $\mu$ l Buffer RLT + 1% 2-mercaptoethanol and collected in 1.5 ml microcentrifuge tubes on ice. Now working at room temperature, the RLT lysates were sheared repeatedly with a pipette tip and transferred to QIAshredder spin columns (Qiagen, 79654). The columns were subjected to centrifugation for 2 minutes at 16,000 x g and room temperature. The QIAshredder columns were discarded, and 350  $\mu$ l of 70% ethanol was added to each

lysate, mixed by pipetting and transferred to RNeasy spin columns. The columns were subjected to centrifugation for 15 seconds at 8,000 x g and room temperature. The flow-through was discarded, 350 µl of Buffer RW1 was added to each column and the columns were again subjected to centrifugation for 15 seconds at 8,000 x g. The flow-through was discarded, 80 µl of DNase I mix (70 µl Buffer RDD + 10 µl DNase I) was added to each column and the columns were incubated for 15 minutes at room temperature. After the incubation, 350 µl of Buffer RW1 was added to each column and the columns were subjected to centrifugation for 15 seconds at 8,000 x g. The flow-through was discarded and 500 µl of Buffer RPE was added to each column. The columns were subjected to centrifugation for 15 seconds at 8,000 x g, the flow-through was discarded and another 500 µl of Buffer RPE was added to each column. The columns were centrifuged for 2 minutes at 8,000 x g and then transferred into new 2 ml collection tubes. The columns were subjected to centrifugation for 1 minute at 16,000 x g and the columns were transferred into 1.5 ml microcentrifuge tubes. Twenty-five µl RNase-free dH<sub>2</sub>O was added to each column, incubated for 1 minute at room temperature and subjected to centrifugation for 1 minute at 8,000 x g in order to elute the RNA. RNA concentrations were determined for each sample using the NanoVue Plus spectrophotometer (GE Healthcare) and the RNA samples were stored in the -80° C freezer.

### **2.5.2 Qualitative Assessment of RNA**

RNA integrity was evaluated using the RNA 6000 Nano Kit (Agilent) and the 2100 Bioanalyzer (Agilent). First, the gel matrix was prepared by aliquotting 550 µl of the matrix into a supplied spin filter and centrifuging the filter for 10 minutes at 1,500 x g and room temperature. Subsequently, the gel-dye mix was prepared by aliquotting 65 µl of the filtered gel matrix into a 1.5 ml microcentrifuge tube and mixing it with 1 µl of the RNA 6000 Nano dye concentrate. The gel-dye mix was vortexed thoroughly and subjected to centrifugation for 10 minutes at 13,000 x g and room temperature.

To prepare the RNA samples, 1 µl of each sample was aliquotted into RNase-free 0.2 ml PCR tubes, mixed with 9 µl RNase-free dH<sub>2</sub>O and kept on ice. The tubes were then placed into a thermal cycler and denatured for 2 minutes at 70° C to prevent the formation of secondary structure. The denatured RNA samples were then immediately placed on ice.

An RNA 6000 Nano chip was placed into the priming station and 9  $\mu$ l of gel-dye mix was dispensed into the appropriately marked well. The priming station syringe was then depressed, held in place for 30 seconds and released. Next, 9  $\mu$ l of gel-dye mix was dispensed into the two additional appropriately marked wells. Five  $\mu$ l of the RNA 6000 Nano marker reagent was dispensed into the ladder well and each of the 12 sample wells. One  $\mu$ l of the supplied RNA 6000 Nano ladder was added to the indicated ladder well. For the denatured RNA samples, 1  $\mu$ l of each sample was added to the indicated sample wells. The RNA 6000 Nano chip was placed into the foam adapter and vortexed for 1 minute on the 2400 rpm setting and then immediately run on the Agilent 2100 Bioanalyzer. Upon completion of the run, an RNA integrity number (RIN) was generated for each RNA sample and used to evaluate the quality of the samples.

### **2.5.3 Affymetrix Microarray Analysis**

The Paterson Institute for Cancer Research Microarray Facility (Manchester, UK) conducted gene expression analysis of RS and OIS cells using Affymetrix Human Genome U133 Plus 2.0 GeneChIPs. Using 50 ng total RNA, the first and second strand cDNA synthesis steps were performed sequentially using the Ovation Pico WTA System (NuGEN Technologies, #3300). The resulting double-stranded cDNA was purified using Agencourt RNAClean beads (Beckman Coulter) and subjected to SPIA amplification to produce single-stranded cDNA complementary to the original RNA template. The resulting single-stranded cDNA was again purified using the Agencourt RNAClean beads. For each sample, 5  $\mu$ g of purified, SPIA-amplified, single-stranded cDNA was subjected to fragmentation and subsequent biotin labelling using the Encore Biotin Module kit (NuGEN Technologies, #4200).

Hybridization cocktails were prepared by mixing 50  $\mu$ l of biotin-labelled, single-stranded cDNA with a buffer containing 50 pM control oligonucleotide B2, 1.5 pM bioB, 5 pM bioC, 25 pM bioD and 100 pM cre eukaryotic hybridization controls, 0.1 mg/ml herring sperm DNA, 0.5 mg/ml acetylated BSA, 1X hybridization buffer (100 mM MES, 1 M [Na<sup>+</sup>], 20 mM EDTA, 0.01% Tween-20) and 10% DMSO in a final volume of 220  $\mu$ l. The hybridization cocktails were then heat denatured for 2 minutes at 99° C, incubated for 5 minutes at 45° C on a heat block and subjected to centrifugation for 5 minutes at 16,000 x g.

Affymetrix GeneChip Human Genome U133 Plus 2.0 arrays were filled with 1X hybridization buffer and pre-incubated for 10 minutes in a 45° C rotating hybridization oven. The pre-hybridization buffer was removed from the arrays, replaced with 200 µl of the denatured cDNA hybridization cocktails and hybridized for 16 hours at 45° C in the hybridization oven. The arrays were then washed and stained with streptavidin phycoerythrin (SAPE) and a biotinylated anti-streptavidin antibody on the Affymetrix GeneChip Fluidics Station. After an additional washing procedure, the hybridized and stained arrays were scanned with the Affymetrix GeneChip Scanner 3000 and the images managed with the GeneChip Operating Software (GCOS).

#### **2.5.4 Microarray Data Analysis**

Tony McBryan, our laboratory computational biologist, performed the microarray data processing and analysis. The raw data files (.CEL files) for each Affymetrix GeneChip were imported into the R software application and analyzed using the Bioconductor packages (<http://www.bioconductor.org>). All samples were subjected to background correction and normalization using the GC Robust Multi-array Average (GCRMA) method. Differential expression was determined by performing T-tests based on the log-normalized values produced by the GCRMA method. Genes were considered differentially expressed if the fold difference between the control (i.e., proliferating) and experimental (i.e., senescent) groups exceeded 1.5 fold (or less than -1.5 fold) and exhibited a Benjamini–Hochberg false discovery rate (BH-FDR) adjusted p-value less than 0.05. BH-FDR is an error control method for multiple testing procedures first proposed by Benjamini and Hochberg that involves the ordered ranking of each comparison in a dataset by its unadjusted p-value in order to calculate the likelihood of any statistically significant change being a false positive (i.e., the false discovery rate) (Benjamini & Hochberg, 1995). In this manner, the BH-FDR method provides a more statistically stringent and conservative method for evaluating differential gene expression data.

Gene Set Enrichment Analysis (GSEA; [www.broad.mit.edu/gsea](http://www.broad.mit.edu/gsea)) was applied to the microarray datasets in order to identify altered pathways and functions. Probes from the Affymetrix microarrays were collated into individual gene features and arranged by signal to noise ratios into a rank-ordered list (L). For each gene set (S), an enrichment score (ES) derived from the Kolmogorov-Smirnov statistic and

reflecting the degree to which the gene set was overrepresented at either the top or bottom of the entire ranked list (L) and was calculated. The statistical significance (nominal p-value) of the ES was determined by empirical phenotype-based permutation analysis. Significance levels of the ES were subsequently adjusted to account for multiple hypotheses testing, initially by normalizing the ES for each gene set to account for the size of the set (NES) and then by controlling the proportion of false positives by calculating the FDR for each NES. The respective gene sets were obtained from the Broad Institute Molecular Signatures Database.

The microarray data were also evaluated to identify affected pathways and functions using Ingenuity Pathway Analysis (IPA, [www.ingenuity.com](http://www.ingenuity.com)). Previously determined lists of differentially expressed genes were compiled in a standard (.txt) file format and uploaded to the IPA application using the Core Analysis feature. Based on the input datasets, IPA subsequently generated lists of biological functions and canonical pathways that were affected in a statistically significant manner. Statistical significance was calculated for each function/pathway using the right-tailed Fisher's Exact Test, by considering the following parameters: the number of genes included in the specific IPA function/pathway, the total number of function/pathway eligible genes annotated in IPA and the total number of genes in the input dataset.

## **2.6 Protein Analysis**

### **2.6.1 Protein Isolation**

Working with 100 mm tissue culture dishes of adherent cells, the growth medium was aspirated and the cells were washed once with 10 ml of 1X PBS at room temperature. The PBS was aspirated completely and 300-500  $\mu$ l of freshly boiled 1X sample buffer (62.5 mM Tris-HCl pH 6.8, 2% SDS, 10% glycerol, 0.1 M DTT, 0.01% bromophenol blue) was added to each plate. Using a plastic cell scraper, the cells were collected in the 1X sample buffer and the contents of the plate transferred to 1.5 ml microcentrifuge tubes. The lysates were boiled for 4 minutes and homogenized by vigorous vortexing. Lysates were subjected to centrifugation for 5 minutes at 12,000 x g and room temperature, transferred to new 1.5 ml microcentrifuge tubes and snap frozen in a dry ice/ethanol bath. The lysates were transferred to the -80° C freezer for long-term storage.

### **2.6.2 Protein Quantification**

The protein concentrations of lysates prepared in 1X sample buffer were determined using the Bradford method. To each of three 1.5 ml microcentrifuge tubes 0, 5 or 10  $\mu$ l of 1 mg/ml BSA was aliquotted and mixed with 1  $\mu$ l 1X sample buffer. In a separate set of 1.5 ml microcentrifuge tubes, 1  $\mu$ l of each lysate was aliquotted. To each BSA standard and lysate sample, 700  $\mu$ l 1X Bradford reagent (BioRad) was added and mixed by pipetting. Each sample was transferred to a disposable plastic cuvette and the absorbance at 595 nm was determined using a spectrophotometer. The values for the BSA standards were utilized to construct a standard curve and the protein concentrations of the respective lysates determined by extrapolating from the curve.

### **2.6.3 Polyacrylamide Gel Electrophoresis (SDS-PAGE)**

Glass electrophoresis plates were washed thoroughly with water, rinsed with 100% ethanol and allowed to dry. The glass plates were then assembled and placed into the gel casting apparatus. Separating gels of appropriate acrylamide composition were prepared according to the recipes contained in Table 2.1. The separating gels were poured into the assembled plates and a layer of water-saturated butanol was applied to the top of the gel. Following gel polymerization, the butanol layer was decanted and the top of the gel washed repeatedly with water to remove residual butanol and unpolymerized acrylamide. Stacking gels were prepared according to the following recipe: 6.34 ml H<sub>2</sub>O, 2.5 ml 4X Upper Tris pH 6.8, 1.3 ml 30% Acryl/0.8% MBA, 100  $\mu$ l 10% APS, 10  $\mu$ l TEMED. The stacking gels were poured above the separating gels, gel combs were inserted and the gels were allowed to polymerize. Prepared gels were then placed into the electrophoresis apparatus and the tanks were filled with 1X SDS-PAGE running buffer (25 mM Tris, 192 mM glycine, 0.1% SDS, pH 8.3). The gel combs were carefully removed and each well flushed repeatedly with running buffer in order to remove unpolymerized acrylamide.

When the gels were ready, protein lysates previously prepared in 1X sample buffer were subjected to boiling for 4 minutes and collected by brief centrifugation. The boiled protein lysates were loaded into the gels and separated by the application of a constant electric current. Total electrophoresis time varied according to the

Separating Gel Percentage						
Reagent	5%	7.5%	8.75%	10%	12%	15%
dH <sub>2</sub> O (ml)	22.7	19.35	17.68	16.12	12.72	9.42
4X Lower Tris pH 8.8 (ml)	10.0	10.0	10.0	10.0	10.0	10.0
30% Acr/0.8% MBA (ml)	6.7	10.0	11.7	13.3	16.7	20.0
10% APS (ml)	0.4	0.4	0.4	0.4	0.4	0.4
TEMED (μl)	40	40	40	40	40	40

**Table 2.1 Separating gel recipes.** Separating gels of the appropriate percentage were prepared by mixing the specified volumes of the respective reagents. Abbreviations: Acr, acrylamide; MBA, N,N'-methylenebisacrylamide; APS, ammonium persulfate; TEMED, tetramethylethylenediamine.

acrylamide composition of the gels and the molecular weights of the intended protein targets.

#### **2.6.4 Immobilization of Protein**

Following the completion of SDS-PAGE, the fractionated proteins were immobilized to polyvinylidene fluoride (PVDF) membranes. To prepare the PVDF for electrophoretic transfer, the membranes were placed into 100% ethanol for approximately 30 seconds, rinsed with dH<sub>2</sub>O and equilibrated in cold 1X SDS-PAGE transfer buffer (25 mM Tris, 192 mM Glycine, 0.01% SDS, 20% methanol). The SDS-PAGE electrophoresis apparatus was disassembled and transfer cassettes were assembled in the following order: (1) foam pad, (2) Whatman paper equilibrated in transfer buffer, (3) SDS-PAGE gel, (4) PVDF equilibrated in transfer buffer, (5) Whatman paper equilibrated in transfer buffer, (6) foam pad. The assembled cassettes were placed into the transfer apparatus containing 1X SDS-PAGE transfer buffer and immobilized to PVDF through the application of constant electric current. After the transfer was complete, the cassettes were disassembled and the PVDF membranes were allowed to dry at room temperature.

#### **2.6.5 Western Blotting**

Following protein fractionation by SDS-PAGE and immobilization to PVDF, the membranes were immersed in 100% ethanol and subjected to gentle agitation for 30 seconds. The ethanol was removed and the membranes were washed several times in TBS with gentle agitation. The membranes were blocked with TBS + 5% non-fat dry milk for 1 hour at room temperature and then washed briefly in TBS + 4% BSA + 0.02% NaN<sub>3</sub>. Membranes were then incubated with primary antibodies typically diluted to 0.1-1 µg/ml in TBS + 4% BSA + 0.02% NaN<sub>3</sub> for either 1 hour at room temperature or overnight at 4° C, depending on the manufacturer's instructions. A list of the antibodies used in this study is included in Table 2.2. The membranes were washed three times for 15 minutes each in TBS + 0.05% Tween 20. Membranes were incubated with horseradish peroxidase-coupled secondary antibodies diluted in TBS + 4% BSA + 0.02% NaN<sub>3</sub> according to the manufacturer's instructions for 1 hour at room temperature. The membranes were washed three times for 15 minutes each in TBS + 0.05% Tween 20. Membranes were transferred to a 1:1 solution of ECL Plus Western blotting substrate (Pierce), developed for 1 minute with gentle agitation and

Target	Species	Manufacturer	Application	Dilution
Actin	Mouse IgG <sub>1</sub>	Sigma, A1978	WB	1 µg/ml
Cyclin A	Rabbit IgG	Santa Cruz, sc-751	WB	0.2 µg/ml
GAPDH	Rabbit IgG	Cell Signaling, 2118	WB	1:1000
Histone H4	Rabbit serum	Active Motif, 39269	WB	1:2000
H4K20me1	Rabbit IgG	Millipore, 05-735	WB	1:4000
H4K20me2	Rabbit serum	Active Motif, 39174	WB	1:2000
H4K20me3	Rabbit IgG	Abcam, ab9053	ChIP	6 µg/ChIP
H4K20me3	Rabbit IgG	Abcam, ab9053	IF	1 µg/ml
H4K20me3	Rabbit IgG	Abcam, ab9053	WB	1 µg/ml
H4K20me3	Rabbit serum	Active Motif, 39180	IF	1:2000
H4K20me3	Rabbit serum	Active Motif, 39180	WB	1:2000
H4K20me3	Rabbit IgG	Cell Signaling, 5737	ChIP	6 µg/ChIP
H4K20me3	Rabbit IgG	Cell Signaling, 5737	WB	1:1000
H4K20me3	Rabbit IgG	Millipore, 04-079	ChIP	6 µg/ChIP
H4K20me3	Rabbit IgG	Millipore, 04-079	WB	1 µg/ml
Lamin A/C	Rabbit IgG	Cell Signaling, 2032	WB	1:1000
Lamin B1	Rabbit IgG	Abcam, ab16048	WB	0.3 µg/ml
MYC	Mouse IgG <sub>1</sub>	Santa Cruz, sc-40	IF	1 µg/ml
MYC	Mouse IgG <sub>1</sub>	Santa Cruz, sc-40	WB	1 µg/ml
p16INK4a	Mouse IgG <sub>1</sub>	BD, 51-1325GR	WB	0.25 µg/ml
p21WAF1	Rabbit IgG	Abcam, ab7960	WB	0.2 µg/ml
RAS	Mouse IgG <sub>1</sub>	BD, 610001	WB	0.125 µg/ml
RB	Mouse IgG <sub>2a</sub>	Cell Signaling, 9309	WB	1:1000
SUV420H2	Rabbit IgG	Abcam, ab91224	WB	0.25 µg/ml

**Table 2.2 Summary of antibodies that were used in this study.** The antibodies contained within this table were utilized in the specified applications at the described concentrations or dilutions. Abbreviations: chromatin immunoprecipitation (ChIP), immunofluorescence (IF), Western blot (WB).

dried quickly between blotting paper. The membranes were covered with plastic wrap, exposed to film for appropriate time intervals and the films developed.

## **2.7 Chromatin Analysis**

### **2.7.1 Chromatin Immunoprecipitation**

Proliferating and replicative senescent IMR90 cells were cultured as described previously. For chromatin immunoprecipitation, cells were cultured to approximately 95% confluence in 100 mm cell culture dishes containing 10 ml growth medium. This corresponds to approximately 4-5 million proliferating cells or 1-2 x million senescent cells per 100 mm culture dish. Cells were subjected to cross-linking in the presence of 1% formaldehyde by the addition of 271  $\mu$ l of 37% formaldehyde (Sigma) to 10 ml of growth medium. Cross-linking was conducted for 10 minutes at room temperature, with gentle agitation on a rocking platform. The cross-linking reaction was quenched for 5 minutes at room temperature by the addition of 500  $\mu$ l 2.5 M glycine to a final concentration of 125 mM. Cells were detached from the culture dishes using plastic cell scrapers and collected in 50 ml centrifuge tubes kept on ice. Cells were subjected to centrifugation for 5 minutes at 200 x g and 4° C. The supernatant was removed by aspiration, the cell pellets were washed with cold 1X PBS and subjected to centrifugation for an additional 5 minutes at 200 x g and 4° C. The supernatant was removed by aspiration, cell pellets were snap frozen with dry ice and ethanol and stored at -80° C.

Frozen pellets comprised of approximately 10 million cross-linked proliferating or senescent IMR90 cells were resuspended with 1 ml cold (1:1) modified nuclear lysis buffer (mNLB):IP dilution buffer (IPDB) (35 mM Tris-HCl pH 8.0, 75 mM NaCl, 5.5 mM EDTA pH 8.0, 3 mM EGTA pH 8.0, 0.5% SDS, 0.5% Triton X-100) supplemented with inhibitors (10  $\mu$ g/ml aprotinin, 5  $\mu$ g/ml leupeptin and 50  $\mu$ g/ml PMSF) and incubated on ice for 10 minutes. The cells were subjected to centrifugation for 5 minutes at 200 x g and 4° C. The supernatant was removed by careful aspiration and the cell pellets were resuspended with 0.5 ml cold (1:1) mNLB:IPD and inhibitors. Cell suspensions were transferred to 2 ml centrifuge tubes (Eppendorf) on ice and subjected to sonication in a Bioruptor XL water bath sonicator (Diagenode). Cells were sonicated at the highest amplitude setting for 22.5 minutes, with cycles of 24 seconds on/24 seconds off.

Each 2 ml tube of sonicated chromatin was subjected to centrifugation for 5 minutes at 12,000 x g and 4° C. The supernatants were collected, transferred to fresh 1.5 ml microcentrifuge tubes and subjected an additional round of centrifugation for 5 minutes at 12,000 x g and 4° C. The supernatants were collected, identical chromatin samples pooled in 15 ml centrifuge tubes and stored on ice. Aliquots were taken from the chromatin samples and used to determine the protein and DNA concentrations, respectively. Protein concentrations were determined using the Bradford assay, while DNA concentrations were determined using the Qubit dsDNA HS Assay Kit and a Qubit fluorometer (Life Technologies). Depending on the experiment, the respective chromatin solutions were diluted to either equal protein concentrations or equal DNA concentrations with (1:1) mNLB:IPDB + inhibitors. The chromatin solutions were then diluted with IPDB to a final mNLB:IPDB ratio of 1:10 and kept on ice.

The appropriate ChIP antibodies were pre-bound to Dynabeads M-280 Sheep anti-Rabbit IgG magnetic beads (Life Technologies) as follows. For each ChIP reaction, 100 µl of Dynabeads was aliquotted into a 1.5 ml microcentrifuge tube. The beads were washed 3 times with 1X PBS + 0.5% BSA using a magnetic rack. After the final wash, the beads were resuspended with 0.5 ml 1X PBS + 0.5% BSA. In order to facilitate the formation of antibody-bead complexes, 6 µg of primary antibody was added to each tube of Dynabeads and the tubes were incubated for 6 hours at 4° C, on a rotating wheel. Following the incubation, the antibody-bead complexes were washed 3X with ice-cold IPDB using the magnetic rack. During the final wash, the IPDB was aspirated completely and the antibody-bead complexes were combined with the appropriate diluted chromatin solutions. After combining the chromatin and antibody-bead complexes, the reactions were incubated overnight (12-16 hours) at 4° C, on a rotating wheel.

Following the overnight incubation, the beads were kept on ice and washed with the following ice-cold buffers: 2X with IPDB, 1X with High Salt Wash Buffer (20 mM Tris-HCl pH 8.0, 500 mM NaCl, 2 mM EDTA, 0.1% SDS, 1% Triton X-100), 1X with LiCl Wash Buffer (10 mM Tris-HCl pH 8.1, 250 mM LiCl, 1 mM EDTA, 1% NP-40, 1% deoxycholic acid) and 2X with TE (10 mM Tris-HCl pH 8.0, 1 mM EDTA). After the last wash, the beads were aspirated to dryness, resuspended in 500 µl IP Elution Buffer (50 mM Tris-HCl pH 8.0, 300 mM NaCl, 10 mM EDTA pH 8.0, 1% SDS) and added 0.5 µl 100 mg/ml RNase A and incubated at 65° C for

4-6 hours. To each tube, 6  $\mu$ l 20 mg/ml proteinase K was added and the tubes were incubated at 45° C for 12 hours. The ChIP DNA was subsequently purified by phenol/chloroform extraction followed by ethanol precipitation, resuspended with 20  $\mu$ l nuclease-free dH<sub>2</sub>O and quantified using the Qubit dsDNA HS Assay Kit and a Qubit fluorometer (Life Technologies).

### **2.7.2 Preparation of ChIP-Seq Libraries**

ChIP-Seq libraries were generated using the NEBNext® ChIP-Seq Sample Prep Master Mix Set 1 (New England Biolabs, E6240S) as follows. End Repair: 10 ng ChIP or input DNA (in a 44  $\mu$ l volume) was mixed the DNA with 5  $\mu$ l NEBNext End Repair Reaction Buffer and 1  $\mu$ l NEBNext End Repair Enzyme Mix in a PCR tube and incubated for 30 minutes at 20° C in a thermal cycler. The end-repaired DNA was purified using the QIAquick PCR Purification Kit (Qiagen, 28104) and eluted in 44  $\mu$ l dH<sub>2</sub>O. dA-Tailing of End-Repaired DNA: 44  $\mu$ l end-repaired DNA was mixed with 5  $\mu$ l NEBNext dA-Tailing Reaction Buffer (10X) and 1  $\mu$ l Klenow Fragment in a PCR tube and incubated at 37° C for 30 minutes in a thermal cycler. The dA-tailed DNA was purified using the MinElute PCR Purification Kit (Qiagen, 28004) and eluted in 20  $\mu$ l dH<sub>2</sub>O. Adaptor Ligation of dA-Tailed DNA: 19  $\mu$ l dA-tailed DNA was mixed with 6  $\mu$ l Quick Ligation Reaction Buffer (5X), 1  $\mu$ l 1.5  $\mu$ M DNA Adaptors and 4  $\mu$ l Quick T4 DNA Ligase in a PCR tube and incubated at 20° C for 15 minutes in a thermal cycler. The adaptor-ligated DNA was purified using the MinElute PCR Purification Kit (Qiagen, 28004) and eluted in 10  $\mu$ l dH<sub>2</sub>O.

The purified adaptor-ligated DNA samples were subsequently fractionated on 2% regular melting point agarose TAE gels containing 1  $\mu$ g/ml ethidium bromide. The samples were oriented with empty wells between them so as to avoid cross-contamination between wells. The gels were subjected to electrophoresis for 1 hour 45 minutes at 60 volts, constant voltage. Using fresh scalpels for each sample, bands corresponding to 225 to 275 base pairs were excised and placed into sterile 1.5 ml microcentrifuge tubes. The gels were photographed before and after excision, to ensure uniform size selection occurred for all of the samples. The excised gel fragments were weighed, purified using the QIAquick Gel Extraction Kit (Qiagen, 28704) and eluted in 37  $\mu$ l dH<sub>2</sub>O. It is important to note that the gel digestion step of the gel extraction protocol was performed at room temperature as opposed to the recommended 65° C.

The purified size-selected, adaptor-ligated DNA was then subjected to PCR amplification: 36 µl size selected, adaptor-ligated was mixed with 10 µl 5X Phusion HF Buffer, 1.5 µl dNTP Mix, 0.9 µl Primer 1 (25 µM stock), 0.9 µl Primer 2 (25 µM stock), 0.5 µl Phusion High-Fidelity DNA Polymerase and 0.1 µl nuclease-free dH<sub>2</sub>O in a PCR tube. The samples were PCR amplified using the following cycling parameters: initial denaturation at 98° C for 30 seconds; 18 cycles of denaturation at 98° C for 10 seconds, annealing at 65° C for 30 seconds, extension at 72° C for 30 seconds; and final extension at 72° C for 5 minutes. The PCR-amplified, size-selected, adaptor ligated DNA was then purified using the MinElute PCR Purification Kit (Qiagen, 28004) and eluted in 16 µl dH<sub>2</sub>O. The ChIP-Seq libraries were quantified using the Qubit dsDNA HS Assay Kit and a Qubit fluorometer (Life Technologies).

### **2.7.3 Qualitative Assessment of ChIP-Seq Libraries**

The ChIP-Seq libraries were evaluated using the DNA 1000 Assay (Agilent) and the 2100 Bioanalyzer (Agilent). The gel-dye mix was prepared by combining 25 µl of DNA dye concentrate with an entire DNA gel matrix vial. The gel-dye mix was vortexed, transferred to a supplied spin filter and subjected to centrifugation for 15 minutes at 2240 x g. A DNA 1000 Assay chip was placed into the priming station and 9 µl of gel-dye mix was dispensed into the appropriately marked well. The priming station syringe was depressed, held in place for 60 seconds and then released. Nine µl of gel-dye mix was dispensed into the two additional marked wells of the chip. Five µl of the assay marker reagent was dispensed into the ladder well and each of the 12 sample wells of the chip. One µl of the supplied DNA ladder was added to the indicated well. For the ChIP-Seq library samples, 1 µl of each library was added to an appropriately indicated sample well. The DNA 1000 chip was placed into the foam adapter and vortexed for 1 minute on the 2400 rpm setting and then immediately run on the Agilent 2100 Bioanalyzer. The resulting electropherograms were used to evaluate the size range and integrity of the ChIP-Seq libraries.

### **2.7.4 ChIP-Sequencing**

Billy Clark, from the Beatson Institute for Cancer Research Molecular Technology Services department, performed the sequencing. The ChIP libraries were

diluted to 2 nM stocks with nuclease-free dH<sub>2</sub>O. The libraries were then denatured with 0.1 N NaOH and diluted to 5 pM stocks. The denatured and diluted libraries were hybridized to Illumina flowcells using the TruSeq SR Cluster v2–cBot-GA kit (Illumina) on the Illumina cBot cluster generation instrument. Following cluster generation, the flowcells were inserted into the Illumina Genome Analyzer IIX sequencer and subjected to single-read sequencing using the TruSeq SBS Kit v5-GA kit (Illumina).

### **2.7.5 ChIP-Seq Data Analysis**

Tony McBryan, our laboratory computational biologist, performed the ChIP-Seq data processing and analysis as follows. Raw intensity files obtained from the Illumina GAIIX were converted into the standard textual FASTQ format using the Consensus Assessment of Sequence and Variation (CASAVA) version 1.8.2 software. The default settings were used except for the FASTQ-cluster-count parameter, which was set to 500 million (far in excess of the GAIIX capacity) such that all reported clusters were retained within a single FASTQ file. The FASTQ files were subsequently inspected for quality using FastQC version 0.10.0 (Babraham Bioinformatics). FastQC provides basic statistics, per base and per sequence quality scores and additional metrics such as per base GC content, N counts, length distribution, estimated duplication levels and over-represented sequences.

The FASTQ files were subsequently aligned to the human genome (assembly hg18, NCBI Build 36) using Bowtie version 0.12.9 (Langmead et al., 2009). The following settings were used: chunkmbs 512 to provide additional memory for backtracking of difficult to map reads; m 1 to limit the reported alignments to reads which map uniquely to the genome; phread33-quals for input quality scores in FASTQ files compatible with CASAVA 1.8; p 8 to enable the processor to use additional CPU cores for alignment; best to guarantee that the reported reads were the best possible alignments in terms of the number of mismatches and quality values at mismatched positions.

For the purpose of visualization, reads were extended to account for the fact that the estimated ChIP DNA fragment size (150 bp) was larger than the sequenced reads. Duplicate reads containing identical start and end positions were removed as potential PCR artifacts. The genome-wide distributions of the input and ChIP reads were generated in bigWig format representing the number of detected fragments at a

given location normalized by the library size and visualized using the UCSC Genome Browser (Kent et al., 2002).

SICER version 1.1 was utilized in order to identify enriched regions within the H4K20me3 ChIP samples relative to the total histone H4 ChIP samples. SICER is particularly designed to identify enriched domains of histone modifications under contexts in which such domains might be diffuse (Zang et al., 2009). SICER specifically identifies clusters of signal unlikely to occur by chance by comparison to an idealized Poisson distribution. Briefly, reads were shifted by 75 bp from the 5' start to represent the center of the DNA fragment that was sequenced. The genome was then divided into non-overlapping windows of 200 bp. For each window, the number of reads mapped to the window was counted and a score was assigned as the negative log probability of detecting that number of reads within the window. Candidate islands were defined as a contiguous series of windows with a score greater than or equal to a threshold determined by the Poisson distribution. Candidate islands were compared to the control sample using an FDR criterion ( $FDR \leq 0.01$ ).

Domains of differential H4K20me3 enrichment between the proliferating (PD32) and senescent (PD86) samples were identified using the DiffBind (version 1.2.0) Bioconductor package. Each SICER-identified region within each PD32 and PD86 sample was Trimmed Mean of M-values (TMM) normalized and scored for each sample as H4K20me3 ChIP read counts minus histone H4 ChIP read counts (after normalization) (Robinson & Oshlack, 2010). Specifically, the `DBA_SCORE_TMM_MINUS_FULL` scoring scheme was utilized. Four samples were used (two PD32 replicates and two PD86 replicates). Regions were only analyzed if they were present in at least two of the four samples, as identified by SICER. As with UCSC and SICER, insert lengths were again extended to 150 bp to account for DNA fragment size. Identified regions of differential H4K20me3 enrichment between the PD32 and PD86 samples were extracted ( $FDR \leq 0.1$ ) and used in subsequent downstream analyses. `Iranges` (version 1.14.4) and `GenomicRanges` (version 1.8.7) were used as dependencies.

Clustering analysis was performed using the R statistics environment (version 2.15.1). Regions of differential H4K20me3 enrichment between the PD32 and PD86 samples were overlapped with the coordinates of defined genomic features and assigned positive (1) or negative (0) values for either presence or absence of overlap. A matrix of the overlaps was loaded into the R environment, clustered using the

hclust function within the fastcluster package (version 1.1.6) and visualized using the heatmap.2 function from the gplots package (version 2.11.0).

In order to evaluate whether the PD86-specific H4K20me3 enrichment correlated with changes in gene expression, a scatterplot was generated to display the Affymetrix fold change of a gene (x-axis) plotted against the H4K20me3 ChIP difference (y-axis) within the promoter (5 kb upstream, 1 kb downstream) region of the gene. The Affymetrix NetAffx annotation (version 29) was used to annotate each probeset from the replicative senescence Affymetrix Human Genome U133 Plus 2.0 array and to assign it to an Ensembl gene identifier. Any probesets targeting multiple Ensembl genes were discarded. Ensembl genes containing multiple probesets were assigned a fold change equal to the geometric average of valid probesets. H4K20me3 ChIP signal was determined by measuring the number of reads (extended to 150 bp) within the promoter region of each gene normalized by the library size, with the histone H4 reads subtracted after similar normalization. ChIP difference was defined as the senescent (PD86) ChIP signal minus the proliferating (PD32) ChIP signal.

In order to visualize H4K20me3 distribution upstream, downstream and within gene bodies, composite gene profiles were assembled. To generate composite gene profiles, the Ensembl gene annotation (version 54) was used to identify gene transcription start (TSS) and termination (TES) sites for each of the Ensembl genes in the replicative senescence microarray dataset. For each gene, the area between the TSS and TES was defined as the gene body and divided into forty windows of equal size (each corresponding to 2.5% of the total gene body). Ten additional 500 bp windows were added in front of the TSS or after the TES of the gene in order to provide genomic context. For each site within the composite gene (e.g., 0-2.5%, 2.5-5%, etc), the H4K20me3 ChIP signal was calculated for each gene as previously described. The mean H4K20me3 ChIP signal was then plotted for subsets of genes (e.g., upregulated, downregulated or unchanged). Upregulated and downregulated genes were defined as genes for which at least one probeset changed 1.5-fold or greater in the appropriate direction and exhibited a BH-FDR value of less than or equal to 0.05. Unchanged genes were defined as the genes for which every probeset for that gene exhibited a BH-FDR greater than or equal to 0.9. ZNF genes were defined by their inclusion on the Zinc finger gene list available from HGNC (<http://www.genenames.org/genefamily/znf.php>), including a wildcard for ZNF\* pattern genes.

Statistical analysis of the overlap between H4K20me3 ChIP enrichment (as defined by SICER) and defined genomic features (e.g. ZNF genes, non-ZNF genes, DNA repeats) was performed as follows. The genomic coordinates of H4K20me3 ChIP enriched regions and specific genes/features were compared and the number of basepairs that were present in both datasets expressed as a percentage of the total number of gene basepairs occupied by H4K20me3. For example, for a given set of genes, a figure of 10% would indicate that an H4K20me3 enriched region overlapped 10% of all basepairs contained within that set of genes. A random overlap percentage was also computed, which is the result of random distribution of the gene set across the genome and the calculation of the overlap between this random gene set and the ChIP enriched signal. The random distribution was carried out 1000 times and the average overlap was used. P-values were also calculated by observing the frequency that a random overlap was greater than or equal to the true overlap. All p-values were below the detectable level using 1000 iterations ( $p < 0.001$ ).

## **2.8. Immunological Methods**

### **2.8.1. Immunofluorescence**

Proliferating and presenescent IMR90 cells were seeded onto sterile glass coverslips, allowed to adhere and transferred to 6-well tissue culture dishes. The cells were washed twice with 1X PBS. The PBS was aspirated, the cells were covered with 2 ml freshly prepared 4% paraformaldehyde in 1X PBS and subjected to fixation for 10 minutes at room temperature. The coverslips were washed twice with 1X PBS. The PBS was aspirated and the cells were permeabilized for 2 minutes by the addition of 2 ml of 0.2% Triton X-100 in 1X PBS to each well. The coverslips were washed 3 times with 1X PBS. The PBS was aspirated, the cells were covered with 2 ml 1X PBS with 3% BSA, 1% goat serum and incubated for 1 hour at room temperature to block. After blocking, the coverslips were inverted cell-containing side down onto 100  $\mu$ l drops of primary antibody diluted in 1X PBS containing 3% BSA and 1% goat serum and incubated for 1 hour at room temperature. In most cases, the primary antibodies were used within a concentration range of 0.1-10  $\mu$ g/ml. A list of the antibodies used in this study is included in Table 2.2. Following the incubation, the coverslips were transferred back into 6-well plates containing 1X

PBS + 1% Triton X-100 and washed 3 x 5 minutes at RT. After the last wash, the coverslips were incubated for 1 hour at room temperature with either Alexa Fluor® 488 F(ab')<sub>2</sub> Fragment of Goat Anti-Mouse IgG (H+L) or Alexa Fluor® 594 Donkey Anti-Rabbit IgG (H+L) (Life Technologies) secondary antibodies diluted 1:5000 in 1X PBS + 3% BSA, 1% goat serum. The coverslips were kept in the dark from this point. After the secondary antibody incubation, the coverslips were washed 3 x 5 minutes with 1X PBS. The 1X PBS was aspirated and replaced with 1X PBS + 0.1 µg/ml 4',6-diamidino-2-phenylindole (DAPI) for 5 minutes. The coverslips were then washed 3 x 5 minutes with 1X PBS, mounted onto glass microscope slides with ProLong Gold Antifade mounting medium (Life Technologies), sealed with clear fingernail polish and stored at 4° C, in the dark.

### **2.8.2 Epifluorescence Microscopy and Imaging**

Immunofluorescence slides were viewed using a Nikon Eclipse 80i epifluorescence microscope. Microscopic images were captured using a Hamamatsu ORCA-ER digital camera, controlled by the MetaMorph Microscopy Automation and Image Analysis Software (Molecular Devices). To enable accurate comparison between samples, all images from a given experiment were captured using identical exposure settings.

### **2.8.3 MODified Histone Peptide Array**

H4K20me<sub>3</sub> antibody specificity was evaluated using the MODified Histone Peptide Array (Active Motif, 13005) as follows. Individual peptide arrays were immersed in 3 ml Blocking Solution (10 mM Tris-HCl pH 7.4, 150 mM NaCl, 0.05% Tween 20, 5% non-fat milk) and incubated for 1 hour at room temperature on a rocking platform. The Blocking Solution was removed and the arrays were rinsed briefly and then washed 3 x 5 minutes with TTBS Buffer (10 mM Tris-HCl pH 7.4, 150 mM NaCl, 0.05% Tween 20) at room temperature. After the last wash, the TTBS was removed and each array was incubated with a different primary H4K20me<sub>3</sub> antibody diluted 1:2000 in Blocking Solution. The arrays were incubated with the H4K20me<sub>3</sub> antibodies for 1 hour at room temperature, on a rocking platform. Each array was rinsed briefly and then washed 3 x 5 minutes with TTBS Buffer at room temperature. Following the last wash, the arrays were incubated with anti-rabbit-HRP (Cell Signaling Technology, 7074) diluted 1:2500 in 3 ml Blocking Solution

for 1 hour at room temperature, on a rocking platform. Each array was rinsed briefly and then washed 3 x 5 minutes with TTBS Buffer at room temperature. The arrays were developed for 1 minute at room temperature with ECL Plus Western Blotting Substrate (Pierce) and exposed to film (Kodak).

The resulting autoradiographic films were scanned with a conventional flatbed scanner and saved as TIFF files. The scanned images were then aligned to a reference grid to identify individual peptide spots using the Array Analyse software (Active Motif). Spot intensities for the individual peptides were determined and used to generate a specificity factor for each H4K20me3 antibody. The specificity factor is a calculated ratio of the average intensity of all spots that contain a specific modification to the average intensity of all of the other spots that lack the specific modification.

## **Chapter 3. Establishing Model Systems of Cell Senescence**

### **3.1 Rationale**

Cell senescence provides a potent mechanism of tumor suppression and is mediated through a specific program that entails the establishment of a stable proliferation arrest and altered secretory phenotype. The induction and maintenance of senescence is concurrently accompanied by profound changes to chromatin structure and regulation. Despite considerable progress in the senescence field, it is not definitively known how the extensive chromatin remodeling might facilitate the various features of the senescence program. In order to interrogate the putative relationship between chromatin structure and the senescence program, it was first important to develop and validate relevant model systems. In this manner, I set out to establish multiple *in vitro* models of cell senescence in order to determine how changes in chromatin structure could promote proliferation arrest and other aspects of the senescence program. More specifically, I sought to define a molecular and transcriptional profile of cell senescence that could be used as a framework to understand the functional impact of the chromatin changes.

### **3.2 Results**

#### **3.2.1 Establishing Experimental Models of Cell Senescence**

The ability to investigate a cellular state as complex as senescence is largely contingent upon the successful establishment and implementation of a robust model system. Therefore, in order for any senescence model system to provide maximum insight, it must be able to withstand experimental manipulation and respond in a reproducible manner. In addition, because the senescence program is such a complicated biological phenomenon, the utilization of multiple senescence models can lend an added level of confidence and specificity to a given observation. For this reason, models of both replicative senescence and oncogene-induced senescence were selected for use in studies to examine the contribution of chromatin structure to the regulation of the senescence program.

Primary human diploid fibroblasts (HDFs) are a commonly employed cell type used in the mechanistic investigation of cell senescence. More specifically,

IMR90 cells, a thoroughly characterized HDF strain isolated from fetal lung has been utilized for nearly 30 years in the study of replicative lifespan and senescence (Nichols et al., 1977). As such, IMR90 cells were selected as an appropriate cell line for use as a model of replicative senescence. To facilitate replicative senescence, young IMR90 cells were subjected to serial passage in culture and maintained in a low (3%) oxygen incubator. To minimize stress, the cells were kept between 30 and 95% confluence at all times and removed from low oxygen conditions for only the minimal amount of time required for sub-culturing. At each passage the cells were counted, cumulative population doubling values calculated and then plotted graphically (Figure 3.1a). The cells were assayed for features of replicative senescence once the population doubling time exceeded 14 days.

To confirm senescence, whole cell extracts were prepared from proliferating (PD30) and replicative senescent (PD88) IMR90 cells, fractionated by SDS-PAGE and transferred to PVDF membranes for subsequent Western blot analysis. The membranes were then blotted to assess expression of several markers of cell proliferation and the senescence program. While lamin A/C expression appeared unaffected in the PD88 cells, a marked reduction of lamin B1 levels was observed (Figure 3.1b). Likewise, cyclin A was largely depleted from the PD88 cells, indicating that the cells had undergone cell cycle exit. Consistent with the PD88 cells being senescent, a robust induction of p16INK4a was noted, along with induction of another inhibitor of cell cycle progression, p21WAF1. As a loading control, GAPDH levels remained relatively consistent between the PD30 and PD88 lysates.

Detection of increased  $\beta$ -galactosidase activity is commonly utilized as an important diagnostic assay to distinguish senescent cells from other cellular states. To evaluate the cells for  $\beta$ -galactosidase activity, PD30 and PD80 cells were subjected to fixation and incubated in a buffer containing the synthetic substrate 5-bromo-4-chloro-3-indolyl- $\beta$ -d-galactopyranoside (X-gal). Cells that contained lysosomal  $\beta$ -galactosidase activity were detected by the formation of a perinuclear blue precipitate. While fewer than 5% of the PD30 cells stained positively for  $\beta$ -galactosidase, more than 95% of the PD88 cells exhibited visually detectable perinuclear  $\beta$ -galactosidase staining (Figure 3.1c). Bright field microscopy of the stained cells also revealed profound differences in cellular morphology between the PD30 and PD88 cells. Whereas, the PD30 cells exhibited a characteristic spindly fibroblast morphology, the PD88 cells had an enlarged, flattened shape, often

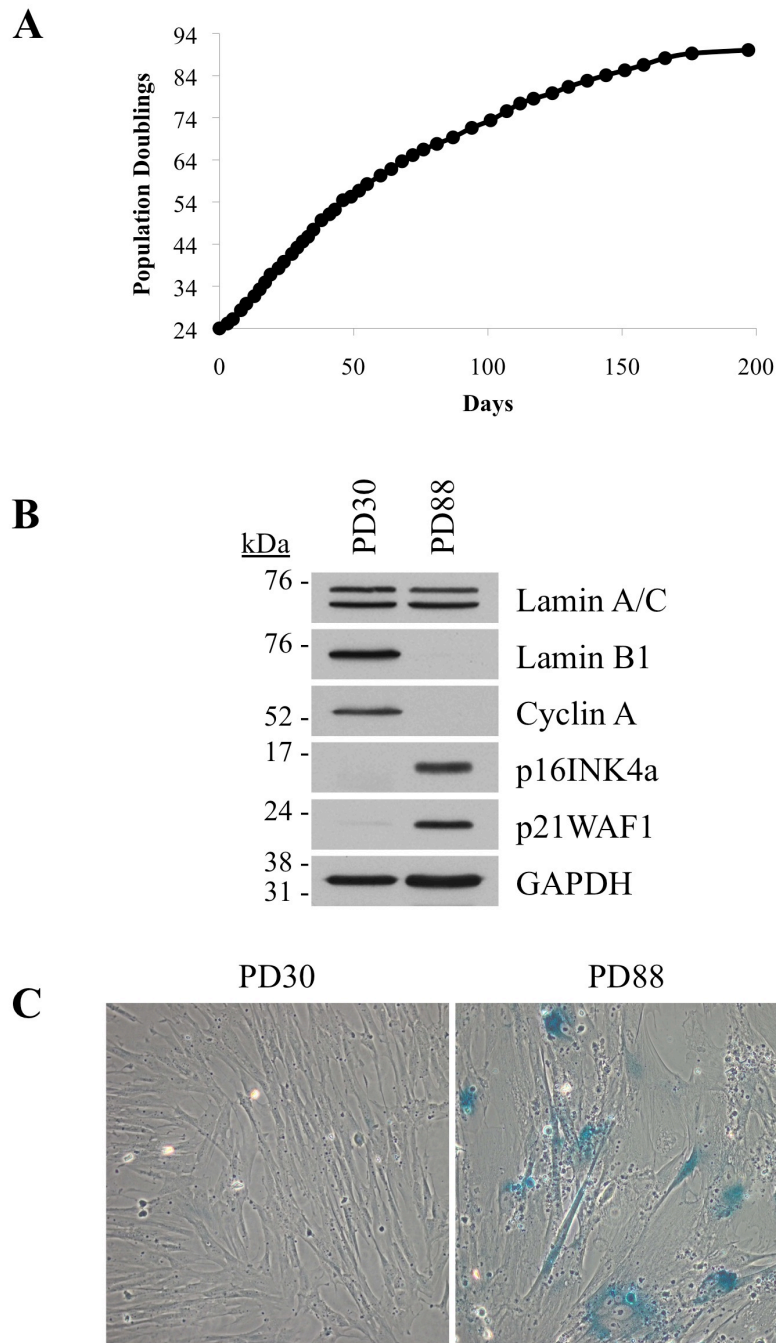


**Figure 3.1 Characterizing an *in vitro* model of RS.** (A) Proliferation curve for IMR90 cells that were cultured to replicative senescence under low (3%) O<sub>2</sub> conditions. (B) Whole cell lysates from PD30 and PD88 IMR90 cells were fractionated by SDS-PAGE and Western blotted for markers of proliferation and senescence. GAPDH serves as a loading control. (C) SA β-gal staining of PD30 and PD88 IMR90 cells.

contained multiple nuclei per cell and possessed prominent vacuoles. The latter PD88 morphology is a commonly observed feature of replicative senescent IMR90 cells.

The combined growth curve data, Western blotting analyses,  $\beta$ -galactosidase staining and cellular morphology of the PD30 and PD88 IMR90 cells validated that the PD88 cells were truly senescent. In this manner, a seemingly uniform population of senescent cells was generated with relative technical ease. In fact, during multiple subsequent rounds of culturing IMR90 cells to replicative senescence under the same conditions, the cells reproducibly underwent senescence between 86 and 90 cumulative population doublings. As such, this confirmed that the IMR90 replicative senescence model would provide a robust and predictable system with which to interrogate aspects of the senescence program.

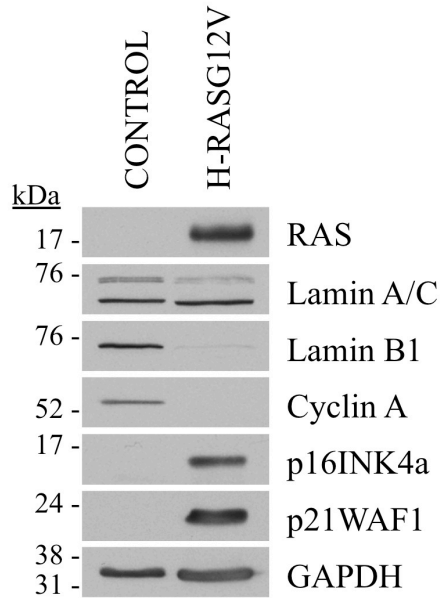
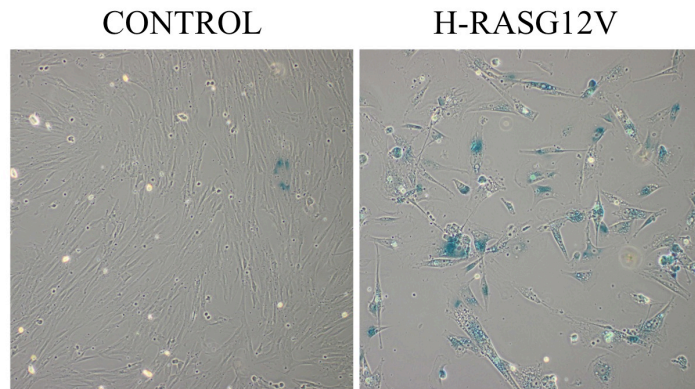
Constitutive oncogene activation is also capable of inducing senescence in normal primary human cells and can be exploited experimentally to provide an additional model of cell senescence. Although a variety of oncogenes can induce senescence, ectopic expression of a constitutively active mutant *H-RAS* allele (*H-RASG12V*) is commonly utilized to confer senescence in HDFs (Serrano et al., 1997). To accomplish this, early passage IMR90 cells were infected with either a control retrovirus or a retroviral construct directing the expression of *H-RASG12V*, subjected to drug selection and maintained in culture. Infection efficiency was controlled for using several approaches. First, the transfection efficiency of the Phoenix retroviral packaging cells was evaluated by transfecting a parallel plate with a GFP expression construct and scoring for GFP-positive cells. The transfection was considered successful as greater than 95% of the Phoenix cells exhibited GFP expression twenty-four hours after transfection. Second, 100% of the control and *H-RASG12V*-infected IMR90 cells survived puromycin selection, whereas the drug killed 100% of cells from an uninfected plate of IMR90 cells. These criteria were applied to all subsequent retroviral infection experiments in order to confirm that a comparable if not identical viral multiplicity of infection (MOI) was attained for each experiment.

Ten days after retroviral infection, the control and *H-RASG12V*-infected cells were harvested and assayed for key markers of cell proliferation and senescence. Whole cell extracts prepared from the control and *H-RASG12V* cells were fractionated by SDS-PAGE and immobilized to PVDF membranes. The PVDF

membranes were then Western blotted to confirm expression of ectopic H-RAS. As anticipated, the H-RASG12V-infected cells exhibited high levels of H-RAS (Figure 3.2a). Western blot analysis of lamin A/C revealed a subtle decrease in the upper lamin A band in the H-RASG12V cells, while the lower lamin C band remained unaffected. Similar to replicative senescent cells, lamin B1 and cyclin A expression were both greatly reduced in the H-RASG12 cells. In addition, both p16INK4a and p21WAF1 were induced to high levels in the H-RASG12V cells but not in the control cells. As a control, GAPDH expression levels remained comparable in both the control and H-RASG12V cells. These data collectively suggested that whereas the control cells continued to proliferate, the H-RASG12V-infected cells had undergone H-RAS-induced cell cycle exit.

Control and H-RASG12V-infected cells were also fixed and stained to detect  $\beta$ -galactosidase activity. Similar to normal early passage IMR90 cells, very few cells (< 5%) stained positive for  $\beta$ -galactosidase activity (Figure 3.2b). In contrast, the majority of the H-RASG12V-infected cells showed robust staining for  $\beta$ -galactosidase activity. In addition, the H-RASG12V expressing cells exhibited several morphological hallmarks of senescent cells including a large flattened shape and prominent vacuole formation. Importantly, the observed change in morphology in the H-RASG12V cells was not simply a consequence of viral infection, as the majority of the control-infected cells retained a normal spindly fibroblast morphology. Taken together, the Western blotting data,  $\beta$ -galactosidase staining and altered morphology confirmed that the H-RASG12V-infected cells were senescent. The results also confirmed that retroviral mediated introduction of an activated H-RAS allele into IMR90 cells could be utilized as a second and complimentary model to study senescence in vitro.

Two defining features characterize the cell senescence program: the maintenance of a stable proliferation arrest and an altered secretory phenotype. Although these two hallmarks have been studied individually in considerable detail, it is important to recognize that cellular states other than senescence may often share either feature of the senescence program. For example, whereas both quiescent and terminally differentiated cells possess a phenotype defined by proliferation arrest, unlike senescence these cellular states typically do not involve p16INK4a induction and SA  $\beta$ -gal activity. Therefore, one of the key challenges of investigating cell senescence at the molecular level is to distinguish whether a given observation

**A****B**

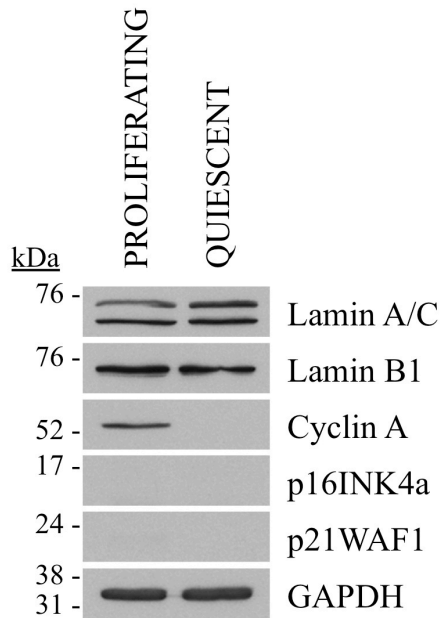
**Figure 3.2 Characterizing an *in vitro* model of OIS.** (A) Whole cell lysates from control (empty viral vector) and H-RASG12V-infected IMR90 cells were fractionated by SDS-PAGE and Western blotted for markers of proliferation and senescence. GAPDH serves as a loading control. (B) SA  $\beta$ -gal staining of control and H-RASG12V-infected IMR90 cells.

represents a specific aspect of the senescence program, or is alternatively simply a consequence of cell cycle exit. In order to make this distinction, it is critical to determine whether a particular effect observed using models of cell senescence is unique to senescence, or whether it also occurs in the context of other non-proliferative cellular states. To this end, the specificity of any putative senescence-associated finding should first be validated using a model of quiescence. Although cell cycle arrest is a hallmark of both senescence and quiescence, the proliferation arrest associated with quiescence is by definition transient and can be reversed following exposure to sufficient mitogenic stimuli (Coller, Sang & Roberts, 2006).

Experimentally, quiescent cells can be generated in culture by growing primary cells to high confluence in medium containing low serum content. To accomplish this, early passage IMR90 cells were seeded at approximately 90% confluence in medium containing only 0.1% FBS as opposed to the standard 20% FBS that is routinely used to culture IMR90 cells. Four days after seeding, whole cell extracts were prepared from the cells, subjected to fractionation by SDS-PAGE and immobilized to PVDF membranes for assessment of proliferation and senescence markers. Western blot analysis revealed that similar to senescent cells, quiescent cells maintain lamin A/C levels and exhibit a marked reduction of cyclin A expression (Figure 3.3a). The overall depletion of cyclin A confirmed that very few cells, if any within the quiescent population were actively progressing through S phase and therefore no longer proliferating. However, in contrast to senescent cells, no decrease of lamin B1 expression was observed in the quiescent cells. Also contrary to senescent cells, no induction of the cell cycle inhibitors p16INK4a and p21WAF1 was observed in the quiescent lysates. These data confirmed that although the quiescent cells had undergone cell cycle exit, they did not exhibit gene expression changes reflective of an activation of the senescence program.

Although quiescent cells share a phenotype characterized by proliferative arrest with senescent cells, quiescent cells should not possess the increased lysosomal  $\beta$ -galactosidase activity that is associated with senescence. In parallel with the whole cell lysate preparation, proliferating and quiescent IMR90 cells were fixed and assayed to detect increased lysosomal  $\beta$ -galactosidase activity. As expected, in both the proliferating and quiescent IMR90, fewer than 5% of the cells stained positive for SA  $\beta$ -galactosidase activity (Figure 3.3b). Collectively, the general absence of  $\beta$ -galactosidase activity and failure to induce known molecular markers of

**A**



**B**

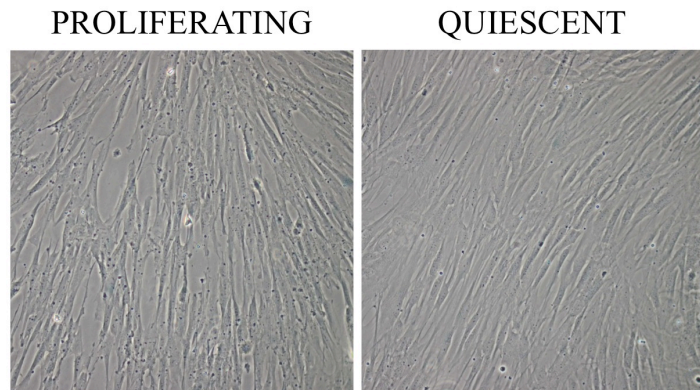


**Figure 3.3 Characterizing an *in vitro* model of quiescence.** (A) Whole cell lysates from proliferating and quiescent IMR90 cells were fractionated by SDS-PAGE and Western blotted for markers of proliferation and senescence. GAPDH serves as a loading control. (B) SA β-gal staining of proliferating and quiescent IMR90 cells.

senescence, coupled with a robust reduction of cyclin A expression, indicate that although quiescent cells are non-proliferative, they are phenotypically distinct from senescent cells. As such, this confirmed that quiescent cells could provide a useful model for evaluating the specificity of senescence-associated findings.

### **3.2.2 Identifying Gene Expression Changes in RS**

In order to further characterize and validate the replicative and oncogene-induced senescence models, it was important to evaluate the respective systems on a more global level. To this end, transcriptional profiling provides a comprehensive and informative snapshot of a cell population's state at a given time. Moreover, by evaluating the transcriptional status of a particular cell population, it is possible to gain insight into the pathways and processes that are engaged under a defined cellular state. Therefore, by obtaining gene expression profiles for replicative and oncogene-induced senescent IMR90 cells, it might be possible to identify additional transcriptional changes that might reveal novel aspects of the senescence program.

To facilitate transcriptional profiling, total RNA was isolated from low passage, proliferating IMR90 cells (PD28) and late passage, replicative senescent IMR90 cells (PD90). The RNA samples were subsequently processed and hybridized to Affymetrix Human Genome U133 Plus 2.0 Arrays by the Cancer Research UK Microarray Facility (Paterson Institute for Cancer Research, Manchester, UK). The hybridized arrays were scanned and the resulting raw data (.CEL) files were imported into R and analyzed using the Bioconductor software packages. Each sample was subjected to background correction and normalization using the GC Robust Multi-array Average (GCRMA) method. Normalized intensity values for each probe from the PD28 and PD90 microarrays were compared and displayed as a scatter plot (Figure 3.4). Although the majority of probes exhibited comparable normalized intensity values between the PD28 and PD90 arrays, a smaller subset of probes contained higher intensity values on either the PD28 or PD90 arrays, respectively.

Differential expression was calculated from the log-normalized values of the proliferating and replicative senescent cells. T-tests were performed to determine statistical significance and genes were considered differentially expressed if the absolute fold difference between the proliferating and senescent samples exceeded 1.5-fold and the BH-FDR adjusted p-value was lower than 0.05. For genes that were

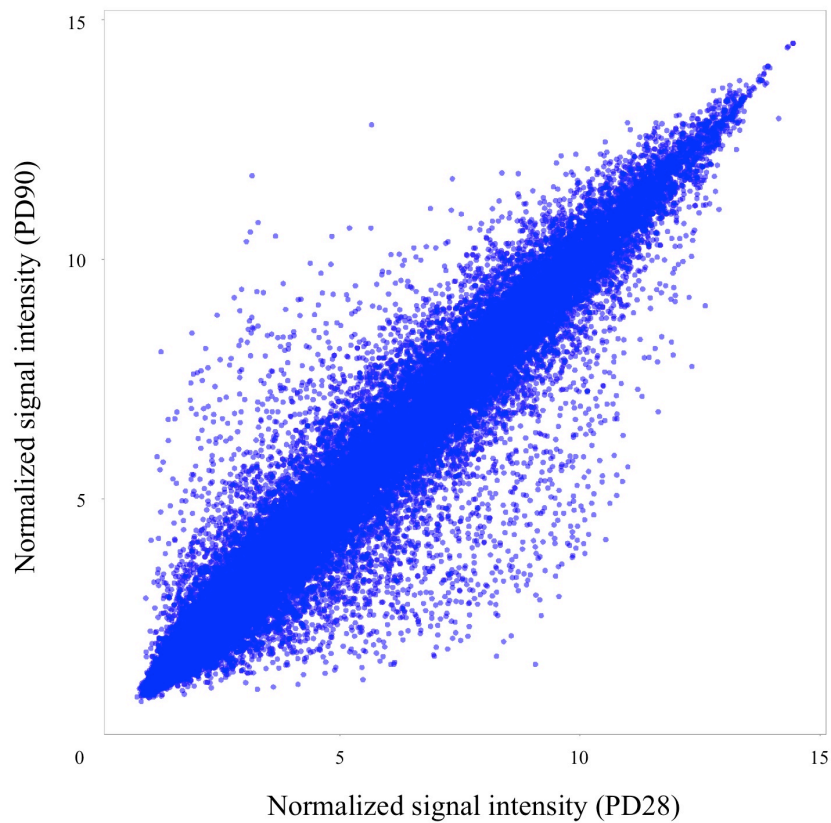


**Figure 3.4 Global assessment of RS gene expression changes.** The signal intensity values after GCRMA normalization for all probes from the proliferating (PD28) and replicative senescent (PD90) Affymetrix Human Genome U133 Plus 2.0 microarrays were compared and displayed graphically as a scatter plot.

represented by multiple probe sets on the microarray, the gene was only considered differentially expressed if all probe sets changed in the same direction and met the statistical criteria. Using these parameters, 5,447 differentially expressed genes were identified in the PD90 replicative senescent cells when compared to PD28 proliferating cells. Of the 5,447 genes, 2,711 genes were significantly upregulated in the PD90 cells, while 2,736 genes were significantly downregulated.

In order to identify biological processes that were altered in the PD90 replicative senescent cells, the microarray intensity data were collated into individual gene values, ranked by signal to noise ratio and subjected to Gene Set Enrichment Analysis (GSEA). GSEA is a statistical method used to identify sets of genes within a dataset that are coordinately regulated by comparing the expression changes to predefined gene ontology categories (Subramanian et al., 2005). The resulting analyses reveal biological pathways and functions based on sets of genes that are either enriched in the control group (i.e., proliferating cells) or enriched in the experimental group (i.e., senescent cells). To this end, gene sets identified as enriched in replicative senescent cells predominantly contained genes that were upregulated in senescence, whereas gene sets enriched in proliferating cells were largely comprised of genes downregulated in the senescent cells.

Based on GSEA, a number of gene sets were identified as significantly enriched in PD90 replicative senescent IMR90 cells (i.e., derived from genes that were upregulated in the PD90 cells). These gene sets represented diverse biological processes and functions (Table 3.1). The most significantly enriched gene set in the PD90 cells was the extracellular structure organization & biogenesis category. Remarkably, the identification of this category was seemingly influenced by the increased expression of numerous protocadherin genes (e.g., PCDHB2, PCDHB3, PCDHB6, PCDHB9, PCDHB10, PCDHB13, PCDHB14, PCDHB16) in the PD90 cells. Elevated expression of the protocadherin genes, as well as another adhesion-related gene, NRCAM, also contributed to high enrichment scores for additional gene sets (e.g., synapse organization and biogenesis, synaptogenesis). Consistent with the senescence-associated secretory phenotype, a category related to cytokine activity (hematopoietin interferon class D2000 cytokine receptor activity) was also highly enriched in the PD90 cells.

In addition to the categories that were enriched in the senescent cells, GSEA also identified multiple significant gene sets that were enriched in the PD28

Gene Set	Number of Genes	NES	NOM p-value
Extracellular structure organization & biogenesis	30	2.03	0
Synapse organization & biogenesis	22	2.03	0
Female pregnancy	46	2.01	0
Synaptogenesis	18	1.96	0
Hematopoietin interferon class D2000 cytokine receptor activity	34	1.91	0
Positive regulation of phosphate metabolic process	25	1.79	0.002
Positive regulation of phosphorylation	23	1.79	0.004
Positive regulation of protein amino acid phosphorylation	18	1.77	0
Multi organism process	150	1.73	0
Anion transmembrane transporter activity	55	1.71	0.002

**Table 3.1 Gene sets enriched in RS cells.** List of the top 10 most significantly enriched gene sets in replicative senescent IMR90 cells (i.e., genes that were upregulated in replicative senescent cells). Gene sets were ranked according to the normalized enrichment score (NES), which is the primary statistic for how enriched the original dataset is for a given gene set classification. In order to derive the NES, an enrichment score (ES), which is defined as the degree to which a gene set is overrepresented at the head/tail of a ranked gene list, is first calculated. Next, the NES is determined by applying a normalization factor to the ES based on the size of the queried gene set. In this manner, the NES provides a more accurate assessment of whether a dataset is enriched for any particular defined gene list, while reducing the bias contributed by the size of the dataset.

proliferating cells (i.e., derived from genes that were downregulated in the PD90 senescent cells). Of the top 10 gene sets significantly enriched in proliferating cells, 8 sets involved processes related to cell cycle progression (e.g., cell cycle process, cell cycle phase, mitosis), while 2 sets related specifically to chromosomes (e.g., chromosome, chromosomal part) (Table 3.2). The 8 cell cycle-related categories contained a number of overlapping genes that were robustly downregulated including KIF15, TTK, CDC25C, KIF2C, NCAPH, NEK2, CDKN3 and CDKN2C. The fact that nearly all of the most significantly enriched categories in the proliferating cells related to cell cycle progression, indicated that the replicative senescent cells had truly undergone proliferation arrest and provided additional validation of the RS model.

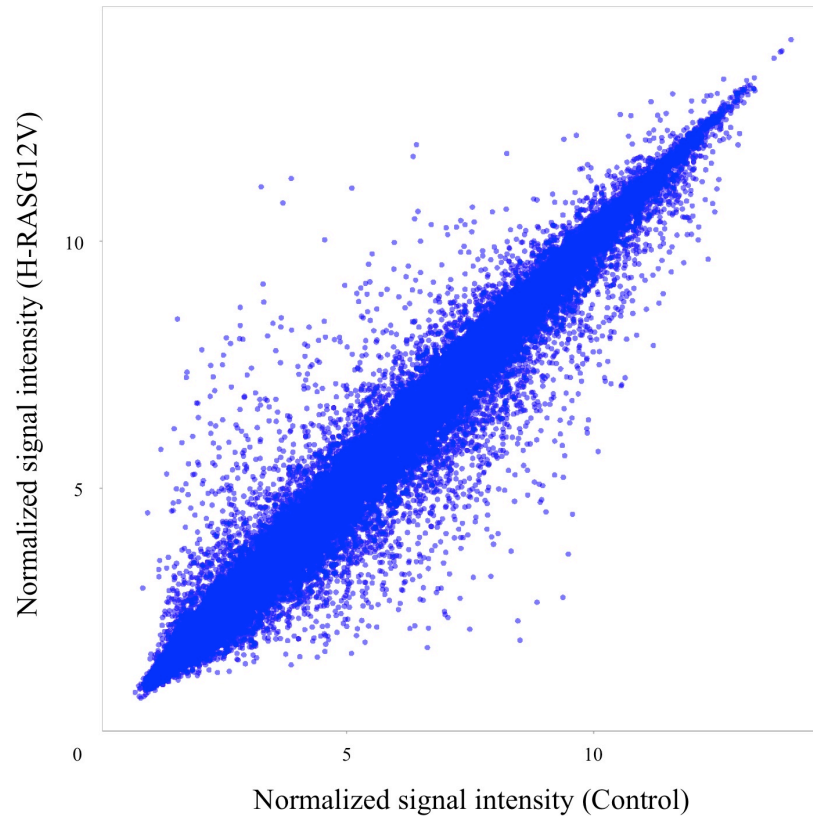
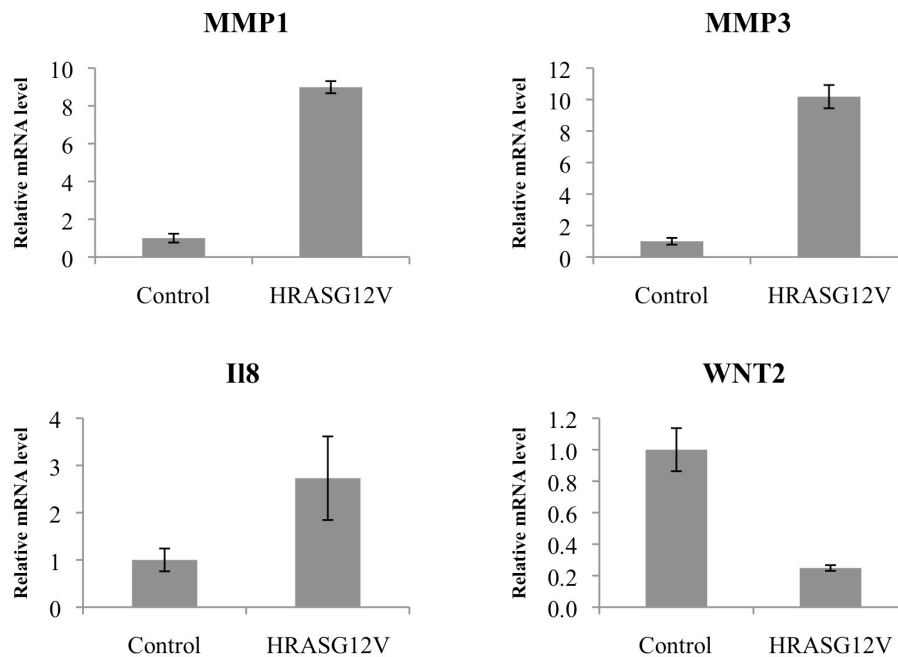
### **3.2.3 Identifying Gene Expression Changes in OIS**

Transcriptional profiling was also performed on oncogene-induced senescent cells. Total RNA was isolated from proliferating control-infected and senescent H-RASG12V-infected IMR90 cells 10 days after infection and prepared for microarray analysis in the same manner as for the replicative senescent cells. As before, control and H-RASG12V samples were hybridized to Affymetrix Human Genome U133 Plus 2.0 Arrays, scanned to obtain raw (.CEL) files, imported into R and analyzed with Bioconductor. Each control and H-RASG12V replicate was subjected to background correction and normalization using the GC Robust Multi-array Average (GCRMA) method. Normalized intensity values for each probe from the control and H-RASG12V arrays were compared graphically as a scatter plot (Figure 3.5a). Similar to the RS dataset, the majority of probes displayed comparable normalized intensity values for both the control and H-RASG12V arrays, while a smaller subset of probes contained higher intensity values for either the control or H-RASG12V arrays.

Gene changes exhibiting an absolute fold change greater than 1.5-fold and a BH-FDR adjusted p-value lower than 0.05 were considered differentially expressed. By these criteria, 3,189 genes were identified as being differentially expressed in the H-RASG12V-induced senescent IMR90 cells when compared to control-infected proliferating cells. Of the 3,189 genes, 1,502 genes were significantly upregulated in the H-RASG12V cells, while 1,687 genes were significantly downregulated. To evaluate the general performance of the microarray, several genes reported to

Gene Set	Number of Genes	NES	NOM p-value
Cell cycle process	181	-2.64	0
Cell cycle phase	158	-2.60	0
Mitotic cell cycle	140	-2.59	0
Chromosome	115	-2.52	0
Cell cycle GO 0007049	297	-2.49	0
M phase	106	-2.47	0
Chromosomal part	89	-2.44	0
M phase of mitotic cell cycle	79	-2.41	0
Mitosis	76	-2.40	0
Spindle	39	-2.30	0

**Table 3.2 Gene sets enriched in proliferating cells.** List of the top 10 most significantly enriched gene sets in low passage proliferating IMR90 cells (i.e., genes that were downregulated in replicative senescent cells). Gene sets were ranked according to the normalized enrichment score (NES), which is the primary statistic for how enriched the original dataset is for a given gene set classification. The NES accounts for variations in the size of each gene set.

**A****B**

**Figure 3.5 Global assessment of OIS gene expression changes.** (A) The signal intensity values after GCRMA normalization for all probes from the control and H-RASG12V Affymetrix Human Genome U133 Plus 2.0 microarrays were displayed graphically as a scatter plot. (B) To validate the microarray data, qPCR was performed on selected genes using the same control and H-RASG12V RNA samples that were used for the microarray analysis. MMP1, MMP3, IL8 and WNT2 were selected as genes previously reported to undergo altered expression in OIS. For each gene, the qPCR data were normalized to GAPDH mRNA levels and expressed as relative abundance. The error bars denote standard error values.

undergo expression changes during senescence were selected for measurement by quantitative real-time PCR (qPCR) (Figure 3.5b). Consistent with the microarray data, qPCR confirmed an upregulation of MMP1, MMP3 and IL8 and a repression of WNT2 in the OIS cells.

Similar to the analyses conducted for the RS microarray data, the OIS gene expression data were also subjected evaluation by GSEA. Based on GSEA, multiple gene sets were identified as enriched in H-RASG12V-infected senescent IMR90 cells. Assessment of the 10 most highly enriched gene sets in the H-RASG12V cells indicated that a variety of biological processes were affected, including cell differentiation, metal ion binding, metalloendopeptidase activity and the regulation of protein translation (Table 3.3). The identification of categories related to metalloendopeptidase activity was anticipated, as the matrix metalloproteinases (MMPs) comprise a family of genes that are induced in senescent cells as part of the secretory phenotype. Specifically, the metalloendopeptidase activity category revealed elevated expression for MMP3, MMP8, MMP9, MMP12, MMP13, MMP14 and MMP16 in the H-RASG12V-infected senescent cells. To this end, the findings provided evidence that H-RASG12V infection of IMR90 cells resulted in the characteristic secretory phenotype and could therefore be utilized as a viable model of senescence.

GSEA also identified diverse gene sets that were enriched in the control-infected proliferating cells (i.e., comprised of genes that were downregulated in the H-RASG12V-infected senescent cells). As expected, several categorical gene sets related to cell cycle progression (e.g., spindle, cell division, cytokinesis) were identified as highly enriched in the control-infected proliferating cells (Table 3.4). In fact, the spindle and cell division gene sets exhibited the highest enrichment scores in the control cells, and were largely influenced by downregulation of cell cycle genes in the H-RASG12V-infected senescent cells. Multiple gene sets related to extracellular matrix composition (e.g., extracellular matrix structural constituent, proteinaceous extracellular matrix, extracellular matrix) were also significantly enriched in the control-infected cells. This revealed that genes involved in the structure of the extracellular matrix, including matrilin (MATN3), fibulin (FBLN1, FBLN2), collagen (COL4A2) and laminin (LAMA1), were downregulated in the H-RASG12V cells. Collectively, downregulation of genes related to the cell cycle and

Gene Set	Number of Genes	NES	NOM p-value
Myeloid cell differentiation	36	2.04	0
Zinc ion binding	87	1.95	0
Transition metal ion binding	105	1.89	0
Metalloendopeptidase activity	26	1.87	0
Regulation of translational initiation	19	1.87	0
Translational initiation	26	1.85	0.002
Metallopeptidase activity	45	1.84	0.002
Enzyme inhibitor activity	118	1.80	0
Oxygen & reaction oxygen species metabolic process	20	1.79	0.008
Rhythmic process	24	1.77	0.012

**Table 3.3 Gene sets enriched in H-RASG12V cells.** List of the top 10 most significantly enriched gene sets in H-RASG12V-induced senescent IMR90 cells (i.e., genes that were upregulated in H-RASG12V cells). Gene sets were ranked according to the normalized enrichment score (NES), which is the primary statistic for how enriched the original dataset is for a given gene set classification. The NES accounts for variations in the size of each gene set.

Gene Set	Number of Genes	NES	NOM p-value
Spindle	39	-1.94	0
Cell division	20	-1.91	0
Extracellular matrix structural constituent	25	-1.87	0.004
Proteinaceous extracellular matrix	92	-1.83	0
Sodium ion transport	20	-1.80	0.006
Cytokinesis	18	-1.80	0.004
Regulation of heart contraction	25	-1.78	0
Extracellular matrix	94	-1.77	0
Glutathione transferase activity	15	-1.75	0.010
Integrin binding	30	-1.75	0.002

**Table 3.4 Gene sets enriched in control cells.** List of the top 10 most significantly enriched gene sets in control-infected proliferating IMR90 cells (i.e., genes that were downregulated in H-RASG12V cells). Gene sets were ranked according to the normalized enrichment score (NES), which is the primary statistic for how enriched the original dataset is for a given gene set classification. The NES accounts for variations in the size of each gene set.

extracellular matrix are both hallmarks of senescence and further validated H-RASG12 infection of IMR90 cells as a robust model of senescence.

### **3.2.4 Defining a Transcriptional Profile of Cell Senescence**

Although the identification of differentially expressed genes in both replicative and oncogene-induced senescent cells could provide relevant biological insight into the respective model systems, a direct comparison of the two models could provide a more comprehensive understanding of the universal features of cell senescence. To this end, the replicative senescence and oncogene-induced senescence microarray datasets were queried to identify gene expression changes that were either common or unique between the two systems. For the respective datasets, a gene was considered differentially expressed if it exhibited an absolute fold change greater than 1.5-fold with a BH-FDR adjusted p-value lower than 0.05. According to these criteria, 1,770 genes were identified as being differentially expressed in both replicative senescent and oncogene-induced senescent IMR90 cells (Figure 3.6a).

While the expression of 1,770 genes changed significantly in both models of senescence, the initial analysis did not account for the directionality of change. For example, some genes were identified as having met the statistical cutoff and found to be upregulated in one senescence model, but downregulated in the other. To address this discrepancy, analyses of upregulated and downregulated genes were performed separately. Of the 2,711 genes that were upregulated in replicative senescent cells and 1,502 genes that were upregulated in oncogene-induced senescent cells, 424 genes were identified as upregulated in both senescence models (Figure 3.6b). Likewise, while 2,736 genes were downregulated significantly in replicative senescent cells and 1,687 genes downregulated in oncogene-induced senescent cells, 584 genes were identified as downregulated in both model systems (Figure 3.6c). In all, the expression of 1,008 genes was altered in common between the replicative senescent and oncogene-induced senescent IMR90 cells.

Based on prior investigation of cell senescence by many laboratories and the fact that 1,008 genes were differentially expressed in two models of senescence, it was reasonable to hypothesize that specific pathways and processes might be altered as part of the senescence program. In order to identify potentially affected biological processes, the genes that were differentially expressed in both the replicative senescent and oncogene-induced senescent IMR90 cells were evaluated using

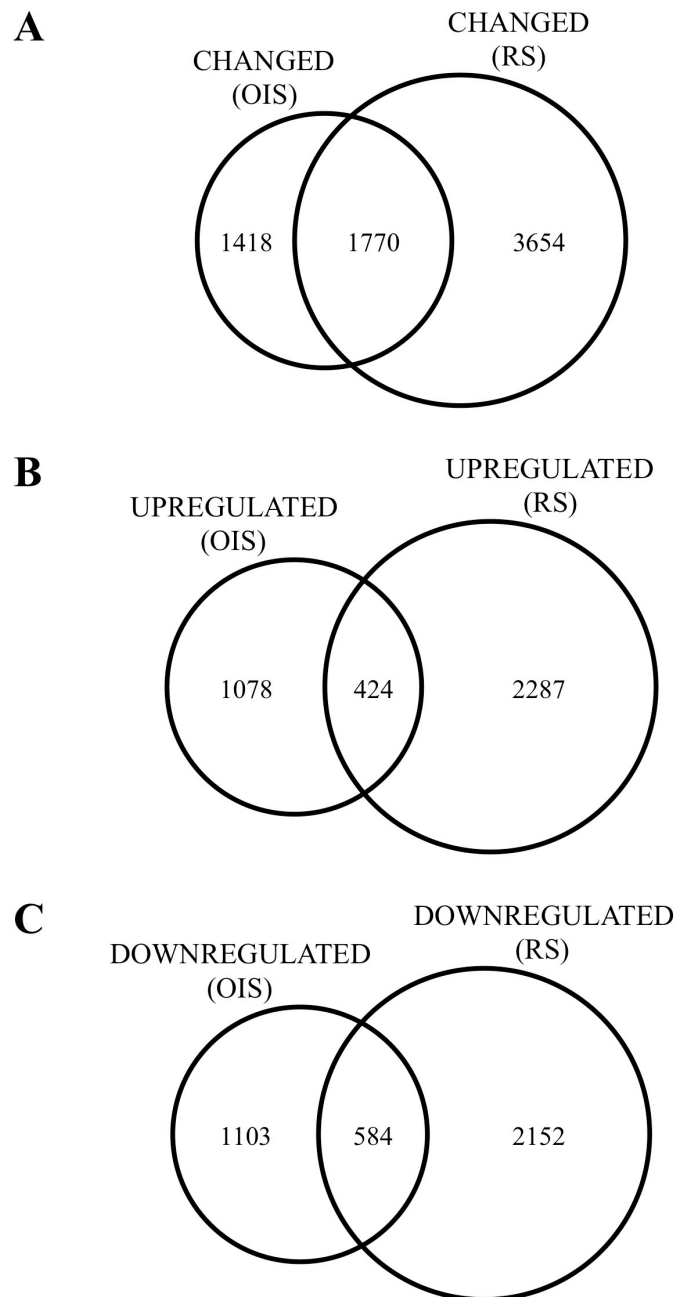


**Figure 3.6 Comparison of RS and OIS gene expression changes.** Differentially expressed genes from the RS and OIS Affymetrix Human Genome U133 Plus 2.0 microarray datasets were compared in order to identify common changes. Genes exhibiting a fold change  $> 1.5$  or  $< -1.5$  and a BH-FDR adjusted p-value  $< 0.05$  were considered differentially expressed. (A) Identification of genes that change significantly in RS and OIS cells. (B) Identification of genes that were upregulated in RS and OIS cells. (C) Identification of genes that were downregulated in RS and OIS cells.

Ingenuity Pathway Analysis (IPA). IPA utilizes literature-based findings to predict cellular phenotypes, biological interactions and physiological or disease processes based on user provided transcriptional profiling datasets. To help delineate between processes that were potentially activated or inhibited, the gene expression changes were queried as three distinct datasets: genes that were upregulated in common, genes that were downregulated in common and all genes that changed in common between the replicative senescent and oncogene-induced senescent cells.

Through IPA evaluation of the 424 genes upregulated in both the RS and OIS models, multiple canonical signaling and metabolic pathways were identified as being affected in a statistically significant manner (Figure 3.7a). Several well-characterized cancer associated pathways were identified (e.g., bladder cancer signaling, ErbB signaling, pancreatic adenocarcinoma signaling). In addition, multiple pathways related to the regulation of apoptosis and cell death were also significantly affected (e.g., retinoic acid mediated apoptosis signaling, death receptor signaling). In fact, retinoic acid mediated apoptosis signaling was identified as the most significantly altered pathway derived from the upregulated genes dataset. Specifically, key pro-apoptotic genes including TNFRSF10A, TNFRSF10D, DAP3, IFNA1, PARP8 and TIPARP were all induced in both RS and OIS (Figure 3.7b). However, it is important to recognize that regulation of signal transduction can be highly complex and elevated expression of pathway components may not be solely sufficient to activate a given pathway. To this end, the anti-apoptotic regulators CFLAR/FLIP and XIAP were also upregulated significantly in RS and OIS, suggesting that as expected, the apoptotic pathway is not fully engaged in senescent cells.

Despite exhibiting some similar molecular characteristics, senescence and apoptosis reflect distinct cellular programs that result in separate endpoints. The senescence program involves the establishment of a permanent proliferation arrest and promotion of a proinflammatory environment through expression of the SASP (Coppé et al., 2010). In contrast, apoptosis is characterized by a caspase-mediated cell death program that involves rapid self-destruction and clearance, yet fails to elicit an inflammatory response (Taylor, Cullen & Martin, 2008). Thus, while senescence and apoptosis both restrict the proliferative capacity of damaged cells and suppress tumorigenesis, whether these processes cooperate at the molecular level is yet to be fully elucidated.

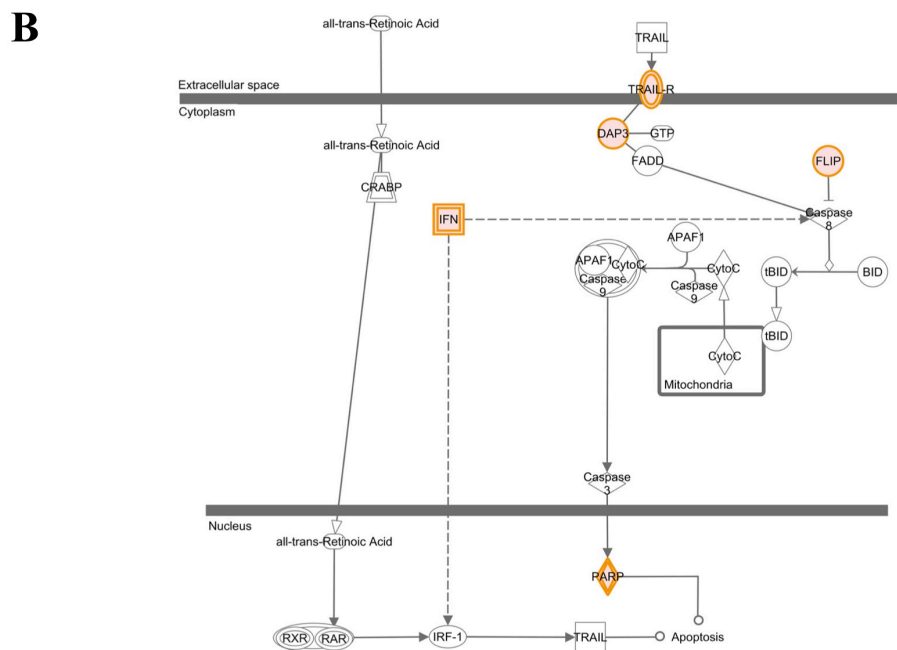
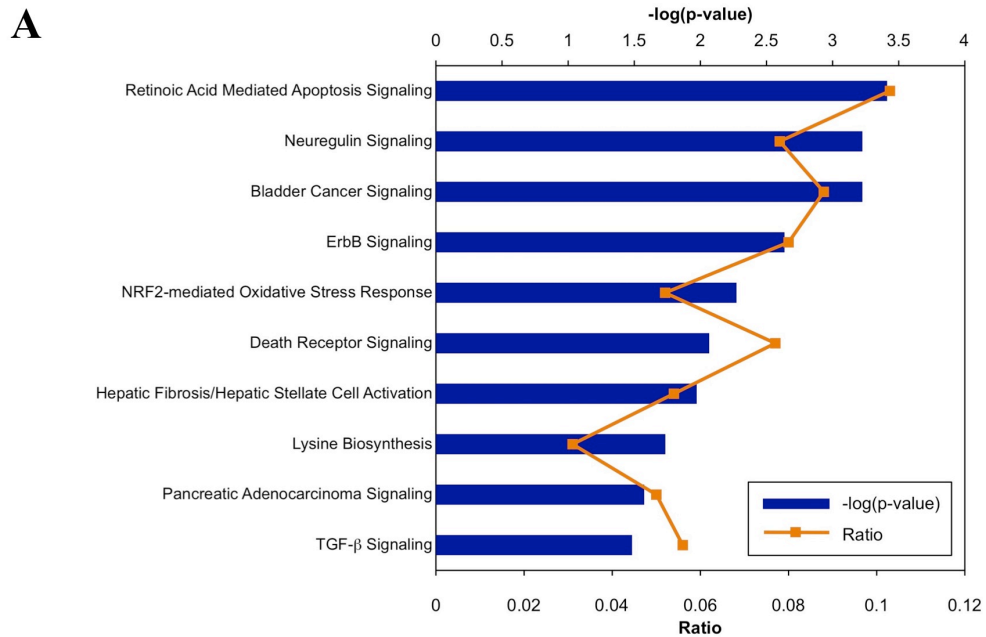


**Figure 3.7 IPA of genes upregulated in RS and OIS.** Genes that were significantly upregulated in both RS and OIS cells were evaluated using Ingenuity Pathway Analysis. (A) List of the top 10 significantly altered canonical pathways, ranked by significance. (B) Schematic diagram of the most significantly altered pathway: retinoic acid-mediated apoptosis signaling. Red shaded genes represent genes within the pathway that were upregulated in both RS and OIS cells.

The 584 genes downregulated in both the RS and OIS IMR90 cells were also subjected to evaluation with IPA, which revealed several significantly affected pathways (Figure 3.8a). Remarkably, 4 of the top 10 altered canonical pathways involved aspects of the DNA damage response (e.g., G2/M DNA damage checkpoint regulation, role of BRCA1 in DNA damage response, ATM signaling, GADD45 signaling). This was a little surprising as DNA damage signaling is a known effector mechanism of the senescence program. Importantly, each of the DNA damage response related pathways also incorporate elements of cell cycle regulation. This was also the case for the most significantly affected canonical pathway: mitotic roles of polo-like kinase. This pathway summarizes several distinct stages of mitosis: centrosome separation and maturation, mitotic entry, metaphase to anaphase transition, mitotic exit and cytokinesis (Figure 3.8b). In both RS and OIS cells, the mitosis genes EG5 (KIF11), PLK, CDC2 (CDK1), CCNB1, CDC20, PRC1, EMI1 (FBXO5), PTTG1, MKLP1 (KIF23) were all significantly downregulated. Although the reduced expression of these genes could suggest a mitotic defect in senescent cells, it is more likely that these genes were downregulated as a secondary consequence of the senescence proliferation arrest.

In order to obtain a more comprehensive assessment of the senescence-associated gene expression changes, both the upregulated and downregulated gene lists were combined into a single dataset and evaluated with IPA. Similar to the individual upregulated and downregulated gene analyses, analysis of the combined dataset revealed multiple metabolic and signaling pathways were significantly affected in common between the RS and OIS IMR90 cells (Figure 3.9a). Four of the top 10 identified pathways involved diverse processes relating to intermediary metabolism (e.g., nitrogen metabolism, lysine biosynthesis, nicotinate and nicotinamide metabolism, ascorbate and aldarate metabolism). In each case, the metabolic pathways included upregulated and downregulated genes, complicating interpretation of the status of the pathways. Comparable to analysis of the downregulated gene list, IPA identified the mitotic roles of polo-like kinase pathway as the most significantly affected process based on the combined upregulated and downregulated dataset. In addition, G2/M DNA damage checkpoint regulation also scored highly in the pathway analysis of the combined gene list. Evaluation of this pathway revealed that key regulators of DNA replication and cell cycle progression including CDC2 (CDK1), CCNB1, CNNB2, SFN (14-3-3 s), CDC25B, TPO2A and

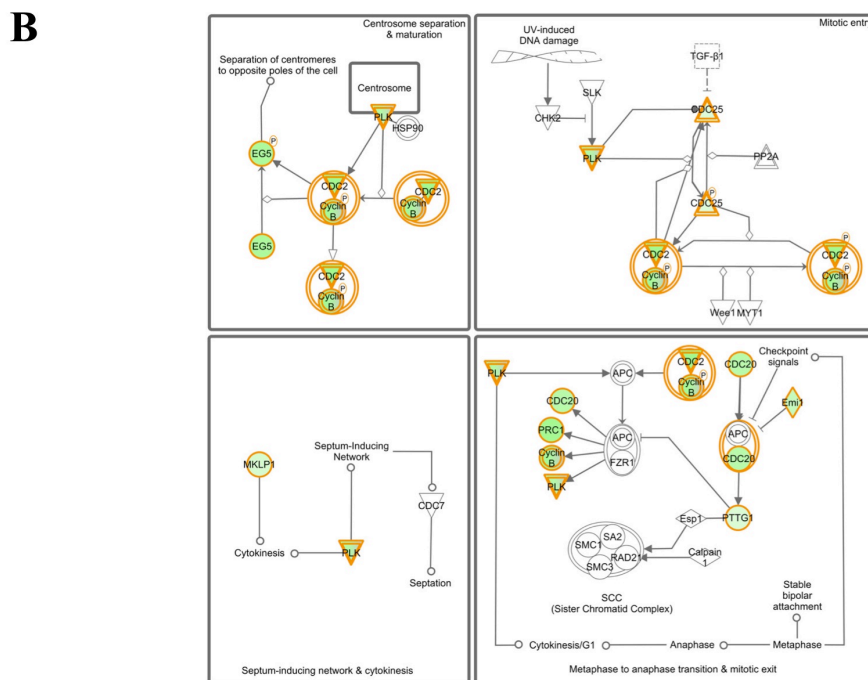
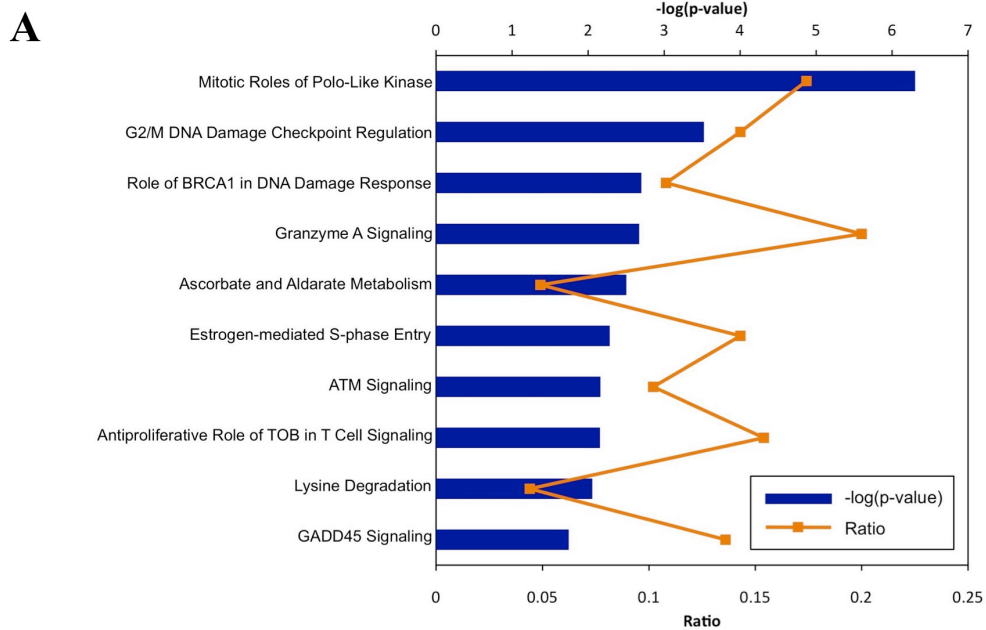


**Figure 3.8 IPA of genes downregulated in RS and OIS.** Genes that were significantly downregulated in both RS and OIS cells were evaluated using Ingenuity Pathway Analysis. (A) List of the top 10 significantly altered canonical pathways, ranked by significance. (B) Schematic diagram of the most significantly altered pathway: mitotic roles of polo-like kinase. Green shaded genes represent genes within the pathway that were downregulated in both RS and OIS cells.

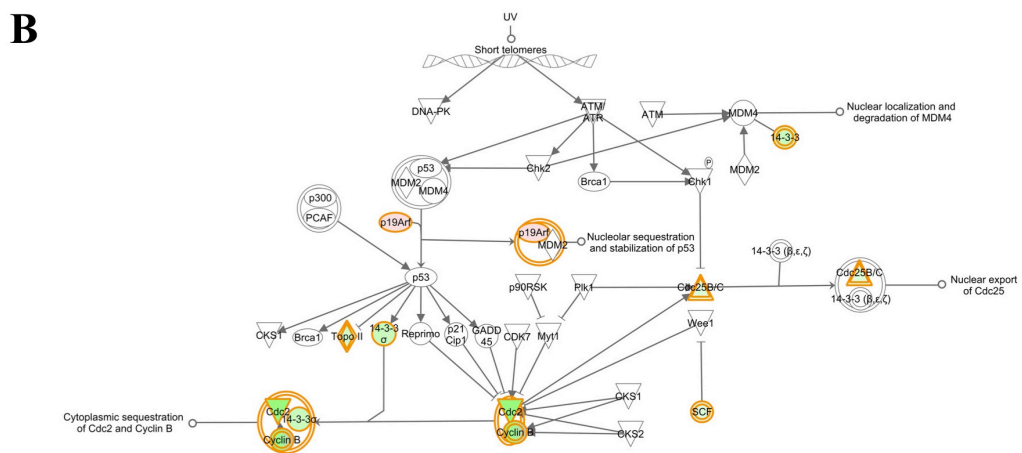
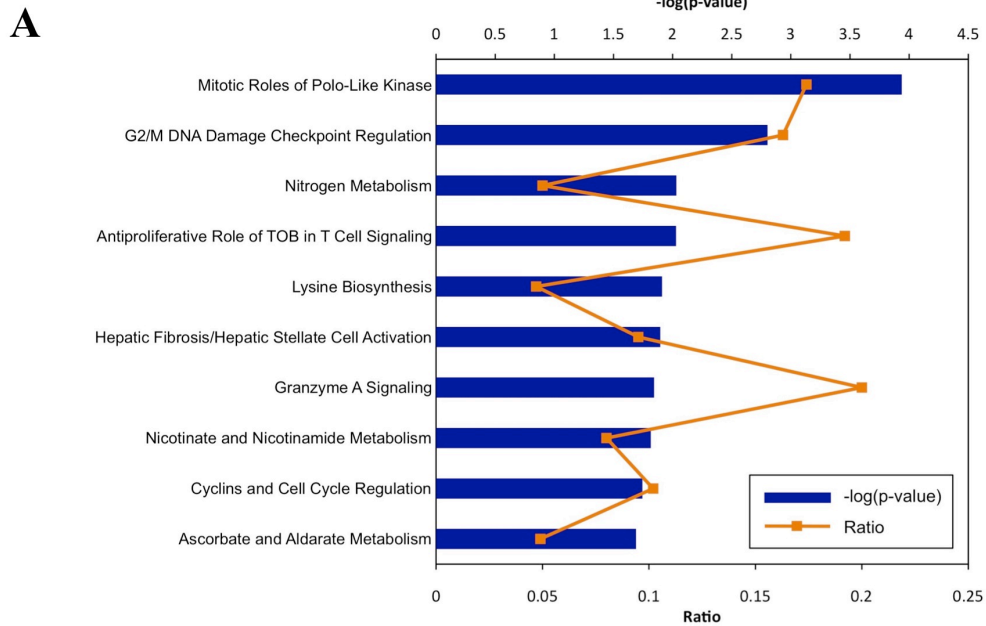


**Figure 3.9 IPA of genes that changed in common in RS and OIS.** Genes that changed significantly in both RS and OIS cells were evaluated using Ingenuity Pathway Analysis. (A) List of the top 10 significantly altered canonical pathways, ranked by significance. (B) Schematic diagram of the second most significantly altered pathway: G2/M DNA damage checkpoint regulation. Red shaded genes represent genes within the pathway that were upregulated in both RS and OIS cells; green shaded genes represent genes that were downregulated in both.

SKP2 were all significantly downregulated (Figure 3.9b). Another component of the pathway, the tumor suppressor p19ARF, was upregulated in both RS and OIS cells. This was not entirely surprising as p19ARF, an alternative gene product of the INK4/ARF locus known to increase in senescent cells, helps stabilize p53 by binding and sequestering MDM2. To this end, the gene expression analyses confirmed that both RS and OIS IMR90 cells exhibited a transcriptional profile consistent with cell cycle arrest and promotion of tumor suppression.

### 3.3 Discussion

Before initiating mechanistic studies of a complex biological phenomenon, it is first critical to identify and implement an appropriate model system. Because several well-documented triggers of cell senescence have been identified, I selected two in vitro systems that were the most relevant to cancer and ageing: replicative senescence and oncogene-induced senescence. Both of these models have been utilized extensively to study senescence in the laboratory and were therefore relatively simple to establish and optimize. I selected IMR90 cells as a relevant cell line in which to induce senescence as this HDF line is not only well-characterized, but has been widely used by others to investigate senescence in vitro.

Upon implementation, both model systems were critically assessed for parameters of cell senescence including proliferation arrest, the expression of key senescence regulatory proteins and SA  $\beta$ -galactosidase activity. Both the late passage IMR90 and H-RASG12V-infected IMR90 cells exhibited clear indicators of cell cycle exit and senescence onset (e.g., reduction of cyclin A and lamin B1 expression, induction of p16INK4a and p21WAF1), while the respective early passage and control-infected IMR90 cells did not. Likewise, the late passage and H-RASG12V-infected IMR90 cells stained uniformly positive for SA  $\beta$ -galactosidase activity. These data collectively confirmed that both models were suitable to generate senescent cells in a robust and reproducible manner.

Gene expression profiles were also generated for the RS and OIS models in order to further verify the senescent phenotype and to provide a transcriptional framework that could be used to assess the impact of chromatin changes. GSEA and IPA were employed to identify biological processes that were significantly affected during senescence. As expected, genes related to cell cycle progression and extracellular matrix composition were primarily downregulated, whereas genes

associated with cell cycle inhibition and the secretory phenotype were significantly upregulated. The consistency of these gene expression data with earlier findings from other laboratories further validated the two models as appropriate tools for studying cell senescence (Shelton et al., 1999; Zhang et al., 2003; Krizhanovsky et al., 2008).

Genes differentially expressed in both the RS and OIS models were also identified and used to define a composite transcriptional profile of cell senescence. Although expression changes specific to either model might have provided some insight, it was formally possible that any given change could reflect a nuance or artifact of the individual model systems. By identifying genes that were differentially expressed in both RS and OIS senescent cells, it increased the likelihood that the gene changes were specific to senescence. However, one caveat to the interpretation of the RS and OIS gene expression data was that the analyses failed to account for any transcriptional changes that might have occurred as a secondary consequence of the proliferation arrest. One way to address this caveat would be to compare the overlapping senescence datasets with a gene expression profile derived from quiescent IMR90 cells. Any genes that would change in union between the RS, OIS and quiescence datasets could be eliminated as being related to proliferation arrest and not specific to the senescence program. This would provide a more accurate and definitive transcriptional representation of the senescence program. Despite this caveat, the derived gene expression signature of senescence could still serve as a baseline to evaluate the functional consequences of specific chromatin changes during senescence.

In the process of defining a common RS and OIS transcriptional profile, it was evident that none of the IPA canonical pathways and processes was completely saturated. In fact, no single pathway exhibited altered expression for every gene within the pathway, raising the issue of how robust the pathway changes were. However, it is important to consider that the activity of a given pathway can be affected even in the absence of expression changes for all members of the pathway. For some genes, regulation is mediated through mechanisms other than transcription, including posttranslational modification or protein stabilization. For example, altered transcription of a rate-limiting gene within a pathway can have a profound effect on the overall activity of the pathway. In this context, an upstream member of a pathway might be regulated at the transcriptional level and still affect the activity of downstream pathway members without altering their absolute expression levels.

Importantly, IPA was employed in the current study simply as an exploratory tool in order to identify pathways and gene networks that were likely to be altered in a statistically significant manner during cell senescence. To this end, all of the pathways presented in Figures 3.5, 3.6 and 3.7 were ranked on the basis of statistical significance and had p-values lower than 0.5 (expressed as  $-\log[\text{p-value}]$ ). As described in Chapter 2 (Materials and Methods), the p-value was calculated for each pathway using the right-tailed Fisher Exact Test and incorporated several parameters: the number of genes within the IPA pathway, number of pathway eligible genes annotated in IPA and the total number of genes in the input dataset. Ultimately, a complete biochemical validation would be required to demonstrate that a specific pathway was truly altered, but is beyond the scope of the present study. Instead, the transcriptional profiling of RS and OIS was conducted primarily to provide a context for evaluating the impact of chromatin changes in cell senescence.

Having now established and validated two separate in vitro models of cell senescence, I was subsequently in a position to evaluate the chromatin structure of senescent cells. The formation of SAHF in senescent IMR90 cells represents an extreme remodeling of chromatin that is thought to facilitate aspects of the senescence program. To this end, I set out to examine how other epigenetic features of chromatin might similarly contribute to the establishment and maintenance of cell senescence.

## **Chapter 4. Characterization of H4K20me3 in Senescence**

### **4.1 Rationale**

The senescence program is characterized by an altered pattern of gene expression that simultaneously promotes both a permanent proliferation arrest and a secretory phenotype. In addition to these characteristic features, senescent cells concurrently undergo extensive chromatin remodeling. Although important research by several laboratories has already examined how changes in chromatin structure (e.g., SAHF formation) can promote senescence, little emphasis has been placed on elucidating the role of individual histone modifications in the regulation of the senescence program. Histone H4 lysine 20 trimethylation (H4K20me3) represents a key epigenetic marker of heterochromatin that is elevated in aged tissues and cells isolated from Hutchinson–Gilford Progeria Syndrome patients, but is lost in human cancers (Sarg et al., 2002; Shumaker et al., 2006; Fraga et al., 2005). Given the role of senescence in tumor suppression and its putative contribution to organismal aging, the H4K20me3 modification is of major interest in the senescence program. Consequently, I set out to characterize the H4K20me3 histone modification in proliferating and senescent cells.

### **4.2 Results**

#### **4.2.1 Evaluation of H4K20me3 Antibody Specificity**

Before attempting to investigate a particular protein or post-translation modification, it is important to obtain and validate the appropriate tools and reagents. This is particularly crucial when the experimental approach necessitates the use specific antibodies to detect a desired protein target. As such, possessing the ability to definitively confirm the specificity for a given signal in any antibody-based assay is fundamentally critical to the interpretation of the assay. Antibody specificity is a particularly important consideration in the assessment of histone modifications, as antibodies that exhibit some degree of cross-reactivity may not allow for discrimination between subtle differences in posttranslational modification. For example, the dimethylation or trimethylation of a particular histone residue may not result in discrete differences in mobility by SDS-PAGE, thus confounding the

interpretation of Western blotting results. As a result, it is essential to confirm that a given antibody detects the desired histone modification with high specificity and exhibits minimal cross-reactivity.

Based on information provided in the literature, publicly accessible databases (<http://compbio.med.harvard.edu/antibodies/>) and commercial availability, several H4K20me3 antibodies were selected and obtained for evaluation (Egelhofer et al., 2010). The utilization of spotted arrays comprised of diverse combinations of unmodified and modified histone peptides has proven to be an effective method of evaluating the specificity of antibodies raised against various histone modifications (Bock et al., 2011). To this end, the MODified Histone Peptide Array (Active Motif) was selected for use in assessing the binding specificities of the obtained H4K20me3 antibodies. The array is comprised of 384 separate peptides containing various combinations of acetylation, methylation, phosphorylation and citrullination modifications of the N-terminal tails of the four core histones. The H4K20me3 modification is represented by seven different peptides on the array, either alone or in combination with additional modifications.

In order to evaluate binding specificity, three H4K20me3 antibodies (Millipore, 04-079; Cell Signaling Technology, 5737; Abcam, ab9053) were subjected to a 2000-fold dilution and incubated with separate peptide arrays. The arrays were subsequently incubated with species-appropriate HRP-conjugated secondary antibodies and developed with standard enhanced chemiluminescence (ECL) reagents. The arrays were then exposed to film and the resulting autoradiographic images captured using a conventional flatbed scanner. Each of the three H4K20me3 antibodies detected only a few of the 384 total peptides on the array (Figure 4.1a). Both the Millipore and Cell Signaling Technology antibodies primarily detected the seven H4K20me3-containing peptides as indicated by the red circles, and exhibited only minimal signal for the other peptides. Although the Abcam antibody also detected the seven H4K20me3-containing peptides, it displayed moderate signal intensity for several other peptides as well. The arrows on the radiographic images denote examples of antibody cross-reactivity with peptides lacking the H4K20me3 modification.

To obtain a more quantitative metric of the binding specificities of the respective H4K20me3 antibodies, the scanned images of the arrays were analyzed using the Array Analyse software (Active Motif). Array Analyse generates a

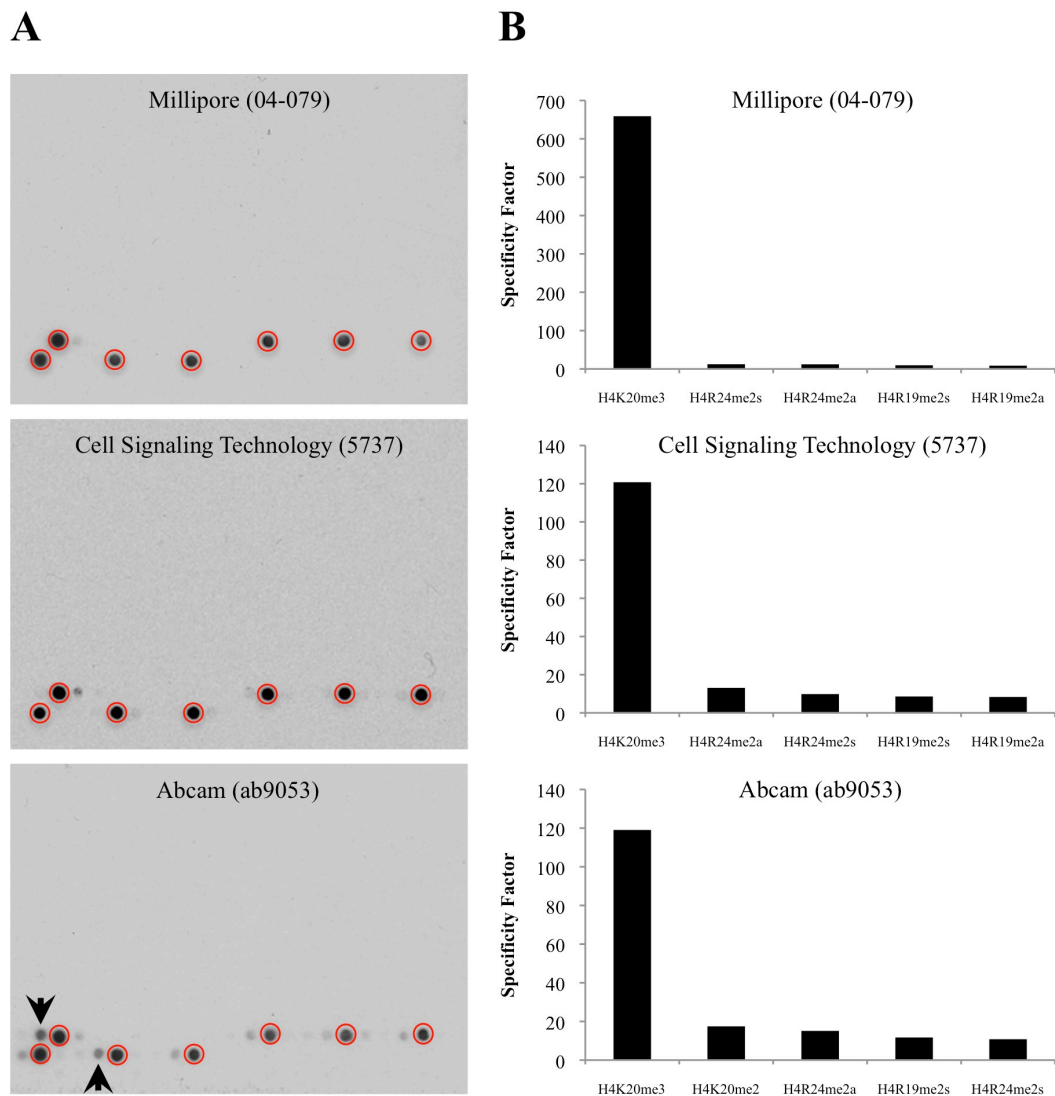


**Figure 4.1 Evaluation of H4K20me3 antibody specificity.** Three H4K20me3 antibodies (Millipore, 04-079; Cell Signaling Technology, 5737; Abcam, ab9053) were evaluated for specificity using the MODified Histone Peptide Array (Active Motif). (A) Autoradiographic images of the respective peptide arrays. Spots containing the H4K20me3 modification are indicated by red circles. Arrows denote antibody cross-reactivity with the H4K20me2 modification. (B) Specificity factors were calculated for each antibody using the Array Analyse software. For each antibody, the peptides were ranked from the greatest (i.e., highest specificity factor) to least degree of binding.

numerical value (i.e., specificity factor) that indicates how specific a given antibody is for each of the histone modifications on the array. The specificity factor is determined by dividing the average intensity of all spots that contain a given modification by the average intensity of all the other spots that lack the modification. Consistent with the autoradiographic images, both the Millipore and Cell Signaling Technology antibodies displayed high specificity factors for the H4K20me3 modification and low values for the other modifications (Figure 4.1b). Although the Abcam antibody had an acceptable specificity factor for the H4K20me3 modification, it also exhibited moderate cross-reactivity with the H4K20me2 modification. Genome wide, H4K20me2 is far more abundant than H4K20me3, which might interfere with the interpretation of any results obtained using the Abcam antibody. For this reason, the Millipore and Cell Signaling Technology antibodies were utilized exclusively for all subsequent immunological-based assays of H4K20me3.

#### **4.2.2 H4K20me3 is Selectively Retained in Senescent Cells**

Having tested and validated multiple H4K20me3 antibodies, it became important to characterize the H4K20me3 modification in proliferating and senescent cells. In order to determine the relative abundance of H4K20me3 in proliferating and senescent cells, whole cell extracts were prepared from low passage (PD28) proliferating and late passage (PD90) senescent IMR90 cells. In parallel, whole cell extracts were also obtained from control and H-RASG12V-infected IMR90 cells. To accurately determine the stoichiometry of a histone modification between samples, it is important to utilize volumes of extract that contain an equivalent amount of total histone. To determine this, the volumes of both sets of extracts were titrated, subjected to fractionation by SDS-PAGE and Western blotted to quantify total histone H4 levels (data not shown). Optimal loading volumes were determined in order to ensure that an equal amount of total histone H4 was loaded for each sample. Based on this determination, extract volumes containing equal amounts of total histone H4 from the PD28, PD90, control-infected and H-RASG12V-infected cells were fractionated by SDS-PAGE and immobilized to PVDF. The PVDF membranes were then subjected to Western blotting to determine abundances of total histone H4 and the H4K20me1, H4K20me2 and H4K20me3 modifications.

As anticipated, the PD28 proliferating and PD90 senescent samples contained normalized levels of total histone H4 (Figure 4.2a). Likewise, the control-infected proliferating and H-RASG12V-infected senescent cells contained normalized amounts of total histone H4. H4K20me1 levels were lower in the PD90 cells and to a lesser extent in the H-RASG12V senescent cells, relative to the respective proliferating cell extracts. In contrast, H4K20me2 abundance was higher in the PD90 senescent cells but remained unchanged in H-RASG12V senescent cells, when compared to levels in proliferating cells. Intriguingly, the level of H4K20me3 in the PD90 cells was markedly elevated relative to the PD28 cells. Similarly, the H-RASG12V-infected senescent cell extracts also contained a higher level of H4K20me3 than extracts from the control-infected proliferating cells. To demonstrate the specificity of the observed differences in H4K20me3 abundance, Western blots were performed with two independent H4K20me3 antibodies (Millipore and Cell Signaling) and these yielded comparable results.

However, it was formally possible that H4K20me3 levels were elevated in RS and OIS cells simply as a consequence of either the cell cycle position or non-proliferative state of the senescent cells. In either of these scenarios, the observed elevation of H4K20me3 levels might have been a secondary effect of cell cycle exit and not specific to senescence. To address this, whole cell extracts from proliferating, replicative senescent and quiescent IMR90 cells were titrated, fractionated by SDS-PAGE and Western blotted to assess histone H4 levels. As before, extract volumes that would permit loading of equal amounts of total histone H4 were determined for each sample (data not shown). Appropriate extract volumes for the samples were subsequently fractionated by SDS-PAGE and transferred to a PVDF membrane. The membrane was then subjected to Western blotting to detect histone H4 and H4K20me3 (Figure 4.2b). As expected, H4K20me3 levels were again markedly higher in the senescent cells when compared to the proliferating cells. In contrast, the quiescent cells exhibited only modestly higher levels of H4K20me3 than the proliferating cells, suggesting that the robust increase of the modification in senescent cells is not merely a consequence of proliferation arrest or cell cycle position.

Although the Western blot data demonstrated that H4K20me3 levels were seemingly higher in senescent cells, the analyses relied on normalization to total histone H4. As a result, it was only possible to conclude that the ratio of H4K20me3-

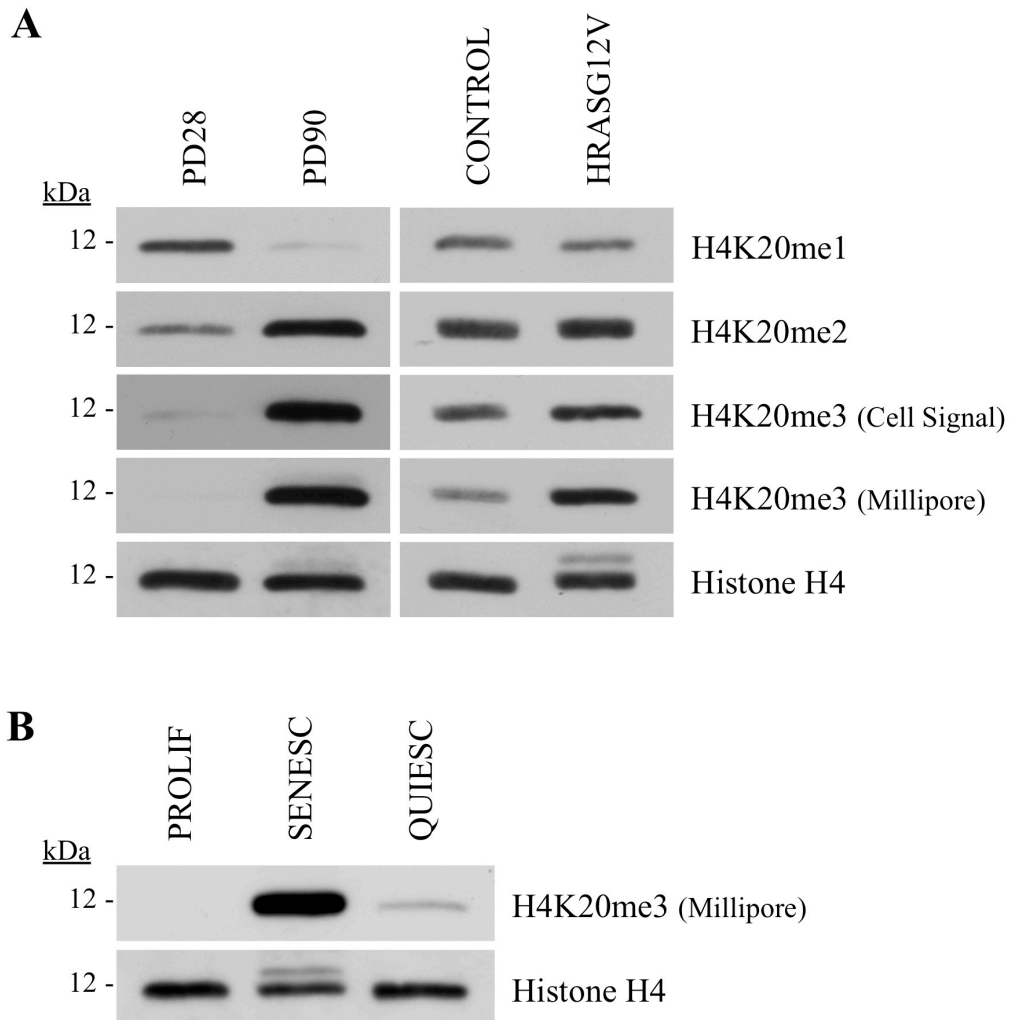


**Figure 4.2 Determination of H4K20me3 levels in RS and OIS.** (A) Whole cell extracts from proliferating (PD28), replicative senescent (PD90), control-infected and H-RASG12V-infected senescent IMR90 cells were fractionated and Western blotted for total histone H4, H4K20me1, H4K20me2 and H4K20me3. Extract volumes were titrated so that an equal amount of total histone H4 was run in each lane. (B) Whole cell extracts from proliferating, senescent and quiescent IMR90 cells were fractionated and Western blotted for total histone H4 and H4K20me3. Extract volumes were titrated so that normalized amounts of total histone H4 were run in each lane.

containing histone H4 to total histone H4 was higher in senescent cells than in proliferating cells. It has been reported that total histone levels undergo a marked reduction in senescent cells, so the higher levels of H4K20me3 could have simply reflected an overloading of the senescent samples in order to attain equal total histone H4 levels. As such, the Western blot data failed to provide any information about the actual abundance of H4K20me3 on a per cell basis, in the respective proliferating and senescent populations. In order to address this caveat, low passage (PD33) proliferating IMR90 cells and late passage (PD87) senescent IMR90 cells were dislodged by treatment with trypsin, subjected to manual cell counting with a hemocytometer and used to generate whole cell extracts. Additional plates of PD87 senescent cells were harvested in a similar manner 1, 2, 3 or 4 weeks after the onset and confirmation of senescence. For each timepoint, the amount of lysis buffer was varied so that the proliferating and senescent extracts contained equal numbers of cells per volume of buffer.

Whole cell extracts from the RS timecourse containing equivalent numbers of cells were fractionated by SDS-PAGE, immobilized to PVDF membranes and subjected to Western blot analysis of proliferation/senescence markers and histones (Figure 4.3). As expected, levels of lamin A/C remained largely unchanged for the duration of the timecourse. Consistent with a senescent phenotype, lamin B1 and cyclin A expression underwent a robust decline beginning with the PD87 cells and continued over the course of the experiment. Further confirming senescence, marked induction of p16INK4a was observed in the PD87 cells and was maintained at comparable levels for up to 4 weeks after the onset of senescence. Beginning with the PD87 senescent cells, a progressive loss of total histone H4 content occurred over the remainder of the timecourse. Despite the significant decrease in total histone H4 expression, H4K20me3 levels remained unchanged between the PD33 proliferating cells and PD87 senescent cells. Remarkably, H4K20me3 levels also remained unaltered for up to 4 weeks from the onset of senescence. These data indicated that on a per cell basis, the total amount of H4K20me3 was unaffected as cells underwent RS. The data also suggested that the previously observed elevation of H4K20me3 levels during RS was primarily a consequence of normalizing the Western blot samples for total histone content. In other words, the total amount of H4K20me3 per cell does not change, but the proportion of H4 carrying this modification is

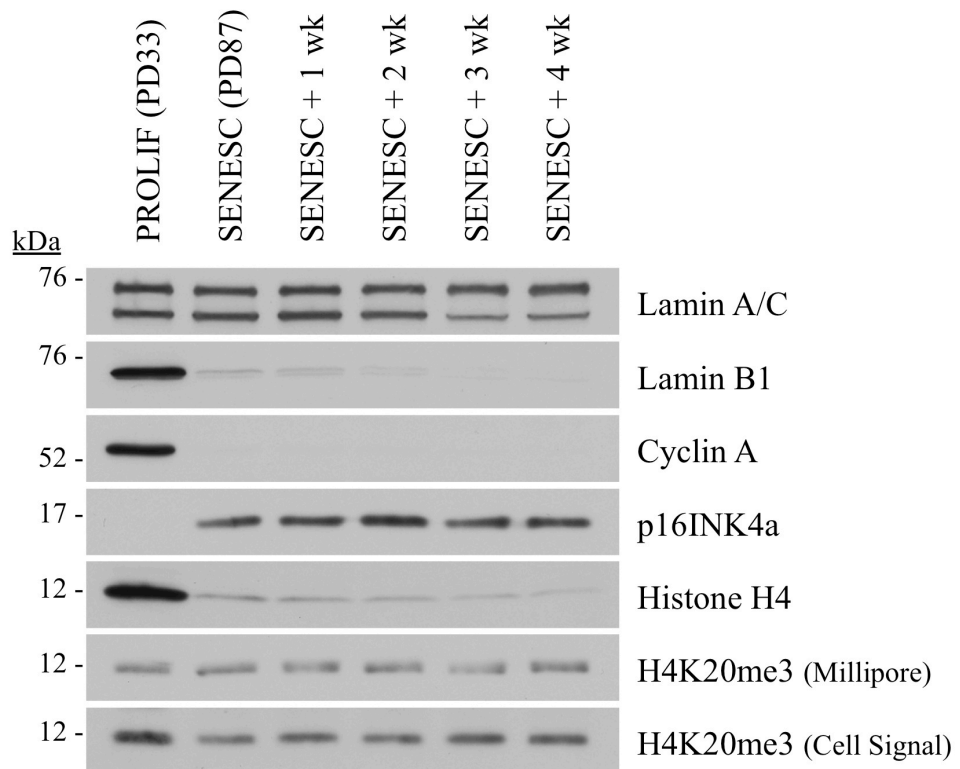


**Figure 4.3 H4K20me3 levels remain stable during RS.** Whole cell extracts were prepared from low passage (PD33) proliferating and late passage (PD87) replicative senescent IMR90 cells, as well as from cells that were maintained for an additional 1-4 weeks after the onset of senescence. For each sample, volumes of extract containing equal numbers of cells were fractionated by SDS-PAGE and Western blotted for proliferation/senescence markers, histone H4 and H4K20me3.

increased. This in turn implies that H4K20me3 is selectively retained in senescent cells, relative to other forms of histone H4.

#### **4.2.3 Assessment of H4K20me3 Localization in Senescent Cells**

In addition to measuring H4K20me3 abundance in proliferating and senescent cells, it was important to ask whether the nuclear localization of H4K20me3 in senescent cells differed from that of proliferating cells. To accomplish this, proliferating and senescent cells were subjected to indirect immunofluorescence staining with H4K20me3 antibodies. Low passage proliferating (PD22) and high passage senescent (PD85) IMR90 cells were fixed, permeabilized and stained with an H4K20me3 antibody and DAPI. The stained cells were subsequently visualized by fluorescence microscopy. The PD22 cells exhibited even predominantly nuclear DAPI staining and a diffuse, granular nuclear H4K20me3 staining pattern (Figure 4.4a). By comparison, the PD85 senescent cells displayed a DAPI staining pattern characteristic of SAHF and H4K20me3 staining that revealed distinct, variably sized nuclear foci. Control-infected proliferating and H-RASG12V-infected senescent IMR90 cells were also fixed, permeabilized and subjected to H4K20me3 and DAPI staining (Figure 4.4b). Comparable to low passage IMR90 cells, control-infected cells displayed an even predominantly nuclear DAPI staining pattern and diffuse, granular H4K20me3 staining in the nucleus. In the H-RASG12V cells, DAPI staining revealed prominent SAHF formation and an H4K20me3 pattern that exhibited defined nuclear foci of variable size.

Whereas proliferating cells mostly displayed a uniformly diffuse H4K20me3 nuclear staining pattern, senescent cells contained intensely staining H4K20me3 nuclear foci. Several distinct types of nuclear foci have been previously described in senescent cells. The promyelocytic leukemia (PML) protein forms punctate nuclear bodies that increase in number and size during RS and OIS and contribute to the senescence program (Ferbeyre et al., 2000; Pearson et al., 2000; Bischof et al., 2002). Because PML forms prominent foci that mediate aspects of cell senescence, it was relevant to ask whether H4K20me3 foci co-localized with PML nuclear bodies in senescent cells. To examine this, control-infected proliferating and H-RASG12V-infected senescent IMR90 cells were fixed, permeabilized and co-stained with DAPI and antibodies against H4K20me3 and PML. The stained cells were detected by indirect immunofluorescence and visualized by fluorescence microscopy. While the

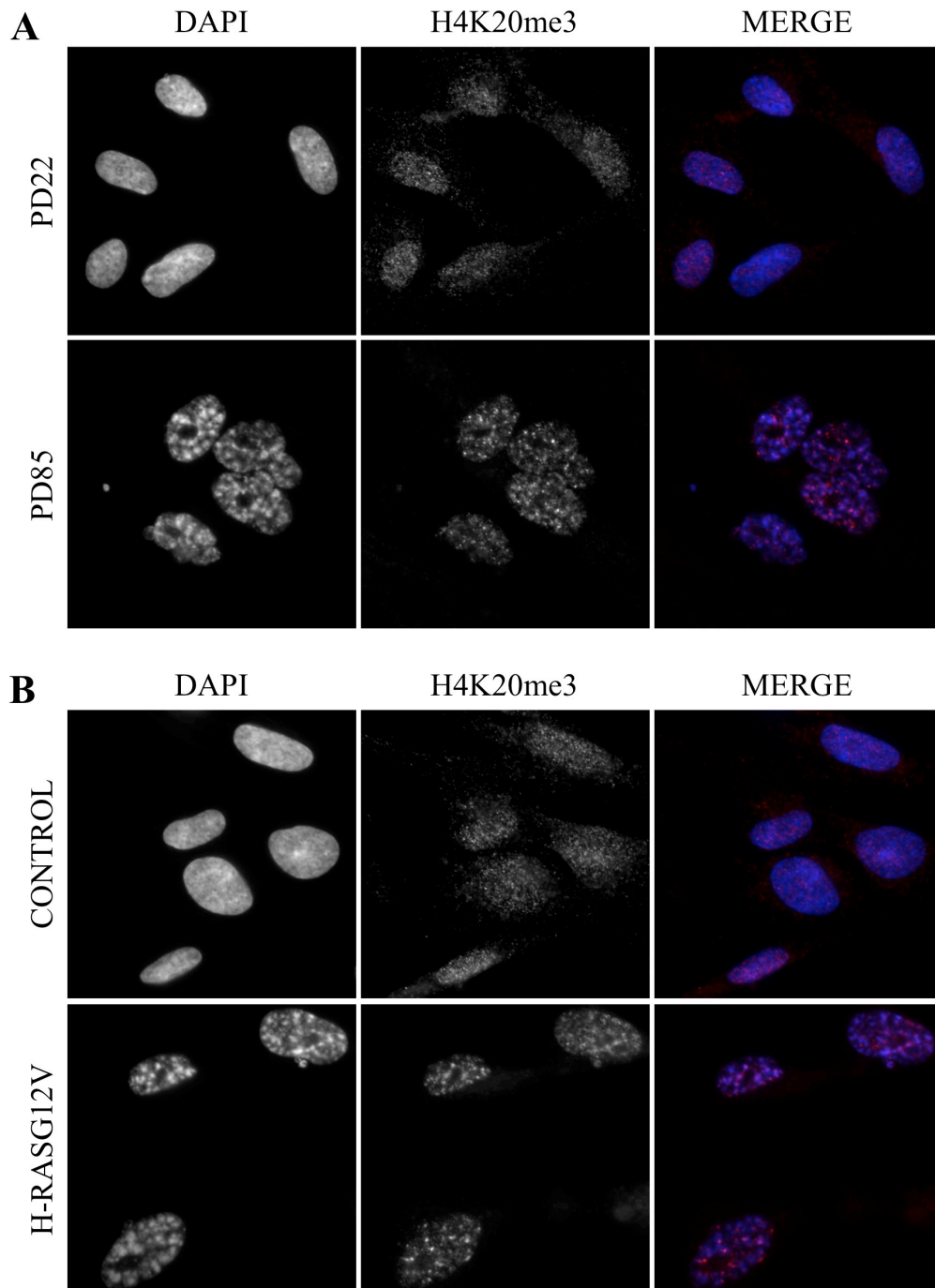


**Figure 4.4 Senescent cells exhibit punctate nuclear H4K20me3 staining.** (A) Proliferating (PD22) and replicative senescent (PD85) IMR90 cells were stained with H4K20me3 antibody and DAPI and visualized by fluorescence microscopy. (B) Control and H-RASG12V-infected IMR90 cells were stained with H4K20me3 antibodies and DAPI and visualized by fluorescence microscopy. Images were captured with identical exposure settings under the 100X objective.

DAPI and H4K20me3 nuclear staining patterns remained diffuse and even in the control cells, the H-RASG12V cells again exhibited SAHF formation and the presence of H4K20me3 foci (Figure 4.5a). As expected, both the number and size of the PML nuclear bodies increased in the H-RASG12V cells compared to control cells. Despite the prominence of both the H4K20me3 and PML foci in the H-RASG12V cells, no spatial co-localization was observed. In fact, the respective foci appeared to occupy mutually exclusive nuclear locations in the senescent H-RASG12V cells, indicating that H4K20me3 was not present at sites of PML nuclear bodies.

Given the important contribution of DNA damage signalling as an effector mechanism of the senescence program, several nuclear structures indicative of DNA damage have also been identified in senescent cells. To this end, the DNA damage signalling mediator 53BP1 and phosphorylated histone H2AX ( $\gamma$ -H2AX), which marks DNA double-strand breaks, both form discrete nuclear foci in senescent cells (d'Adda di Fagagna et al., 2003). To examine whether H4K20me3 foci were present at these nuclear sites of DNA damage in senescent cells, cells were subjected to co-staining by immunofluorescence. Control-infected proliferating and H-RASG12V-infected senescent cells were fixed, permeabilized and co-stained with DAPI, an H4K20me3 antibody and antibodies against either 53BP1 or  $\gamma$ -H2AX. Control cells exhibited even DAPI staining and diffuse nuclear staining patterns for both H4K20me3 and 53BP1 (Figure 4.5b). In contrast, H-RASG12V-infected cells displayed SAHF, H4K20me3 staining of greater intensity with some foci and large discrete 53BP1 foci. Although some foci were adjacent, no overt co-localization was observed between the H4K20me3 and 53BP1 foci.

Control and H-RASG12V cells were also assayed by immunofluorescence to compare H4K20me3 and  $\gamma$ -H2AX staining patterns. As anticipated, control cells contained even DAPI staining, a diffuse H4K20me3 pattern and the presence of very few, small nuclear  $\gamma$ -H2AX foci (Figure 4.5c). H-RASG12V cells again contained distinct SAHF and prominent H4K20me3 foci, as well as an increased number of larger  $\gamma$ -H2AX puncta. No co-localization between H4K20me3 and  $\gamma$ -H2AX occurred, as the  $\gamma$ -H2AX foci were mostly present at H4K20me3-poor regions of the nucleus. Taken together, the 53BP1 and  $\gamma$ -H2AX immunofluorescence data indicated that H4K20me3 foci did not mark regions of DNA damage in senescent cells. As

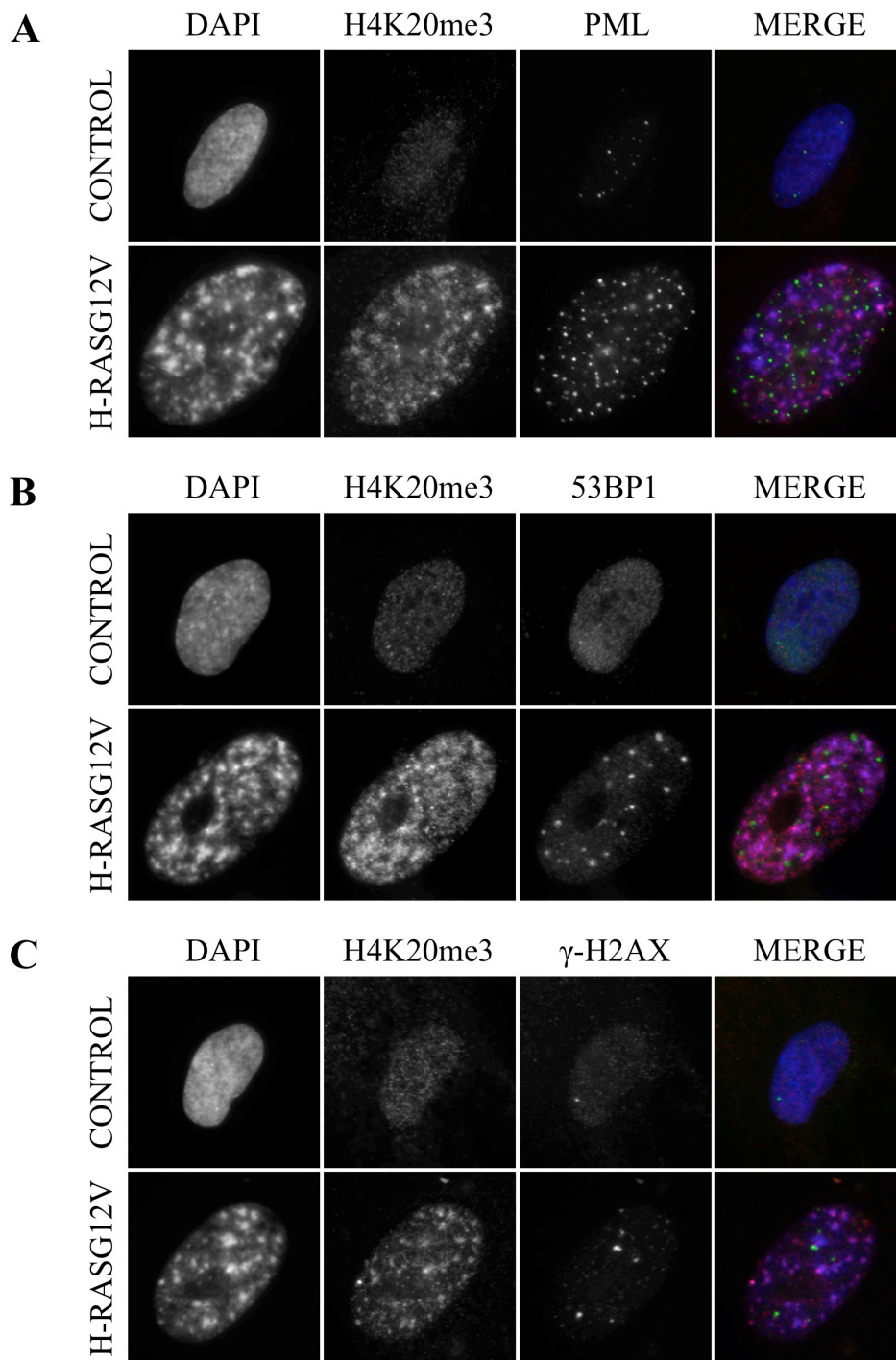


**Figure 4.5 H4K20me3 does not co-localize with PML, 53BP1 or  $\gamma$ -H2AX.** Control and H-RASG12V-infected IMR90 cells were subjected to immunofluorescence co-staining of H4K20me3 and (A) PML, (B) 53BP1 or (C)  $\gamma$ -H2AX. Nuclei were visualized with DAPI. All images were obtained under equal exposure settings with the 100X objective.

such, the data suggested that H4K20me3 is likely not involved in mediating the DNA damage signalling aspect of the senescence program.

Despite the lack of co-localization between H4K20me3 and PML, 53BP1 or  $\gamma$ -H2AX, H4K20me3 appeared as distinct nuclear foci in senescent cells, suggesting a possible structural role for the modification during senescence. Senescent cells often appeared to harbour two distinct types of H4K20me3 nuclear structures: large globular foci and smaller, intensely staining puncta. In terms of size, shape and abundance, the larger globular H4K20me3 foci resembled SAHF. Therefore, it became important to address whether the H4K20me3 foci co-localized with SAHF in senescent cells. To examine this possibility, proliferating and replicative senescent IMR90 cells were fixed, permeabilized and stained with DAPI and an antibody against H4K20me3. The stained cells were visualized by epifluorescence microscopy and images were captured using identical exposure settings. As before, the proliferating cells displayed uniform DAPI and H4K20me3 nuclear staining patterns (Figure 4.6a). In contrast, the senescent cells exhibited SAHF formation and the presence of defined H4K20me3 foci.

Merged images of the DAPI and H4K20me3 immunofluorescence signals revealed that H4K20me3 frequently co-localized with SAHF in the senescent cells (Figure 4.6a). In order to provide an unbiased assessment of the co-localization, line scans were performed on the merged DAPI/H4K20me3 images and fluorescence intensity values (gray level) were determined for the respective channels (Figure 4.6b). In proliferating cells, both the DAPI and H4K20me3 signals remained relatively uniform across the section of the nucleus measured by the line scan. In the senescent cells, more uneven line scan profiles of the DAPI and H4K20me3 staining were revealed. Regions of the nucleus that exhibited higher DAPI signal also displayed higher H4K20me3 signal in a strongly correlative manner. Because the images were captured by standard epifluorescence microscopy and not by confocal sectioning, it was formally possible that the SAHF and H4K20me3 foci existed in different focal planes. However, despite this caveat, it was reasonable to conclude that the larger H4K20me3 foci were located in close spatial proximity to SAHF in senescent cells. As such, the data suggested that H4K20me3 might be a structural component of SAHF.

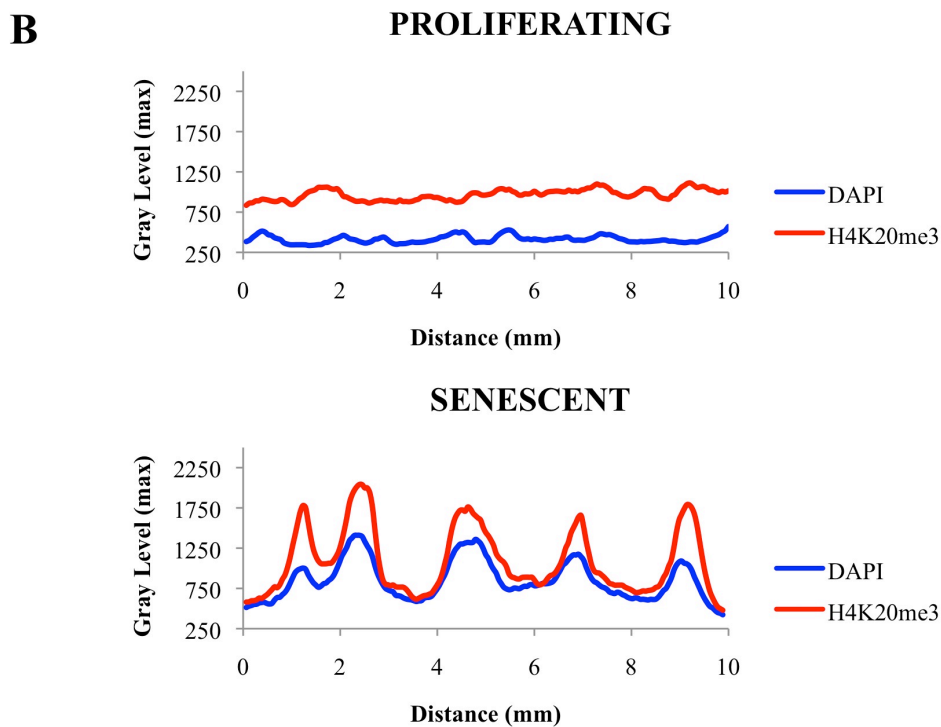
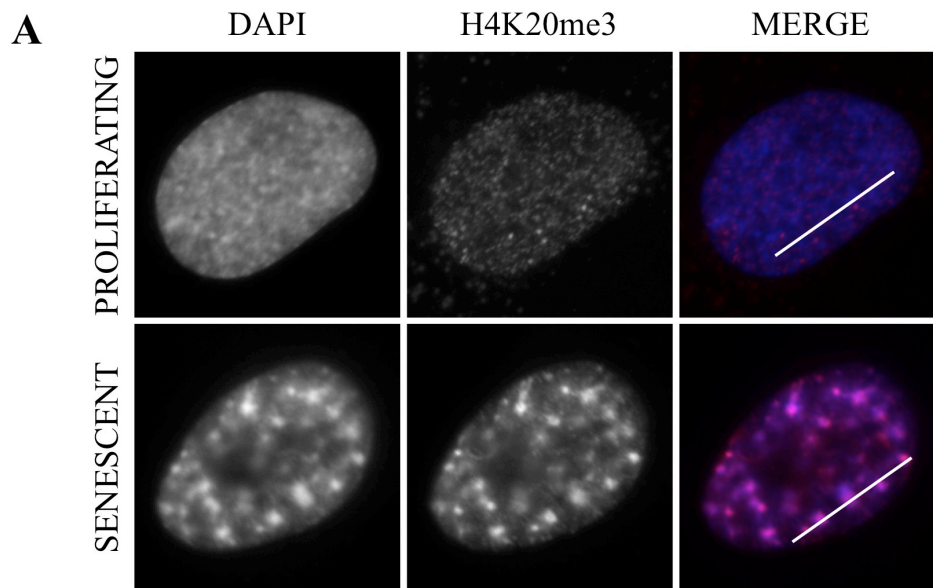


**Figure 4.6 H4K20me3 co-localizes with SAHF in senescent cells.** (A) Proliferating and replicative senescent IMR90 cells were stained with DAPI and an H4K20me3 antibody. (B) Line scans were performed on the merged DAPI/H4K20me3 images. Fluorescence intensity values (gray level) were determined for the respective channels and plotted graphically.

#### 4.2.4 SUV420H2 Expression is Modestly Altered in Senescent Cells

Having established that levels of H4K20me3 remained stable in senescent cells and that the modification co-localized with SAHF, it became important to ask how H4K20me3 was maintained given the dramatic reduction of histone content during senescence. To this end, there were two plausible scenarios that could explain how H4K20me3 levels remained unaltered in senescent cells despite a net decrease in histone expression: (1) H4K20me3-containing nucleosomes were protected from being lost during senescence or (2) H4K20me3-containing nucleosomes were lost during senescence, but the modification was deposited to remaining nucleosomes such that the steady state level of H4K20me3 appeared unchanged. As such, the latter argument would presumably require the activity of an H4K20me3-depositing enzyme.

The majority of H4K20me3 is catalyzed *in vivo* by the activity of the histone methyltransferase SUV420H2 (Schotta et al., 2004; Schotta et al., 2008). In order to determine whether SUV420H2 expression was maintained as cells underwent senescence, the RS and OIS microarray datasets were queried. The Affymetrix Human Genome U133 Plus 2.0 Array contained multiple probesets for the SUV420H2 gene. Therefore, data for each probeset was compiled and assessed to determine whether SUV420H2 expression was altered in senescent cells. No statistical difference was observed for either of the SUV420H2 probesets from the RS microarray (Table 4.1). Likewise, no change in expression was observed for either of the SUV420H2 probesets from the OIS microarray. Based on the microarray data, it was reasonable to conclude that SUV420H2 mRNA expression was not significantly altered in senescent cells.

Although the microarray expression data for SUV420H2 were not confirmed by quantitative PCR, it was reasonable to measure expression of the enzyme at the protein level in RS and OIS cells. Before proceeding with analysis of SUV420H2 expression, it was first necessary to identify and obtain a suitable SUV420H2 antibody. To this end, it was important to verify that the antibody was specific and could be used for Western blot detection of SUV420H2. One approach commonly employed to confirm antibody specificity is to demonstrate that several independent antibodies are capable of detecting the same protein band by Western blot. However, due to the limited commercial availability of SUV420H2 antibodies, only a single antibody was obtained and tested for specificity.

Dataset	Affymetrix Probe ID	Gene Symbol	Fold Change	BY-FDR p-value
RS microarray	1570058_at	SUV420H2	-1.10	1.000
	224431_s_at	SUV420H2	1.05	1.000
OIS microarray	1570058_at	SUV420H2	1.02	1.000
	224431_s_at	SUV420H2	-1.02	1.000

**Table 4.1 Evaluating SUV420H2 gene expression in RS and OIS.** Expression values for both SUV420H2 probe sets from the Affymetrix Human Genome U133 Plus 2.0 Arrays were examined to determine whether SUV420H2 was altered at the transcriptional level. Values from both the RS and OIS microarray datasets were included.

In order to determine whether the SUV420H2 antibody could recognize the specified epitope, a control plasmid (pBABE-puro) or plasmids encoding MYC-tagged full-length SUV420H1 (pBABE-puro-MYC-SUV420H1) or SUV420H2 (pBABE-puro-MYC-SUV420H2) were transfected into Phoenix-Ampho cells. Forty-eight hours after transfection, whole cell extracts were prepared, subjected to fractionation by SDS-PAGE and immobilized to a PVDF membrane. The PVDF was cut vertically into two equal halves, containing the control, MYC-SUV420H1 and MYC-SUV420H2 cell lysates. The two membranes were Western blotted with either an antibody raised against the MYC tag or the SUV420H2 antibody. As anticipated, the MYC antibody detected a single band that migrated just above the 52 kDa molecular weight marker in the MYC-SUV420H2 lane, but not in the control or MYC-SUV420H1 lanes (Figure 4.7a). Importantly, the band corresponded with the predicted molecular weight (~ 53 kDa) of MYC-SUV420H2. The other half of the membrane was probed with the SUV420H2 antibody, which detected a band in the MYC-SUV420H2 lane that migrated at the same position as the band from the MYC Western blot. Although the signal from the SUV420H2 Western blot was considerably less intense than that of the MYC tag blot, the data indicated that the SUV420H2 antibody was capable of detecting ectopically expressed SUV420H2.

It was also important to demonstrate that the SUV420H2 antibody could detect endogenous levels of SUV420H2. In the absence of several distinct SUV420H2 antibodies, an RNA interference approach was utilized to evaluate specificity. To this end, whole cell extracts were prepared from low passage IMR90 cells infected with variable amounts of shControl or shSUV420H2 lentiviruses. The whole cell extracts were fractionated by SDS-PAGE, transferred to a PVDF membrane and Western blotted with the SUV420H2 antibody. A prominent band that migrated just above the 52 kDa molecular weight marker was detected (Figure 4.7b). While the band remained unchanged across the shControl lanes, the shSUV420H2-infected cells exhibited markedly lower levels of expression. In fact, the cells that received the maximal amount of the shSUV420H2 lentivirus displayed the lowest expression of the putative SUV420H2 band. Because the band of interest migrated at the predicted molecular weight for SUV420H2 and underwent a reduction in expression following shSUV420H2 gene silencing, it was reasonable to conclude that the band represented endogenous SUV420H2. Based on this

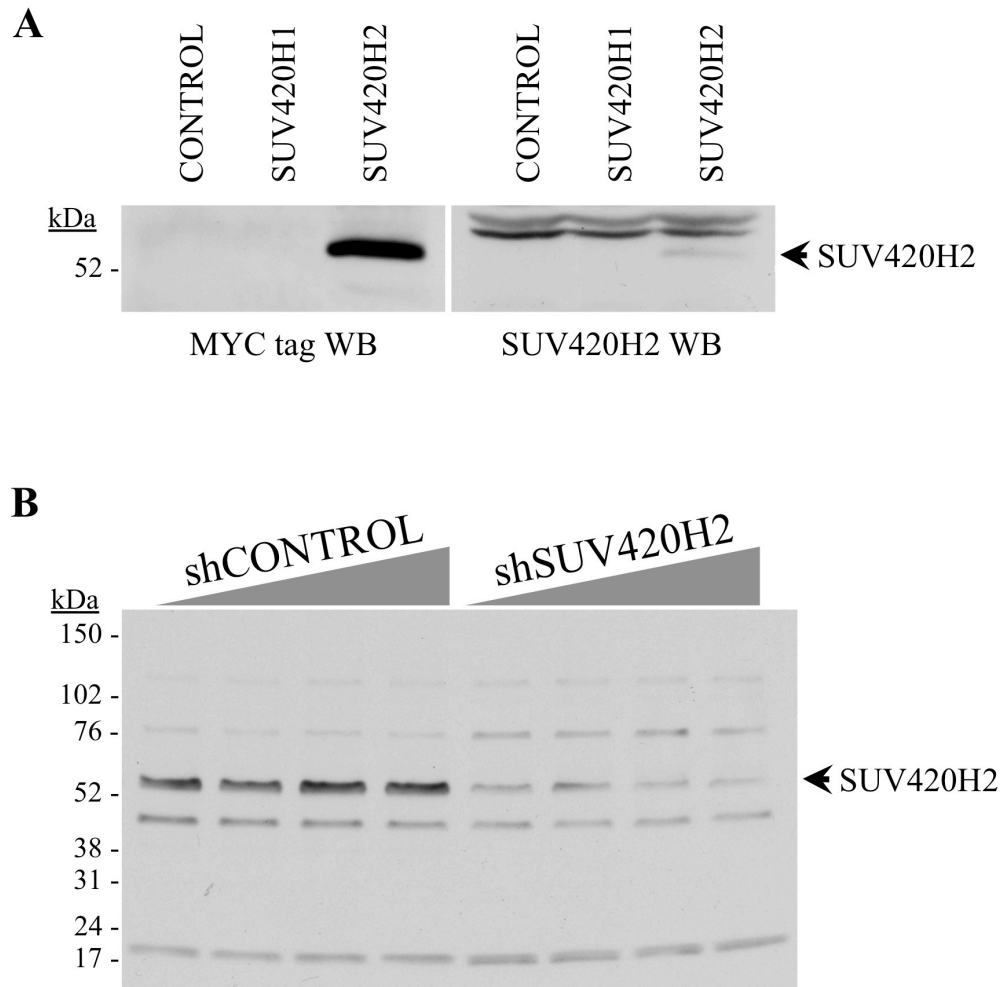


**Figure 4.7 Validation of the SUV420H2 antibody.** (A) Whole cell extracts were prepared from Phoenix-Ampho cells transfected with pBABE-puro, pBABE-puro-MYC-SUV420H1 or pBABE-puro-MYC-SUV420H2, fractionated and Western blotted with antibodies against the MYC tag or SUV420H2. (B) Whole cell extracts were prepared from cells infected with shControl or shSUV420H2 lentiviruses, fractionated and Western blotted with the SUV420H2 antibody.

evaluation, the SUV420H2 antibody could be used to accurately assess SUV420H2 expression in proliferating and senescent cells.

To evaluate SUV420H2 protein expression, whole cell extracts prepared from low passage (PD22) proliferating and high passage (PD85) senescent IMR90 cells were fractionated by SDS-PAGE and transferred to PVDF membrane for subsequent Western blot analysis. In parallel, whole cell extracts from control-infected proliferating and H-RASG12V-infected senescent IMR90 cells were also fractionated and immobilized to PVDF. The PVDF membrane was Western blotted with antibodies against SUV420H2 and GAPDH and quantified using the Image J software (Figure 4.8). A modest increase in SUV420H2 expression was observed in the PD85 replicative senescent cells relative to the PD22 proliferating cells, following normalization for GAPDH expression (Figure 4.8a & b). In contrast, SUV420H2 expression levels underwent a modest decrease in the H-RASG12V-infected senescent cells relative to control-infected cells, following normalization for GAPDH expression (Figure 4.8c & d). Although SUV420H2 levels appear to undergo subtle changes in expression in RS and OIS, respectively, the findings do not provide any conclusive evidence to suggest that altered SUV420H2 expression is solely responsible for the maintenance of H4K20me3 levels in senescent IMR90 cells. In OIS cells this is particularly unlikely to be the case, as H4K20me3 levels are maintained even in a context of reduced SUV420H2 expression. Consequently, whether H4K20me3 levels are maintained in senescent cells through a SUV420H2-dependent mechanism remains to be tested using loss-of-function approaches.

### **4.3 Discussion**

In addition to the proliferation arrest and secretory phenotypes, senescent cells may also be characterized by a dynamic and extensively remodelled chromatin landscape. One of the more striking observations related to the chromatin state of senescent cells is that the cells undergo a loss of histone content. Importantly, despite the reduction of global histone levels, some histones are retained within the chromatin of senescent cells. Such is the case for histones that contain the H4K20me3 posttranslational modification, as levels of this mark remain identical in proliferating and senescent cells, when normalized per cell or to lamin A/C. The apparent stabilization of H4K20me3 is particularly intriguing as it occurs in both the contexts of RS and OIS, suggesting it might be a universal feature of the chromatin

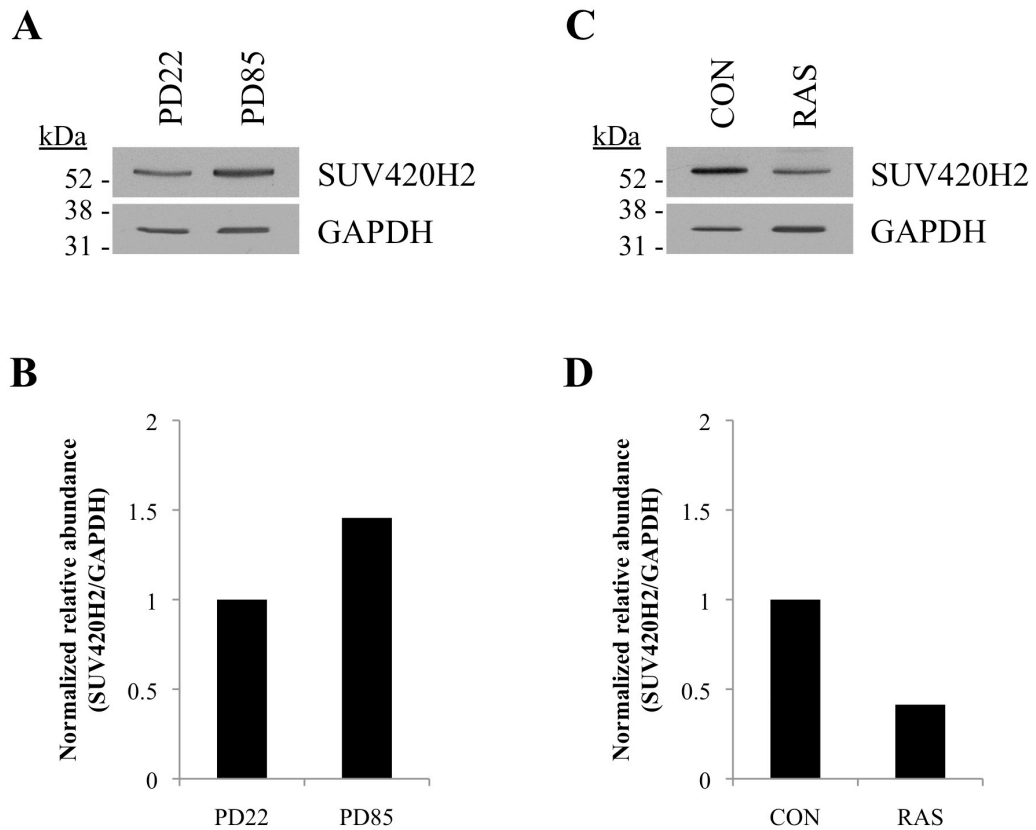


**Figure 4.8 SUV420H2 expression is modestly altered in RS and OIS.** Whole cell lysates containing equal numbers of proliferating (PD22), replicative senescent (PD85), control-infected and H-RASG12V-infected IMR90 cells were subjected to SDS-PAGE and Western blotted for SUV420H2 and GAPDH. (A) SUV420H2 and GAPDH Western blot analysis of proliferating and replicative senescent cells. (B) SUV420H2 and GAPDH were quantified using Image J and expressed as normalized relative abundance (SUV420H2/GAPDH). (C) SUV420H2 and GAPDH Western blot analysis of control and H-RASG12V-infected cells. (D) SUV420H2 and GAPDH were quantified using Image J and expressed as normalized relative abundance (SUV420H2/GAPDH).

of senescent cells. The observation that H4K20me3 level per cell is sustained for weeks following the onset of senescence is also of significance, possibly indicating that the modification plays a role in the long-term implementation of the senescence program.

Although the global level of H4K20me3 remains unaltered per senescent cell, the nuclear localization of the modification changes considerably as cells undergo senescence. In normal proliferating IMR90 cells, H4K20me3 exhibits a diffuse and even nuclear distribution as revealed by immunofluorescence staining. In striking contrast, replicative and oncogene-induced senescent cells display a pattern of H4K20me3 staining characterized by the formation of discrete nuclear foci. Several additional key nuclear proteins, including PML, 53BP1 and  $\gamma$ -H2AX, also form prominent foci during senescence, but surprisingly do not co-localize with H4K20me3. However, H4K20me3 does co-localize with SAHF in senescent IMR90 cells, implying that the mark might help to facilitate the extensive chromatin remodelling that occurs as cells senesce. Given the proposed contribution of SAHF to the transcriptional silencing of proliferation genes, H4K20me3 might indirectly mediate the gene regulatory aspects of the senescence program (Narita et al., 2003; Zhang et al., 2007).

While the current findings provide convincing evidence that total H4K20me3 levels remain unaltered in individual senescent cells, the data fail to provide clear insight into how abundance of the mark is maintained. One possibility is that nucleosomes containing the H4K20me3 modification are preferentially protected from removal during senescence. Alternatively, H4K20me3-containing nucleosomes might actually comprise a fraction of the histones that are lost during senescence, but the mark is maintained at steady state levels through the concomitant activity of an H4K20-specific histone methyltransferase acting upon the remaining nucleosomes. By either model, Western blotting analysis of H4K20me3 in proliferating and senescent cells and normalized for cell number would presumably reveal equivalent levels of the modification.

The histone methyltransferase SUV420H2 has been reported to deposit the majority of H4K20me3 across the genome (Schotta et al., 2008). Similar to global H4K20me3 levels, SUV420H2 expression is only modestly altered in RS and OIS cells. This could imply that basal expression of SUV420H2 is sufficient to maintain H4K20me3 at appropriate levels following removal of H4K20me3-modified histones

during senescence. This also assumes that SUV420H2 is the primary histone methyltransferase for H4K20me3 in IMR90 cells, which remains to be formally tested through loss-of-function experiments. In contrast, the data could imply that H4K20me3 is simply not lost from senescent cells, thus no significant change in SUV420H2 expression is required.

Another possibility that is not formally addressed in the present study is that H4K20me3 is maintained in senescent cells through a SUV420H2-independent mechanism. For example, H4K20me3 might be deposited by a different histone methyltransferase. To this end, several additional histone methyltransferases including NSD1, SMYD3 and SMYD5 have been reported to confer histone H4 lysine 20 trimethylation either *in vitro* or *in vivo* (Rayasam et al., 2003; Foreman et al., 2011; Stender et al., 2012). Alternatively, H4K20me3 levels might be maintained in senescent cells through the inhibition of a specific histone lysine demethylase. The enzyme PHF2 was recently reported to demethylate H4K20me3 at the promoters of pro-inflammatory genes in macrophages (Stender et al., 2012). Although PHF2 expression levels do not change by microarray in either RS or OIS (data not shown), it is possible that PHF2 undergoes enzymatic inhibition in senescent IMR90 cells. Although not tested in the present study, inhibition of PHF2 remains a potential mechanistic explanation for the stabilization of H4K20me3 during senescence.

Regardless, the question of whether H4K20me3 is simply retained at existing sites of deposition during senescence or is actively deposited to different nucleosomes following senescence-associated histone loss, is an important consideration. Possessing the ability to delineate between these two potential scenarios could provide valuable insight regarding the function of H4K20me3 during senescence. Probably the most effective way to address the question would be to obtain detailed genome-wide profiles of H4K20me3 occupancy in proliferating and senescent cells, respectively. Recent advancements in high-throughput sequencing technologies currently enable the rapid and accurate determination of nucleic acid sequence. Therefore, in order to better define the genomic distribution of H4K20me3 in proliferating and senescent cells, chromatin immunoprecipitation of H4K20me3 coupled to high-throughput sequencing will be employed and analyzed in the subsequent chapter.

## **Chapter 5. Mapping H4K20me3 Distribution in Senescence**

### **5.1 Rationale**

Senescent cells are governed by a defined program of altered gene expression that culminates in the establishment of a stable proliferation arrest and secretory phenotype. Considerable evidence supports a model in which the senescence program is regulated at least in part by directed chromatin remodeling. However, despite widespread changes in chromatin structure, not all features of the epigenome undergo alteration during senescence. For example, total abundance of the H4K20me3 histone modification remains identical between proliferating and senescent cells. Even more remarkable, this maintenance of H4K20me3 levels occurs within the context of a profound reduction of total histone content from senescent cells, suggesting that H4K20me3 might be selectively retained at some regions of the genome or otherwise redistributed in senescent cells. To this end, chromatin immunoprecipitation followed by high-throughput sequencing (ChIP-Seq) can generate high-resolution profiles of the genomic distribution of specific histone modifications. By comparing the genome-wide localization of H4K20me3 in proliferating and senescent cells, it might be possible to gain insight into the modification's contribution to chromatin remodeling and ultimately the senescence program. Therefore, I set out to map the genomic localization of H4K20me3 in senescent cells by ChIP-Seq and then compare distribution of the mark to other defined features of the human genome.

### **5.2 Results**

#### **5.2.1 Optimization of ChIP-Seq Conditions**

Over the last decade, considerable advancements in next-generation sequencing technologies have enabled the acquisition of genome-wide sequence data in a timely, accurate and cost-effective manner. Thus, as the sequencing technology has become more accessible, it has facilitated numerous important discoveries pertaining to chromatin structure, regulation and function. A valuable extension of next-generation sequencing has been to combine it with chromatin immunoprecipitation (i.e., ChIP-Seq) in order to obtain a detailed description of the

epigenetic landscape for a given cellular context (Barski et al., 2007; Wang et al., 2008). To this end, I was interested in utilizing a ChIP-Seq approach to map the genome-wide distribution of the H4K20me3 histone modification in proliferating and senescent IMR90 cells.

However, in order to generate meaningful and reproducible data, ChIP-Seq can require considerable methodological optimization. To this end, the success of a ChIP-Seq experiment can be dictated by myriad factors including parameters for chromatin preparation, abundance of the ChIP target, ability to immunoprecipitate the target, antibody specificity and the selection of relevant controls (Kidder et al., 2011). Another important consideration is the model system being used, as it may necessitate the optimization of additional parameters. Consequently, before proceeding with a wide-scale study of H4K20me3 in proliferating and senescent IMR90 cells, I first opted to systematically evaluate and optimize several of the key factors discussed above.

Because many of the downstream steps of the ChIP procedure are contingent upon efficient fragmentation of chromatin, it was first necessary to determine empirically the optimal conditions to achieve this. Chromatin fragmentation can be accomplished by multiple methods including sonication for cross-linked chromatin or nuclease digestion for native, unfixed chromatin. A standard ChIP protocol that relies on formaldehyde cross-linking and sonication-mediated fragmentation of chromatin was selected for the studies. Sonication of cross-linked chromatin occurs in a stochastic manner but can be influenced by several factors including cell density and the amplitude and duration of sonication. To determine optimal sonication conditions, a defined number of cross-linked IMR90 cells were resuspended in nuclear lysis buffer, divided evenly into multiple microcentrifuge tubes and subjected to water bath sonication for variable amounts of time at a fixed amplitude. As expected, chromatin fragmentation efficiency increased in a time-dependent manner, with optimal sonication occurring between 20 and 25 minutes (Figure 5.1). Excessive sonication can detrimentally affect ChIP target integrity, so a standard sonication time of 22.5 minutes was utilized for all subsequent experiments.

The ability to efficiently bind and immunoprecipitate an intended chromatin target is another requisite step of the ChIP procedure. Having previously assessed the binding specificity of a panel of H4K20me3 antibodies using the MODified Histone Peptide Array, the antibodies were subsequently evaluated for ability to

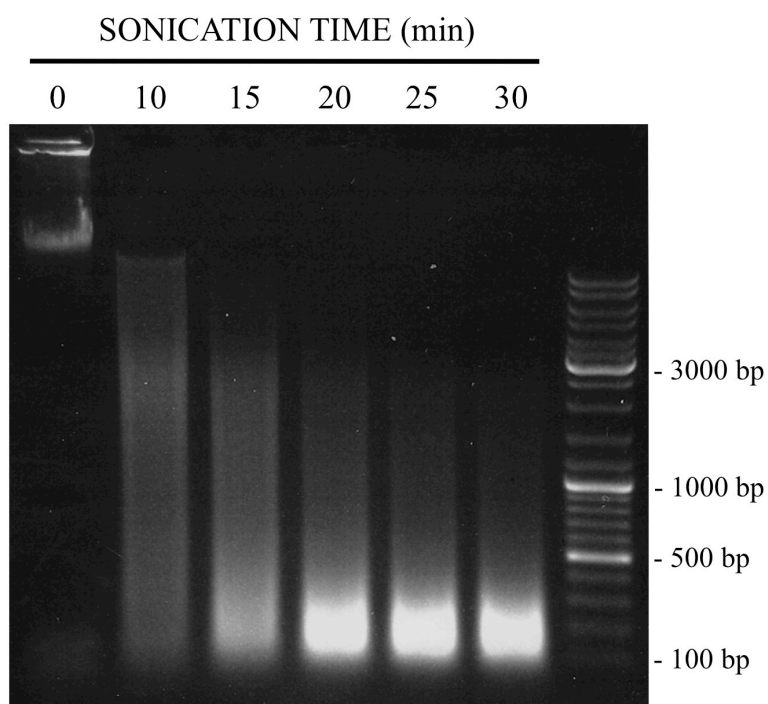


**Figure 5.1 Optimization of chromatin fragmentation.** Nuclei prepared from formaldehyde cross-linked IMR90 cells were subjected to sonication for variable amounts of time in a water bath sonicator. The sonicated samples were subsequently purified by phenol-chloroform extraction and fractionated on a 1% agarose TAE gel. The gel was stained with ethidium bromide, visualized on a UV transilluminator and photographed.

immunoprecipitate H4K20me3 from cross-linked chromatin preparations. Based on the prior specificity assessment, H4K20me3 rabbit antibodies supplied by Millipore (04-079), Cell Signaling Technology (5737), Abcam (ab9053) and Active Motif (39180) were selected for testing by ChIP. Sonicated cross-linked IMR90 chromatin solutions were subjected to immunoprecipitation with 2 or 10  $\mu\text{g}$  of the Abcam and Cell Signaling Technology H4K20me3 antibodies, 10  $\mu\text{g}$  of a total histone H4 antibody (Millipore, 05-858), and 2 or 10  $\mu\text{g}$  of a negative control rabbit IgG antibody (Sigma, M7023).

Following ChIP, bound chromatin and antibodies were eluted from the beads by boiling in SDS sample buffer, fractionated by SDS-PAGE and immobilized to a PVDF membrane. The membrane was subsequently Western blotted for histone H4 and ChIP efficiency was estimated by the amount of total histone H4 immunoprecipitated by the H4K20me3 antibodies compared to the histone H4 ChIP and input lanes (Figure 5.2a). While the negative control antibody (lanes 1 and 2) failed to immunoprecipitate any detectable histone H4, both the Abcam (lanes 3 and 4) and Cell Signaling Technology (lanes 5 and 6) antibodies precipitated amounts of histone H4 comparable to the total histone H4 ChIP (lane 7). Use of an anti-rabbit IgG-HRP conjugated secondary antibody for the Western blot also enabled visualization of the ChIP antibody heavy and light chains and confirmed that equal amounts of the respective antibodies were used for each ChIP reaction.

In addition to testing the Abcam and Cell Signaling Technology H4K20me3 antibodies by ChIP, rabbit antibodies produced by Millipore (04-079) and Active Motif (39180) were subjected to evaluation. Chromatin eluted from the Millipore and Active Motif H4K20me3 ChIP reactions was assessed by Western blot analysis of total histone H4 and compared to the previously validated Abcam antibody. Whereas even 10  $\mu\text{g}$  of the Active Motif antibody was insufficient to precipitate any detectable histone H4 (Figure 5.2b, lane 5), the Millipore antibody (lane 3) precipitated a moderate amount of histone H4, but not as much as the Abcam antibody (lane 2). Utilization of an anti-rabbit IgG-HRP conjugated secondary antibody for the Western blot again facilitated detection of the ChIP antibody heavy and light chains, ensuring that equivalent amounts of the ChIP antibodies were used for each reaction. Based on the composite results of the two ChIP antibody evaluation experiments, three separate antibodies were found capable of immunoprecipitating H4K20me3 from cross-linked chromatin preparations.

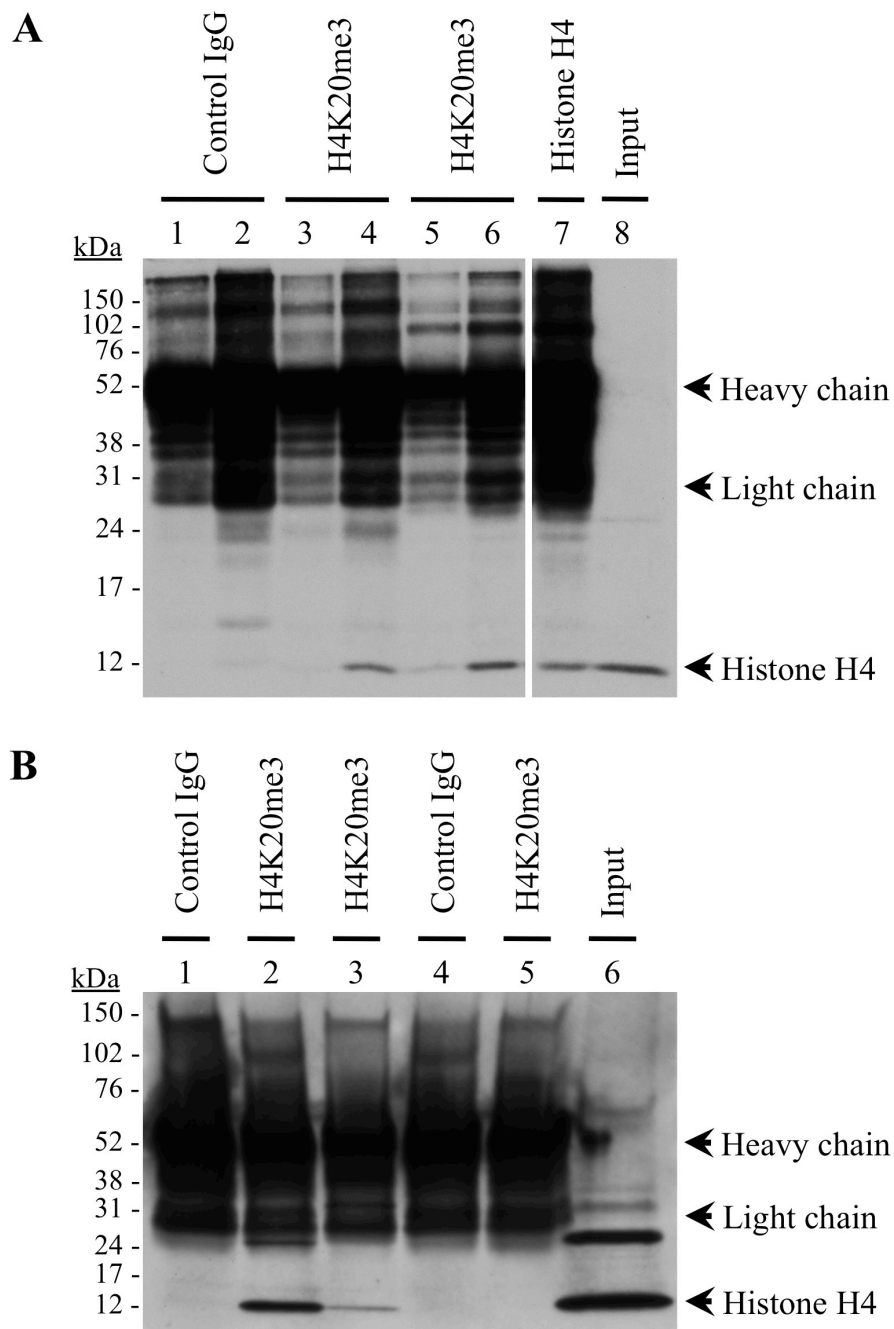


**Figure 5.2 Evaluation of antibody binding by ChIP.** Sonicated cross-linked chromatin from IMR90 cells was subjected to ChIP with the following antibodies. (A) Lane 1: 2  $\mu$ g rabbit IgG (M7023), Lane 2: 10  $\mu$ g rabbit IgG (M7023), Lane 3: 2  $\mu$ g H4K20me3 (ab9053), Lane 4: 10  $\mu$ g H4K20me3 (ab9053), Lane 5: 2  $\mu$ g H4K20me3 (5737), Lane 6: 10  $\mu$ g H4K20me3 (5737), Lane 7: 10  $\mu$ g Histone H4 (05-858), Lane 8: input chromatin. The ChIP samples were boiled, fractionated and Western blotted for histone H4. (B) Lane 1: 10  $\mu$ g rabbit IgG (M7023), Lane 2: 10  $\mu$ g H4K20me3 (ab9053), Lane 3: 10  $\mu$ g H4K20me3 (04-079), Lane 4: 10  $\mu$ g rabbit IgG (serum), Lane 5: 10  $\mu$ g H4K20me3 (39180), Lane 6: input chromatin. The ChIP samples were boiled, fractionated and Western blotted for histone H4.

However, because the Millipore and Cell Signaling Technology H4K20me3 antibodies both demonstrated higher specificity than the Abcam antibody in the peptide array evaluation, these two antibodies were selected for use in all subsequent H4K20me3 ChIP experiments.

Although the relative specificities of histone modification antibodies can be effectively evaluated *in vitro* using a method such as the MODified Histone Peptide Array, it is important to recognize that all antibodies can exhibit a certain degree of nonspecific binding. Nonspecific antibody binding in the context of ChIP can be exacerbated by a variety of factors including antibody concentration, ChIP buffer composition and the stringency of wash conditions. Having previously ascertained that the Millipore and Cell Signaling Technology H4K20me3 antibodies were both highly specific and capable of immunoprecipitating cross-linked chromatin, the next step was to determine which ChIP conditions would permit sufficient H4K20me3 pull-down while minimizing antibody cross-reactivity. To this end, a series of H4K20me3 ChIP reactions were set up to simultaneously evaluate the parameters of antibody concentration, ChIP buffer composition and wash stringency.

Most standard ChIP protocols suggest the inclusion of SDS in the ChIP lysis buffer as it helps facilitate fragmentation of chromatin during sonication. However, excessive SDS concentration can be detrimental to the subsequent antibody binding steps of ChIP. In order to determine the optimal SDS concentration for H4K20me3 ChIP, chromatin was prepared from cross-linked IMR90 cells in lysis buffer containing 1% SDS and diluted to a final SDS concentration of either 0.25% or 0.1%. The respective chromatin solutions were then subjected to immunoprecipitation using either 2 or 10  $\mu$ g of the Millipore H4K20me3 antibody (04-079) or 10  $\mu$ g of control rabbit IgG. Following immunoprecipitation, each ChIP reaction was washed either in accordance with the standard protocol or with an additional stringent wash buffer comprised of 10 mM Tris, 250 mM LiCl, 1 mM EDTA, 1% NP-40, 1% deoxycholic acid. The ChIP reactions were then boiled in SDS sample buffer, fractionated by SDS-PAGE, immobilized to a PVDF membrane and assessed by Western blotting of H4K20me3.

As expected, the control rabbit IgG ChIP failed to precipitate H4K20me3 (Figure 5.3, lane 9), while the H4K20me3 ChIP reactions conducted under differing conditions produced variable amounts of H4K20me3 (lanes 1-8). The combined use of ChIP lysis buffer containing 0.25% SDS and 2  $\mu$ g of H4K20me3 antibody was

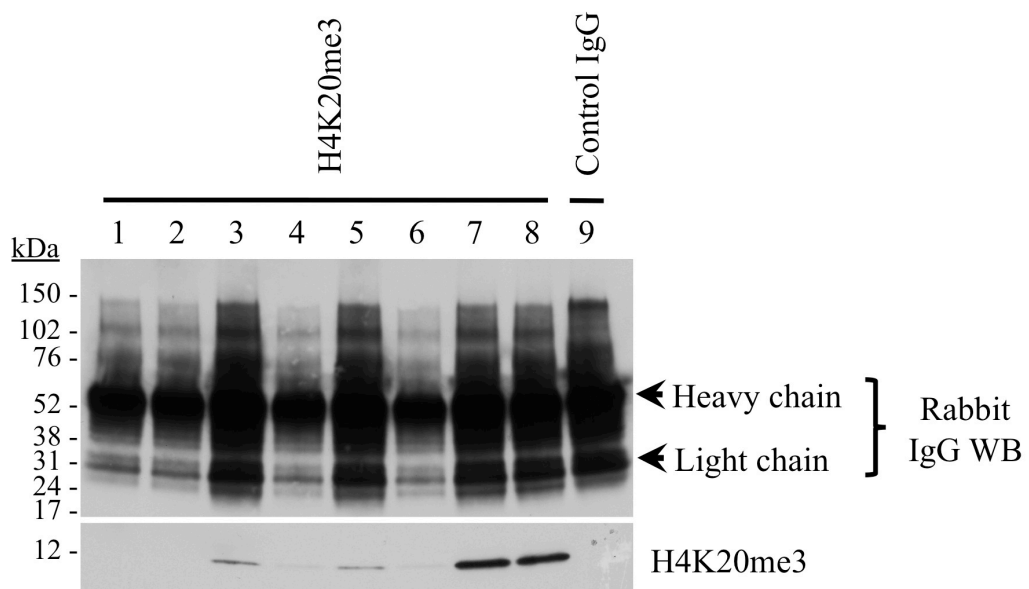


**Figure 5.3 Optimization of ChIP stringency conditions.** Cross-linked, sonicated chromatin solutions were diluted to final SDS concentrations of either 0.1 or 0.25% and subjected to immunoprecipitation under the following conditions: (1) 0.25% SDS, 2  $\mu$ g H4K20me3 antibody, LiCl wash; (2) 0.25% SDS, 2  $\mu$ g H4K20me3 antibody, no LiCl wash; (3) 0.25% SDS, 10  $\mu$ g H4K20me3 antibody, LiCl wash; (4) 0.1% SDS, 2  $\mu$ g H4K20me3 antibody, LiCl wash; (5) 0.25% SDS, 10  $\mu$ g H4K20me3 antibody, no LiCl wash; (6) 0.1% SDS, 2  $\mu$ g H4K20me3 antibody, no LiCl wash; (7) 0.1% SDS, 10  $\mu$ g H4K20me3 antibody, LiCl wash; (8) 0.1% SDS, 10  $\mu$ g H4K20me3 antibody, no LiCl wash; (9) 0.1% SDS, 10  $\mu$ g control antibody, no LiCl wash. Each ChIP reaction was subsequently boiled in 1X sample buffer, fractionated by SDS-PAGE and immobilized to PVDF. The top portion of the PVDF membrane was Western blotted with anti-rabbit IgG secondary antibody to detect the ChIP antibody heavy and light chains. The bottom portion of the membrane was Western blotted with anti-H4K20me3 antibody to evaluate ChIP efficiency.

insufficient to precipitate detectable levels of H4K20me3, irrespective of the inclusion or exclusion of the stringent LiCl wash (lanes 1 and 2). By reducing the SDS concentration to 0.1%, 2 µg of H4K20me3 became sufficient to precipitate low but detectable levels of H4K20me3 in either the presence or absence of the LiCl wash step (lanes 4 and 6). By increasing the amount of H4K20me3 antibody to 10 µg, the ChIP reactions yielded considerably more H4K20me3 as assessed by Western blotting. The condition that facilitated the most robust precipitation of H4K20me3 was the combination of lysis buffer containing 0.1% SDS and 10 µg of H4K20me3 antibody (lanes 7 and 8). Under all conditions, the inclusion of the LiCl wash step did not appear to adversely affect the overall ChIP yield as determined by Western blotting for H4K20me3. As a result, the high stringency LiCl wash step was incorporated into all subsequent ChIP experiments.

### **5.2.2 ChIP-Seq of H4K20me3 in Proliferating and Senescent Cells**

Based on the series of experiments discussed above, I determined that the following conditions were optimal for ChIP of H4K20me3 from cross-linked IMR90 cells: 22.5 minutes of sonication, dilution of chromatin solutions to 0.1% SDS, utilization of 6 µg of antibody per ChIP reaction and inclusion of the LiCl wash step. I arbitrarily selected 6 µg of antibody per ChIP as it represented the average of the two antibody amounts I had tested. Using these parameters, cross-linked, sonicated chromatin solutions isolated from proliferating (PD32) and replicative senescent (PD86) IMR90 cells were subjected to immunoprecipitation with 6 µg of control rabbit IgG, histone H4 antibody (Millipore, 05-858) or H4K20me3 antibody (Millipore, 04-079). For each ChIP reaction, 500 µg of chromatin protein, as determined by the Bradford assay, was utilized. Following overnight incubation with primary antibodies and beads, the ChIP reactions were washed, eluted, subjected to reverse cross-linking and purified by phenol-chloroform extraction. The purified ChIP DNA was subsequently quantified using the Qubit fluorometer (Invitrogen), of which 10 ng DNA was utilized to generate ChIP-Seq libraries according to the standard Illumina protocol. Prepared libraries underwent quality control analysis using the Agilent 2100 Bioanalyzer. The libraries were then hybridized to an Illumina flow cell for cluster generation, and subjected to single read sequencing on the Illumina Genome Analyzer Iix (GAIIx) by the Beatson Institute for Cancer Research's Molecular Technology Services personnel.

Sequence (read) lengths of 75 basepairs for the first experiment and 76 basepairs for the second experiment were extracted from the GAIIX as FASTQ files and inspected for quality as described in Chapter 2 (Materials and Methods). The resulting reads were then aligned to the human genome (assembly NCBI36/hg18) using the Bowtie alignment tool and the settings described in Chapter 2. It is important to note that Tony McBryan, our laboratory computational biologist, performed all of the sequence alignment and subsequent analysis. Any sequences that failed to align or align to more than one site in the genome were excluded from subsequent analyses. Because the standard ChIP-Seq library preparation protocol utilizes a PCR amplification step, preferential amplification of certain sequences can occur. PCR clonality is a particularly relevant issue when generating ChIP-Seq libraries from samples with a low ChIP yield, as low yield often corresponds with low sample complexity. In this context, an individual DNA fragment may undergo excessive amplification and become overrepresented in the sequencing run, reducing the specificity of the experiment. This can create bias in the process of identifying regions of the genome that are enriched for a particular chromatin modification. In order to account for this, any multiple identical reads were also excluded from the subsequent analyses.

As summarized in Table 5.1, the first ChIP-Seq experiment generated between 28 and 42 million total reads for the DNA inputs and histone H4 and H4K20me3 ChIP reactions. After removing reads that failed to align uniquely to the human genome and multiple identical reads, between 7 and 33 million uniquely alignable reads remained (Table 5.1). For the PD32 input and histone H4 ChIP samples respectively, 24,478,131 (63%) and 25,455,213 (66%) of the total reads remained after filtering, whereas for the PD32 H4K20me3 ChIP sample only 14,319,405 (36%) of the total reads were uniquely alignable sequences. Likewise, 20,520,747 (71%) and 31,894,106 (76%) of the total reads from the PD86 input and histone H4 ChIP samples were uniquely alignable, while only 7,941,385 (20%) of the PD86 H4K20me3 ChIP reads remained after filtering. Although initially surprising, many of the PD32 and PD86 H4K20me3 ChIP reads were likely excluded by filtering because they represented repetitive regions of the genome, including pericentromeres and telomeres (Mravinac et al., 2009, Ernst & Kellis, 2010). Consequently, these repetitive sequences would not be aligned as unique regions of the genome.

Sample	Antibody	Total Reads	Aligned Reads	PCR Filtered
PD32 Input	--	38,866,790	26,366,982	24,478,131
PD32 Histone H4 ChIP	Millipore (05-858)	38,424,942	29,888,728	25,455,213
PD32 H4K20me3 ChIP	Millipore (04-079)	39,675,337	16,119,043	14,319,405
PD86 Input	--	28,979,919	21,951,984	20,520,747
PD86 Histone H4 ChIP	Millipore (05-858)	42,000,639	33,811,135	31,894,106
PD86 H4K20me3 ChIP	Millipore (04-079)	40,397,075	8,533,969	7,941,385

**Table 5.1 H4K20me3 ChIP-Seq experiment 1 summary statistics.** Summary of the reads that were generated in the first H4K20me3 ChIP-Seq experiment. Total reads obtained from the GAIIX were aligned to the human genome (assembly NCBI36/hg18). Identical aligned reads were subsequently removed as they likely reflected products of preferential PCR amplification.

There is some debate as to whether reads that align to multiple genomic locations should be excluded from downstream analysis. The advantage of removing multiple alignments is that it improves the specificity of the analysis, by ensuring that the remaining reads align to single, unambiguous genomic sites. The disadvantage of removing multiple alignments is that it can create bias and decrease the sensitivity of the experiment, as certain genomic classes such as DNA repeats might be excluded from analysis due to the inherently repetitive nature of the sequences. Ultimately, the decision to include or exclude multiple alignments comes down to a trade-off between specificity and sensitivity and is largely dictated by the nature of the experiment. For example, for a ChIP-Seq experiment conducted on a chromatin modification reported to associate with repetitive elements, it might be beneficial to perform the analysis two ways, both including and excluding multiple alignments.

Before performing any comprehensive analysis of the first H4K20me3 ChIP-Seq data, a second experiment was conducted. Whereas the first set of H4K20me3 ChIPs were performed using equal amounts of chromatin protein from proliferating and senescent cells, the second experiment was carried out using equal amounts of chromatin DNA. Because senescent cells can contain more protein per cell than proliferating cells, by using equal amounts of protein for each ChIP reaction, I might unintentionally utilize fewer senescent cells per ChIP. DNA content is arguably less variable between proliferating and senescent cells and was therefore used to ensure that the ChIP reactions utilized equivalent numbers of proliferating or senescent cells. As before, solutions of sonicated chromatin from proliferating (PD32) or replicative senescent (PD86) IMR90 cells were subjected to immunoprecipitation with 6  $\mu$ g of control rabbit IgG or histone H4 antibody (Millipore, 05-858). However, for this second experiment, a different H4K20me3 antibody (Cell Signaling Technology, 5737) was used. The second H4K20me3 was utilized in order to confirm the specificity of any observed regions of H4K20me3 localization. Therefore, any H4K20me3-containing regions that appeared with both antibodies likely represented genuine regions of enrichment for the modification. Aside from the differences just described, the second H4K20me3 ChIP-Seq experiment was conducted in the same manner as the first experiment. The resulting ChIP DNA samples were used to generate libraries and sequenced as before using the Illumina GAIIx.

The reads obtained from the second ChIP-Seq experiment were similarly aligned to the human genome using the Bowtie alignment tool. All reads that failed to align to a unique region of the genome and any identical reads were filtered from the data. Comparable to the first ChIP-Seq experiment, the second experiment yielded between 33 and 39 million reads per input or ChIP sample (Table 5.2). However, after considering the alignment requirements discussed above, between 7 and 29 million uniquely alignable, non-redundant reads per sample remained (Table 5.2). Similar to the first experiment, 23,638,627 (62%) and 24,221,792 (66%) of the PD32 input and histone H4 ChIP total reads, respectively, aligned uniquely to the genome, while only 7,824,101 (24%) of the total reads from the PD32 H4K20me3 ChIP aligned uniquely to the genome. For the PD86 input and histone H4 ChIP samples, 25,474,711 (68%) and 29,646,203 (75%) of the total reads, respectively, aligned uniquely to the human genome. In contrast, only 12,222,896 (34%) of the PD86 H4K20me3 ChIP total reads aligned uniquely. Although both the PD32 and PD86 H4K20me3 ChIP samples from the second experiment exhibited considerably lower degrees of sequence alignment, the observation was consistent with the first experiment. Again, the majority of the PD32 and PD86 H4K20me3 ChIP reads failed to align to unique regions of the genome presumably because they corresponded to repetitive genomic loci.

### **5.2.3 Senescent Cells Contain Regions of H4K20me3 Enrichment**

Having obtained H4K20me3 ChIP-Seq data from proliferating and replicative senescent IMR90 cells using two separate H4K20me3 antibodies, it was next important to determine whether the modification occupied identical or unique locations in the respective cell states. Because net abundance of the H4K20me3 modification was comparable in proliferating and senescent cells, two scenarios were possible. Either H4K20me3 distribution remained identical in proliferating and senescent cells, or the profile of the modification was altered in senescent cells, being lost from one region and deposited at another, such that the absolute levels of the mark remained constant. Using the respective ChIP-Seq datasets, it was possible to distinguish between the two scenarios. To this end, it was first necessary to identify regions of H4K20me3 enrichment in proliferating and senescent cells.

In order to accomplish this, the uniquely aligned H4K20me3 reads were compared to the uniquely aligned histone H4 reads using SICER (version 1.1).

Sample	Antibody	Total Reads	Aligned Reads	PCR Filtered
PD32 Input	--	37,836,691	25,314,813	23,638,627
PD32 Histone H4 ChIP	Millipore (05-858)	36,644,970	28,146,115	24,221,792
PD32 H4K20me3 ChIP	CST (5737)	33,176,191	25,289,029	7,824,101
PD86 Input	--	37,503,717	27,697,302	25,474,711
PD86 Histone H4 ChIP	Millipore (05-858)	39,657,464	31,325,531	29,646,203
PD86 H4K20me3 ChIP	CST (5737)	35,946,004	26,137,817	12,222,896

**Table 5.2 H4K20me3 ChIP-Seq experiment 2 summary statistics.** Summary of the reads that were generated in the second H4K20me3 ChIP-Seq experiment. Total reads obtained from the GAIIX were aligned to the human genome (assembly NCBI36/hg18). Identical aligned reads were subsequently removed as they likely reflected products of preferential PCR amplification.

SICER is a tool used to identify regions of significant enrichment for specific chromatin modifications, including histone marks, by defining clusters of sequencing reads that are unlikely to occur at a given location due to chance (Zang et al., 2009). SICER was specifically selected for the analysis as it performs optimally for modifications that occur diffusely across the genome. As described in detail in Chapter 2 (Materials and Methods), SICER works by computing the likelihood that an accumulation of chromatin modification ChIP reads (e.g., H4K20me3) occurs specifically within a defined region, rather than occurring in the region in a stochastic manner. For each region, SICER was used to evaluate the H4K20me3 reads relative to the total histone H4 ChIP reads, in order to reduce the likelihood that the H4K20me3 reads accumulated due to regional variation in chromatin solubility. Based on the SICER analysis, statistically significant clusters (i.e., domains) of H4K20me3 reads were identified in the PD32 and PD86 samples.

Following the identification of H4K20me3 domains in the PD32 and PD86 samples using SICER, the respective datasets were compared using the DiffBind Bioconductor package in order to determine regions of differential H4K20me3 enrichment between the PD86 and PD32 samples. In total, DiffBind identified 10,786 domains of H4K20me3 differential abundance between the PD32 and PD86 samples. Remarkably, the PD86 sample from experiment 1 contained differentially enriched H4K20me3 domains spanning 87,878,460 bp or 3.0% of genome, while the PD86 sample from experiment 2 contained H4K20me3 domains covering 75,658,200 bp or 2.6% of the genome.

The 10,786 domains of H4K20me3 differential enrichment were subsequently displayed as a cluster diagram (Figure 5.4a) using the R version 2.15.1 `hclust` function from the `fastcluster` library, as described in Chapter 2 (Materials and Methods). Each row in the cluster diagram represents one of the 10,786 differentially enriched domains. It is important to note that the color intensity of each domain reflects the level of H4K20me3 enrichment over histone H4 (after normalization for library size) for each replicate, rather than the level of H4K20me3 differential enrichment between the PD86 and PD32 samples. As revealed in Figure 5.4a, the PD86 samples displayed numerous H4K20me3 domains that were either not present in the PD32 samples or present at a considerably lower abundance. Remarkably, the distribution of these differentially enriched H4K20me3 domains was strikingly similar between the PD86 samples from both experiments. Importantly, this

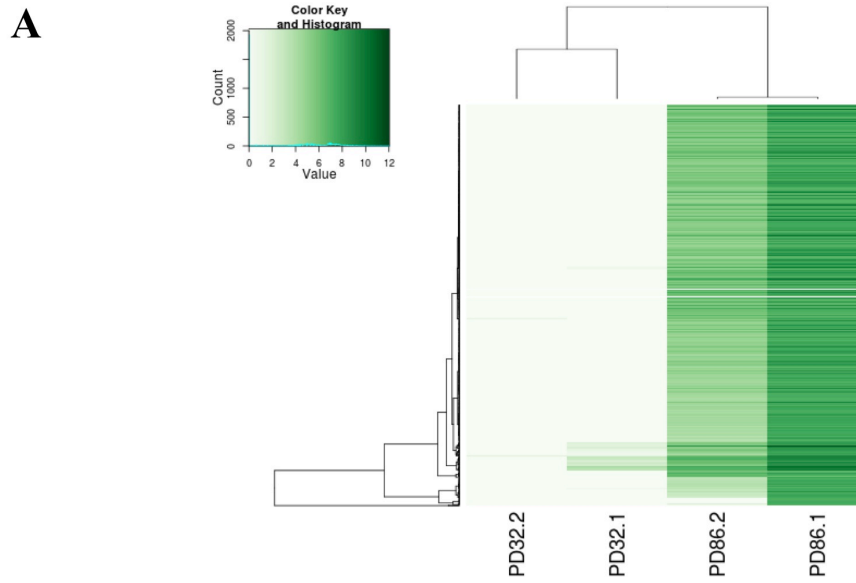


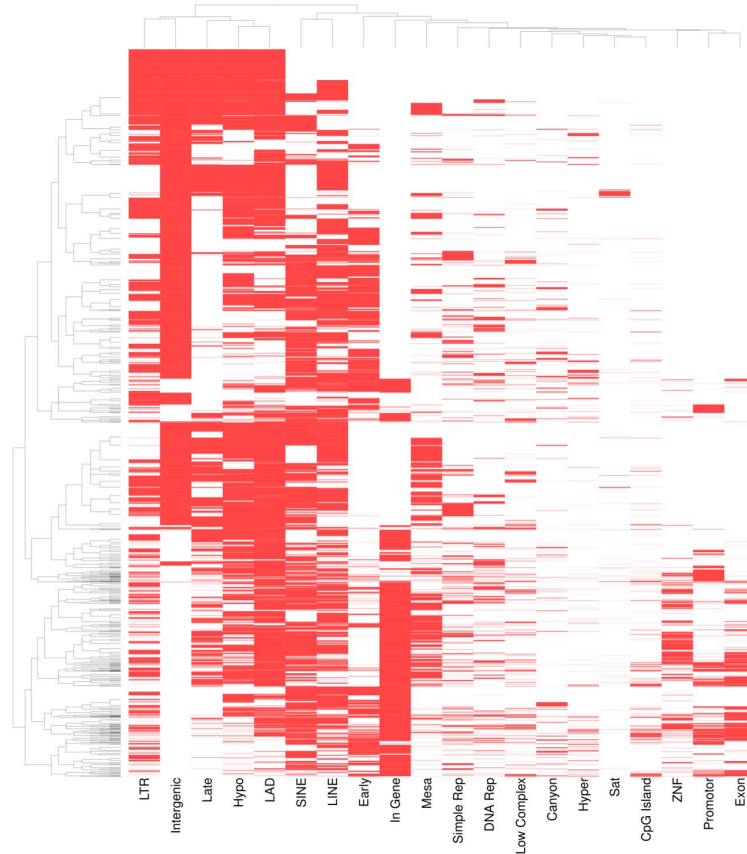
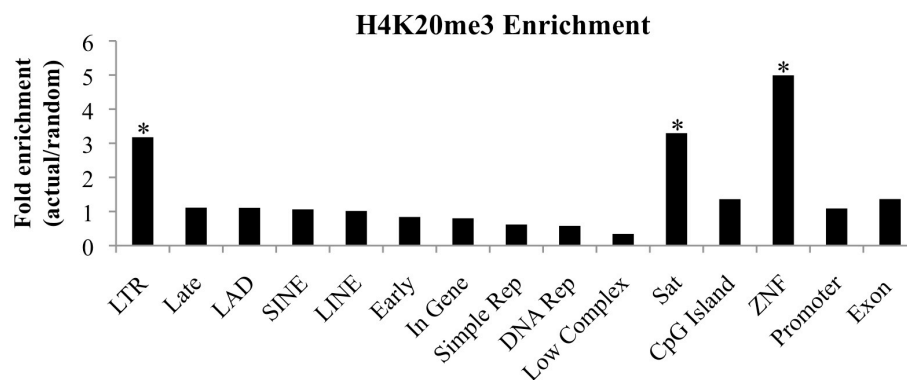
**Figure 5.4 Identification of H4K20me3 differentially enriched domains.** (A) 10,786 statistically significant domains of H4K20me3 differential enrichment were identified between the PD86 and PD32 samples using SICER and DiffBind and displayed as a cluster diagram using the R version 2.15.1 hclust function. Each row represents a single domain of PD86-specific H4K20me3 differential enrichment and the color intensity reflects the relative H4K20me3 enrichment over histone H4 within each sample. (B) The domains of H4K20me3 differential enrichment were plotted in the genomic context using UCSC Genome Browser and displayed graphically as a chromosome ideogram.

indicated that both the Millipore and Cell Signaling Technology H4K20me3 antibodies immunoprecipitated chromatin from comparable regions of the genome. In this way, the data provided supporting evidence that the individual H4K20me3 antibodies were highly specific to the modification and added confidence in interpreting the distribution of H4K20me3 in senescent cells.

To provide additional insight into the genomic distribution of the SICER/DiffBind defined regions of H4K20me3 enrichment, the domains identified in Figure 5.4a were plotted as a chromosome ideogram (Figure 5.4b). As evident in the ideogram, regions of PD86-specific H4K20me3 differential enrichment were present across all chromosomes. Although some chromosomes exhibited regions devoid of H4K20me3 enrichment, the mark was distributed widely across the genome and occasionally present as larger blocks of enrichment (e.g., chromosome 19).

In order to better characterize the distribution of H4K20me3 in senescent cells, the regions of PD86-specific H4K20me3 differential enrichment identified in Figure 5.4a were compared to defined features of the human genome. To accomplish this, the coordinates of the H4K20me3 differentially enriched domains were assessed for overlap with a panel of well-defined genomic features. The 10,786 H4K20me3 domains were clustered by hierarchical clustering, using the R 2.15.1 `hclust` function from the `fastcluster` library. As described in Chapter 2 (Materials and Methods), each differential domain was treated as a k-dimensional vector, for which each entry within the vector was either the presence or absence of a genomic feature of interest. The domains were then clustered both row and column-wise using Euclidian distance as the distance metric and the complete linkage function. The data were then reordered to conform to the clustering analysis and plotted using the R `heatmap.2` function in the `gplots` library (Figure 5.5a). Each row represents one of the 10,786 H4K20me3 differentially enriched domains and each column reflects a specific genomic feature. It is important to note that because each feature was scored for either presence or absence of overlap with H4K20me3, this analysis did not provide any ranking based on the level of H4K20me3 differential enrichment.

As presented in Figure 5.5a, the domains of H4K20me3 differential enrichment coincided with a variety of genomic features, including long terminal repeats (LTR), intergenic regions, late replicating regions (Late), regions that become DNA hypomethylated in senescent cells (Hypo), lamina-associated domains

**A****B**

**Figure 5.5 H4K20me3 is enriched at defined genomic features.** (A) Domains of H4K20me3 differential enrichment (as defined in Figure 5.4a) were clustered using hierarchical clustering (performed using the R 2.15.1 hclust function from the fastcluster library). Each differential region was treated as a k-dimensional vector where each entry within the vector was the presence/absence of a genomic feature of interest (e.g., LTR, LINE, etc). The regions were clustered both row and column-wise using Euclidian distance as the distance metric and the complete linkage function. The data was then reordered to conform to the clustering analysis and plotted using the R heatmap.2 function in the gplots library. Each row represents a single domain of H4K20me3 differential enrichment and each column represents a specific genomic feature. (B) H4K20me3 domains and genomic features were compared and percentage overlap was calculated for each feature. A random overlap percentage was also calculated for each feature. The actual H4K20me3 overlap with each feature was expressed as fold enrichment over random overlap and plotted graphically. \* Denotes the p-value of the enrichment was below the level of detection.

(LAD), short interspersed elements (SINE) and long interspersed elements (LINE). The late replicating regions were defined by the work of Hellman and colleagues (Aran et al., 2011). Regions of DNA hypomethylation were based on recent work from Peter Adams' laboratory (Cruickshanks et al., submitted). Likewise, the lamina-associated domains were defined by work from Shelley Berger's laboratory (Shah et al., submitted). Finally, considerably more of the senescence-specific H4K20me3 domains mapped to intergenic regions of the genome than to genes. This was not surprising however, as protein-coding genes comprise approximately only 1.5% of the human genome (Venter et al., 2001; International Human Genome Sequencing Consortium, 2004).

Several of the genomic features identified in Figure 5.5a as containing H4K20me3 enrichment in senescent cells, represented interspersed DNA repeats (e.g., LTRs, SINEs and LINEs). Although H4K20me3 was previously identified at another class of DNA repeats, the tandem satellite repeats, fewer of the senescence-specific H4K20me3 domains appeared to occur at satellite sequences (Sat) in our analysis (Ernst & Kellis, 2010). This may be partially explained by the fact that satellite repeats only account for approximately 3% of the human genome, whereas LTR retrotransposons (9%), SINES (15%) and LINES (21%) comprise a considerably larger proportion of the genome (Treangen & Salzberg, 2012). It is also important to point out that some of the H4K20me3 reads which might have aligned to DNA repeats were presumably removed from the analysis due to our intentional exclusion of sequences that could not be aligned to singly unique locations in the genome.

It is important to note that each of the genomic features included in the clustering analysis in Figure 5.5a comprised different proportions of the genome. Consequently, it was formally possible that some of the overlap between the H4K20me3 domains and individual genomic features might be attributed to the frequency that a specific feature occurred throughout the genome. To address this, the genomic coordinates of the H4K20me3 differentially enriched regions and defined genomic features were compared and the number of basepairs present in both datasets was calculated as a percentage of the total number of basepairs for each individual feature. For each genomic feature, a random overlap percentage was also calculated, which involved random distribution of the feature across the genome and the calculation of the overlap between this random feature and the H4K20me3

differentially enriched signal. The random distribution was carried out 1000 times and the mean percentage overlap was utilized. The data were then expressed as the fold enrichment of the observed H4K20me3 percentage overlap over the random percentage overlap for each genomic feature, and displayed graphically in Figure 5.5b. P-values were calculated by observing the frequency that the random overlap was greater than or equal to the observed overlap.

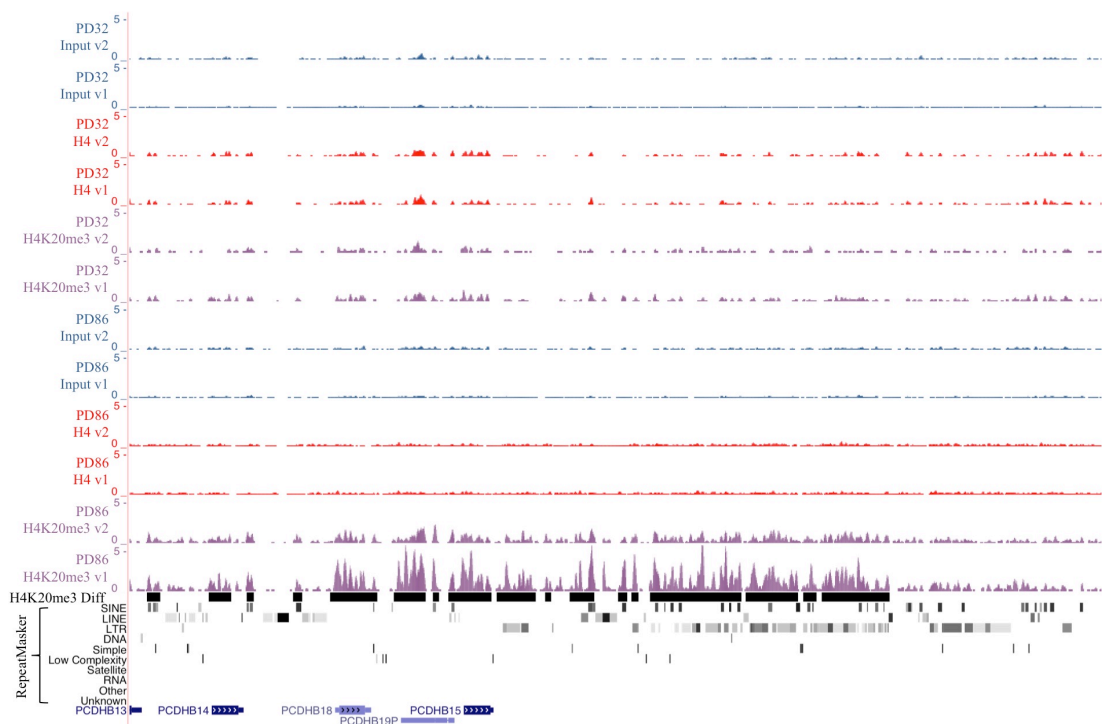
Based on this analysis, three genomic features exhibited significant H4K20me3 enrichment over random chance: LTRs, satellite repeats and ZNF genes (Figure 5.5b). Approximately 3-fold enrichment over random chance was observed for H4K20me3 at both LTRs and satellites, with a p-value below the limit of detection. Likewise, 5-fold enrichment over random chance was observed for H4K20me3 at ZNF genes, with a p-value similarly below the limit of detection. Importantly, these data are largely consistent with a previous genome-wide study that reported marked enrichment of H4K20me3 at satellite DNA and ZNF genes in human CD4<sup>+</sup> T cells (Barski et al., 2007). However, Barski and colleagues failed to observe significant H4K20me3 enrichment at LTRs, which may be attributed to one of several factors. First, it is possible that H4K20me3 enrichment varies between cell types, as the study by Barski and colleagues utilized T cells while the present study was conducted using IMR90 cells. Second, H4K20me3 enrichment may only occur at LTRs in senescent cells, as the enrichment at LTRs was only observed for the senescence-specific domains of H4K20me3 differential enrichment. Finally, the discrepancy between the study by Barski and colleagues and the present analysis may reflect differences in H4K20me3 antibody quality. Whereas the data from the report by Barski and colleagues was generated using the Abcam (ab9053) H4K20me3 antibody, the present study was conducted using Millipore (04-079) and Cell Signaling Technology (5737) antibodies, which I have previously demonstrated to exhibit higher specificity than the Abcam (ab9053) antibody (see Figure 4.1). Regardless of any discrepancies with the previous literature, the current data indicate that H4K20me3 is significantly enriched at LTRs, satellites and ZNF genes in senescent IMR90 cells.

Based on the analysis presented in Figure 5.5, domains of statistically significant H4K20me3 enrichment coincided with several features of heterochromatin and repetitive DNA in the PD86 senescence cells. In order to validate the observed overlap between H4K20me3 and these features, it was

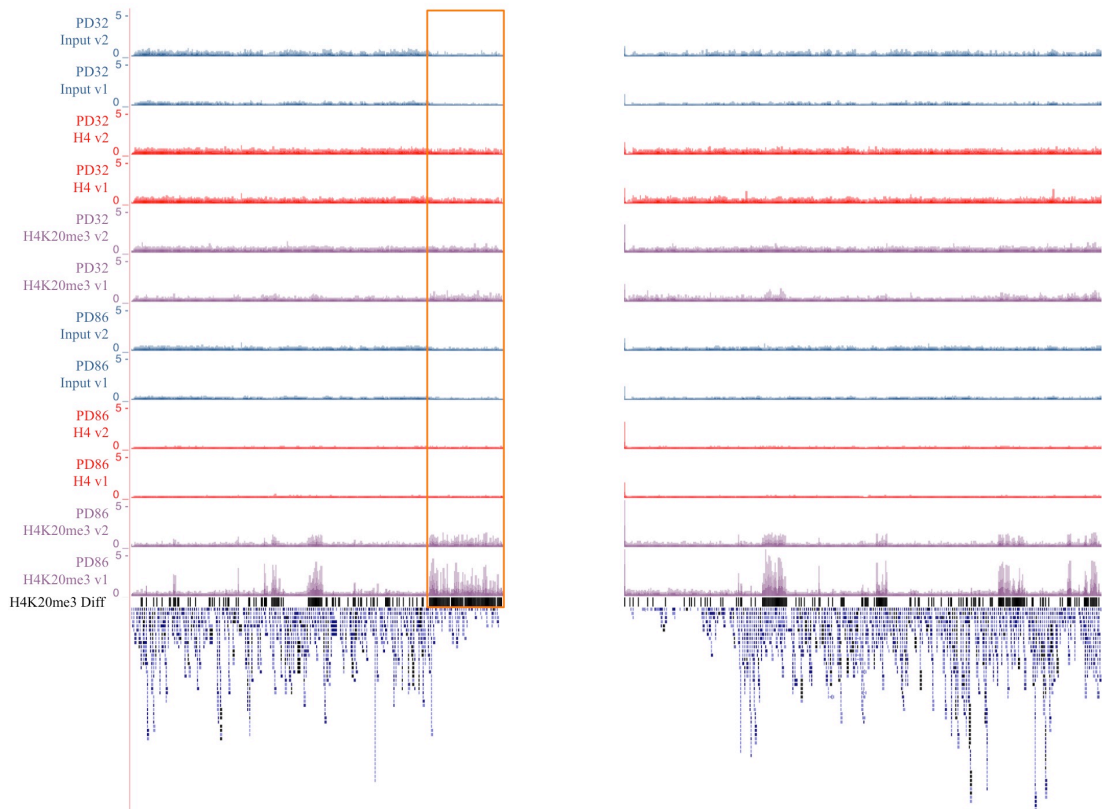
important to examine the H4K20me3 enriched domains within the genomic context. To this end, all uniquely alignable reads from the input DNA, histone H4 ChIP and H4K20me3 ChIP samples were assembled as individual bigWig tracks and uploaded to the UCSC Genome Browser for visualization. The SICER/DiffBind defined domains of H4K20me3 differential enrichment identified in Figure 5.4a were included as a parallel track in the Genome Browser viewer. Using the RepeatMasker tool, a program that identifies regions of low complexity DNA and interspersed repeats throughout the genome, a track showing domains of repetitive DNA and potential heterochromatin was also included in the viewer. As evident in Figure 5.6b, several domains of H4K20me3 differential enrichment exhibited distinct overlap with LTRs within an 85 kb region of chromosome 5 (5q31.3). Although occasional minor overlap between H4K20me3 and LINEs or SINEs was also apparent, the majority of the overlap occurred between H4K20me3 and LTRs. While LTRs are not exclusive to heterochromatic domains, this class of repeats is frequently associated with heterochromatin and was therefore considered a feature of heterochromatin for the present analysis (Cordaux & Batzer, 2009). It is important to note that alignment of the H4K20me3 differentially enriched domains to two of the most prominent examples of heterochromatin (e.g., centromeres and telomeres) was not possible, as these sequences are omitted from the current version of the UCSC Genome Browser.

In order to provide a less biased interrogation of the ChIP-Seq data, I next wished to examine the distribution of H4K20me3 across the broader genomic context. To this end, input DNA, histone H4 ChIP and H4K20me3 ChIP samples were again assembled as individual bigWig tracks and visualized using the UCSC Genome Browser. Whereas the previously discussed analysis was based on H4K20me3 differential enrichment, utilizing the Genome Browser enabled simultaneous viewing of each PD32 and PD86 sample from the two ChIP-Seq experiments. After viewing the input, histone H4 ChIP and H4K20me3 ChIP tracks aligned to each chromosome, chromosome 19 was selected as it contained discrete regions of marked H4K20me3 enrichment in the senescent samples (Figure 5.7b). As indicated by the schematic chromosomal ideogram displayed in Figure 5.7a, the tracks represented in Figure 5.7b spanned the entire length of chromosome 19 (p13.3-q13.34).

Importantly, based on each of the input and ChIP tracks in Figure 5.7b, no regions appeared obviously devoid of reads, suggesting that sufficient sequencing

**A****B**

**Figure 5.6 H4K20me3 is enriched at features of heterochromatin.** Uniquely alignable reads from proliferating (PD32) and senescent (PD86) input, histone H4 ChIP and H4K20me3 ChIP samples were visualized with the UCSC Genome Browser. (A) Schematic ideogram of the 85 kb genomic region being visualized (chromosome 5 q31.3, indicated by the red box). (B) Individual ChIP-Seq bigWig tracks aligned to chromosome 19. The y-axis represents total reads. The black bars below the bigWig tracks represent regions of H4K20me3 differential enrichment (H4K20me3 Diff) as defined by SICER and DiffBind. A track indicating domains of repetitive elements and low complexity DNA (RepeatMasker) has been included at the bottom of the Genome Browser.

**A****B**

**Figure 5.7 Distribution of H4K20me3 across chromosome 19.** Uniquely alignable reads from proliferating (PD32) and senescent (PD86) input, histone H4 ChIP and H4K20me3 ChIP samples were visualized with the UCSC Genome Browser. (A) Schematic ideogram of the genomic region being visualized. The resolution is set so that the full linear length of chromosome 19 is present in the viewing window. (B) Individual ChIP-Seq bigWig tracks aligned to chromosome 19. The y-axis represents total reads. The black bars along the bottom of the viewer represent domains of H4K20me3 differential enrichment (H4K20me3 Diff) as defined by SICER and DiffBind. The orange box indicates the presence of an approximately 5 megabase region of H4K20me3 enrichment in the PD86 samples.

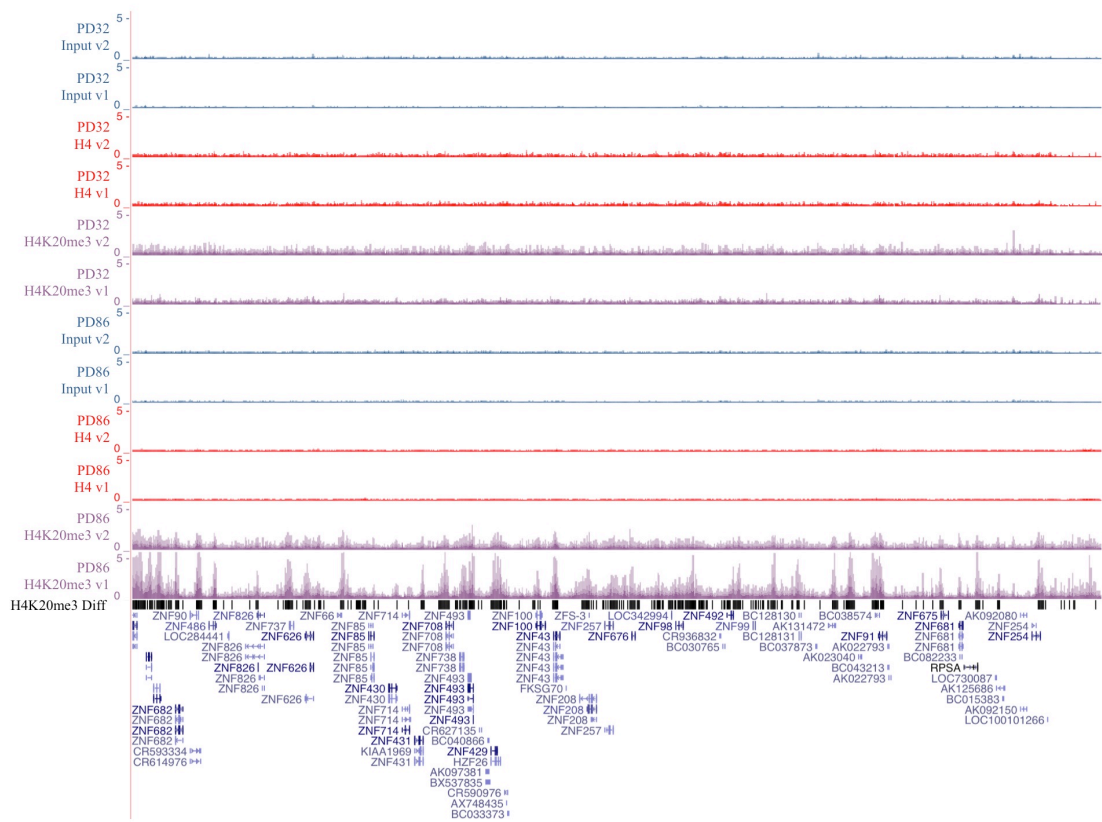
coverage had been achieved. However, a better and less ambiguous indicator of sequencing coverage is reflected in the total number of reads obtained for each ChIP-Seq replicate. As recommended in the current guidelines of the ENCODE and modENCODE consortia, 10 million uniquely alignable reads per replicate is considered to provide sufficient sequencing coverage for binding factors and modifications that localize to specific positions across the genome, while 20 million uniquely alignable reads per replicate is considered adequate for chromatin modifications with a broad genomic distribution (Landt et al., 2012). As summarized in Tables 5.1 and 5.2, each input and histone H4 ChIP sample yielded in excess of 20 million uniquely alignable reads, suggesting sufficient coverage. The H4K20me3 ChIP samples ranged from 7.8-14 million reads per replicate, which is on the low end for a broadly distributed histone modification, but within an acceptable range for a localized modification. H4K20me3 is not a broadly distributed modification, as it only occupies approximately 2-3% of all histone H4 molecules present in chromatin and predominantly localizes to defined genomic regions including certain DNA repeats and ZNF genes (Pesavento et al., 2008; Ernst & Kellis, 2010). Consequently, the current H4K20me3 ChIP samples likely provide sufficient sequencing coverage.

As presented in Figure 5.7b, all of the input and histone H4 tracks for the PD32 proliferating and PD86 senescent cells exhibited a predominantly even distribution across chromosome 19, with very few regions of variability. This was important as it signified that there were unlikely any regions exhibiting solubility bias. For example, if multiple tracks had displayed identical regions lacking reads, it might have been formally possible that those particular genomic coordinates were resistant to solubilization during the ChIP process. Fortunately, this did not appear to be the case. Both of the PD32 H4K20me3 tracks contained some regions of subtle H4K20me3 enrichment over background, with slightly higher levels of enrichment observed in the track from the first experiment (PD32 H4K20me3 v1). Interspersed regions of H4K20me3 enrichment over background were even more apparent in both of the PD86 H4K20me3 tracks, again with higher numbers of clustered H4K20me3 reads in the track from the first experiment (PD86 H4K20me3 v1). Domains of H4K20me3 enrichment in the PD86 cells relative to the PD32 cells were identified using SICER and DiffBind and represented graphically as a track of black bars plotted along the bottom of the Genome Browser window. Remarkably, both of the PD86 H4K20me3 tracks exhibited an extensive cluster of H4K20me3 enrichment

spanning nearly 5 megabases and located within the 19p12 locus (Figure 5.7b, indicated by the orange box). Similar clusters of robust H4K20me3 enrichment were also present at several additional regions of chromosome 19.

Several regions located within the p13.11-p12 locus of chromosome 19 displayed high levels of H4K20me3 enrichment in the PD86 replicates. Consequently, this region was selected for visualization at a higher resolution. While no enrichment was observed in this 4.4 Mb region for the PD32 and PD86 input and histone H4 ChIP samples, marked H4K20me3 enrichment (ranging from 2- to 5-fold over background) was present in both PD86 replicates (Figure 5.8b). Domains of H4K20me3 enrichment in the PD86 versus PD32 replicates were confirmed using SICER and DiffBind and plotted graphically as a track of black bars along the bottom of the Genome Browser window. Surprisingly, whereas the initial comparison of PD86-specific H4K20me3 enrichment to defined genomic features indicated that H4K20me3 frequently resided within intergenic regions (Figure 5.5), the H4K20me3 enrichment observed in the PD86 replicates with the 19p13.11-p12 locus seemingly occurred at a genic region (Figure 5.8b). Intriguingly, although numerous genes were present within this locus, much of the H4K20me3 enrichment appeared to localize to a specific cluster of ZNF genes.

Given that the PD86 replicates exhibited considerable H4K20me3 enrichment across multiple regions of chromosome 19 and appeared to localize to genes, it was important to inspect these regions at a higher resolution. To accomplish this, a 97-kilobase region of chromosome 19 containing PD86-specific H4K20me3 enrichment was selected for visualization using the UCSC Genome Browser (Figure 5.9). At this resolution, three distinct genes (ZNF563, ZNF442, ZNF799) were visible and each displayed a PD86-specific accumulation of H4K20me3 reads within the gene body, as evident in the bigWig tracks and black SICER/DiffBind bars (Figure 5.9b). Although some of the H4K20me3 reads occurred within the intergenic regions adjacent to the genes, for each gene the most abundant accumulation of H4K20me3 reads existed within the gene body, particularly toward the 3' end. This strongly suggests that the domains of H4K20me3 enrichment in the PD86 samples likely originate within the gene bodies and extend into the adjacent intergenic regions, rather than the inverse. In order to explore this further, I next decided to evaluate the genomic distribution of H4K20me3 enrichment in the PD86 senescent cells with respect to genes.

**A****B**

**Figure 5.8 H4K20me3 is enriched at discrete regions of chromosome 19.** Uniquely alignable reads from proliferating (PD32) and senescent (PD86) input, histone H4 ChIP and H4K20me3 ChIP samples were visualized with the UCSC Genome Browser. (A) Schematic ideogram of the genomic region being visualized (chromosome 19 p13.11-p12, indicated by the red box). (B) Individual ChIP-Seq bigWig tracks aligned to a 4.4 Mb region of chromosome 19. The y-axis represents total reads. The black bars along the bottom of the viewer represent domains of H4K20me3 differential enrichment (H4K20me3 Diff) as defined by SICER and DiffBind.

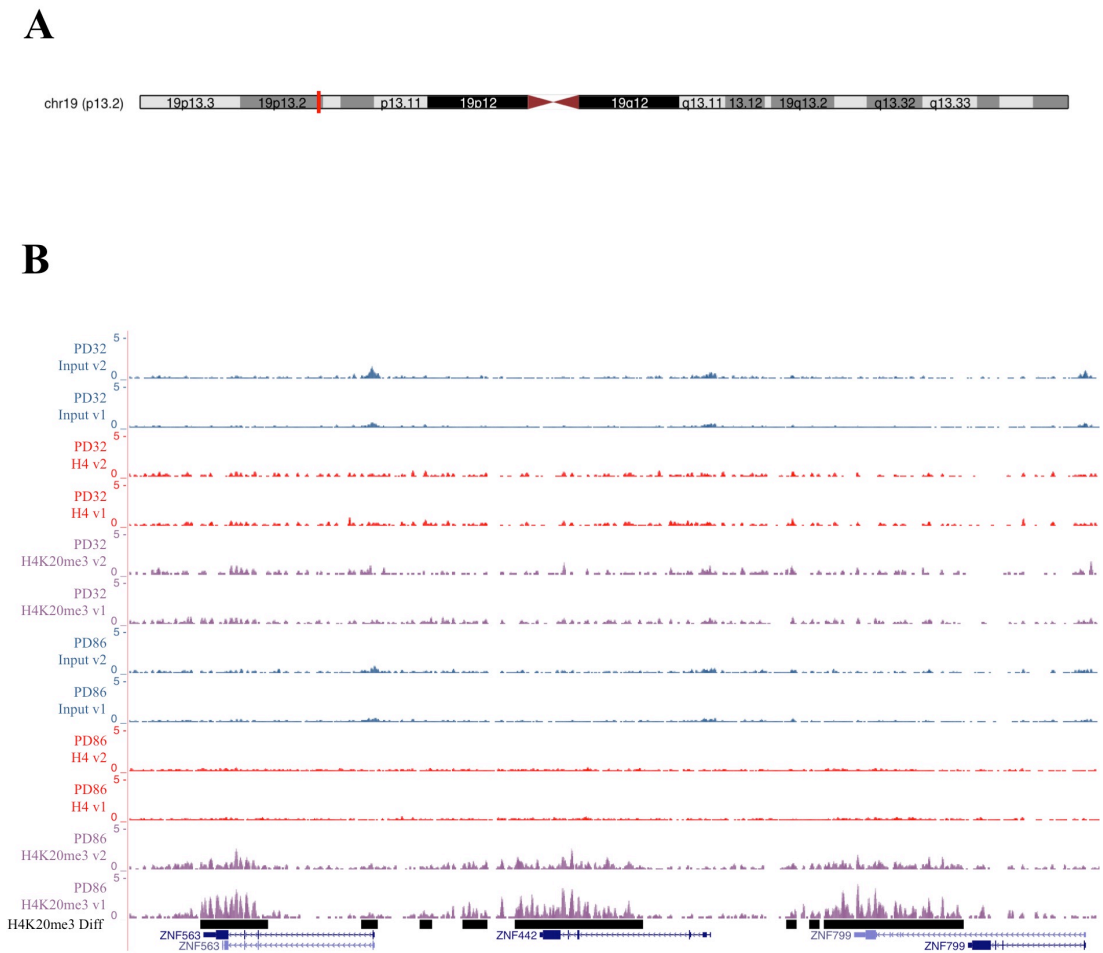


**Figure 5.9 H4K20me3 is enriched at ZNF genes on chromosome 19.** Uniquely alignable reads from proliferating (PD32) and senescent (PD86) input, histone H4 ChIP and H4K20me3 ChIP samples were visualized with the UCSC Genome Browser. (A) Schematic ideogram of the genomic region being visualized (chromosome 19 p13.2, indicated by the red box). (B) Individual ChIP-Seq bigWig tracks aligned to a 97 kb region of chromosome 19. The y-axis represents total reads. The black bars along the bottom of the viewer represent domains of H4K20me3 differential enrichment (H4K20me3 Diff) as defined by SICER and DiffBind.

#### 5.2.4 H4K20me3 Does Not Correlate with Transcriptional Changes

Given that the senescence program is regulated in part through a characteristic set of transcriptional changes, it was important to determine whether H4K20me3 was significantly enriched at specific genes in the PD86 senescent cells. As an extension, it was equally relevant to ask whether there was a correlation between H4K20me3 enrichment at genes and altered expression of those genes. To address this, the H4K20me3 ChIP data were directly compared to the replicative senescence gene expression data obtained from the Affymetrix Human Genome U133 Plus 2.0 microarrays.

In order to visualize any potential correlation between H4K20me3 distribution in senescent cells and gene expression, a scatter plot was generated (Figure 5.10a). Each individual data point represented an individual gene from the array with the relative expression levels of the genes (log of the fold change of senescent versus proliferating) plotted along the x-axis and relative H4K20me3 ChIP Difference plotted along the y-axis. As described in Chapter 2 (Materials and Methods), H4K20me3 ChIP Difference is defined as the senescent (PD86) H4K20me3 ChIP signal minus the proliferating (PD32) H4K20me3 ChIP signal. The respective PD32 and PD86 H4K20me3 ChIP signals were first determined by measuring the number of H4K20me3 reads (extended to 150 bp) within the promoter region of each gene, normalized by the library size, with the corresponding histone H4 library subtracted following similar normalization. For this analysis, the gene promoter was broadly defined as the gene body plus 5 kb upstream and 1 kb downstream of the gene body.

The majority of genes localized to the center of the plot indicating that those genes had neither undergone a change in expression in senescent cells nor contained different levels of the histone H4K20me3 modification in the proliferating and senescent states (Figure 5.10a). While there was a modest shift left along the x-axis for some genes, indicating reduced expression in PD86 senescent cells, these genes clustered around the zero point of the y-axis, revealing no relative H4K20me3 enrichment was present at those genes. Likewise, although some genes contained relatively high enrichment of H4K20me3 in the PD86 senescent cells, these genes remained essentially unchanged at the level of expression and clustered around the zero point of the x-axis. Thus, gain or loss of H4K20me3 at genes does not appear to be tightly linked to activation or repression of gene expression in senescent cells.

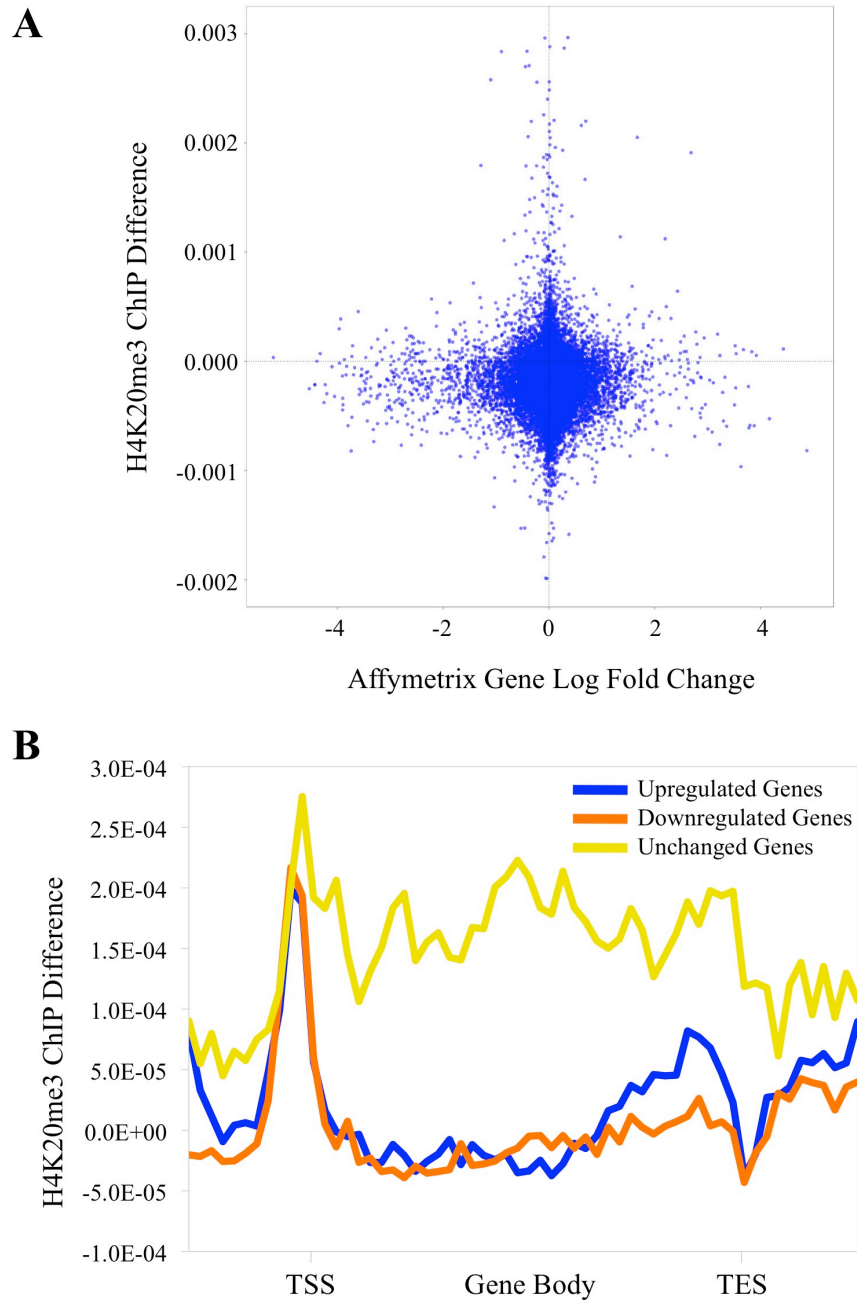


**Figure 5.10 H4K20me3 does not correlate with gene expression changes.** (A) Scatter plot comparing H4K20me3 ChIP difference and gene expression values from the RS microarray. X-axis: expression values plotted as log fold change; y-axis: H4K20me3 ChIP Difference, defined as senescent (PD86) H4K20me3 ChIP signal minus the proliferating (PD32) H4K20me3 ChIP signal. PD32 and PD86 H4K20me3 ChIP signals were determined by measuring the number of H4K20me3 reads (extended to 150 bp) within the promoter region of each gene, normalized by the library size, with the corresponding histone H4 library subtracted after similar normalization. (B) Composite gene profiles of average H4K20me3 enrichment across three classes of genes: genes upregulated, downregulated or unchanged in senescence. x-axis: position along the gene spanning from 5 kb upstream of the gene to the transcription start site (TSS), through the gene body and 5 kb downstream of the gene from the transcription end site (TES). y-axis: H4K20me3 ChIP Difference.

Interestingly, a subset of genes showed marked enrichment of H4K20me3 but did not change expression between proliferating and senescent cells. It is possible that if more stringent criteria were applied in defining gene promoters then the results might exhibit a different pattern. For example, if gene promoters were more conservatively defined as the TSS +/- 1 kb, it is possible that a stronger correlation between H4K20me3 abundance and gene expression might emerge. Although this analysis was not performed for the present study, it could be useful in evaluating a potential role for H4K20me3 in the regulation of gene expression in senescent cells.

To investigate the relationship between H4K20me3 and gene expression in senescent cells further, all of the genes from the replicative senescence microarray dataset were categorized into one of three classes: those that were upregulated in senescence, those that were downregulated in senescence and those that remained unchanged. As before, the expression changes were considered significant if the fold difference between proliferating and senescent cells exceeded 1.5 fold (or less than -1.5 fold) and the BH-FDR adjusted p-value was less than 0.05. Using these lists of genes, composite gene profiles were generated for each of the three groups.

To generate composite gene profiles, the gene body for each gene from the respective lists was divided into forty equally sized compartments and then queried for H4K20me3 ChIP Difference within each compartment. This enabled comparison of H4K20me3 distribution along genes while accounting for variations in gene length. Gene body was defined as any sequence that occurred between the transcription start site (TSS) and transcription end site (TES) of each gene. In addition, 5 kb of sequence up- and downstream of the gene body was also included in the analysis. Upon assembly of the three composite genes (e.g., upregulated, downregulated and unchanged), the compartments within each composite gene were interrogated for the level of H4K20me3 ChIP Difference. As with the analysis in Figure 5.10a, H4K20me3 ChIP Difference was defined as senescent (PD86) H4K20me3 ChIP signal (normalized for library size and histone H4 signal) minus the proliferating (PD32) H4K20me3 ChIP signal (normalized for library size and histone H4 signal). Mean H4K20me3 ChIP Difference was calculated within each compartment of the respective composite genes and plotted graphically.

As displayed in Figure 5.10b, the composite gene profiles of H4K20me3 distribution across the upregulated and downregulated genes were essentially identical, with modest levels of H4K20me3 present around the TSS and TES,

respectively. The fact that H4K20me3 abundance was comparable at both the upregulated and downregulated genes again confirmed that no obvious functional relationship existed between the histone mark and expression of those genes. Interestingly, as in the previous analysis, the set of genes that remained unchanged between proliferating and senescent cells exhibited the highest average levels of H4K20me3 ChIP Difference. Although data from only the first ChIP-Seq experiment were presented here, the composite gene profiles were nearly identical for the second experiment.

One potential caveat to the interpretation of the composite gene profiles presented in Figure 5.10b is that not every gene from the microarray overlapped with a domain of H4K20me3 enrichment. Because the composite gene profiles represent the mean H4K20me3 ChIP Difference within the respective gene categories and there are likely numerous genes within each category devoid of H4K20me3 signal, the plots potentially underestimate the distribution of the mark. For example, if the composite gene profiles were generated for only those genes which contained overlap with SICER/DiffBind defined domains of H4K20me3 enrichment, the profiles would likely provide a better representation of H4K20me3 distribution across the three categories of genes in senescent cells. This approach would undoubtedly increase the overall mean H4K20me3 enrichment observed for the respective profiles, with the greatest increase likely occurring in the profile of the unchanged genes (based on Figure 5.10a). However, it is difficult to predict whether specific features of the composite gene profiles, such as the observed peaks at the TSS and TES, would become even more evident using only genes that overlap with the SICER/DiffBind defined H4K20me3 domains.

It should also be noted that the H4K20me3 peaks present at the TSS of the composite gene profiles in Figure 5.10b were surprising. This was particularly unexpected for the profile of upregulated genes, as it has been widely reported that the TSS of active genes is ordinarily largely devoid of nucleosomes (Ozsolak et al., 2007; Schones et al., 2008). As discussed earlier, the H4K20me3 ChIP Difference calculation involves subtraction of PD32 H4K20me3 reads (after normalization to histone H4 reads and library size) from PD86 H4K20me3 reads (after normalization to histone H4 reads and library size). Consequently, any signal observed for H4K20me3 at a histone H4-depleted TSS might be interpreted as a domain of H4K20me3 enrichment after normalization for histone H4. For this reason,

normalization to the respective DNA input samples might reduce any bias generated as a consequence of the histone H4-depleted regions. Although the present analyses were performed using normalization to histone H4, it might be useful to separately normalize to input DNA in order to determine whether H4K20me3 was indeed enriched at the TSS of genes in senescent cells.

### **5.2.5 H4K20me3 is Enriched at ZNF Genes in Senescent Cells**

Although the presence of H4K20me3 in senescent cells did not appear to overtly impact gene expression, it was still important to assess whether the modification was enriched at any specific classes of genes. Significantly, as revealed by the hierarchical clustering analysis (Figure 5.5) and visualized by the UCSC Genome Browser bigWig tracks (Figures 5.7, 5.8 and 5.9), replicative senescent IMR90 cells displayed considerable H4K20me3 enrichment at several distinct clusters of ZNF genes. In order to obtain a more definitive picture of the extent to which H4K20me3 was specifically enriched at ZNF genes, a composite gene approach was again employed to compare H4K20me3 enrichment at ZNF genes versus non-ZNF genes. In order to keep this analysis comparable with the previous comparisons of H4K20me3 enrichment and gene expression, only genes contained on the Affymetrix Human Genome U133 Plus 2.0 were included. In this case, composite genes were generated for two categories of genes: ZNF genes (of which there were 547) and all other non-ZNF genes (of which there were 18,056).

The composite genes were subsequently interrogated for H4K20me3 enrichment in the PD32 proliferating and PD86 senescent ChIP datasets, respectively. It is critical to note that in this case, regions of significant H4K20me3 enrichment were defined in the PD32 and PD86 samples by comparing H4K20me3 reads to the corresponding histone H4 reads from the same ChIP sample. In the PD32 proliferating cells, relatively low levels of H4K20me3 enrichment were observed across the ZNF and non-ZNF composite genes, with only modest H4K20me3 enrichment present around the TSS of the ZNF genes (Figure 5.11a). In the PD86 senescent cells, low levels of H4K20me3 abundance were similarly observed for the non-ZNF genes (Figure 5.11b). In contrast, the PD86 cells exhibited significantly higher levels of H4K20me3 across the entire ZNF composite gene, with considerable enrichment noted at the TSS and increasingly toward the TES. This

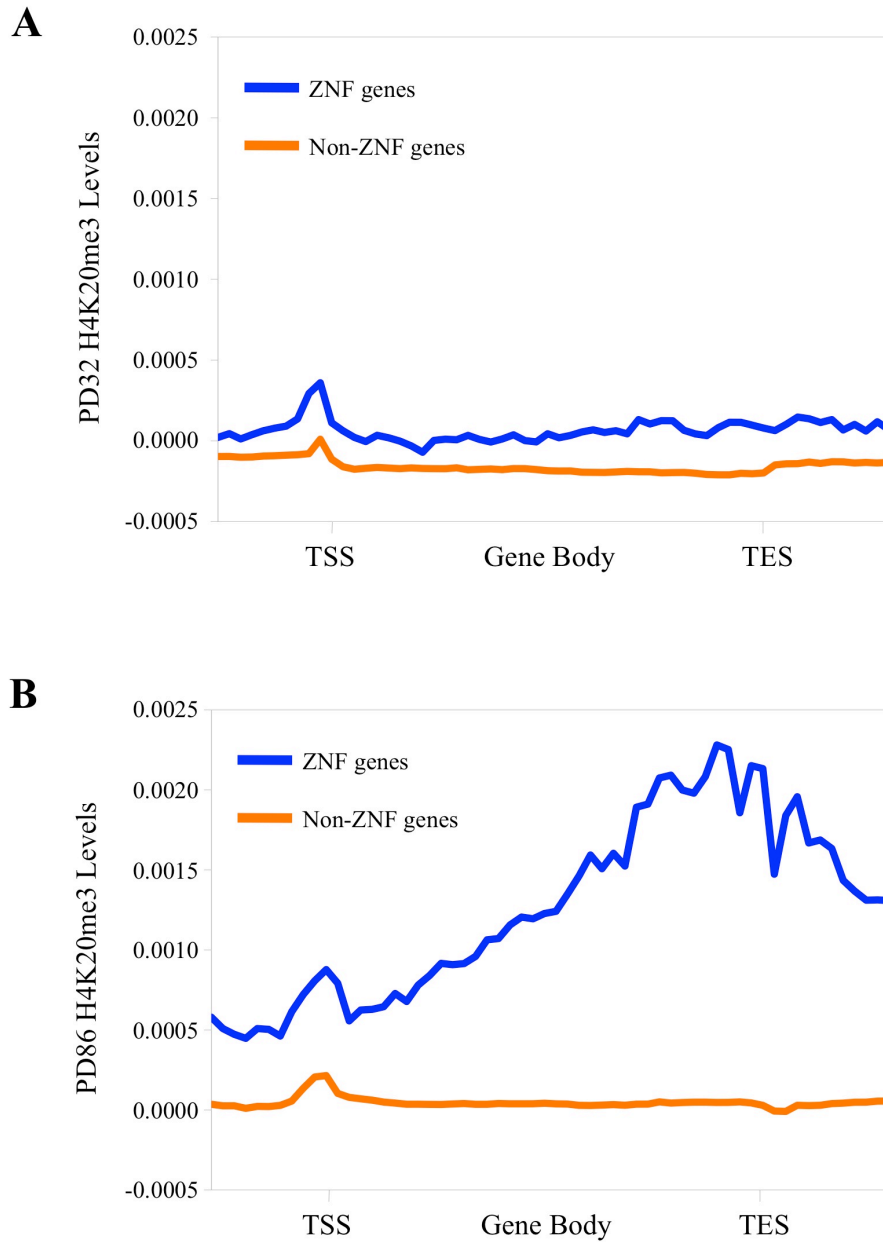


**Figure 5.11 H4K20me3 is specifically enriched at ZNF genes in RS.** Composite gene profiles of average H4K20me3 enrichment over two classes of genes: ZNF genes and all other non-ZFN genes; x-axis: position along the gene spanning from 5 kb upstream of the gene to the transcription start site (TSS), through the gene body and 5 kb downstream of the gene from the transcription end site (TES). y-axis: H4K20me3 abundance. The genes used for the comparison were those contained on the Affymetrix Human Genome U133 Plus 2.0 array. (A) H4K20me3 enrichment across ZNF and non-ZNF genes in PD32 cells. (B) H4K20me3 enrichment across ZNF and non-ZNF genes in PD86 cells.

data strongly suggests that in senescent cells, H4K20me3 is specifically enriched at ZNF finger genes, relative to all other genes.

It is important to note that the current ChIP-seq methodology does not provide a truly quantitative measure between samples, but rather a semi-quantitative measure. While the present analysis can detect differences in the distribution of a given histone modification between samples, it does not provide absolute levels of the modification for the respective samples. Although we did not utilize spike-in controls in the present ChIP-seq experiments, such an approach might provide a method for improving the quantitative capability of the analysis. By incorporating a fixed amount of known DNA into each ChIP sample prior to the library preparation, it is subsequently possible to determine the amount of the spike-in control that is recovered for each library after sequencing and to utilize the percentage of recovered spike-in control to provide a weighting normalization factor for the respective samples. However, one potential caveat of utilizing a spike-in control is that it might alter the complexity of the library sample and potentially be subjected to preferential amplification, thus providing an inaccurate measure of the spike-in recovery. In this case, the PCR amplification efficiency of the known spike-in DNA and sample DNA could not be assumed to be equivalent, ultimately compromising the accuracy of the normalization factor. Despite this caveat, spike-in controls provide a valid approach toward developing a more quantitative ChIP-seq assay and should be considered for future experiments.

In order to provide a more quantitative assessment of the apparent enrichment of H4K20me3 at ZNF genes in senescent cells, it was necessary to calculate the frequency with which the modification was present at ZNF genes relative to all other non-ZNF genes. To accomplish this, ZNF genes and non-ZNF genes were evaluated for H4K20me3 enrichment at the individual base pair level. To this end, the coordinates of H4K20me3 enrichment over histone H4 in PD32 and PD86 cells, respectively, were compared at the coordinates of ZNF and non-ZNF genes and the percentage of gene base pairs that were occupied by H4K20me3 was calculated. For each condition (i.e., PD32 ZNF genes, PD32 non-ZNF genes, PD86 ZNF genes, PD86 non-ZNF genes) the percentage of base pairs that was likely to overlap due to chance was also calculated. In both the PD32 and PD86 cells, H4K20me3 overlapped with a higher percentage of ZNF gene base pairs than non-ZNF gene base pairs, with as much as 14% of all ZNF gene base pairs overlapping with

H4K20me3 in the PD86 senescent cells (Figure 5.12). Importantly, in both the PD32 and PD86 cells, the observed percentage of ZNF gene base pairs overlapping with H4K20me3 exceeded that which might have occurred due to random chance.

### 5.3 Discussion

By mapping the genome-wide distribution of a specific histone modification, it is possible to gain significant insight regarding the mark's contribution to the broader chromatin landscape of the system being studied. Given the dynamic chromatin changes that take place as cells undergo senescence, I set out to further characterize the senescent chromatin state and investigate its role in mediating the senescence program. To this end, I first endeavored to map the genomic distribution of H4K20me3, a histone modification that I had previously demonstrated is selectively retained in senescent cells despite a net reduction of total histone content. In order to accomplish this, I opted to utilize a ChIP-sequencing based methodology, as it could facilitate the rapid acquisition of robust genome-wide sequence data.

Despite significant advances in sequencing technologies, conducting ChIP-Seq experiments is not a trivial technical undertaking and typically requires considerable optimization. As such, great effort was made toward optimizing several of the key ChIP parameters including choice of antibody, sonication time, antibody concentration, chromatin dilution and wash stringency. Following optimization, immunoprecipitation of histone H4 and H4K20me3 was successfully performed on cross-linked chromatin isolated from proliferating and replicative senescent IMR90 cells. Because antibody cross-reactivity is always a concern with any immunological-based assay, the ChIP experiments were performed with two independent H4K20me3 antibodies.

Analysis of the H4K20me3 ChIP-Seq data revealed a markedly altered distribution of H4K20me3 in replicative senescent cells, relative to proliferating cells. Utilizing SICER and DiffBind, 10,786 domains of senescence-specific H4K20me3 differential enrichment were identified. Comparison of these domains to a panel of well-characterized genomic features showed that a large proportion of the H4K20me3-rich domains coincided with various classes of DNA repeats (e.g., LTRs and satellite DNA). Importantly, H4K20me3 enrichment has also been previously reported at regions of repetitive DNA, including satellite repeats (Ernst & Kellis, 2010). Although sequencing reads corresponding to DNA repeats can be difficult to

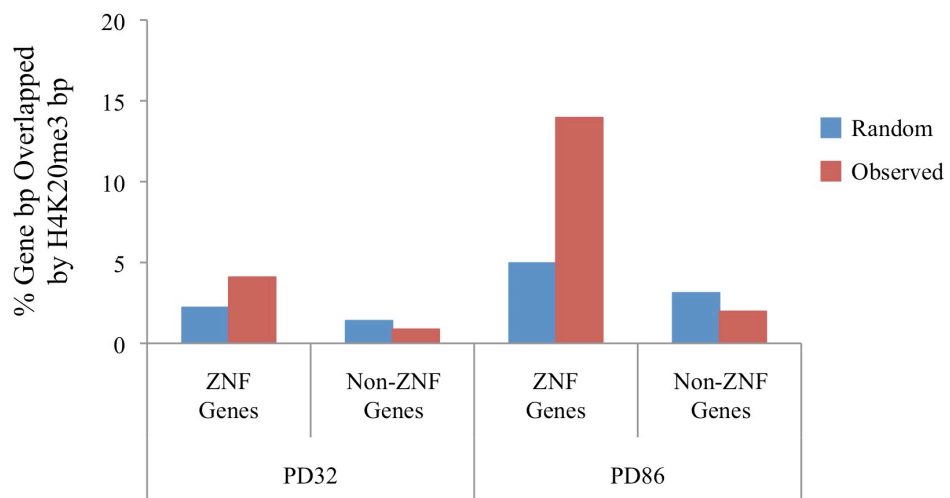


**Figure 5.12 H4K20me3 is highly enriched at ZNF genes.** Determination of the percentage overlap between H4K20me3 peaks and ZNF and non-ZNF genes in proliferating (PD32) and senescent (PD86) cells. Statistically significant H4K20me3 peaks were identified in PD32 and PD86 cells, respectively, by comparison to histone H4 reads. The coordinates of the H4K20me3 peaks were compared to the coordinates of all genes contained on the Affymetrix Human Genome U133 Plus 2.0 array and the percentage of basepair overlap was calculated. The data were plotted as the percentage of total gene basepairs overlapped by H4K20me3 peak basepairs. For each condition, the percentage overlap that was likely to occur by random chance was also calculated.

align uniquely to the human genome and are often excluded from downstream analyses, the inexact and variable composition of DNA repeats allows for some reads to be aligned in an unambiguous manner (Treangen & Salzberg, 2012).

It should be noted that to identify the domains of H4K20me3 differential enrichment, the default settings were utilized for both SICER and DiffBind, as described in Chapter 2 (Materials and Methods). Ideally, by increasing the stringency of the settings it might be possible to improve the accuracy of the H4K20me3 domain calling, while minimizing the false discovery rate. In the present study, the true false discovery rate was not determined, as this would require validation using an independent method such as quantitative PCR performed across hundreds of regions from different positions in the FDR ranking. However, there are several lines of evidence to suggest that SICER/DiffBind defined accurate domains of H4K20me3 enrichment. First, the domains that exhibited the most statistically significant H4K20me3 enrichment coincided with satellite repeats and ZNF genes, two genomic features that have previously been reported to contain H4K20me3 (Barski et al., 2007). In addition, the 10,786 H4K20me3 domains identified by SICER/DiffBind were essentially identical across two separate experiments, performed using independent H4K20me3 antibodies and under different conditions (e.g., normalization to protein in experiment 1, normalization to DNA in experiment 2). Taken together, this provides compelling evidence to suggest that SICER/DiffBind defined accurate domains of H4K20me3 enrichment in senescent cells.

In addition to DNA repeats, H4K20me3 was also present to a lesser degree within genic regions in senescent cells. Because senescence is regulated through a program of well-defined transcriptional changes, it was important to determine whether enrichment of H4K20me3 influenced gene expression in senescent cells. However, no clear correlation between the presence of H4K20me3 and changes in gene expression was observed. This was surprising, as H4K20me3 has previously been reported to contribute toward the establishment of a repressive chromatin state in a variety of contexts. For example, in humans, inactive female X chromosomes are highly enriched for H4K20me3 and additional epigenetic marks of heterochromatin (Chadwick & Willard, 2004). High levels of H4K20me3 have also been observed at imprinting control regions, presumably contributing to monoallelic gene silencing (Henckel et al., 2009; McEwen & Ferguson-Smith, 2010). Likewise, a role for

H4K20me3 in the repression of specific genes has been reported (Donati et al., 2008; Gurtner et al., 2008a; Kwon et al., 2010; Ma et al., 2011; Stender et al., 2012).

Although no direct functional impact on gene expression was observed for H4K20me3, the modification was highly enriched at numerous ZNF genes in senescent cells. In fact, 59% of all ZNF genes exhibited some H4K20me3 enrichment in senescent cells, whereas only 26% of non-ZNF genes contained H4K20me3 overlap. Enrichment of H4K20me3 at ZNF genes has also been previously reported for human CD4<sup>+</sup> T cells (Barski et al., 2007; Ernst & Kellis, 2010). In the absence of any overt role for H4K20me3 in the regulation of gene expression in senescent cells, it is likely that enrichment of H4K20me3 at ZNF genes serves some other functional or structural purpose.

The H4K20me3 modification is an intriguing component of the senescent chromatin landscape. As I demonstrated previously, the histone mark is preferentially retained in senescent cells, despite an overall reduction of histone levels. Building on that observation, I have now shown that H4K20me3 is enriched in senescent cells at distinct regions of the genome, including DNA repeats and the ZNF genes. Although the present analyses do not suggest a direct role for H4K20me3 in the regulation of gene expression, it is entirely plausible that the modification facilitates some other aspect of senescence. To this end, I next set out to investigate whether H4K20me3 contributes functionally to arguably the most important feature of the senescence program: the induction and maintenance of a stable proliferation arrest.

## Chapter 6. Functional Dissection of H4K20me3

### 6.1 Rationale

As established earlier, the chromatin of senescent cells undergoes profound remodeling, characterized in part by a progressive loss of the core histones. However, as evidenced by the H4K20me3 histone modification, it is apparent that not all modified histones behave uniformly during senescence. In replicative senescent cells, levels of histone H4K20me3 remained stable despite a net loss of global histone content. Likewise, in cells induced to senescence by the expression of oncogenic H-RASG12V, H4K20me3 levels remained stable. These findings provide compelling evidence that histone H4 proteins containing trimethylation of lysine 20 are preferentially retained as cells undergo senescence and suggest that this specific histone modification might serve a crucial function in the senescence program. To understand this function, I next set out to manipulate the level of H4K20me3 and assess the impact on cell senescence.

### 6.2 Results

#### 6.2.1 Technical Approaches for Depleting H4K20me3

One of the most effective ways to decipher the molecular function of a protein is to eliminate or reduce its expression and assess any resulting phenotypic changes. To reduce the abundance of an individual histone modification it is first necessary to reduce or eliminate expression of the specific enzyme responsible for the modification. To this end, shRNA-mediated gene silencing can provide an efficient tool for attenuating the expression of a given protein target. The H4K20me3 modification is primarily deposited *in vivo* by the histone methyltransferase SUV420H2. Therefore, in an effort to evaluate the functional contribution of H4K20me3 to the senescence program, I set out to deplete IMR90 cells of SUV420H2 using a lentiviral shRNA approach.

To accomplish this, a complete set of SUV420H2 shRNA clones contained within the pLKO.1 lentiviral expression vector was obtained. Control and SUV420H2 shRNA constructs were transfected into 293T packaging cells, which were used to produce infectious lentiviral particles. The resulting control and

shSUV420H2 lentiviruses were purified by centrifugation and applied to low passage IMR90 cells. The shRNA-infected cells were drug selected and used to prepare whole cell extracts four days after infection. The cell extracts were then fractionated by SDS-PAGE, immobilized to PVDF membranes and subjected to Western blot analysis to assess the efficiency of the SUV420H2 knockdown. Of the five SUV420H2 shRNAs tested, three hairpins efficiently reduced SUV420H2 expression (Figure 6.1). However, although both shSUV420H2 #1 and shSUV420H2 #5 depleted SUV420H2, infection with either virus resulted in considerable cell death (data not shown). Additional SUV420H2 shRNA clones encoded within the pRS retroviral expression vector were also tested for knockdown, but none of the five constructs yielded efficient silencing (data not shown).

It is formally possible that the cell death observed following infection with the shSUV420H2 #1 and shSUV420H2 #5 viruses was a consequence of low infection efficiency, although unlikely as both hairpins markedly reduced SUV420H2 expression. It is also unlikely that a puromycin concentration of 1  $\mu\text{g/ml}$  was too high, as I previously determined that this dose is sufficient to kill uninfected cells within two to three days, but well tolerated by positively infected IMR90 cells (data not shown). Although drug selection can exacerbate the stress associated with viral infection, it simultaneously provides a critical control by ensuring that each target cell has undergone viral transduction. This is particularly important when screening shRNAs for efficient depletion, as without drug selection, low infection efficiencies could be misinterpreted as suboptimal knockdown. Consequently, only the shSUV420H2 #4 construct remained a viable option for reducing SUV420H2 expression.

In order to evaluate whether reduction of H4K20me3 levels would have a functional impact on the senescence program, it was first necessary to establish stable SUV420H2 knockdown cells. Having previously determined that the shSUV420H2 #4 hairpin could effectively reduce SUV420H2, low passage IMR90 cells were infected with either shControl or shSUV420H2 #4 lentiviruses and subjected to drug selection. As before, both the control and shSUV420H2 cells survived drug selection and exhibited morphological features comparable to uninfected IMR90 cells. In order to generate a sufficient number of cells, the respective lines were expanded in culture and maintained under puromycin selection. However, by seven days after infection, most of the shSUV420H2 cells exhibited an

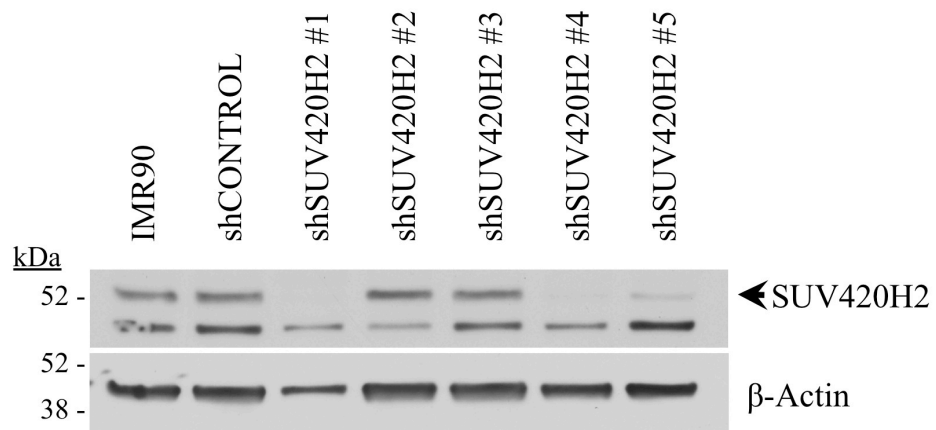


**Figure 6.1 shRNA-mediated knockdown of SUV420H2.** Four days after infection, whole cell extracts were prepared from uninfected cells, shControl-infected cells and cells infected with each of five different shSUV420H2 lentiviruses. The extracts were subsequently fractionated by SDS-PAGE and Western blotted for SUV420H2 and  $\beta$ -actin.

irregular morphology and began to die (Figure 6.2). Most of the control-infected cells continued to survive. Drug selection of IMR90 cells with puromycin typically occurs with rapid kinetics, as all of the uninfected, drug-selected IMR90 cells died within 3 days of treatment. As such, the cell death observed in the shSUV420H2 cells after seven days in culture was likely unrelated to drug selection and was either reflective of a SUV420H2 knock down phenotype or an off-target effect of RNA interference. In the absence of an additional viable SUV420H2 hairpin, it was impossible to distinguish between these two possibilities.

Because the establishment of viable SUV420H2-depleted cells was not initially feasible, an alternative strategy to downregulate the modification was developed. In many cases, ectopic expression of a specific mutant form of a protein may serve as a dominant negative by antagonizing the function of the endogenous wild-type protein. Functionally, SUV420H2 contains two major domains: a 120 amino acid N-terminal SET domain that catalyzes trimethylation of histone H4 at lysine 20 and an 88 amino acid C-terminal domain that is required for recruitment to heterochromatin (Schotta et al., 2004; Souza et al., 2009). In fact, ectopic expression of a SUV420H2 mutant comprised solely of the 88 amino acid heterochromatin recruitment domain is sufficient to target the construct to heterochromatic regions of the genome (Souza et al., 2009). To exploit this for use as a potential dominant negative, an N-terminal truncation mutant of SUV420H2 lacking amino acids 1-280 of the wild-type protein, but still retaining the C-terminal heterochromatin recruitment domain, was cloned into the pBABE retroviral vector along with an N-terminal MYC-tag (pBABE-puro-MYC-SUV420H2 281-462). As a control, a construct encoding MYC-tagged, full-length SUV420H2 was also cloned into pBABE (pBABE-puro-MYC-SUV420H2 1-462) (Figure 6.3a).

In order to address whether SUV420H2 281-462 could function as a dominant negative, early passage IMR90 cells were stably infected with a control retrovirus or retroviruses encoding either full length MYC-SUV420H2 1-462 or the MYC-SUV420H2 281-462 truncation mutant, subjected to drug selection and maintained in culture. The three cell lines survived drug selection, exhibited normal IMR90 morphology and continued to proliferate. Although no overt morphological or proliferation alterations were observed, it was first important to confirm that both the wildtype and mutant SUV420H2 constructs were expressed adequately and localized to the cell nucleus as expected. To this end, each cell line was seeded onto

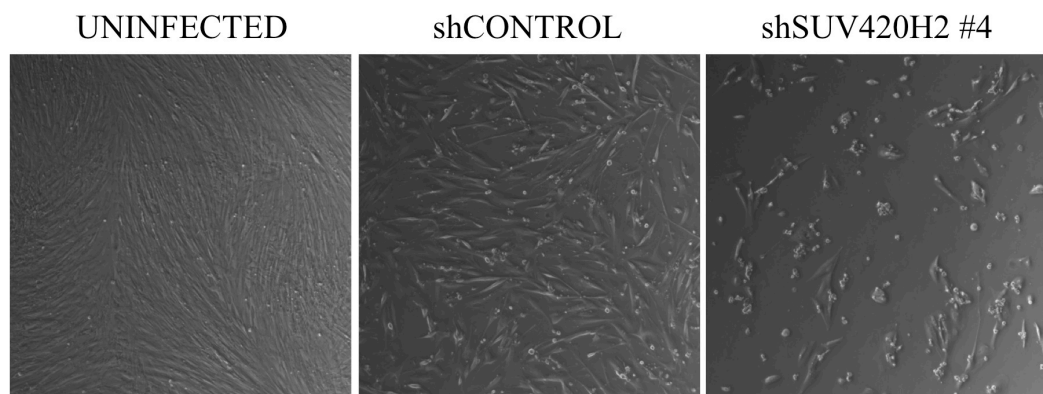


**Figure 6.2 SUV420H2 knockdown cells are not viable.** shControl- and shSUV420H2-infected IMR90 cells were maintained in culture under drug selection for seven days after infection. Uninfected IMR90 cells were maintained in parallel. All images were captured using the 4X objective.

glass coverslips and subjected to indirect immunofluorescence staining to detect expression of the MYC-tagged SUV420H2 constructs as well as the H4K20me3 modification. As anticipated, only a negligible level of background MYC-tag staining was present in the control-infected cells (Figure 6.3b). The control-infected cells also possessed a diffuse nuclear staining pattern for H4K20me3, consistent with that of uninfected, early passage IMR90 cells. In contrast, both the MYC-SUV420H2 1-462 and MYC-SUV420H2 281-462 overexpressing cell lines exhibited marked MYC-tag nuclear staining patterns, containing punctate foci of high signal intensity. The MYC-SUV420H2 1-462 cells showed a similar pattern for H4K20me3, with an overall higher nuclear intensity than the control cells and regions of brightly staining H4K20me3 foci. Intriguingly, in the MYC-SUV420H2 1-462 cells there also appeared to be a high degree of spatial co-localization between the MYC-SUV420H2 1-462 foci and H4K20me3 foci. Although not proven definitively, it is possible that the intensely staining MYC-SUV420H2 1-462 foci reflect recruitment of the enzyme to defined heterochromatic regions of the genome.

Conversely, the MYC-SUV420H2 281-462 overexpressing cells showed a different H4K20me3 staining pattern. Although both the MYC-SUV420H2 1-462 and 281-462 cells contained high levels of ectopic enzyme expression including discrete nuclear foci, the H4K20me3 staining intensity in the MYC-SUV420H2 281-462 cells remained comparable to that of the control cells and lacked discernible foci (Figure 6.3b). This suggests that as predicted, in cells overexpressing MYC-SUV420H2 281-462, the mutant SUV420H2 enzyme is capable of being recruited to defined genomic loci, but incapable of catalyzing the H4K20me3 modification due to absence of the SET domain. Despite this, overexpression of MYC-SUV420H2 281-462 apparently failed to serve a dominant negative function, as the cells retained basal levels of H4K20me3 staining in this assay. It is important to note that while immunofluorescence can provide some insight regarding the relative abundance of the H4K20me3 modification, the assay is inherently non-quantitative and can be artificially influenced by differences in epitope conformation or exposure.

To account for this caveat, whole cell extracts were prepared from control, MYC-SUV420H2 1-462 and MYC-SUV420H2 281-462 cells, fractionated by SDS-PAGE and immobilized to PVDF membranes. The membranes were then assayed by Western blot to assess expression of the ectopic enzymes and the H4K20me3 modification. Consistent with the immunofluorescence data, Western blot analysis

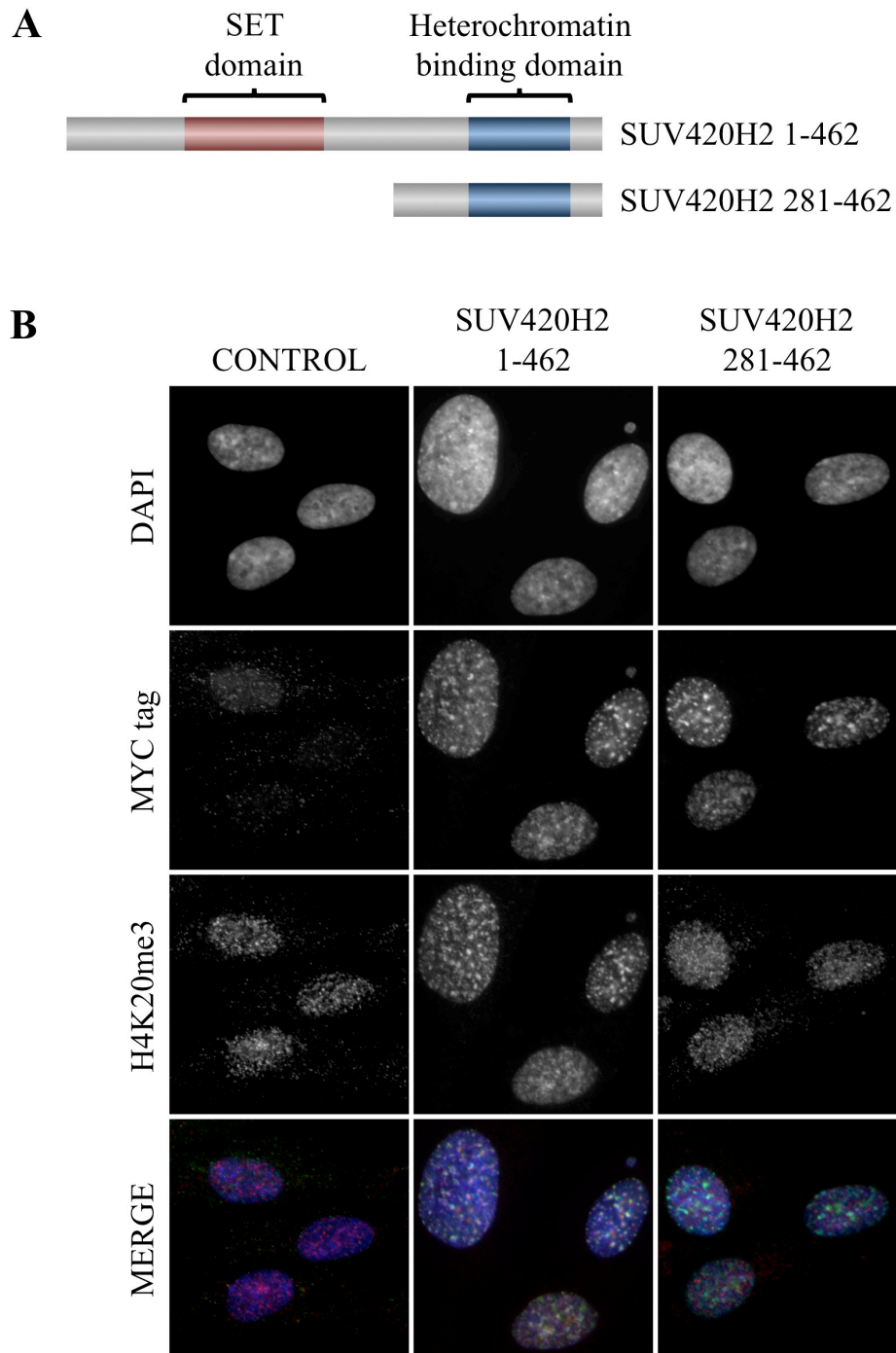


**Figure 6.3 SUV420H2 281-462 expression is insufficient to deplete H4K20me3.** (A) Schematic diagram of the MYC-SUV420H2 constructs. (B) Cells infected with control, MYC-SUV420H2 1-462 or MYC-SUV420H2 281-462 retroviruses were stained with DAPI and antibodies against the MYC tag and H4K20me3. All images were captured at identical exposure settings under the 100X objective.

using an antibody raised against the MYC tag revealed equivalent and robust expression of MYC-SUV420H2 1-462 and MYC-SUV420H2 281-462 in the respective cell lines, and no expression in control cells (Figure 6.4). Also similar to the immunofluorescence findings, the MYC-SUV420H2 1-462 cells contained elevated levels of the H4K20me3 modification compared to control cells. In contrast, cells expressing the mutant MYC-SUV420H2 281-462 exhibited low H4K20me3 levels identical to the basal levels observed in the control cells. A longer exposure of the H4K20me3 Western blot confirmed that although H4K20me3 levels were generally low in the MYC-SUV420H2 281-462 cells, there was no additional reduction of the modification relative to control cells. As a result, the MYC-SUV420H2 281-462 construct does not function in a dominant negative capacity and cannot be utilized to modulate levels of the H4K20me3 modification.

There are several potential explanations that may account for the inability of the MYC-SUV420H2 281-462 construct to function as a dominant negative. First, while both the immunofluorescence and Western blot assays revealed robust expression of the MYC-SUV420H2 281-462 mutant, it is formally possible that the ectopic protein levels were not sufficient to displace or compete with the endogenous wild-type SUV420H2 protein. To this end, neither assay provided any information about the capacity to bind chromatin or the enzymatic activity of endogenous wild-type SUV420H2 in the presence of ectopic MYC-SUV420H2 281-462. Alternatively, truncated MYC-SUV420H2 281-462, although capable of recruitment to heterochromatin, might not retain enough of the full-length protein to compete with other SUV420H2 binding partners. For example, proteins might bind to the SET domain or other N-terminal regions of SUV420H2 to facilitate catalysis of the H4K20me3 modification. Because MYC-SUV420H2 281-462 lacks 280 N-terminal amino acids, the mutant might be unable to efficiently titrate binding partners away from the endogenous enzyme. One way of addressing this would be to introduce a single point mutation within the catalytic SET domain of SUV420H2 that would attenuate histone methyltransferase activity but retain all other functions of the wild-type protein. Finally, it is possible that some degree functional redundancy exists between SUV420H1 and SUV420H2. In this context, even a true dominant negative of SUV420H2 might be insufficient to fully abolish H4K20me3 genome-wide, as SUV420H1 could maintain basal levels of the modification.

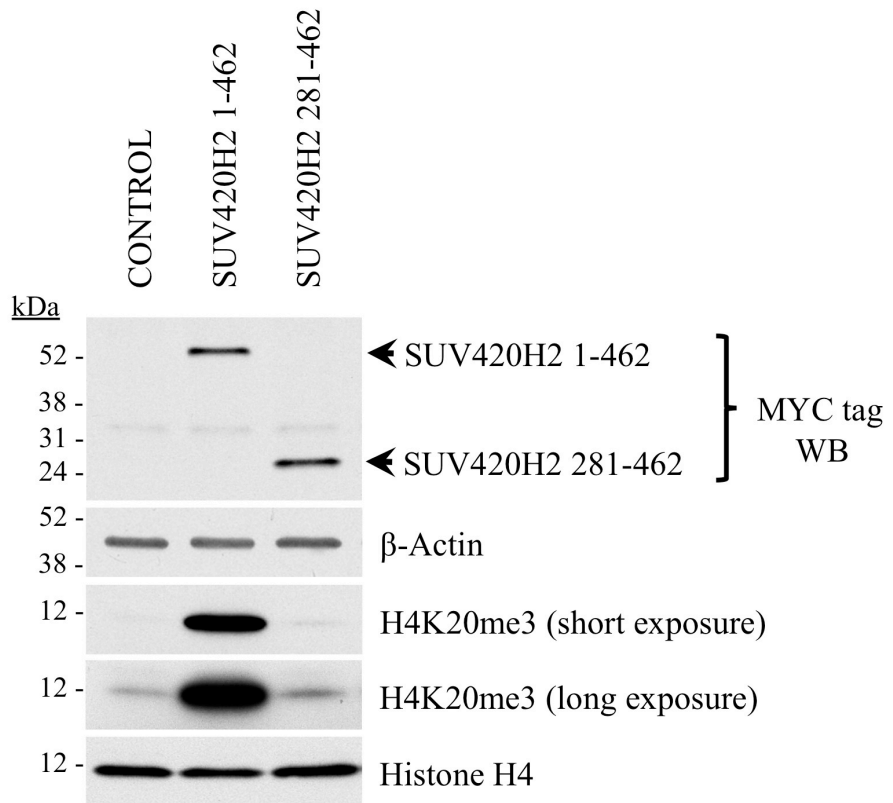


**Figure 6.4 SUV420H2 281-462 expression is insufficient to reduce H4K20me3 levels.** Whole cell lysates were prepared from cells infected with control, MYC-SUV420H2 1-462 or MYC-SUV420H2 281-462 retroviruses. The extracts were fractionated by SDS-PAGE and Western blotted for the MYC tag,  $\beta$ -actin, H4K20me3 and histone H4.

Regardless of the reason for the failure of the dominant negative mutant, to this point I have been unable to devise a strategy to suppress abundance of the H4K20me3 mark in viable cells. In fact, based on the results from shRNA knock down, it is a formal possibility that suppression of H4K20me3 is incompatible with cell viability.

### **6.2.2 MYC-SUV420H2 Cells Proliferate Despite Elevated H4K20me3**

As an alternative approach to functionally assess how H4K20me3 might contribute to the various features of the senescence program, I decided to develop a model system in which H4K20me3 levels could be elevated efficiently. To accomplish this, an additional retroviral plasmid directing the expression of N-terminally MYC-tagged SUV420H1 was generated in pBABE-puro by standard molecular biology procedures. A construct encoding full-length SUV420H2 was described earlier. Early passage IMR90 cells were stably infected with control retrovirus or a retrovirus encoding either N-terminally MYC-tagged SUV420H1 or SUV420H2. The infected cells were maintained under drug selection and monitored microscopically for viability and overall morphologic appearance. Fourteen days after infection, whole cell extracts were prepared from the cells, subjected to fractionation by SDS-PAGE and Western blotted to confirm expression of MYC-SUV420H1 and MYC-SUV420H2 (Figure 6.5a). As anticipated, both MYC-SUV420H1 and MYC-SUV420H2 were expressed to comparable levels and migrated at expected apparent molecular weights of 120 and 52 kDa, respectively.

Whole cell extracts were additionally assayed by Western blot for markers of active cell proliferation and senescence (Figure 6.5a). Cyclin A, a key regulator of the cell cycle that binds to cyclin-dependent kinase 2 (CDK2) and promotes S phase progression, can be utilized as an indicator of cell proliferation. Both MYC-SUV420H1 and MYC-SUV420H2 infected cells exhibited cyclin A expression levels comparable to that of the control cells, suggesting similar levels of proliferation among the respective cell populations. In contrast, cells infected in parallel with a retroviral construct encoding H-RASG12V showed a marked reduction in cyclin A expression, indicating a considerable decrease in the number of proliferating cells in the population, as expected in association with H-RASG12V-induced senescence.

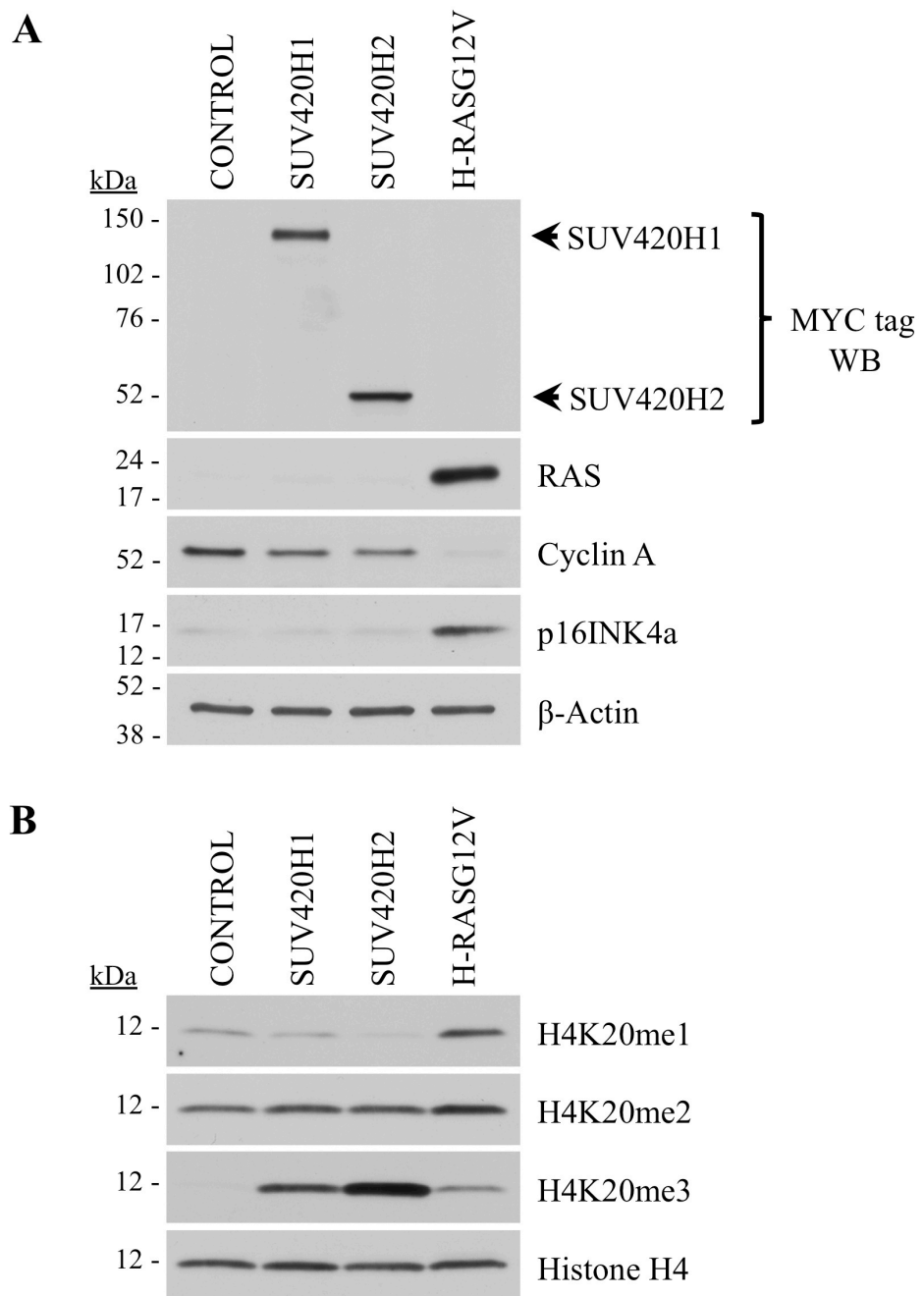


**Figure 6.5 MYC-SUV420H1 and MYC-SUV420H2 increase H4K20me3 but do not induce cell cycle arrest.** Whole cell lysates were prepared from cells infected with control, MYC-SUV420H1, MYC-SUV420H2 or H-RASG12V retroviruses. (A) Extracts were fractionated and Western blotted for proliferation and senescence markers. (B) Extracts were fractionated and Western blotted for histone H4 and H4K20 modifications.

The tumor suppressor protein p16INK4a blocks cell cycle progression through inhibition of cyclin D/CDK4 and CDK6 activity, and is commonly used as a senescence biomarker (Alcorta et al., 1996; Serrano et al., 1997). In order to further evaluate the proliferative status of the MYC-SUV420H1 and MYC-SUV420H2 overexpressing cells, the lysates were Western blotted for p16INK4a. Whereas H-RASG12V infected cells showed a robust increase in p16INK4a expression linked to induction of senescence, the control, MYC-SUV420H1 and MYC-SUV420H2 cells maintained minimal levels of expression (Figure 6.5a).

Consistent with continued expression of cyclin A and failure to upregulate p16INK4a, MYC-SUV420H1 and MYC-SUV420H2 over-expressing cells showed no proliferative impairment compared to control infected cells, as judged by cell counting and cumulative population doublings. Collectively these data affirm that cells ectopically expressing SUV420H1 or SUV420H2 are viable, maintain proliferative capacity in the short-term and do not undergo immediate senescence.

Before SUV420H1 or SUV420H2 overexpression could be considered a relevant model with which to dissect the functional contribution of H4K20me3 to senescence, it was essential to confirm that the H4K20me3 histone modification was appropriately modulated in the cells. Whole cell extracts obtained from control, MYC-SUV420H1, MYC-SUV420H2 and H-RASG12V-infected cells were titrated such that an equal amount of histone H4 from each sample was fractionated by SDS-PAGE. The blots were subsequently probed with antibodies to detect total histone H4 as well as the H4K20me1, H4K20me2 and H4K20me3 modifications of histone H4 (Figure 6.5b). While H4K20me3 levels were markedly elevated in H-RASG12V-infected senescent cells, an even more robust increase of lysine 20 trimethylation was observed upon SUV420H1 and SUV420H2 overexpression, with the highest levels occurring in the MYC-SUV420H2 cells. Although H4K20me2 levels remained largely unaffected in all of the cell lines, a marked decrease in the H4K20me1 modification was also noted in the MYC-SUV420H2 cells.

To further characterize the MYC-SUV420H1 and MYC-SUV420H2 cells, the localization patterns of the MYC-tagged SUV420H enzymes and H4K20me3 modification were evaluated by indirect immunofluorescence microscopy. Control, MYC-SUV420H1 and MYC-SUV420H2 cells were stained with DAPI and antibodies to detect the MYC tag and H4K20me3. Control cells exhibited an even nuclear DAPI staining pattern, no staining with the MYC tag antibody and a diffuse

granular nuclear pattern for H4K20me3 (Figure 6.6). MYC-SUV420H1 cells contained an even DAPI staining pattern and strong yet largely diffuse nuclear signals for both the MYC-tagged SUV420H1 and H4K20me3. In contrast, the MYC-SUV420H2 cells were characterized by a generally even nuclear DAPI pattern with some subtle foci present and intense punctate staining patterns for both the MYC-tagged SUV420H2 enzyme and the H4K20me3 modification. As evident in the merged image, a high degree of co-localization occurred between the ectopically expressed SUV420H2 and H4K20me3 in the MYC-SUV420H2 cells, suggesting that either SUV420H2 remains at sites where the histone mark has been deposited or the modification undergoes rapid turnover and the enzyme co-localizes to the newly deposited mark.

Although not investigated here, it is formally possible that the subtle DAPI-rich foci present in the MYC-SUV420H2 cells might represent SAHF-like heterochromatic structures. Functional roles for SAHF in reinforcing senescence by silencing proliferation-promoting genes and dampening the DNA damage response have been proposed (Narita et al., 2003; Di Micco et al., 2011). However, it is unlikely that the DAPI-rich foci in the MYC-SUV420H2 cells reflect the formation of bona fide SAHF, as the cells failed to exhibit any overt proliferation defect or express the senescence biomarker p16INK4a (Figure 6.5, panel A). Whether the MYC-SUV420H2 cells exhibit an altered DNA damage response, another putative function of SAHF, has not been evaluated in the present study but could prove useful in the subsequent characterization of these cells. Consequently, based on the present data it is not possible to conclude whether the subtle DAPI foci in the MYC-SUV420H2 cells reflect true SAHF formation.

Alternatively, the MYC-SUV420H2 cell DAPI foci might coincide with centromeric or telomeric constitutive heterochromatin. To this end, the potential co-localization of the MYC-SUV420H2 DAPI foci with domains of constitutive heterochromatin could be evaluated using immunofluorescence staining for defined heterochromatin features (e.g., H3K9me3, HP1 proteins) (Richards & Elgin, 2002). Finally, in order to further delineate the specific nature of the DAPI foci in the MYC-SUV420H2 cells, fluorescence *in situ* hybridization (FISH) could be performed utilizing centromere and telomere-specific probes. Likewise, the DAPI-rich foci could be assayed for co-localization with centromeres and telomeres through immunofluorescence staining with antibodies to detect either centromere-specific

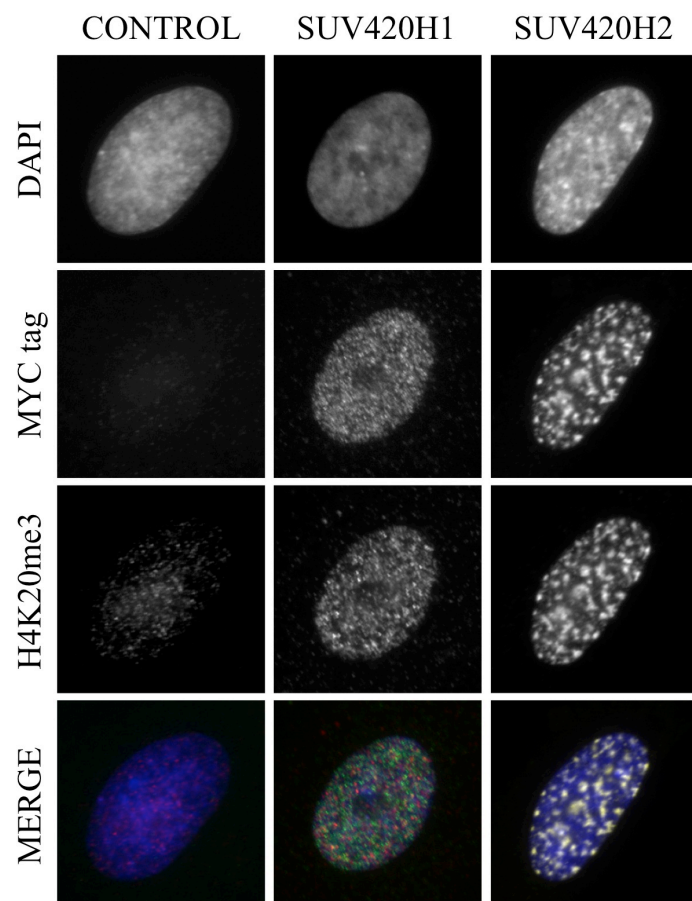


**Figure 6.6 MYC-SUV420H1 and MYC-SUV420H2 exhibit distinct nuclear staining patterns.** IMR90 cells infected with either control, MYC-SUV420H1 or MYC-SUV420H2 retroviruses were stained with DAPI and antibodies against the MYC tag and H4K20me3. All images were captured at identical exposure settings under the 100X objective.

(e.g., CENPA) or telomere-specific (e.g., TRF2) proteins (Palmer et al., 1987; Smogorzewska et al., 2000). Although not conducted as part of the present study, these additional data might enhance the characterization of the MYC-SUV420H2 cells as a model system.

Regardless, based on the combined Western blot and immunofluorescence analyses of the MYC-SUV420H1 and MYC-SUV420H2 cells, both lines were capable of increasing levels of the H4K20me3 modification and could therefore be utilized as appropriate model systems. Although both of the overexpressing cell lines elevated H4K20me3 abundance well above the basal levels observed in control cells, the MYC-SUV420H2 cells consistently yielded the highest levels of H4K20me3. Additionally, the apparent differences in H4K20me3 localization patterns in the MYC-SUV420H1 and MYC-SUV420H2 cell lines might indicate that while SUV420H1 appears capable of catalyzing H4K20me3 uniformly across the genome, SUV420H2 might deposit the modification at specifically defined genomic regions.

### **6.2.3 SUV420H2 Overexpression Accelerates Senescence Onset**

Since the relative abundance of H4K20me3 is increased in senescent cells compared to total histone H4, I set out to determine whether elevated levels of H4K20me3 exert an effect on cellular senescence. In order to address this, control, MYC-SUV420H1 and MYC-SUV420H2 cells were exposed to either of two well-defined triggers of senescence *in vitro*, prolonged passage in culture or ectopic expression of an activated oncogene, and evaluated for effects on senescence.

To evaluate what effect an elevated level of H4K20me3 would have on cellular lifespan, early passage IMR90 cells were stably infected with a control retrovirus or viruses encoding either MYC-SUV420H1 or MYC-SUV420H2. Positively infected cells were maintained under drug selection and subjected to serial passage in culture. At every passage, the cells were counted and the number of population doublings calculated using the following equation:  $[\log(\text{number of cells counted}) - \log(\text{number of cells plated})] / \log(2)$ . Importantly, and consistent with previous short-term experiments, the control, MYC-SUV420H1 and MYC-SUV420H2 cells exhibited nearly identical population doubling times for approximately the first 70 days in culture (Figure 6.7). This confirms that elevation of H4K20me3 is not acutely stressful or toxic to the cells. However, beginning around 80 days in culture, a noticeable slowing of population doubling time was

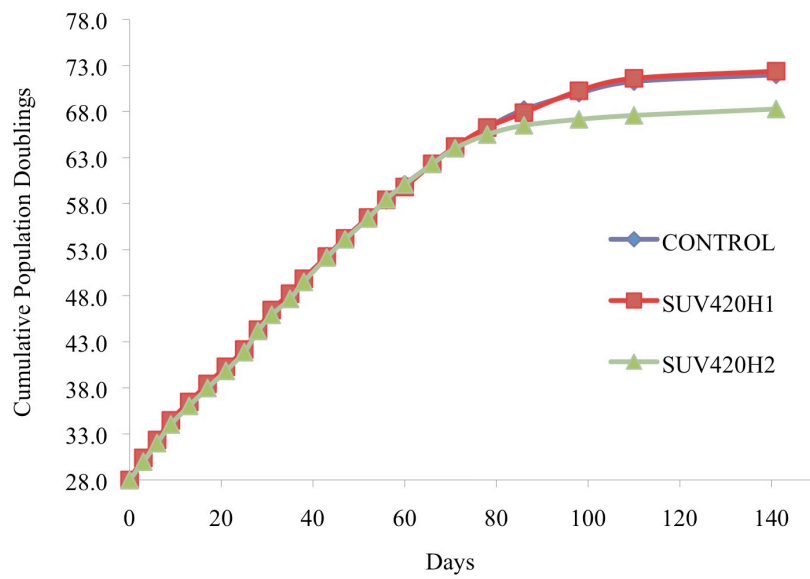


**Figure 6.7 MYC-SUV420H2 accelerates the onset of senescence.** Low passage IMR90 cells were infected with control, MYC-SUV420H1 or MYC-SUV420H2 retroviruses, subjected to drug selection and maintained in culture under low (3%) O<sub>2</sub> conditions. Cells were cultured under drug selection for the remainder of the experiment. At each passage, cells were counted, the cumulative population doublings calculated and plotted graphically. For each condition, the curves reflect the mean of three independent infections.

observed in the MYC-SUV420H2 cells, while the control and MYC-SUV420H2 continued to divide at comparable rates. MYC-SUV420H2 cells reached a proliferative plateau at 86 days, ultimately manifesting in a four cumulative population doublings advanced onset of senescence in the MYC-SUV420H2 cells compared to the control and MYC-SUV420H1 cells. These data indicate that while a high level of the H4K20me3 modification is not sufficient to drive an immediate cell cycle exit, increased abundance of the mark does accelerate proliferation arrest in the context of replicative senescence.

Next, I asked whether a SUV420H2 mediated increase in H4K20me3 could elicit a similar effect on senescence induced by an activated oncogene. To this end, early passage control, MYC-SUV420H1 and MYC-SUV420H2 cells were infected with either a control retrovirus or a virus encoding oncogenic H-RASG12V and assayed for expression of SA  $\beta$ -gal, a marker of senescence, 14 days after infection. Importantly, in the absence of H-RASG12V, neither the MYC-SUV420H1 nor MYC-SUV420H2 showed elevated SA  $\beta$ -gal, supporting the previous conclusion that elevated H4K20me3 does not inappropriately stress the cells. In contrast, nearly all of the H-RASG12V-infected control, MYC-SUV420H1 and MYC-SUV420H2 cells stained positively for SA  $\beta$ -gal activity (Figure 6.8). The MYC-SUV420H2 + H-RASG12V cells revealed a subtle yet consistently higher SA  $\beta$ -gal staining intensity compared to SUV420H1 + H-RASG12V and control + H-RASG12V, possibly reflecting an increased lysosomal compartment in the cells, an enhanced senescence or a combination thereof. Importantly, it is unlikely that the observed differences in SA  $\beta$ -gal activity among the H-RASG12V-infected control, MYC-SUV420H1 and MYC-SUV420H2 cells were due to variations in the multiplicity of infection (MOI), as the respective cell lines were all infected with equal volumes of the same H-RASG12V viral stock. Similarly, no cell death was noted following puromycin selection of the H-RASG12V-infected control, MYC-SUV420H1 and MYC-SUV420H2 cells, indicating a sufficient and comparable MOI for each of the respective infections.

To better characterize the senescence program, whole cell extracts prepared from the same cells were fractionated by SDS-PAGE and probed for markers of proliferation and senescence. As anticipated, both MYC-SUV420H1 and MYC-SUV420H2 were expressed abundantly in the respective cell lines, resulting in a robust elevation of H4K20me3 levels in the MYC-SUV420H2 cells and a more

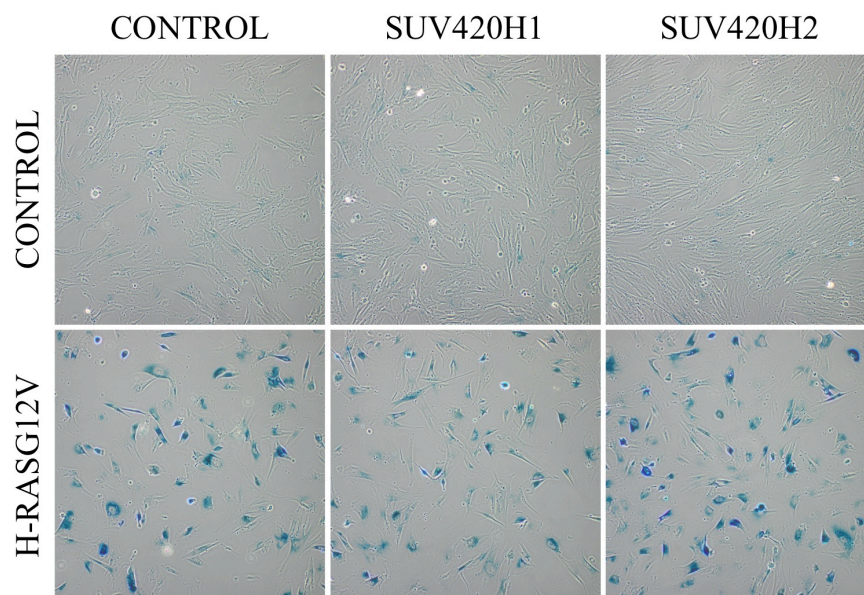


**Figure 6.8 H-RASG12V-infected MYC-SUV420H2 cells exhibit enhanced senescence.** Control, MYC-SUV420H1 and MYC-SUV420H2 cells were infected with control or H-RASG12V retroviruses, drug selected and maintained in culture. Fourteen days after infection the cells were subjected to SA  $\beta$ -gal staining, visualized by bright field microscopy under the 4X objective and photographed.

modest increase in the MYC-SUV420H1 cells (Figure 6.9). Consistent with previous findings, both total histone H4 and lamin B1 levels dropped precipitously in all three of the H-RASG12V-infected cell lines. Cyclin A expression and pRB phosphorylation (judged by the slower mobility of the hyperphosphorylated form), two biochemical indices of cell proliferation, were also reduced significantly in all of the H-RASG12V infected cells. However, longer exposures of the cyclin A and pRB Western blots revealed marked differences in the degree to which these proteins were regulated in the H-RASG12V expressing cells, with and without MYC-SUV420H2. Although low but detectable levels of cyclin A and phosphorylated pRB were observed in the H-RASG12V + control or MYC-SUV420H1 cells, cyclin A was essentially undetectable and pRB almost entirely in the unphosphorylated form in the H-RASG12V + MYC-SUV420H2 cells (Figure 6.9). Likewise, while p16INK4a induction occurred in all three H-RASG12V infected cell lines, absolute levels were slightly higher in the MYC-SUV420H2 cells.

To summarize, in both the replicative and oncogene-induced models of senescence, the MYC-SUV420H2 cells consistently exhibited either an accelerated onset or enhanced senescence compared to the control or MYC-SUV420H1 cells. This accelerated or enhanced senescence in the MYC-SUV420H2 cells was evident through multiple parameters, including the precise measurement of population doublings prior to replicative senescence, a reduction in proliferation indicators (i.e. cyclin A expression, pRB phosphorylation) and the induction of senescence markers (i.e. SA  $\beta$ -gal activity, p16INK4a expression). Importantly, elevated H4K20me3 levels mediated by SUV420H2 overexpression, but not SUV420H1 overexpression, appears to be critical for driving the accelerated senescent phenotype. However, it is difficult to distinguish whether this is due to the fact that H4K20me3 is increased to higher levels in the MYC-SUV420H2 cells than in the MYC-SUV420H1 cells, or whether the two enzymes deposit the H4K20me3 modification at different regions of the genome, thus exerting variable effects, or perhaps another non-histone substrate of SUV420H2. Regardless, collectively, these data support the hypothesis that although a high level of H4K20me3 is not sufficient to induce frank and immediate cell senescence, the modification does promote the onset of senescence in response to detrimental factors, including telomere attrition or an activated oncogene.

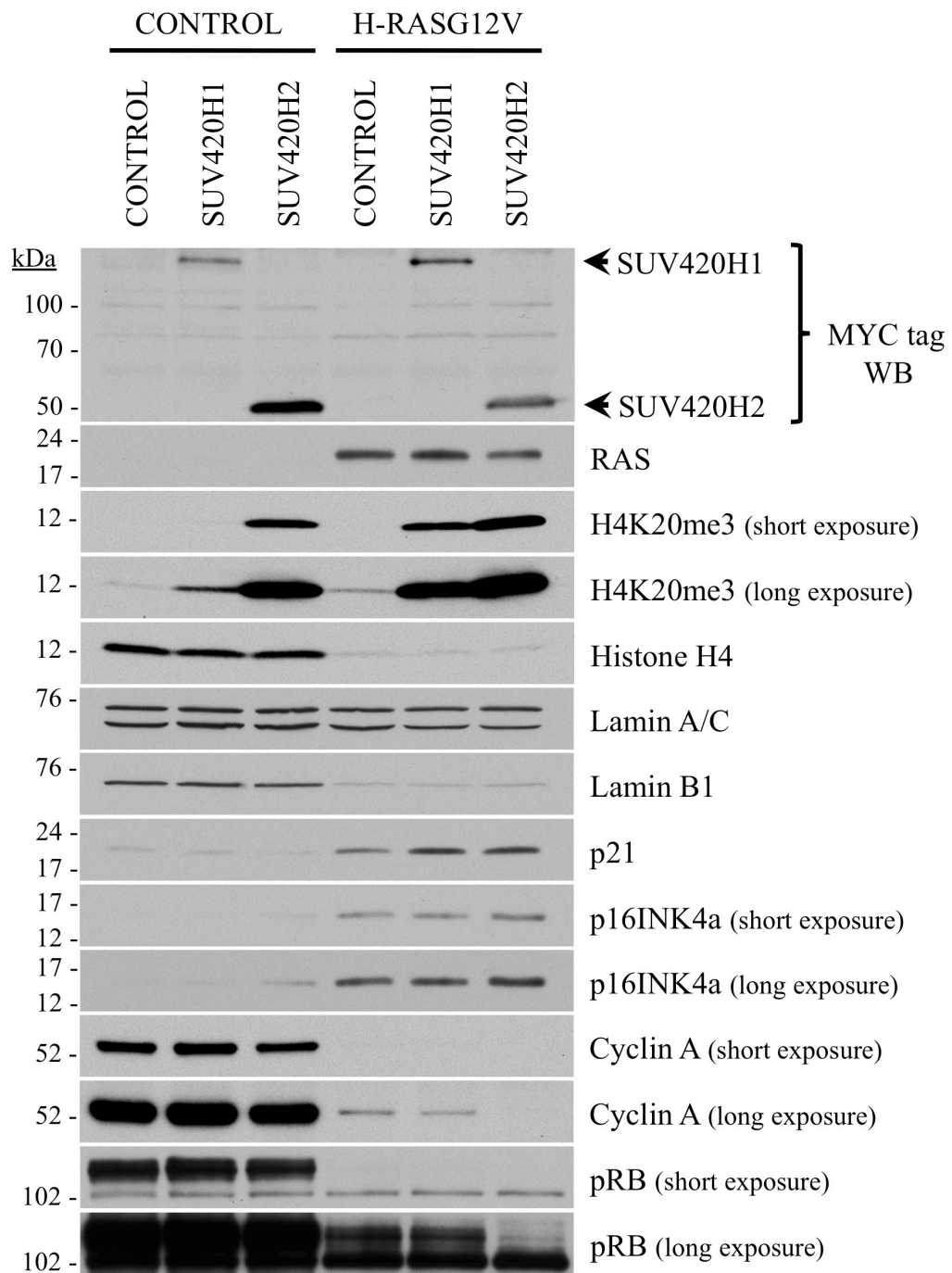


**Figure 6.9 MYC-SUV420H2 enhances H-RASG12V-induced senescence.** Control, MYC-SUV420H1 and MYC-SUV420H2 cells were infected with control or H-RASG12V retroviruses. Whole cell extracts were prepared 14 days after infection, fractionated by SDS-PAGE and Western blotted for a panel of proliferation and senescence markers.

#### 6.2.4 SUV420H2 Protects Against Senescence Escape

Although the MYC-SUV420H2 cells exhibited an enhanced senescent phenotype upon exposure to H-RASG12V compared to H-RASG12V-infected control or MYC-SUV420H1 cells, the experiment relied on assessment of senescence at a fixed endpoint and failed to provide insight regarding the kinetics of the proliferation arrest. To compare the kinetics of entry into senescence, control and MYC-SUV420H2 cells were infected with control or H-RASG12V retroviruses and assayed by Western blot for senescence markers at regular intervals post infection. As expected, high levels of ectopic MYC-SUV420H2 and the resulting H4K20me3 modification were maintained for the duration of the timecourse (Figure 6.10). H-RASG12V was expressed at high levels in both the control and MYC-SUV420H2 cells and also sustained for the entire length of the experiment. As described previously, a marked reduction of total histone H4 was observed by day 5 of H-RASG12V exposure in both the control and MYC-SUV420H2 cells and continued to progress as the timecourse proceeded. By day 10 of H-RASG12V infection, histone levels were depleted to comparable levels in both the control and MYC-SUV420H2 cell lines. However, by the 15-day H-RASG12V timepoint, histone H4 levels appeared to rebound in the control cells, but not in the MYC-SUV420H2 cells. Also by 5 days of H-RASG12V exposure, both the control and MYC-SUV420H2 cells exhibited a considerable reduction in cyclin A expression and p16INK4a induction, consistent with cell cycle exit and the onset of senescence. Similar to the histone H4 kinetics, in the H-RASG12V-infected control cells but not the MYC-SUV420H2 cells, cyclin A levels began to increase around the 15-day timepoint. This partial restoration of proliferation in the H-RASG12V-infected control cells was also accompanied by a decrease in p16INK4a expression. Together, these results indicate that the control cells infected with H-RASG12V had partially bypassed or escaped the senescence-associated proliferation arrest, whereas the MYC-SUV420H2 cells appeared to maintain the senescent state.

The concept that some cells are capable of either escaping or bypassing the H-RASG12V-induced senescence arrest *in vitro* has been previously documented (Kohsaka et al., 2011). Consistent with this, a subset of the control cells infected with H-RASG12V appeared to resume proliferation approximately 15 days after infection. In contrast, H-RASG12V infected MYC-SUV420H2 cells appeared to maintain a more stable proliferation arrest. In order to track the progression of the H-RASG12V

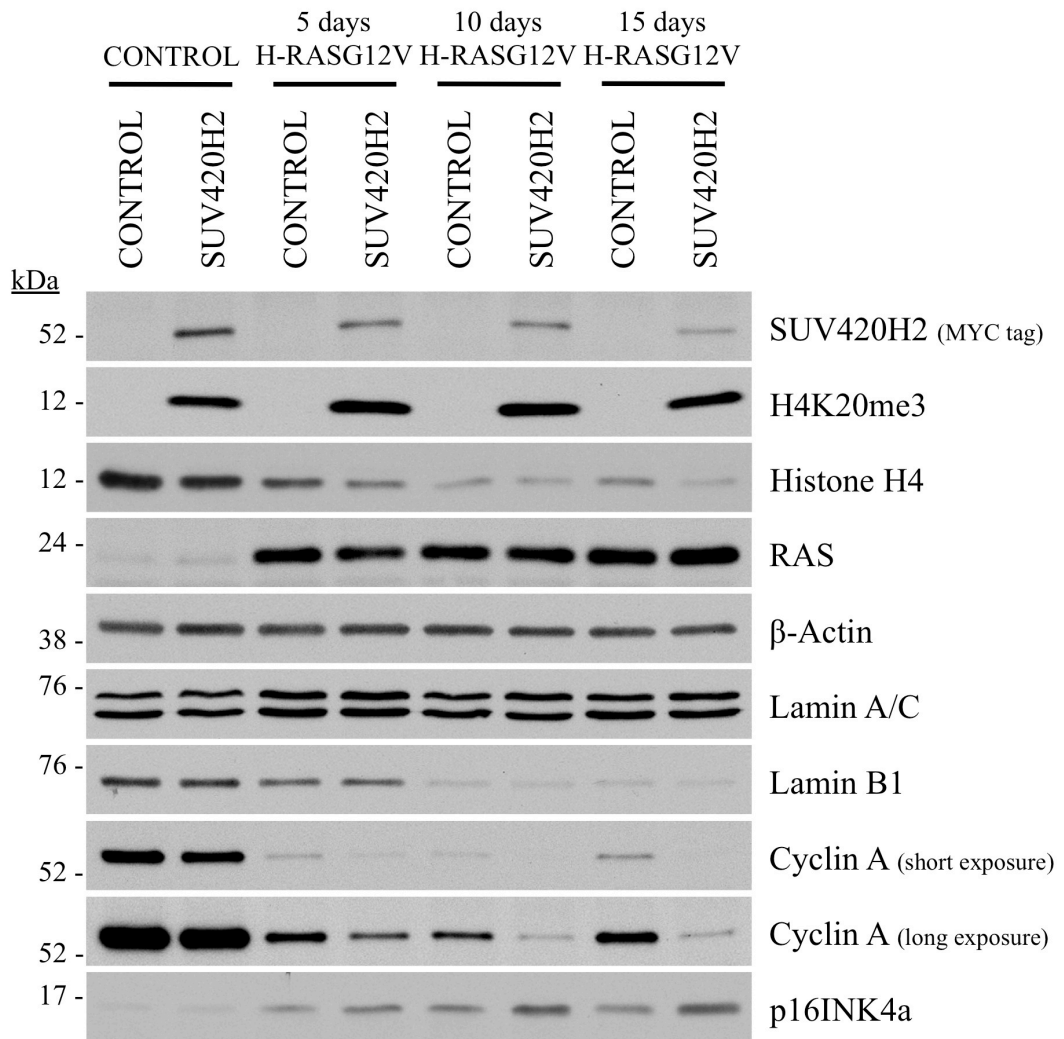


**Figure 6.10 MYC-SUV420H2 prevents escape from H-RASG12V-induced senescence.** Control and MYC-SUV420H2 cells were infected with control or H-RASG12V retroviruses. Cells were harvested at 5 day intervals after infection and whole cell extracts were prepared. The extracts were fractionated by SDS-PAGE and Western blotted for a panel of proliferation and senescence markers.

infected control and MYC-SUV420H2 cell lines, the cells were maintained in culture under continuous drug selection and observed frequently under the microscope. Thirty days after infection, bright field microscopic images of the respective plates were obtained and the cells were stained with crystal violet (N-hexamethylpararosaniline), a basic dye that binds DNA and other negatively charged cellular components, enabling visual quantification of the cells (Gillies et al., 1986).

As revealed in the bright field images, both the H-RASG12V-infected control and MYC-SUV420H2 plates contained a mixture of cells exhibiting either a classically-senescent, large, flattened morphology or concentrated in densely packed colonies of spindly apparently proliferative cells (Figure 6.11a). However, the densely packed colonies were more apparent in the H-RASG12V-infected control cells, compared to the H-RASG12V-infected MYC-SUV420H2 cells. Crystal violet staining confirmed that colony formation in the control cells infected with H-RASG12V vastly exceeded that of the H-RASG12V + MYC-SUV420H2 cells, with the control cells nearly filling the culture dish (Figure 6.11b). Importantly, the H-RASG12V + MYC-SUV420H2 cells did not lose viability, but persisted as viable cells with a classic senescent morphology (Figure 6.11a). Thus, the H-RASG12V-infected control cells managed to overcome the senescence proliferation arrest with relatively high frequency, whereas expression of MYC-SUV420H2 and the corresponding elevation of H4K20me3 levels appeared to restrict the degree to which H-RASG12V-infected cells could bypass senescence. Consequently, the data suggest that H4K20me3 might play an important role in the senescence program by enhancing the stability of the proliferation arrest.

### **6.3 Discussion**

In contrast to the widespread chromatin remodeling that occurs during cell senescence, the H4K20me3 histone modification reflects a relatively stable component of the epigenetic landscape. Remarkably, the absolute levels of H4K20me3 remain seemingly unaffected in the contexts of replicative and oncogene-induced senescence, respectively. Even more compelling, the apparent stability of H4K20me3 levels during senescence occurs despite a profound reduction of overall histone content. Based on this, it was reasonable to hypothesize that the H4K20me3 modification might serve a specific and critical function within the senescence program. In order to test this hypothesis, it became essential to develop

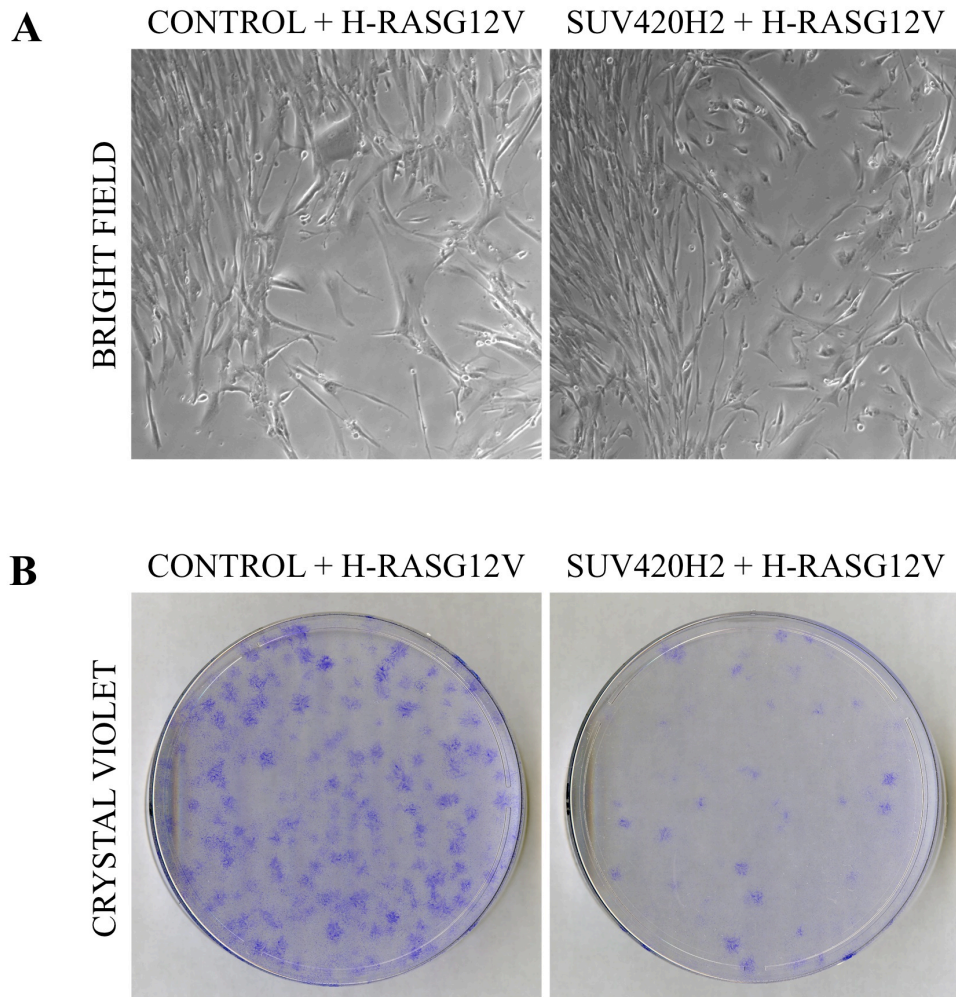


**Figure 6.11 MYC-SUV420H2 promotes stable proliferation arrest.** Control and MYC-SUV420H2 cells were infected with H-RASG12V, drug selected and maintained in culture. The cells were kept in drug for the remainder of the experiment. The cells were subjected to a final passage 6 days post infection and seeded to new 100 mm dishes. Thirty days after infection the plates were photographed and stained with crystal violet to visualize colony formation. (A) The plates were visualized by bright field microscopy and photographed under the 10X objective. (B) The plates were stained with crystal violet in order to visualize colony formation and scanned.

model systems in which H4K20me3 levels could be effectively altered. To this end, approaches were employed to either reduce or enhance endogenous levels of H4K20me3 and interrogate whether modulation of the histone mark was sufficient to affect specific features of the senescence program.

Efforts to reduce or completely abrogate H4K20me3 levels by either shRNA-mediated knockdown of SUV420H2 or through utilization of a dominant negative strategy were largely unsuccessful. Primarily, an inability to obtain multiple short hairpins capable of reducing SUV420H2 while maintaining cell viability posed a considerable technical challenge. One formal possibility is that IMR90 cells are unable to tolerate reduced levels of the H4K20me3 modification and consequently undergo cell death. However, in the absence of multiple active SUV420H2 hairpins, it is not possible to determine whether the observed cell death is an on-target or off-target phenotype. Efficient silencing of SUV420H2 in human cells has been previously reported (Kapoor-Vazirani et al., 2011). While the study by Kapoor-Vazirani and colleagues demonstrated successful knockdown of SUV420H2 in human MDA-MB-231 cells, only a single SUV420H2 hairpin was utilized and the authors failed to include convincing data that global H4K20me3 levels were reduced. Additionally, in contrast to primary IMR90 cells, MDA-MB-231 cells are a transformed breast cancer cell line, which may partially account for the ability of MDA-MB-231 cells to tolerate reduced H4K20me3 levels. Future experiments with additional shRNAs will address this issue in IMR90 cells.

Despite the limited success of efforts to reduce H4K20me3 levels in IMR90 cells, considerable information was obtained from the complimentary SUV420H2 overexpression approach. Infection of IMR90 cells with a retrovirus encoding MYC-tagged SUV420H2 resulted in overexpression of the enzyme and a robust increase in the H4K20me3 histone modification. Although elevated levels of H4K20me3 alone did not directly induce senescence, high abundance of the modification did accelerate the onset of replicative senescence and produced an enhanced senescence phenotype following infection with H-RASG12V. Specifically, MYC-SUV420H2 cells displayed higher levels of p16INK4a expression and lower cyclin A expression than control cells upon induction of senescence, suggesting an enhancement of the senescence proliferation arrest in the MYC-SUV420H2 cells.

High levels of H4K20me3 also appeared to reinforce the stability of the senescence proliferation arrest induced by the expression of a constitutively active

H-RAS allele. In fact, unlike H-RASG12V-infected control cells, the H-RASG12V-infected MYC-SUV420H2 cells were largely resistant to escape of oncogene-induced senescence. This was a compelling finding as it implied that H4K20me3 might be preferentially retained in senescent cells in order to maintain a chromatin state conducive to permanent proliferation arrest. In this manner, retention of H4K20me3 by oncogene-induced senescent cells *in vivo* would prohibit cells from re-entering the cell cycle, thus decreasing the likelihood of cellular transformation and subsequent tumor formation.

## Chapter 7. Discussion

### 7.1 Summary of Findings

Cell senescence is an important biological state that limits the replicative capacity of impaired or damaged cells through a network of programmed processes. As a result, senescence provides a potent barrier to tumorigenesis and contributes to other physiological processes such as aging and wound healing. In addition to a variety of well characterized morphological and biochemical changes, senescent cells exhibit profound changes to chromatin structure. Specifically, the formation of facultative heterochromatin has been proposed to play an important role in mediating several aspects of senescence, including the repression of proliferation genes and limiting the DNA damage response. Therefore, I set out to further investigate how chromatin structure influences senescence, by asking whether the heterochromatic histone modification H4K20me3 contributes to the various features of the senescence program.

In order to investigate the relationship between chromatin structure and senescence, I first established and validated two *in vitro* models of cell senescence. To this end, I established replicative senescent cells by subjecting primary human diploid IMR90 fibroblasts to prolonged passage in culture. Separately, I established an oncogene-induced senescence model by infecting IMR90 cells with a retrovirus encoding oncogenic H-RASG12V. Using common molecular markers of senescence, including proliferation arrest, p16INK4a induction and SA  $\beta$ -gal activity, I was able to confirm that the respective models generated senescent cells. I subsequently generated gene expression profiles for the respective senescence models and defined a common gene signature of senescence that included cell cycle genes, regulators of mitosis and genes involved in DNA damage signaling.

Having established and validated models of replicative and oncogene-induced senescence, I next set out to characterize the H4K20me3 histone modification in proliferating and senescent cells, as the mark has implications for both cancer and aging. Remarkably, although global histone levels decreased in senescent versus proliferating cells, H4K20me3 abundance remained unaltered. As a result, senescent cells contain a higher ratio of H4K20me3 to total histone H4 than proliferating cells. It is important to note that whereas relative H4K20me3 levels were determined by

Western blotting, quantitative mass spectrometry is commonly accepted as the gold-standard method for the accurate determination of histone posttranslational modification abundance (Britton et al., 2011). Importantly, recent work from Scott Lowe's laboratory utilizing mass spectrometry to quantify histone modifications confirmed that H4K20me3 levels are indeed maintained/elevated in H-RASG12V-induced senescent cells (Chicas et al., 2012).

Although the absolute abundance of H4K20me3 did not change during senescence, senescent cells displayed a considerably different nuclear distribution of the mark compared to proliferating cells. Proliferating cells typically exhibited a diffuse nuclear staining pattern for H4K20me3, while senescent cells invariably contained distinct nuclear H4K20me3 foci. The senescence-specific foci did not co-localize with several other well-characterized nuclear foci, including PML, 53BP1 and  $\gamma$ -H2AX. In contrast, the H4K20me3 foci in senescent cells did co-localize with SAHF. Given the apparent stabilization of H4K20me3 abundance and presence of the mark at SAHF, I investigated whether these phenotypes were caused by altered expression of SUV420H2, the enzyme responsible for the majority of H4K20me3 deposition. However, no change in SUV420H2 mRNA or protein expression was observed in senescent cells.

In order to evaluate whether the H4K20me3 modification might influence other features of the senescent chromatin landscape, I mapped the genome-wide distribution of H4K20me3 in proliferating and senescent cells using ChIP-Seq. Importantly, I performed the ChIP-Seq experiments with two independent H4K20me3 antibodies, which allowed for differentiation between specific antibody binding and non-specific binding. Marked H4K20me3 enrichment was noted in senescent cells with both antibodies. The regions of H4K20me3 enrichment were subsequently compared to defined features of the human genome. Regions of senescence-specific H4K20me3 enrichment coincided with intergenic regions, various classes of DNA repeats (e.g., LTRs, LINES, SINES) and regions of senescence-specific DNA hypomethylation.

Although the majority of H4K20me3 enrichment occurred at intergenic regions in senescent cells, some overlap with genes was evident. To investigate a potential role for H4K20me3 in the regulation of gene expression in senescent cells, regions of H4K20me3 enrichment were compared to the replicative senescence microarray data. The presence of H4K20me3 largely failed to correlate with gene

expression changes in senescent cells, suggesting that the mark does not contribute to the regulation of genes in senescence. However, significant enrichment of H4K20me3 was observed at numerous ZNF genes that were arranged in distinct genomic clusters. In addition, the enrichment of H4K20me3 at ZNF genes was far more prominent in senescent cells, with highest levels of the mark observed toward the 3' ends of gene bodies.

In light of the observations that H4K20me3 is maintained in senescent cells and distributed to specific genomic regions, I next set out to ask whether the mark contributed to the defining feature of senescence: stable proliferation arrest. To accomplish this, I attempted to modulate levels of H4K20me3 and test whether the mark was required for permanent cell cycle exit. Due to technical limitations I was unsuccessful in reducing H4K20me3 levels either through shRNA-mediated knock down of SUV420H2 or through ectopic expression of a potential SUV420H2 dominant negative construct. In contrast, ectopic expression of MYC-tagged SUV420H2 markedly increased H4K20me3 levels, but did not immediately yield any overt phenotype. However, following prolonged passage in culture, ectopic expression of MYC-SUV420H2 maintained elevated H4K20me3 levels and resulted in a moderate acceleration of senescence compared to control cells. Similarly, ectopic expression of MYC-SUV420H2 appeared to enhance entry into H-RASG12V-induced senescence. Most remarkably, whereas MYC-SUV420H2 overexpressing cells infected with H-RASG12V maintained a permanent proliferation arrest, control cells infected with H-RASG12V were able to escape the senescence arrest and resume proliferation.

The H4K20me3 modification is an important epigenetic mark involved in maintaining the structure and function of heterochromatin. Here, I have presented several key findings that demonstrate H4K20me3 is selectively retained in senescent cells despite global histone loss, is enriched in senescent cells at DNA repeats and ZNF genes, and helps facilitate the senescence proliferation arrest. Although these observations strongly support a contributory role for H4K20me3 to the senescence program, there are several limitations to the study, which will be subsequently discussed in detail. Despite the limitations, the current body of work contains compelling data to suggest that H4K20me3 plays an integral role in shaping chromatin structure in senescent cells. Thus, I will subsequently explore some of the important implications that the present study has for our understanding of

H4K20me3 regulation and the relationship between H4K20me3, senescence and cancer.

## **7.2 Limitations of the Study**

### **7.2.1 Loss-of-Function Experiments**

Potentially the most significant caveat of the present work is the lack of loss-of-function data. Consequently, one outstanding and critical question that remains to be addressed is whether the H4K20me3 modification is required for cell senescence to occur. In essence, are cells deficient for H4K20me3 still capable of undergoing senescence? This is an important question as the answer could reveal whether selective retention of H4K20me3 in senescent cells is an inconsequential passive event or whether the mark is retained in order to serve a specific function as part of the senescence program. Additionally, it could provide novel insight into how higher-order chromatin structure might suppress tumorigenesis by limiting the proliferative capacity of damaged cells.

As discussed in Chapter 6, the most significant obstacle to addressing whether H4K20me3 is required for senescence was obtaining viable cells in which the modification was sufficiently reduced. Although it is formally possible that reduction of H4K20me3 levels might adversely impact cell viability, there is some evidence that depletion of the mark can be achieved in human cells (Kapoor-Vazirani et al., 2011). Therefore, in order to efficiently reduce global levels of H4K20me3, several experimental approaches could be utilized. First, the selection and testing of additional SUV420H2 shRNAs might enable the identification of short hairpin sequences capable of effectively reducing SUV420H2 and H4K20me3 levels, while maintaining cell viability. Additional shRNAs targeting SUV420H2 have been developed as part of the Broad Institute's RNAi Consortium TRC2 phase (<http://www.broadinstitute.org/rnai/trc>) and are now commercially available. It is possible that these new shRNA constructs might facilitate efficient depletion of H4K20me3 from IMR90 cells.

In the absence of two or more shRNAs that effectively target SUV420H2, it is difficult to differentiate between actual phenotypes and potential off-target effects of RNA interference. In addition, viral infection, the most commonly employed method of delivering shRNAs to primary target cells, can incur a further set of

complications. One way to distinguish between the phenotypic effects of shRNA knockdown and the potentially cytotoxic effects associated with viral introduction of the construct is to utilize an inducible shRNA system (Meerbrey et al., 2011). Inducible shRNA systems enable the initial establishment of stably infected cells and subsequent control over when RNA interference is initiated. By utilizing this strategy, it is possible to temporally separate any phenotypic changes from infection-related complications. Inducible lentiviral shRNA constructs are commercially available and might provide an effective method of modulating H4K20me3 in IMR90 cells.

An alternative technical approach to conducting loss-of-function studies *in vitro* is to utilize cells isolated from genetically modified knockout mice. To this end, *Suv420h2*<sup>-/-</sup> mice have been successfully generated and characterized by Thomas Jenuwein's laboratory (Schotta et al., 2008). Produced by germline disruption of floxed *Suv420h2* alleles, the mice are viable, do not express SUV420H2 protein and are largely depleted of H4K20me3. Primary mouse embryonic fibroblasts (pMEFs) isolated from genetically modified mice provide an important tool for studying loss-of-function. Importantly, pMEFs isolated from *Suv420h2*<sup>-/-</sup> mice remain viable and exhibit marked H4K20me3 depletion (Schotta et al., 2008). Consequently, the *Suv420h2*<sup>-/-</sup> pMEFs might provide an alternative and useful tool for evaluating H4K20me3 function in cell senescence.

Before initiating loss-of-function studies using the *Suv420h2*<sup>-/-</sup> pMEFs, it is important to consider several potential caveats. To this end, there are several limitations to utilizing mouse cells as a surrogate model for studying senescence. First, in human fibroblasts, inactivation of both the p53 and pRB pathways is required in order to abolish senescence (Shay et al., 1991; Bond et al., 1999; Hahn et al., 2002). In contrast, inactivation of either the p53 pathway or pRB along with p107 and p130 is sufficient to abolish senescence in mouse fibroblasts (Harvey et al., 1993; Sage et al., 2000; Dannenberg et al., 2000). This underscores a potentially fundamental difference in how cell senescence is established in humans and mice, respectively.

Second, most proliferating human cells lack telomerase and undergo telomere attrition due to repeated rounds of DNA replication. Ultimately, telomeres reach a critically short length, which produces a DNA damage signal and induces replicative senescence (d'Adda di Fagagna et al., 2003). In contrast, most mouse somatic cells

express telomerase and consequently maintain lengthy telomeres (Kipling, 1997). As a result, telomere attrition is not a characteristic cause of senescence in mice, illustrating another important difference between human and mouse senescence (Parrinello et al., 2003). The difference between human and mouse telomeres also has implications for H4K20me3 loss-of-function experiments, as H4K20me3 has been reported to play a crucial role in the maintenance and function of telomeres (Benetti et al., 2007).

Despite the inherent limitations of utilizing either shRNA mediated gene silencing or *Suv420h2*<sup>-/-</sup> pMEFs to conduct loss-of-function experiments, both approaches provide ways of investigating the role of H4K20me3 in cell senescence. For this reason, I would implement both strategies in order to adequately address the question of whether H4K20me3 is required for senescence. In fact, the use of multiple technical approaches and models can potentially enhance the significance of a finding, by demonstrating that the given phenomenon is a conserved feature of senescence in multiple species and cell types. Alternatively, using different methods might reveal species or cell type-specific features of the senescence program. Either way, the methods discussed above reflect complimentary and viable strategies for deciphering the role of H4K20me3 in cell senescence.

### **7.2.2 H4K20me3 and Senescence *In Vivo***

A second limitation of the present work is the lack of experiments evaluating H4K20me3 in the context of senescence *in vivo*. The data presented in this study convincingly demonstrate that H4K20me3 abundance increases relative to total histone H4 content in replicative and oncogene-induced senescent cells, compared to proliferating cells. Thus, senescent cells appear to selectively retain H4K20me3 despite a decrease of bulk histone content. Although the data are robust, reproducible and consistent across two separate models of senescence, the experiments were only conducted in primary human cells *in vitro*. Thus, it is difficult to conclude whether selective retention of H4K20me3 is a bona fide hallmark of cell senescence, or rather a feature of senescence *in vitro*.

Despite this limitation to the interpretation of the data, there is some evidence of H4K20me3 retention/elevation in an *in vivo* context. Significantly elevated levels of H4K20me3 were observed in the livers of 450-day-old aged rats compared to the livers of 30-day-old young rats (Sarg et al., 2002). Although senescent cells have

been shown to accumulate with age in many mammalian tissues, Sarg and colleagues did not explicitly describe the presence of senescent cells in the livers of the 450-day-old rats. Therefore, the elevated levels of H4K20me3 observed in the livers of aged rats might have resulted from the presence of old, but not necessarily senescent, cells.

Over the last decade, there has been a growing interest in understanding how cell senescence contributes to both normal and pathophysiological processes *in vivo*. As a result, the presence of senescent cells has been described in a variety of *in vivo* contexts. Increased numbers of senescent cells have been detected in various aged mammalian tissues including human skin and liver, primate skin and mouse dermis, liver, spleen, lung and gut epithelium (Dimri et al., 1995; Paradis et al., 2001; Herbig et al., 2006; Jeyapalan et al., 2007; Wang et al., 2009). Accumulation of senescent cells has also been reported in numerous premalignant lesions including benign melanocytic nevi, early-stage thyroid tumors, dermal neurofibroma, pancreatic intraepithelial neoplasia, prostate intraepithelial neoplasia, lung adenoma, colon adenoma and lymphoma (Michaloglou et al., 2005; Gray-Schopfer et al., 2006; Vizioli et al., 2011; Courtois-Cox et al., 2006; Morton et al., 2010; Caldwell et al., 2012; Chen et al., 2005; Acosta et al., 2008; Collado et al., 2005; Bartkova et al., 2006; Fujita et al., 2009; Kuilman et al., 2008; Braig et al., 2005).

Importantly, many of the molecular markers that define senescent cells *in vitro*, including SA  $\beta$ -gal activity, p16INK4a induction and SASP, have also been observed extensively in senescent cells *in vivo* (Dimri et al., 1995; Michaloglou et al., 2005; Coppé et al., 2008). Thus, these markers reflect genuine features of the senescence program, and are not simply contextual artifacts of investigating senescence *in vitro* or *in vivo*, respectively. Whether the selective retention of the H4K20me3 modification similarly reflects a conserved feature of the senescence program remains to be seen. From a technical perspective, determining whether senescent cells exhibit retention or elevation of the H4K20me3 mark *in vivo* should be relatively straightforward. Given the extensive H4K20me3 antibody evaluation that I performed for this study, employing an immunological-based assay such as immunohistochemistry to detect H4K20me3 *in vivo* would be a reasonable approach. Finally, based on the current finding that elevated levels of H4K20me3 serve to reinforce the senescence proliferation arrest induced by oncogenic H-RAS, evaluating H4K20me3 in the senescent cells of pre-malignant lesions might reveal a

novel tumor suppressive function for the modification. To this end, it might be most appropriate to investigate H4K20me3 in the context of pancreatic intraepithelial neoplasia (PanIN), a pre-malignant lesion that often arises from aberrant RAS activation and has been reported to harbor senescent cells (Morton et al., 2010).

### **7.3 Implications of the Study**

#### **7.3.1 Regulation of H4K20me3**

The H4K20me3 histone modification is a repressive epigenetic mark that has important implications for aging, senescence and cancer. As demonstrated in the present study, H4K20me3 is selectively retained in replicative and oncogene-induced senescent cells, despite a net loss of bulk histone content. Additionally, ectopic expression of SUV420H2 in IMR90 cells conferred high levels of H4K20me3 and reinforced the H-RASG12V-induced proliferation arrest. Consequently, this raises the important mechanistic question of how H4K20me3 is regulated in senescent cells.

One possibility is that H4K20me3 levels are simply maintained in senescent cells through the basal activity of the SUV420H2 histone methyltransferase. Indeed, SUV420H2 is responsible for the majority of H4K20me3 deposition *in vivo* (Schotta et al., 2008). In the present study, SUV420H2 mRNA and protein levels remained unaltered in senescent cells, supporting a possible role for the enzyme in stabilizing levels of the mark during senescence. Alternatively, it is possible that H4K20me3 might be regulated through the activity of a different histone methyltransferase in senescent cells. One potential candidate is SUV420H1, an enzyme that primarily deposits the H4K20me2 mark, but also retains the ability to trimethylate H4K20 in some contexts (Schotta et al., 2008; Tsang et al., 2010). In fact, in the current study, ectopic expression of SUV420H1 increased H4K20me3 abundance, but not to the same magnitude as SUV420H2.

There is emerging evidence that additional enzymes can deposit the H4K20me3 modification in a variety of contexts. The nuclear receptor-binding SET domain-containing protein (NSD1) has been reported to methylate H4K20 *in vitro* (Rayasam et al., 2003). Genetic disruption of NSD1 in humans results in Sotos syndrome, an autosomal dominant disorder characterized by tall stature, distinctive facial features, macrocephaly, cognitive disabilities and an increased risk of

developing tumors (Lapunzina, 2005; Tatton-Brown & Rahman, 2007). Remarkably, lymphoblastoid cell lines isolated from Sotos syndrome patients exhibited markedly reduced levels of H4K20me<sub>3</sub>, suggesting a role for NSD1 in the trimethylation of H4K20 (Berdasco et al., 2009).

Recently, several members of the SET and MYND domain (SMYD) family of proteins were shown to play a role in H4K20me<sub>3</sub> regulation. To this end, it was reported that SMYD3 exhibits histone methyltransferase activity *in vitro* and preferentially trimethylates H4K20 in reconstituted chromatin (Foreman et al., 2011). Another SMYD family member, SMYD5, in cooperation with the NCoR corepressor complex, trimethylates H4K20 and silences pro-inflammatory genes in primary mouse macrophages (Stender et al., 2012). Stender and colleagues also showed that upon lipopolysaccharide (LPS)-mediated activation of toll-like receptor 4 (TLR4), PHF2 is recruited by an NF- $\kappa$ B-dependent mechanism to the promoters of pro-inflammatory genes, where it demethylates H4K20me<sub>3</sub>. Whether any of these histone methyltransferases contribute to the regulation H4K20me<sub>3</sub> in senescent cells remains to be tested.

Another potential mechanism by which H4K20me<sub>3</sub> abundance could be maintained in senescent cells might be through the inhibition of an H4K20me<sub>3</sub>-specific histone demethylase. However, to date, no genome-wide demethylase has been identified for H4K20me<sub>3</sub>. Although the histone lysine demethylase JMJD2A has been shown to bind H4K20me<sub>3</sub> with high affinity *in vitro*, it has not been reported to demethylate the mark (Huang et al., 2006; Lee et al., 2008; Ozboyaci et al., 2011). While PHF2 has been identified as a putative H4K20me<sub>3</sub> demethylase, it is possible that the enzyme only functions in a local context (e.g., at pro-inflammatory genes) and does not impact H4K20me<sub>3</sub> on a global scale. Thus, the hypothesis that H4K20me<sub>3</sub> is retained in senescent cells through inhibition of a specific histone demethylase remains a formal possibility, but one that is challenging to test.

Finally, it is formally possible that the H4K20me<sub>3</sub> retention in senescent cells occurs independently of active methylation or inhibition of demethylation. For example, H4K20me<sub>3</sub> stabilization might involve the interaction of other chromatin binding proteins. To this end, technical approaches such as quantitative interaction proteomics might enable identification of novel binding partners involved in the regulation of H4K20me<sub>3</sub> (Wysocka, 2006; Vermeulen et al., 2010). Thus, although

additional work is required in order to fully elucidate how H4K20me3 is maintained in senescent cells, the findings might ultimately inform our current understanding of the relationship between chromatin, senescence and cancer.

### **7.3.2 H4K20me3 and Cancer**

Despite the dynamic nature of chromatin during senescence, net abundance of the H4K20me3 modification remains remarkably stable between proliferating and senescent cells. Additionally, genome-wide mapping of H4K20me3 distribution revealed senescence-specific enrichment of the mark at ZNF gene clusters, DNA repeats (e.g., LTRs, LINES and SINES) and regions of the genome that become DNA hypomethylated during senescence. However, the most compelling finding of the current study was the observation that high levels of H4K20me3, resulting from ectopic expression of MYC-SUV420H2, was sufficient to suppress escape from H-RASG12V-induced senescence *in vitro*. In fact, this result has important implications for not only how H4K20me3 impacts the senescence program, but also how the mark might contribute to tumor suppression.

Epigenetic factors undoubtedly play a significant role in the maintenance and regulation of chromatin. Consequently, epigenetic dysregulation is frequently associated with a variety of pathological processes, including human cancers (Jones & Baylin, 2007). Although considerable attention has been directed toward understanding how altered patterns of DNA methylation impact the initiation and promotion of cancer, an important role for histone modifications in these processes is also emerging (Sharma et al., 2010). Supporting this concept is the striking observation that the H4K16ac and H4K20me3 modifications are frequently lost from a variety of human cancer cell lines and primary tumors (Fraga et al, 2005). Equally compelling, as Fraga and colleagues noted, was the fact that loss of these two marks frequently coincided with DNA hypomethylation at regions of repetitive DNA (e.g., satellite 2).

Subsequent reports have provided additional evidence that loss of H4K20me3 is indeed a common epigenetic feature of cancer. One study of breast cancer showed that compared to non-malignant MCF-10-2A breast epithelial cells, the MDA-MB-231 and MDA-MB-231(S30) malignant breast cancer cell lines exhibited global DNA hypomethylation, marked reduction of H4K20me3 and decreased expression of the H4K20 histone methyltransferase SUV420H2 (Tryndyak et al., 2006). In the

same study, MCF-7 cells, a less invasive cell line that represents an earlier stage of breast cancer, also displayed H4K20me3 loss, but to a lesser extent. Utilizing a rat model of estradiol-17 $\beta$  (E<sub>2</sub>)-induced mammary carcinogenesis, the same group subsequently reported a decrease of global DNA methylation, LINE-1 hypomethylation and loss of the H3K9me3 and H4K20me3 marks in hyperplastic mammary tissue (Kovalchuk et al., 2007). Significantly, the observed epigenetic changes preceded the development of full mammary carcinoma by approximately six weeks.

Evaluation of H4K20me3 abundance in tumors also provides important clinical prognostic insight. In a comparison of 50 lung squamous cell carcinomas and 50 lung adenocarcinomas to normal lung tissue, the tumors frequently displayed H4K5/H4K8 hyperacetylation, H4K12/H4K16 hypoacetylation, loss of H4K20me3 and reduced SUV420H2 expression (Van Den Broeck et al., 2008). Although H4K20me3 loss was generally less frequent in the adenocarcinoma samples, a subgroup of stage I adenocarcinoma patients with reduced H4K20me3 exhibited a significantly lower rate of survival. In a separate study of 880 characterized human breast carcinomas, tumors of the poorest prognostic subgroups (e.g., basal carcinomas, HER-2-positive tumors) displayed moderate to low H4K20me3 levels (Elsheikh et al., 2009). Finally, in a study of bladder cancer, H4K20me3 levels decreased across the clinical spectrum, with highest levels noted in normal urothelium, and progressively lower levels observed in non-muscle-invasive bladder cancer (NMIBC), muscle-invasive bladder cancer (MIBC) and bladder cancer metastases (METS) (Schneider et al., 2011). Remarkably, the METS exhibited lower levels of H4K20me3 than the primary tumors.

Given the evident correlation between H4K20me3 loss and cancer, several critical questions arise. First, is loss of the H4K20me3 mark a driver or consequence of cancer initiation and progression? Evidence from several of the studies discussed above suggests that loss of H4K20me3 is an early event, often beginning in less malignant stages and decreasing progressively with increased tumor grade and severity. If H4K20me3 loss is indeed a mechanistic driver of cancer, it implies that proper maintenance of H4K20me3 levels in the cell might provide a barrier against tumorigenesis. In fact, this model is broadly consistent with two important characteristics of cell senescence: (1) senescent cells selectively retain high levels of

the H4K20me3 mark and (2) senescence is a potent tumor suppressor mechanism. In this manner, one novel way that senescence might block cancer initiation is through the maintained stability of H4K20me3. If so, what is the mechanism by which H4K20me3 reinforces the tumor suppressive properties of senescence?

Revisiting the senescence-specific H4K20me3 mapping data might provide some critical insight toward addressing this mechanistic question. In senescent cells, H4K20me3 is seemingly abundant at a variety of DNA repeats including LTRs, LINES, SINES and DNA satellites (e.g., satellite 2). Based on recent data from Peter Adams' laboratory, some of these same regions also become DNA hypomethylated in replicative senescent IMR90 cells (Cruickshanks et al., submitted). Thus, in senescent cells, DNA methylation and H4K20me3 are clearly separable epigenetic marks. As noted earlier, Fraga and colleagues established that loss of H4K20me3 is commonly associated with hypomethylation of repetitive DNA sequences in human cancer (Fraga et al, 2005). In view of this, it is formally possible that loss of H4K20me3 from hypomethylated DNA repeats allows cancer initiation and progression, whereas the presence of H4K20me3 at hypomethylated DNA repeats in senescent cells might maintain the barrier to tumorigenesis.

If this is the case, it raises an important follow-up question: how might the presence of H4K20me3 at hypomethylated DNA repeats suppress cancer initiation? One possibility is that H4K20me3 prevents aberrant recombination events at regions of hypomethylated repetitive DNA. Loss of DNA methylation at repetitive regions (e.g., LINES, satellite 2) is associated with derepression of repeats, increased rates of insertional mutagenesis, genomic instability and cancer (Wong et al., 2001; Schulz et al., 2002; Howard et al., 2008). H4K20me3 is enriched in senescent cells at many of these regions, including LINES and satellite 2 repeats, suggesting that the mark might play a role in maintaining proper heterochromatin structure, particularly in the context of DNA methylation. Although this argument is largely correlative, a direct role for H4K20me3 in suppressing recombination at DNA repeats has been reported. Work from Maria Blasco's group demonstrated that *Suv420h2*<sup>-/-</sup> pMEFs exhibit marked loss of H4K20me3 at telomeres and subtelomeres, resulting in telomere elongation and a higher frequency of telomere recombination (Benetti et al., 2007). Importantly, the authors noted that telomere recombination occurred independent of any subtelomeric DNA methylation changes, suggesting that H4K20me3 alone might be responsible for suppressing recombination at telomeric repeats.

Finally, marked enrichment of H4K20me3 was also observed at ZNF gene clusters in senescent cells. ZNF genes comprise one of the largest gene families in the human genome, including the Krüppel associated box (KRAB) domain-containing ZNF (KRAB-ZNF) genes, a subgroup of approximately 800 loci that are arranged in large familial clusters (Shannon et al., 2003). Although H4K20me3 was generally not enriched at many genes in senescent cells, specific and marked enrichment was observed at KRAB-ZNF gene clusters. Additional reports have confirmed the presence of several other heterochromatic marks at ZNF genes. The heterochromatic protein HP1b (CBX1) is highly enriched at the 3' ends of KRAB-ZNF genes (Vogel et al., 2006). In a separate study, significant enrichment of another repressive epigenetic mark, H3K9me3, was observed at the 3' exons of ZNF genes, but did not correlate with gene expression (Blahnik et al., 2011). In both studies, the authors proposed that the presence of heterochromatic histone modifications and associated proteins might stabilize chromatin at KRAB-ZNF gene clusters and prevent inappropriate recombination. Thus, the striking enrichment of H4K20me3 at KRAB-ZNF genes in senescent cells might similarly suppress recombination at these loci.

Based on these published observations and the findings of this study, I propose a model of H4K20me3 function in senescence in which H4K20me3 prevents tumorigenesis in response to various triggers, by preventing recombination at DNA repeats and ZNF genes, thus maintaining genomic integrity (Figure 7.1). In this manner, retention of the H4K20me3 mark might compensate for the wide-scale chromatin changes that occur in senescent cells including DNA hypomethylation, shortened telomeres or damage resulting from DNA hyper-replication. Accordingly, cells that initiate the senescence program and retain adequate levels of H4K20me3 might maintain genomic stability and successfully establish a permanent proliferation arrest. In contrast, if H4K20me3 is lost from DNA repeats and ZNF genes, these regions might become predisposed to a higher frequency of recombination and mutational insertions, consequently driving cancer initiation and progression. Indeed, recent data indicate that in cancer, regions of the genome that normally exhibit enrichment of H4K20me3 and other repressive marks, contain the highest rates of mutation, as evidenced by high single nucleotide variant (SNV) densities (Schuster-Böckler & Lehner, 2012). Thus, H4K20me3 represents an

important epigenetic feature of the senescence program that likely stabilizes the genome, prevents recombination and mutation and suppresses tumorigenesis.

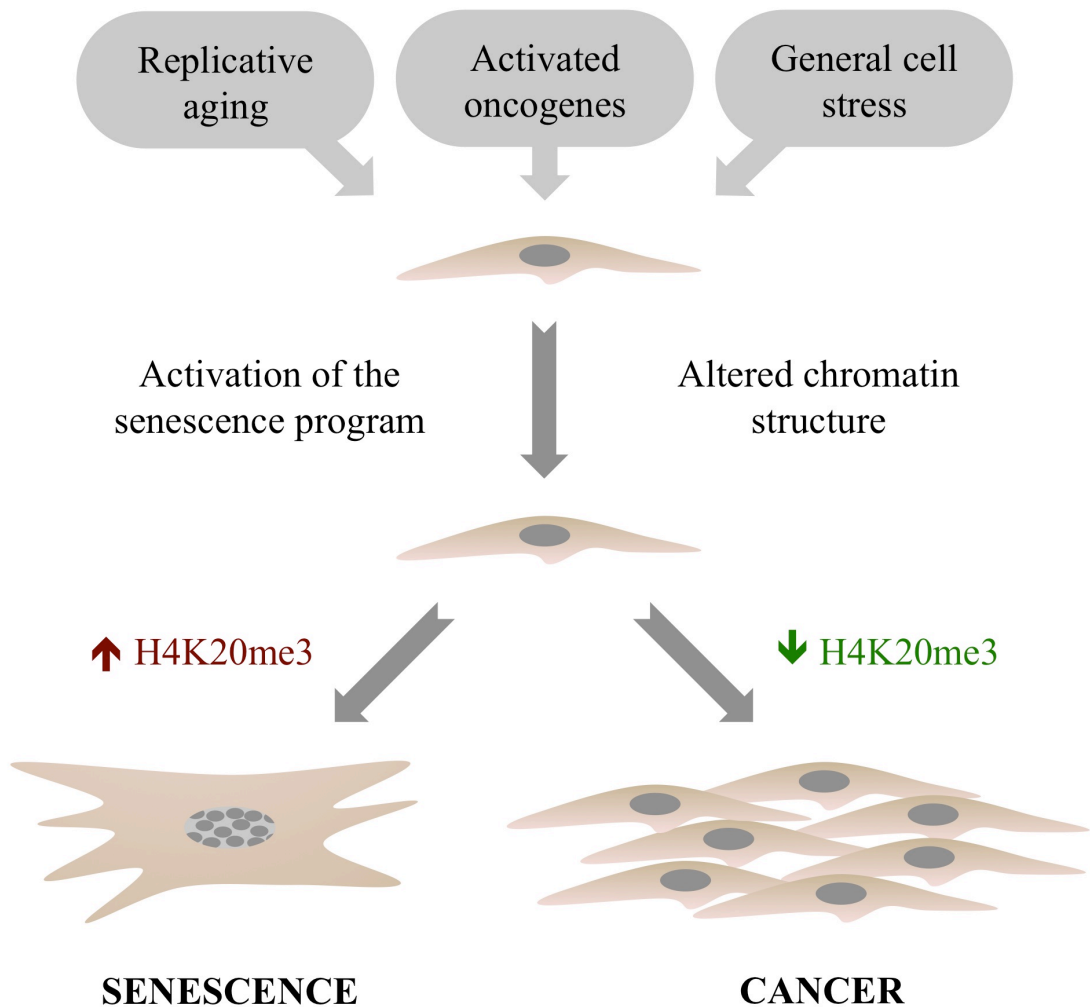


**Figure 7.1 Model of H4K20me3 function in senescence.** In order to limit the proliferative capacity of potentially damaged cells, exposure to several molecular triggers (e.g., telomere loss, activated oncogenes, stress) activates the senescence program. Upon initiation of the program, cells undergo widespread chromatin changes (e.g., DNA hypomethylation, DNA damage from hyper-replication). If H4K20me3 levels remain unaltered, cells maintain the senescence program and commit to a state of permanent proliferation arrest. Alternatively, if H4K20me3 levels are insufficient, cells exhibiting altered chromatin structure might become predisposed to DNA recombination and mutation (particularly at DNA repeats), allowing escape from senescence and subsequent transformation.

## References

- Aapola, U., Liiv, I., Peterson, P. (2002). Imprinting regulator DNMT3L is a transcriptional repressor associated with histone deacetylase activity. *Nucleic Acids Res.* 30(16): 3602-3608.
- Acosta, J. C., O'Loughlen, A., Banito, A., Guijarro, M. V., Augert, A., Raguz, S., Fumagalli, M., Da Costa, M., Brown, C., Popov, N., et al. (2008). Chemokine signaling via the CXCR2 receptor reinforces senescence. *Cell.* 133(6): 1006-1018.
- Adkins, M. W., Tyler, J. K. (2006). Transcriptional activators are dispensable for transcription in the absence of Spt6-mediated chromatin reassembly of promoter regions. *Mol Cell.* 21(3): 405-416.
- Ahmad, K., Henikoff, S. (2002). The histone variant H3.3 marks active chromatin by replication-independent nucleosome assembly. *Mol Cell.* 9(6): 1191-1200.
- Ait-Si-Ali, S., Guasconi, V., Fritsch, L., Yahi, H., Sekhri, R., Naguibneva, I., Robin, P., Cabon, F., Polesskaya, A., Harel-Bellan, A. (2004). A Suv39h-dependent mechanism for silencing S-phase genes in differentiating but not in cycling cells. *EMBO J.* 23(3): 605-615.
- Alcorta, D. A., Xiong, Y., Phelps, D., Hannon, G., Beach, D., Barrett, J. C. (1996). Involvement of the cyclin-dependent kinase inhibitor p16 (INK4a) in replicative senescence of normal human fibroblasts. *Proc Natl Acad Sci U S A.* 93(24): 13742-13747.
- Aran, D., Toperoff, G., Rosenberg, M., Hellman, A. (2011). Replication timing-related and gene body-specific methylation of active human genes. *Hum Mol Genet.* 20(4): 670-680.
- Arents, G., Burlingame, R. W., Wang, B. C., Love, W. E., Moudrianakis, E. N. (1991). The nucleosomal core histone octamer at 3.1 Å resolution: a tripartite protein assembly and a left-handed superhelix. *Proc Natl Acad Sci U S A.* 88(22): 10148-10152.
- Arita, K., Ariyoshi, M., Tochio, H., Nakamura, Y., Shirakawa, M. (2008). Recognition of hemi-methylated DNA by the SRA protein UHRF1 by a base-flipping mechanism. *Nature.* 455(7214): 818-821.
- Avvakumov, G. V., Walker, J. R., Xue, S., Li, Y., Duan, S., Bronner, C., Arrowsmith, C. H., Dhe-Paganon, S. (2008). Structural basis for recognition of hemi-methylated DNA by the SRA domain of human UHRF1. *Nature.* 455(7214): 822-825.
- Bai, L., Morozov, A. V. (2010). Gene regulation by nucleosome positioning. *Trends Genet.* 26(11): 476-483.

- Baker, D. J., Perez-Terzic, C., Jin, F., Pitel, K. S., Niederländer, N. J., Jeganathan, K., Yamada, S., Reyes, S., Rowe, L., Hiddinga, H. J., et al. (2008). Opposing roles for p16Ink4a and p19Arf in senescence and ageing caused by BubR1 insufficiency. *Nat Cell Biol.* 10(7): 825-836.
- Baker, D. J., Wijshake, T., Tchkonja, T., LeBrasseur, N. K., Childs, B. G., van de Sluis, B., Kirkland, J. L., van Deursen, J. M. (2011). Clearance of p16Ink4a-positive senescent cells delays ageing-associated disorders. *Nature.* 479(7372): 232-236.
- Bannister, A. J., Kouzarides, T. (2011). Regulation of chromatin by histone modifications. *Cell Res.* 21(3): 381-395.
- Bardeesy, N., Morgan, J., Sinha, M., Signoretti, S., Srivastava, S., Loda, M., Merlino, G., DePinho, R. A. (2002). Obligate roles for p16(Ink4a) and p19(Arf)-p53 in the suppression of murine pancreatic neoplasia. *Mol Cell Biol.* 22(2): 635-643.
- Barski, A., Cuddapah, S., Cui, K., Roh, T. Y., Schones, D. E., Wang, Z., Wei, G., Chepelev, I., Zhao, K. (2007). High-resolution profiling of histone methylations in the human genome. *Cell.* 129(4): 823-837.
- Bartkova, J., Rezaei, N., Liontos, M., Karakaidos, P., Kletsas, D., Issaeva, N., Vassiliou, L. V., Kolettas, E., Niforou, K., Zoumpourlis, V. C., et al. (2006). Oncogene-induced senescence is part of the tumorigenesis barrier imposed by DNA damage checkpoints. *Nature.* 444(7119): 633-637.
- Benetti, R., Gonzalo, S., Jaco, I., Schotta, G., Klatt, P., Jenuwein, T., Blasco, M. A. (2007). Suv4-20h deficiency results in telomere elongation and derepression of telomere recombination. *J Cell Biol.* 178(6): 925-936.
- Benjamini, Y., Hochberg, Y. (1995). Controlling the false discovery rate: a practical and powerful approach to multiple testing. *Journal of the Royal Statistical Society Series B Methodological.* 57(1): 289 -300.
- Ben-Porath, I., Weinberg, R. A. (2005). The signals and pathways activating cellular senescence. *Int J Biochem Cell Biol.* 37(5): 961-976.
- Berdasco, M., Ropero, S., Setien, F., Fraga, M. F., Lapunzina, P., Losson, R., Alaminos, M., Cheung, N. K., Rahman, N., Esteller, M. (2009). Epigenetic inactivation of the Sotos overgrowth syndrome gene histone methyltransferase NSD1 in human neuroblastoma and glioma. *Proc Natl Acad Sci U S A.* 106(51): 21830-21835.
- Bernstein, B. E., Humphrey, E. L., Erlich, R. L., Schneider, R., Bouman, P., Liu, J. S., Kouzarides, T., Schreiber, S. L. (2002). Methylation of histone H3 Lys 4 in coding regions of active genes. *Proc Natl Acad Sci U S A.* 99(13): 8695-8700.

- Bhaumik, D., Scott, G. K., Schokrpur, S., Patil, C. K., Orjalo, A. V., Rodier, F., Lithgow, G. J., Campisi, J. (2009). MicroRNAs miR-146a/b negatively modulate the senescence-associated inflammatory mediators IL-6 and IL-8. *Aging (Albany NY)*. 1(4): 402-411.
- Biamonti, G., Giacca, M., Perini, G., Contreas, G., Zentilin, L., Weighardt, F., Guerra, M., Della Valle, G., Saccone, S., Riva, S., et al. (1992). The gene for a novel human lamin maps at a highly transcribed locus of chromosome 19 which replicates at the onset of S-phase. *Mol Cell Biol*. 12(8): 3499-3506.
- Bird, A., Tate, P., Nan, X., Campoy, J., Meehan, R., Cross, S., Tweedie, S., Charlton, J., Macleod, D. (1995). Studies of DNA methylation in animals. *J Cell Sci Suppl*. 19: 37-39.
- Bird, A. (2002). DNA methylation patterns and epigenetic memory. *Genes Dev*. 16(1): 6-21.
- Birney, E., Stamatoyannopoulos, J. A., Dutta, A., Guigo, R., Gingeras, T. R., Margulies, E. H., Weng, Z., Snyder, M., Dermitzakis, E. T., Thurman, R. E., et al. (2007). Identification and analysis of functional elements in 1% of the human genome by the ENCODE pilot project. *Nature*. 447(7146): 799-816.
- Bischof, O., Kirsh, O., Pearson, M., Itahana, K., Pelicci, P. G., Dejean, A. (2002). Deconstructing PML-induced premature senescence. *EMBO J*. 21(13): 3358-3369.
- Blahnik, K. R., Dou, L., Echipare, L., Iyengar, S., O'Geen, H., Sanchez, E., Zhao, Y., Marra, M. A., Hirst, M., Costello, J. F., et al. (2011). Characterization of the contradictory chromatin signatures at the 3' exons of zinc finger genes. *PLoS One*. 6(2): e17121.
- Bock, I., Dhayalan, A., Kudithipudi, S., Brandt, O., Rathert, P., Jeltsch, A. (2011). Detailed specificity analysis of antibodies binding to modified histone tails with peptide arrays. *Epigenetics*. 6(2): 256-263.
- Bodnar, A. G., Ouellette, M., Frolkis, M., Holt, S. E., Chiu, C. P., Morin, G. B., Harley, C. B., Shay, J. W., Lichtsteiner, S., Wright, W. E. (1998) Extension of life-span by introduction of telomerase into normal human cells. *Science*. 279(5349): 349-352.
- Bond, J. A., Haughton, M. F., Rowson, J. M., Smith, P. J., Gire, V., Wynford-Thomas, D., Wyllie, F. S. (1999). Control of replicative life span in human cells: barriers to clonal expansion intermediate between M1 senescence and M2 crisis. *Mol Cell Biol*. 19(4): 3103-3114.
- Borun, T. W., Pearson, D., Paik, W. K. (1972). Studies of histone methylation during the HeLa S-3 cell cycle. *J Biol Chem*. 247(13): 4288-4298.
- Bracken, A. P., Kleine-Kohlbrecher, D., Dietrich, N., Pasini, D., Gargiulo, G., Beekman, C., Theilgaard-Mönch, K., Minucci, S., Porse, B. T., Marine, J. C.,

- et al. (2007). The Polycomb group proteins bind throughout the INK4A-ARF locus and are disassociated in senescent cells. *Genes Dev.* 21(5): 525-530.
- Braig, M., Lee, S., Loddenkemper, C., Rudolph, C., Peters, A. H., Schlegelberger, B., Stein, H., Dörken, B., Jenuwein, T., Schmitt, C. A. (2005). Oncogene-induced senescence as an initial barrier in lymphoma development. *Nature.* 436(7051): 660-665.
- Breusing, N., Grune, T. (2008). Regulation of proteasome-mediated protein degradation during oxidative stress and aging. *Biol Chem.* 389(3): 203-209.
- Bridger, J. M., Foeger, N., Kill, I. R., Herrmann, H. (2007). The nuclear lamina. Both a structural framework and a platform for genome organization. *FEBS J.* 274(6): 1354-1361.
- Britton, L. M., Gonzales-Cope, M., Zee, B. M., Garcia, B. A. (2011). Breaking the histone code with quantitative mass spectrometry. *Expert Rev Proteomics.* 8(5): 631-643.
- Brown, C. J., Ballabio, A., Rupert, J. L., Lafreniere, R. G., Grompe, M., Tonlorenzi, R., Willard, H. F. (1991). A gene from the region of the human X inactivation centre is expressed exclusively from the inactive X chromosome. *Nature.* 349(6304): 38-44.
- Burrage, P. S., Mix, K. S., Brinckerhoff, C. E. (2006). Matrix metalloproteinases: role in arthritis. *Front Biosci.* 11: 529-543.
- Byvoet, P., Shepherd, G. R., Hardin, J. M., Noland, B. J. (1972). The distribution and turnover of labeled methyl groups in histone fractions of cultured mammalian cells. *Arch Biochem Biophys.* 148(2): 558-567.
- Caldwell, M. E., DeNicola, G. M., Martins, C. P., Jacobetz, M. A., Maitra, A., Hruban, R. H., Tuveson, D. A. (2012). Cellular features of senescence during the evolution of human and murine ductal pancreatic cancer. *Oncogene.* 31(12): 1599-1608.
- Campisi, J. (2005). Senescent cells, tumor suppression, and organismal aging: good citizens, bad neighbors. *Cell.* 120(4): 513-522.
- Celeste, A., Petersen, S., Romanienko, P. J., Fernandez-Capetillo, O., Chen, H. T., Sedelnikova, O. A., Reina-San-Martin, B., Coppola, V., Meffre, E., Difilippantonio, M. J., et al. (2002). Genomic instability in mice lacking histone H2AX. *Science.* 296(5569): 922-927.
- Chadwick, B. P., Willard, H. F. (2001). A novel chromatin protein, distantly related to histone H2A, is largely excluded from the inactive X chromosome. *J Cell Biol.* 152(2): 375-384.

- Chadwick, B. P., Willard, H. F. (2004). Multiple spatially distinct types of facultative heterochromatin on the human inactive X chromosome. *Proc Natl Acad Sci U S A*. 101(50): 17450-17455.
- Chan, H. M., Narita, M., Lowe, S. W., Livingston, D. M. (2005). The p400 E1A-associated protein is a novel component of the p53 --> p21 senescence pathway. *Genes Dev*. 19(2): 196-201.
- Chandra, T., Kirschner, K., Thuret, J. Y., Pope, B. D., Ryba, T., Newman, S., Ahmed, K., Samarajiwa, S. A., Salama, R., Carroll, T., et al. (2012). Independence of Repressive Histone Marks and Chromatin Compaction during Senescent Heterochromatic Layer Formation. *Mol Cell*. 47(2): 203-214.
- Chen, Q. M., Bartholomew, J. C., Campisi, J., Acosta, M., Reagan, J. D., Ames, B. N. (1998a). Molecular analysis of H<sub>2</sub>O<sub>2</sub>-induced senescent-like growth arrest in normal human fibroblasts: p53 and Rb control G1 arrest but not cell replication. *Biochem J*. 332(Pt 1): 43-50.
- Chen, R. Z., Pettersson, U., Beard, C., Jackson-Grusby, L., Jaenisch, R. (1998b). DNA hypomethylation leads to elevated mutation rates. *Nature*. 395(6697): 89-93.
- Chen, Z., Trotman, L. C., Shaffer, D., Lin, H. K., Dotan, Z. A., Niki, M., Koutcher, J. A., Scher, H. I., Ludwig, T., Gerald, W., et al. (2005). Crucial role of p53-dependent cellular senescence in suppression of Pten-deficient tumorigenesis. *Nature*. 436(7051): 725-730.
- Chicas, A., Kapoor, A., Wang, X., Aksoy, O., Everitts, A. G., Zhang, M. Q., Garcia, B. A., Bernstein, E., Lowe, S. W. (2012). H3K4 demethylation by Jarid1a and Jarid1b contributes to retinoblastoma-mediated gene silencing during cellular senescence. *Proc Natl Acad Sci U S A*. 109(23): 8971-8976.
- Chin, L., Pomerantz, J., Polsky, D., Jacobson, M., Cohen, C., Cordon-Cardo, C., Horner, J. W. 2nd, DePinho, R. A. (1997). Cooperative effects of INK4a and ras in melanoma susceptibility in vivo. *Genes Dev*. 11(21): 2822-2834.
- Chin, H. G., Patnaik, D., Estève, P. O., Jacobsen, S. E., Pradhan, S. (2006). Catalytic properties and kinetic mechanism of human recombinant Lys-9 histone H3 methyltransferase SUV39H1: participation of the chromodomain in enzymatic catalysis. *Biochemistry*. 45(10): 3272-3284.
- Choi, M. R., In, Y. H., Park, J., Park, T., Jung, K. H., Chai, J. C., Chung, M. K., Lee, Y. S., Chai, Y. G. (2012). Genome-scale DNA methylation pattern profiling of human bone marrow mesenchymal stem cells in long-term culture. *Exp Mol Med*. 44(8): 503-512.
- Chuang, L. S., Ian, H. I., Koh, T. W., Ng, H. H., Xu, G., Li, B. F. (1997). Human DNA-(cytosine-5) methyltransferase-PCNA complex as a target for p21WAF1. *Science*. 277(5334): 1996-2000.

- Chung, H. Y., Cesari, M., Anton, S., Marzetti, E., Giovannini, S., Seo, A. Y., Carter, C., Yu, B. P., Leeuwenburgh, C. (2009). Molecular inflammation: underpinnings of aging and age-related diseases. *Ageing Res Rev.* 8(1): 18-30.
- Collado, M., Gil, J., Efeyan, A., Guerra, C., Schuhmacher, A. J., Barradas, M., Benguría, A., Zaballos, A., Flores, J. M., Barbacid, M., et al. (2005). Tumour biology: senescence in premalignant tumours. *Nature.* 436(7051): 642.
- Coller, H. A., Sang, L., Roberts, J. M. (2006). A new description of cellular quiescence. *PLoS Biol.* 4(3): e83.
- Coppé, J. P., Patil, C. K., Rodier, F., Sun, Y., Muñoz, D. P., Goldstein, J., Nelson, P. S., Desprez, P. Y., Campisi, J. (2008). Senescence-associated secretory phenotypes reveal cell-nonautonomous functions of oncogenic RAS and the p53 tumor suppressor. *PLoS Biol.* 6(12): 2853-2868.
- Coppé, J. P., Desprez, P. Y., Krtolica, A., Campisi, J. (2010). The senescence-associated secretory phenotype: the dark side of tumor suppression. *Annu Rev Pathol.* 5: 99-118.
- Coppé, J. P., Rodier, F., Patil, C. K., Freund, A., Desprez, P. Y., Campisi, J. (2011) Tumor suppressor and aging biomarker p16(INK4a) induces cellular senescence without the associated inflammatory secretory phenotype. *J Biol Chem.* 286(42): 36396-36403.
- Coppock, D. L., Kopman, C., Scandalis, S., Gilleran, S. (1993). Preferential gene expression in quiescent human lung fibroblasts. *Cell Growth Differ.* 4(6): 483-493.
- Cordaux, R., Batzer, M. A. (2009). The impact of retrotransposons on human genome evolution. *Nat Rev Genet.* 10(10): 691-703.
- Cortázar, D., Kunz, C., Selfridge, J., Lettieri, T., Saito, Y., MacDougall, E., Wirz, A., Schuermann, D., Jacobs, A. L., Siegrist, F., et al. (2011). Embryonic lethal phenotype reveals a function of TDG in maintaining epigenetic stability. *Nature.* 470(7334): 419-423.
- Cortellino, S., Xu, J., Sannai, M., Moore, R., Caretti, E., Cigliano, A., Le Coz, M., Devarajan, K., Wessels, A., Soprano, D., et al. (2011). Thymine DNA glycosylase is essential for active DNA demethylation by linked deamination-base excision repair. *Cell.* 146(1): 67-79.
- Costanzi, C., Pehrson, J. R. (1998). Histone macroH2A1 is concentrated in the inactive X chromosome of female mammals. *Nature.* 393(6685): 599-601.
- Courtois-Cox, S., Genter Williams, S. M., Reczek, E. E., Johnson, B. W., McGillicuddy, L. T., Johannessen, C. M., Hollstein, P. E., MacCollin, M., Cichowski, K. (2006) A negative feedback signaling network underlies oncogene-induced senescence. *Cancer Cell.* 10(6): 459-472.

- Cui, G., Park, S., Badeaux, A. I., Kim, D., Lee, J., Thompson, J. R., Yan, F., Kaneko, S., Yuan, Z., Botuyan, M. V., et al. (2012). PHF20 is an effector protein of p53 double lysine methylation that stabilizes and activates p53. *Nat Struct Mol Biol.* 19(9): 916-924.
- d'Adda di Fagagna, F., Reaper, P. M., Clay-Farrace, L., Fiegler, H., Carr, P., Von Zglinicki, T., Saretzki, G., Carter, N. P., Jackson, S. P. (2003). A DNA damage checkpoint response in telomere-initiated senescence. *Nature.* 426(6963): 194-198.
- Dang, W., Steffen, K. K., Perry, R., Dorsey, J. A., Johnson, F. B., Shilatifard, A., Kaeberlein, M., Kennedy, B. K., Berger, S. L. (2009). Histone H4 lysine 16 acetylation regulates cellular lifespan. *Nature.* 459(7248): 802-807.
- Dannenberg, J. H., van Rossum, A., Schuijff, L., te Riele, H. (2000). Ablation of the retinoblastoma gene family deregulates G(1) control causing immortalization and increased cell turnover under growth-restricting conditions. *Genes Dev.* 14(23): 3051-3064.
- Dechat, T., Pflieger, K., Sengupta, K., Shimi, T., Shumaker, D. K., Solimando, L., Goldman, R. D. (2008). Nuclear lamins: major factors in the structural organization and function of the nucleus and chromatin. *Genes Dev.* 22(7): 832-853.
- Dennis, J. H., Fan, H. Y., Reynolds, S. M., Yuan, G., Meldrim, J. C., Richter, D. J., Peterson, D. G., Rando, O. J., Noble, W. S., Kingston, R. E. (2007). Independent and complementary methods for large-scale structural analysis of mammalian chromatin. *Genome Res.* 17(6): 928-939.
- Dhalluin, C., Carlson, J. E., Zeng, L., He, C., Aggarwal, A. K., Zhou, M. M. (1999). Structure and ligand of a histone acetyltransferase bromodomain. *Nature.* 399(6735): 491-496.
- Di Leonardo, A., Linke, S. P., Clarkin, K., Wahl, G. M. (1994). DNA damage triggers a prolonged p53-dependent G1 arrest and long-term induction of Cip1 in normal human fibroblasts. *Genes Dev.* 8(21): 2540-2551.
- Dillon, S. C., Zhang, X., Trievel, R. C., Cheng, X. (2005). The SET-domain protein superfamily: protein lysine methyltransferases. *Genome Biol.* 6(8): 227.
- Di Micco, R., Fumagalli, M., Cicalese, A., Piccinin, S., Gasparini, P., Luise, C., Schurra, C., Garre', M., Nuciforo, P. G., Bensimon, A., et al. (2006). Oncogene-induced senescence is a DNA damage response triggered by DNA hyper-replication. *Nature.* 444(7119): 638-642.
- Di Micco, R., Sulli, G., Dobрева, M., Liontos, M., Botrugno, O. A., Gargiulo, G., dal Zuffo, R., Matti, V., d'Ario, G., Montani, E., et al. (2011). Interplay between oncogene-induced DNA damage response and heterochromatin in senescence and cancer. *Nat Cell Biol.* 13(3): 292-302.

- Dimri, G. P., Lee, X., Basile, G., Acosta, M., Scott, G., Roskelley, C., Medrano, E. E., Linskens, M., Rubelj, I., Pereira-Smith, O., et al. (1995). A biomarker that identifies senescent human cells in culture and in aging skin in vivo. *Proc Natl Acad Sci U S A.* 92(20): 9363-9367.
- Dittmer, T. A., Misteli, T. (2011). The lamin protein family. *Genome Biol.* 12(5): 222.
- Donati, G., Gatta, R., Dolfini, D., Fossati, A., Ceribelli, M., Mantovani, R. (2008). An NF-Y-dependent switch of positive and negative histone methyl marks on CCAAT promoters. *PLoS One.* 3(4): e2066.
- Dou, Y., Milne, T. A., Ruthenburg, A. J., Lee, S., Lee, J. W., Verdine, G. L., Allis, C. D., Roeder, R. G. (2006). Regulation of MLL1 H3K4 methyltransferase activity by its core components. *Nat Struct Mol Biol.* 13(8): 713-719.
- Drané, P., Ouararhni, K., Depaux, A., Shuaib, M., Hamiche, A. (2010). The death-associated protein DAXX is a novel histone chaperone involved in the replication-independent deposition of H3.3. *Genes Dev.* 24(12): 1253-1265.
- Dumont, P., Burton, M., Chen, Q. M., Gonos, E. S., Frippiat, C., Mazarati, J. B., Eliaers, F., Remacle, J., Toussaint, O. (2000). Induction of replicative senescence biomarkers by sublethal oxidative stresses in normal human fibroblast. *Free Radic Biol Med.* 28(3): 361-373.
- Dunleavy, E. M., Almouzni, G., Karpen, G. H. (2011). H3.3 is deposited at centromeres in S phase as a placeholder for newly assembled CENP-A in G1 phase. *Nucleus.* 2(2): 146-157.
- Ehrlich, M., Gama-Sosa, M. A., Huang, L. H., Midgett, R. M., Kuo, K. C., McCune, R. A., Gehrke, C. (1982). Amount and distribution of 5-methylcytosine in human DNA from different types of tissues of cells. *Nucleic Acids Res.* 10(8): 2709-2721.
- Elsheikh, S. E., Green, A. R., Rakha, E. A., Powe, D. G., Ahmed, R. A., Collins, H. M., Soria, D., Garibaldi, J. M., Paish, C. E., Ammar, A. A., et al. (2009). Global histone modifications in breast cancer correlate with tumor phenotypes, prognostic factors, and patient outcome. *Cancer Res.* 69(9): 3802-3809.
- Egelhofer, T. A., Minoda, A., Klugman, S., Lee, K., Kolasinska-Zwierz, P., Alekseyenko, A. A., Cheung, M. S., Day, D. S., Gadel, S., Gorchakov, A. A., et al. (2010). An assessment of histone-modification antibody quality. *Nat Struct Mol Biol.* 18(1): 91-93.
- Erukashvily, N. I., Donev, R., Waisertreiger, I. S., Podgornaya, O. I. (2007). Human chromosome 1 satellite 3 DNA is decondensed, demethylated and transcribed in senescent cells and in A431 epithelial carcinoma cells. *Cytogenet Genome Res.* 118(1): 42-54.

- Ernst, J., Kellis, M. (2010). Discovery and characterization of chromatin states for systematic annotation of the human genome. *Nat Biotechnol.* 28(8): 817-825.
- Faast, R., Thonglairoam, V., Schulz, T. C., Beall, J., Wells, J. R., Taylor, H., Matthaei, K., Rathjen, P. D., Tremethick, D. J., Lyons, I. (2001). Histone variant H2A.Z is required for early mammalian development. *Curr Biol.* 11(15): 1183-1187.
- Fair, K., Anderson, M., Bulanova, E., Mi, H., Tropschug, M., Diaz, M. O. (2001). Protein interactions of the MLL PHD fingers modulate MLL target gene regulation in human cells. *Mol Cell Biol.* 21(10): 3589-3597.
- Felsenfeld, G., Groudine, M. (2003). Controlling the double helix. *Nature.* 421(6921): 448-453.
- Ferbeyre, G., de Stanchina, E., Querido, E., Baptiste, N., Prives, C., Lowe, S. W. (2000). PML is induced by oncogenic ras and promotes premature senescence. *Genes Dev.* 14(16): 2015-2027.
- Ferguson-Smith, A. C., Sasaki, H., Cattanaach, B. M., Surani, M. A. (1993). Parental-origin-specific epigenetic modification of the mouse H19 gene. *Nature.* 362(6422): 751-755.
- Ferguson-Smith, A. C., Surani, M. A. (2001). Imprinting and the epigenetic asymmetry between parental genomes. *Science.* 293(5532): 1086-1089.
- Feser, J., Truong, D., Das, C., Carson, J. J., Kieft, J., Harkness, T., Tyler, J. K. (2010). Elevated histone expression promotes life span extension. *Mol Cell.* 39(5): 724-735.
- Filippakopoulos, P., Knapp, S. (2012). The bromodomain interaction module. *FEBS Lett.* 586(17): 2692-2704.
- Filippakopoulos, P., Picaud, S., Mangos, M., Keates, T., Lambert, J. P., Barsyte-Lovejoy, D., Felletar, I., Volkmer, R., Müller, S., Pawson, T., et al. (2012). Histone recognition and large-scale structural analysis of the human bromodomain family. *Cell.* 149(1): 214-231.
- Foreman, K. W., Brown, M., Park, F., Emtage, S., Harriss, J., Das, C., Zhu, L., Crew, A., Arnold, L., Shaaban, S., Tucker, P. (2011). Structural and functional profiling of the human histone methyltransferase SMYD3. *PLoS One.* 6(7): e22290.
- Fraga, M. F., Ballestar, E., Villar-Garea, A., Boix-Chornet, M., Espada, J., Schotta, G., Bonaldi, T., Haydon, C., Roperio, S., Petrie, K., et al. (2005). Loss of acetylation at Lys16 and trimethylation at Lys20 of histone H4 is a common hallmark of human cancer. *Nat Genet.* (4): 391-400.

- Freund, A., Patil, C. K., Campisi, J. (2011). p38MAPK is a novel DNA damage response-independent regulator of the senescence-associated secretory phenotype. *EMBO J.* 30(8): 1536-1548.
- Freund, A., Laberge, R. M., Demaria, M., Campisi, J. (2012). Lamin B1 loss is a senescence-associated biomarker. *Mol Biol Cell.* 23(11): 2066-2075.
- Fu, Y., Sinha, M., Peterson, C. L., Weng, Z. (2008). The insulator binding protein CTCF positions 20 nucleosomes around its binding sites across the human genome. *PLoS Genet.* 4(7): e1000138.
- Fujita, K., Mondal, A. M., Horikawa, I., Nguyen, G. H., Kumamoto, K., Sohn, J. J., Bowman, E. D., Mathe, E. A., Schetter, A. J., Pine, S. R., et al. (2009). p53 isoforms Delta133p53 and p53beta are endogenous regulators of replicative cellular senescence. *Nat Cell Biol.* (9): 1135-1142.
- Fumagalli, M., Rossiello, F., Clerici, M., Barozzi, S., Cittaro, D., Kaplunov, J. M., Bucci, G., Dobrev, M., Matti, V., Beausejour, C. M., et al. (2012). Telomeric DNA damage is irreparable and causes persistent DNA-damage-response activation. *Nat Cell Biol.* 14(4): 355-365.
- Funayama, R., Saito, M., Tanobe, H., Ishikawa, F. (2006). Loss of linker histone H1 in cellular senescence. *J Cell Biol.* 175(6): 869-880.
- Furumoto, K., Inoue, E., Nagao, N., Hiyama, E., Miwa, N. (1998). Age-dependent telomere shortening is slowed down by enrichment of intracellular vitamin C via suppression of oxidative stress. *Life Sci.* 63(11): 935-948.
- Gall, J. G. (1966). Chromosome fibers studied by a spreading technique. *Chromosoma.* 20(2): 221-233.
- Gamerding, M., Hajieva, P., Kaya, A. M., Wolfrum, U., Hartl, F. U., Behl, C. (2009). Protein quality control during aging involves recruitment of the macroautophagy pathway by BAG3. *EMBO J.* 28(7): 889-901.
- Gama-Sosa, M. A., Midgett, R. M., Slagel, V. A., Githens, S., Kuo, K. C., Gehrke, C. W., Ehrlich, M. (1983). Tissue-specific differences in DNA methylation in various mammals. *Biochim Biophys Acta.* 740(2): 212-219.
- Garcia, B. A., Thomas, C. E., Kelleher, N. L., Mizzen, C. A. (2008). Tissue-specific expression and post-translational modification of histone H3 variants. *J Proteome Res.* 7(10): 4225-4236.
- Gardiner-Garden, M., Frommer, M. (1987). CpG islands in vertebrate genomes. *J Mol Biol.* 196(2): 261-282.
- Gautier, T., Abbott, D. W., Molla, A., Verdel, A., Ausio, J., Dimitrov, S. (2004). Histone variant H2ABbd confers lower stability to the nucleosome. *EMBO Rep.* 5(7): 715-720.

- Gil, J., Peters, G. (2006). Regulation of the INK4b-ARF-INK4a tumour suppressor locus: all for one or one for all. *Nat Rev Mol Cell Biol.* 7(9): 667-677.
- Gillies, R. J., Didier, N., Denton, M. (1986). Determination of cell number in monolayer cultures. *Anal Biochem.* 159(1): 109-113.
- Goldberg, A. D., Banaszynski, L. A., Noh, K. M., Lewis, P. W., Elsaesser, S. J., Stadler, S., Dewell, S., Law, M., Guo, X., Li, X., et al. (2010). Distinct factors control histone variant H3.3 localization at specific genomic regions. *Cell.* 140(5): 678-691.
- Gonzalo, S., García-Cao, M., Fraga, M. F., Schotta, G., Peters, A. H., Cotter, S. E., Eguía, R., Dean, D. C., Esteller, M., Jenuwein, T., et al. (2005). Role of the RB1 family in stabilizing histone methylation at constitutive heterochromatin. *Nat Cell Biol.* 7(4): 420-428.
- Gowher, H., Liebert, K., Hermann, A., Xu, G., Jeltsch, A. (2005). Mechanism of stimulation of catalytic activity of Dnmt3A and Dnmt3B DNA-(cytosine-C5)-methyltransferases by Dnmt3L. *J Biol Chem.* 280(14): 13341-13348.
- Grandori, C., Wu, K. J., Fernandez, P., Ngouenet, C., Grim, J., Clurman, B. E., Moser, M. J., Oshima, J., Russell, D. W., Swisshelm, K., et al. (2003). Werner syndrome protein limits MYC-induced cellular senescence. *Genes Dev.* 17(13): 1569-1574.
- Gray-Schopfer, V. C., Cheong, S. C., Chong, H., Chow, J., Moss, T., Abdel-Malek, Z. A., Marais, R., Wynford-Thomas, D., Bennett, D. C. (2006). Cellular senescence in naevi and immortalisation in melanoma: a role for p16? *Br J Cancer.* 95(4):496-505.
- Gray-Schopfer, V., Wellbrock, C., Marais, R. (2007). Melanoma biology and new targeted therapy. *Nature.* 445(7130): 851-857.
- Greer, E. L., Shi, Y. (2012). Histone methylation: a dynamic mark in health, disease and inheritance. *Nat Rev Genet.* 13(5): 343-357.
- Grigoryev, S. A., Woodcock, C. L. (2012). Chromatin organization - the 30 nm fiber. *Exp Cell Res.* 318(12): 1448-1455.
- Guelen, L., Pagie, L., Brasset, E., Meuleman, W., Faza, M. B., Talhout, W., Eussen, B. H., de Klein, A., Wessels, L., de Laat, W., et al. (2008). Domain organization of human chromosomes revealed by mapping of nuclear lamina interactions. *Nature.* 453(7197): 948-951.
- Gurtner, A., Fuschi, P., Magi, F., Colussi, C., Gaetano, C., Dobbelstein, M., Sacchi, A., Piaggio, G. (2008a). NF-Y dependent epigenetic modifications discriminate between proliferating and postmitotic tissue. *PLoS One.* 3(4): e2047.

- Gurtner, G. C., Werner, S., Barrandon, Y., Longaker, M. T. (2008b). Wound repair and regeneration. *Nature*. 453(7193): 314-321.
- Hahn, W. C., Dessain, S. K., Brooks, M. W., King, J. E., Elenbaas, B., Sabatini, D. M., DeCaprio, J. A., Weinberg, R. A. (2002). Enumeration of the simian virus 40 early region elements necessary for human cell transformation. *Mol Cell Biol*. 22(7): 2111-2123.
- Hansen, J. C. (2002). Conformational dynamics of the chromatin fiber in solution: determinants, mechanisms, and functions. *Annu Rev Biophys Biomol Struct*. 31: 361-392.
- Harley, C. B., Futcher, A. B., Greider, C. W. (1990). Telomeres shorten during ageing of human fibroblasts. *Nature*. 345(6274): 458-460.
- Harvey, M., Sands, A. T., Weiss, R. S., Hegi, M. E., Wiseman, R. W., Pantazis, P., Giovanella, B. C., Tainsky, M. A., Bradley, A., Donehower, L. A. (1993). In vitro growth characteristics of embryo fibroblasts isolated from p53-deficient mice. *Oncogene*. 8(9): 2457-2467.
- Hastie, N. D., Dempster, M., Dunlop, M. G., Thompson, A. M., Green, D. K., Allshire, R. C. (1990). Telomere reduction in human colorectal carcinoma and with ageing. *Nature*. 346(6287): 866-868.
- Hayflick, L., Moorhead, P. S. (1961). The serial cultivation of human diploid cell strains. *Exp Cell Res*. 25: 585-621.
- Hayflick, L. (1965). The limited in vitro lifetime of human diploid cell strains. *Exp Cell Res*. 37: 614-36.
- He, G., Siddik, Z. H., Huang, Z., Wang, R., Koomen, J., Kobayashi, R., Khokhar, A. R., Kuang, J. (2005). Induction of p21 by p53 following DNA damage inhibits both Cdk4 and Cdk2 activities. *Oncogene*. 24(18): 2929-2943.
- He, J., Kallin, E. M., Tsukada, Y., Zhang, Y. (2008). The H3K36 demethylase Jhdm1b/Kdm2b regulates cell proliferation and senescence through p15(Ink4b). *Nat Struct Mol Biol*. 15(11): 1169-1175.
- Helenius, M., Mäkeläinen, L., Salminen, A. (1999). Attenuation of NF-kappaB signaling response to UVB light during cellular senescence. *Exp Cell Res*. 248(1): 194-202.
- Hempel, K., Lange, H. W., Birkofer, L. (1968). epsilon-N-trimethyllysine, a new amino acid in histones. *Naturwissenschaften*. 55(1): 37.
- Henckel, A., Nakabayashi, K., Sanz, L. A., Feil, R., Hata, K., Arnaud, P. (2009). Histone methylation is mechanistically linked to DNA methylation at imprinting control regions in mammals. *Hum Mol Genet*. 18(18): 3375-3383.

- Herbig, U., Jobling, W. A., Chen, B. P., Chen, D. J., Sedivy, J. M. (2004). Telomere shortening triggers senescence of human cells through a pathway involving ATM, p53, and p21(CIP1), but not p16(INK4a). *Mol Cell*. 14(4): 501-513.
- Herbig, U., Ferreira, M., Condel, L., Carey, D., Sedivy, J. M. (2006). Cellular senescence in aging primates. *Science*. 311(5765): 1257.
- Höger, T. H., Zatloukal, K., Waizenegger, I., Krohne, G. (1990). Characterization of a second highly conserved B-type lamin present in cells previously thought to contain only a single B-type lamin. *Chromosoma*. 99(6): 379-390.
- Howard, G., Eiges, R., Gaudet, F., Jaenisch, R., Eden, A. (2008). Activation and transposition of endogenous retroviral elements in hypomethylation induced tumors in mice. *Oncogene*. 27(3): 404-408.
- Hsieh, C. L. (1999). In vivo activity of murine de novo methyltransferases, Dnmt3a and Dnmt3b. *Mol Cell Biol*. 19(12): 8211-8218.
- Huang, Y., Fang, J., Bedford, M. T., Zhang, Y., Xu, R. M. (2006). Recognition of histone H3 lysine-4 methylation by the double tudor domain of JMJD2A. *Science*. 312(5774): 748-751.
- Huang, S., Risques, R. A., Martin, G. M., Rabinovitch, P. S., Oshima, J. (2008). Accelerated telomere shortening and replicative senescence in human fibroblasts overexpressing mutant and wild-type lamin A. *Exp Cell Res*. 314(1): 82-91.
- Huisinga, K. L., Brower-Toland, B., Elgin, S. C. (2006). The contradictory definitions of heterochromatin: transcription and silencing. *Chromosoma*. 115(2): 110-122.
- International Human Genome Sequencing Consortium. (2004). Finishing the euchromatic sequence of the human genome. *Nature*. 431(7011): 931-945.
- Iqbal, K., Jin, S. G., Pfeifer, G. P., Szabó, P. E. (2011). Reprogramming of the paternal genome upon fertilization involves genome-wide oxidation of 5-methylcytosine. *Proc Natl Acad Sci U S A*. 108(9): 3642-3647.
- Jenuwein, T., Allis, C. D. (2001). Translating the histone code. *Science*. 293(5532): 1074-1080.
- Jeyapalan, J. C., Ferreira, M., Sedivy, J. M., Herbig, U. (2007). Accumulation of senescent cells in mitotic tissue of aging primates. *Mech Ageing Dev*. 128(1): 36-44.
- Johnson, S. M., Tan, F. J., McCullough, H. L., Riordan, D. P., Fire, A. Z. (2006). Flexibility and constraint in the nucleosome core landscape of *Caenorhabditis elegans* chromatin. *Genome Res*. 16(12): 1505-1516.
- Jones, P. A., Baylin, S. B. (2007). The epigenomics of cancer. *Cell*. 128(4): 683-692.

- Jun, J. I., Lau, L. F. (2010). The matricellular protein CCN1 induces fibroblast senescence and restricts fibrosis in cutaneous wound healing. *Nat Cell Biol.* 12(7): 676-685.
- Kandert, S., Wehnert, M., Müller, C. R., Buendia, B., Dabauvalle, M. C. (2009). Impaired nuclear functions lead to increased senescence and inefficient differentiation in human myoblasts with a dominant p.R545C mutation in the LMNA gene. *Eur J Cell Biol.* 88(10): 593-608.
- Kang, T. W., Yevsa, T., Woller, N., Hoenicke, L., Wuestefeld, T., Dauch, D., Hohmeyer, A., Gereke, M., Rudalska, R., Potapova, A., et al. (2011). Senescence surveillance of pre-malignant hepatocytes limits liver cancer development. *Nature.* (7374): 547-551.
- Kapoor-Vazirani, P., Kagey, J. D., Vertino, P. M. (2011). SUV420H2-mediated H4K20 trimethylation enforces RNA polymerase II promoter-proximal pausing by blocking hMOF-dependent H4K16 acetylation. *Mol Cell Biol.* 31(8): 1594-1609.
- Katakura, Y., Nakata, E., Miura, T., Shirahata, S. (1999). Transforming growth factor beta triggers two independent-senescence programs in cancer cells. *Biochem Biophys Res Commun.* 255(1): 110-115.
- Kennedy, B. K., Barbie, D. A., Classon, M., Dyson, N., Harlow, E. (2000). Nuclear organization of DNA replication in primary mammalian cells. *Genes Dev.* 14(22): 2855-2868.
- Kennedy, A. L., McBryan, T., Enders, G. H., Johnson, F. B., Zhang, R., Adams, P. D. (2010). Senescent mouse cells fail to overtly regulate the HIRA histone chaperone and do not form robust Senescence Associated Heterochromatin Foci. *Cell Div.* 5: 16.
- Kent, W. J., Sugnet, C. W., Furey, T. S., Roskin, K. M., Pringle, T. H., Zahler, A. M., Haussler, D. (2002). The human genome browser at UCSC. *Genome Res.* 12(6): 996-1006.
- Kidder, B. L., Hu, G., Zhao, K. (2011). ChIP-Seq: technical considerations for obtaining high-quality data. *Nat Immunol.* 12(10): 918-22.
- Kipling, D. (1997). Telomere structure and telomerase expression during mouse development and tumorigenesis. *Eur J Cancer.* 33(5): 792-800.
- Klimova, T. A., Bell, E. L., Shroff, E. H., Weinberg, F. D., Snyder, C. M., Dimri, G. P., Schumacker, P. T., Budinger, G. R., Chandel, N. S. (2009). Hyperoxia-induced premature senescence requires p53 and pRb, but not mitochondrial matrix ROS. *FASEB J.* 23(3): 783-794.
- Kobor, M. S., Venkatasubrahmanyam, S., Meneghini, M. D., Gin, J. W., Jennings, J. L., Link, A. J., Madhani, H. D., Rine, J. (2004). A protein complex

containing the conserved Swi2/Snf2-related ATPase Swr1p deposits histone variant H2A.Z into euchromatin. *PLoS Biol.* 2(5): E131.

- Koch, C. M., Jousen, S., Schellenberg, A., Lin, Q., Zenke, M., Wagner, W. (2012). Monitoring of cellular senescence by DNA-methylation at specific CpG sites. *Aging Cell.* 11(2): 366-369.
- Kohsaka, S., Sasai, K., Takahashi, K., Akagi, T., Tanino, M., Kimura, T., Nishihara, H., Tanaka, S. (2011). A population of BJ fibroblasts escaped from Ras-induced senescence susceptible to transformation. *Biochem Biophys Res Commun.* 410(4): 878-884.
- Korber, P., Barbaric, S., Luckenbach, T., Schmid, A., Schermer, U. J., Blaschke, D., Hörz, W. (2006). The histone chaperone Asf1 increases the rate of histone eviction at the yeast PHO5 and PHO8 promoters. *J Biol Chem.* 281(9): 5539-5545.
- Kortlever, R. M., Higgins, P. J., Bernards, R. (2006). Plasminogen activator inhibitor-1 is a critical downstream target of p53 in the induction of replicative senescence. *Nat Cell Biol.* 8(8): 877-884.
- Kosar, M., Bartkova, J., Hubackova, S., Hodny, Z., Lukas, J., Bartek, J. (2011). Senescence-associated heterochromatin foci are dispensable for cellular senescence, occur in a cell type- and insult-dependent manner and follow expression of p16(ink4a). *Cell Cycle.* 10(3): 457-468.
- Kouzarides, T. (2007). Chromatin modifications and their function. *Cell.* 128(4): 693-705.
- Kovalchuk, O., Tryndyak, V. P., Montgomery, B., Boyko, A., Kutanzi, K., Zemp, F., Warbritton, A. R., Latendresse, J. R., Kovalchuk, I., Beland, F. A., et al. (2007). Estrogen-induced rat breast carcinogenesis is characterized by alterations in DNA methylation, histone modifications and aberrant microRNA expression. *Cell Cycle.* 6(16): 2010-2018.
- Krishnamurthy, J., Torrice, C., Ramsey, M. R., Kovalev, G. I., Al-Regaiey, K., Su, L., Sharpless, N. E. (2004). Ink4a/Arf expression is a biomarker of aging. *J Clin Invest.* 114(9): 1299-1307.
- Krishnamurthy, J., Ramsey, M. R., Ligon, K. L., Torrice, C., Koh, A., Bonner-Weir, S., Sharpless, N. E. (2006). p16INK4a induces an age-dependent decline in islet regenerative potential. *Nature.* 443(7110): 453-457.
- Krizhanovsky, V., Yon, M., Dickins, R. A., Hearn, S., Simon, J., Miething, C., Yee, H., Zender, L., Lowe, S. W. (2008). Senescence of activated stellate cells limits liver fibrosis. *Cell.* 134(4): 657-667.
- Krogan, N. J., Kim, M., Tong, A., Golshani, A., Cagney, G., Canadien, V., Richards, D. P., Beattie, B. K., Emili, A., Boone, C., et al. (2003). Methylation of

- histone H3 by Set2 in *Saccharomyces cerevisiae* is linked to transcriptional elongation by RNA polymerase II. *Mol Cell Biol.* 23(12): 4207-4218.
- Krtolica, A., Parrinello, S., Lockett, S., Desprez, P. Y., Campisi, J. (2001). Senescent fibroblasts promote epithelial cell growth and tumorigenesis: a link between cancer and aging. *Proc Natl Acad Sci U S A.* 98(21): 12072-12077.
- Kuilman, T., Michaloglou, C., Vredeveld, L. C., Douma, S., van Doorn, R., Desmet, C. J., Aarden, L. A., Mooi, W. J., Peeper, D. S. (2008). Oncogene-induced senescence relayed by an interleukin-dependent inflammatory network. *Cell.* 133(6): 1019-1031.
- Kurz, E. U., Lees-Miller, S. P. (2004). DNA damage-induced activation of ATM and ATM-dependent signaling pathways. *DNA Repair (Amst).* 3(8-9): 889-900.
- Kwon, M. J., Kim, S. S., Choi, Y. L., Jung, H. S., Balch, C., Kim, S. H., Song, Y. S., Marquez, V. E., Nephew, K. P., Shin, Y. K. (2010). Derepression of CLDN3 and CLDN4 during ovarian tumorigenesis is associated with loss of repressive histone modifications. *Carcinogenesis.* 31(6): 974-983.
- Landt, S. G., Marinov, G. K., Kundaje, A., Kheradpour, P., Pauli, F., Batzoglou, S., Bernstein, B. E., Bickel, P., Brown, J. B., Cayting, P., et al. (2012). CHIP-seq guidelines and practices of the ENCODE and modENCODE consortia. *Genome Res.* 22(9): 1813-1831.
- Langmead, B., Trapnell, C., Pop, M., Salzberg, S. L. (2009). Ultrafast and memory-efficient alignment of short DNA sequences to the human genome. *Genome Biol.* 10(3): R25.
- Lapunzina, P. (2005). Risk of tumorigenesis in overgrowth syndromes: a comprehensive review. *Am J Med Genet C Semin Med Genet.* 137C(1): 53-71.
- Lee, A. C., Fenster, B. E., Ito, H., Takeda, K., Bae, N. S., Hirai, T., Yu, Z. X., Ferrans, V. J., Howard, B. H., Finkel, T. (1999). Ras proteins induce senescence by altering the intracellular levels of reactive oxygen species. *J Biol Chem.* 274(12): 7936-7940.
- Lee, W., Tillo, D., Bray, N., Morse, R. H., Davis, R. W., Hughes, T. R., Nislow, C. (2007). A high-resolution atlas of nucleosome occupancy in yeast. *Nat Genet.* 39(10): 1235-1244.
- Lee, J., Thompson, J. R., Botuyan, M. V., Mer, G. (2008). Distinct binding modes specify the recognition of methylated histones H3K4 and H4K20 by JMJD2A-tudor. *Nat Struct Mol Biol.* 15(1): 109-111.
- Lengauer, C., Kinzler, K. W., Vogelstein, B. (1997). Genetic instability in colorectal cancers. *Nature.* 386(6625): 623-627.

- Levine, B., Kroemer, G. (2008). Autophagy in the pathogenesis of disease. *Cell*. 132(1): 27-42.
- Li, E., Bestor, T. H., Jaenisch, R. (1992). Targeted mutation of the DNA methyltransferase gene results in embryonic lethality. *Cell*. 69(6): 915-926.
- Li, E., Beard, C., Jaenisch, R. (1993). Role for DNA methylation in genomic imprinting. *Nature*. 366(6453): 362-365.
- Li, H., Ilin, S., Wang, W., Duncan, E. M., Wysocka, J., Allis, C. D., Patel, D. J. (2006). Molecular basis for site-specific read-out of histone H3K4me3 by the BPTF PHD finger of NURF. *Nature*. 442(7098): 91-95.
- Lin, F., Worman, H. J. (1993). Structural organization of the human gene encoding nuclear lamin A and nuclear lamin C. *J Biol Chem*. 268(22): 16321-16326.
- Lin, F., Worman, H. J. (1995). Structural organization of the human gene (LMNB1) encoding nuclear lamin B1. *Genomics*. 27(2): 230-236.
- Lin, A. W., Barradas, M., Stone, J. C., van Aelst, L., Serrano, M., Lowe, S. W. (1998). Premature senescence involving p53 and p16 is activated in response to constitutive MEK/MAPK mitogenic signaling. *Genes Dev*. 12(19): 3008-3019.
- Lowe, S. W., Sherr, C. J. (2003). Tumor suppression by Ink4a-Arf: progress and puzzles. *Curr Opin Genet Dev*. 13(1): 77-83.
- Luger, K., Mäder, A. W., Richmond, R. K., Sargent, D. F., Richmond, T. J. (1997). Crystal structure of the nucleosome core particle at 2.8 Å resolution. *Nature*. 389(6648): 251-260.
- Ma, M. K., Heath, C., Hair, A., West, A. G. (2011). Histone crosstalk directed by H2B ubiquitination is required for chromatin boundary integrity. *PLoS Genet*. 7(7): e1002175.
- Ma, T., Van Tine, B. A., Wei, Y., Garrett, M. D., Nelson, D., Adams, P. D., Wang, J., Qin, J., Chow, L. T., Harper, J. W. (2000). Cell cycle-regulated phosphorylation of p220(NPAT) by cyclin E/Cdk2 in Cajal bodies promotes histone gene transcription. *Genes Dev*. 14(18): 2298-313.
- Malik, H. S., Henikoff, S. (2003). Phylogenomics of the nucleosome. *Nat Struct Biol*. 10(11): 882-891.
- Mancini-Dinardo, D., Steele, S. J., Levorse, J. M., Ingram, R. S., Tilghman, S. M. (2006). Elongation of the Kcnq1ot1 transcript is required for genomic imprinting of neighboring genes. *Genes Dev*. 20(10): 1268-1282.
- Marks, H., Chow, J. C., Denissov, S., François, K. J., Brockdorff, N., Heard, E., Stunnenberg, H. G. (2009). High-resolution analysis of epigenetic changes associated with X inactivation. *Genome Res*. 19(8): 1361-1373.

- Martens, U. M., Chavez, E. A., Poon, S. S., Schmoor, C., Lansdorp, P. M. (2000). Accumulation of short telomeres in human fibroblasts prior to replicative senescence. *Exp Cell Res.* 256(1): 291-299.
- McClintock, D., Gordon, L. B., Djabali, K. (2006). Hutchinson-Gilford progeria mutant lamin A primarily targets human vascular cells as detected by an anti-Lamin A G608G antibody. *Proc Natl Acad Sci U S A.* 103(7): 2154-2159.
- McEwen, K. R., Ferguson-Smith, A. C. (2010). Distinguishing epigenetic marks of developmental and imprinting regulation. *Epigenetics Chromatin.* 3(1): 2.
- McKittrick, E., Gafken, P. R., Ahmad, K., Henikoff, S. (2004). Histone H3.3 is enriched in covalent modifications associated with active chromatin. *Proc Natl Acad Sci U S A.* 101(6): 1525-1530.
- Medrano, E. E., Im, S., Yang, F., Abdel-Malek, Z. A. (1995). Ultraviolet B light induces G1 arrest in human melanocytes by prolonged inhibition of retinoblastoma protein phosphorylation associated with long-term expression of the p21Waf-1/SDI-1/Cip-1 protein. *Cancer Res.* 55(18): 4047-4052.
- Meerbrey, K. L., Hu, G., Kessler, J. D., Roarty, K., Li, M. Z., Fang, J. E., Herschkowitz, J. I., Burrows, A. E., Ciccia, A., Sun, T., et al. (2011). The pINDUCER lentiviral toolkit for inducible RNA interference in vitro and in vivo. *Proc Natl Acad Sci U S A.* 108(9): 3665-3670.
- Michaloglou, C., Vredeveld, L. C., Soengas, M. S., Denoyelle, C., Kuilman, T., van der Horst, C. M., Majoor, D. M., Shay, J. W., Mooi, W. J., Peeper, D. S. (2005). BRAFE600-associated senescence-like cell cycle arrest of human naevi. *Nature.* 436(7051): 720-724.
- Min, J., Feng, Q., Li, Z., Zhang, Y., Xu, R. M. (2003). Structure of the catalytic domain of human DOT1L, a non-SET domain nucleosomal histone methyltransferase. *Cell.* 112(5): 711-723.
- Mito, Y., Henikoff, J. G., Henikoff, S. (2005). Genome-scale profiling of histone H3.3 replacement patterns. *Nat Genet.* 37(10): 1090-1097.
- Mizuguchi, G., Shen, X., Landry, J., Wu, W. H., Sen, S., Wu, C. (2004). ATP-driven exchange of histone H2AZ variant catalyzed by SWR1 chromatin remodeling complex. *Science.* 303(5656): 343-348.
- Mizushima, N. (2007). Autophagy: process and function. *Genes Dev.* 21(22): 2861-2873.
- Moir, R. D., Montag-Lowy, M., Goldman, R. D. (1994). Dynamic properties of nuclear lamins: lamin B is associated with sites of DNA replication. *J Cell Biol.* 125(6): 1201-1212.

- Moir, R. D., Spann, T. P., Herrmann, H., Goldman, R. D. (2000). Disruption of nuclear lamin organization blocks the elongation phase of DNA replication. *J Cell Biol.* 149(6): 1179-1192.
- Moiseeva, O., Bourdeau, V., Vernier, M., Dabauvalle, M. C., Ferbeyre, G. (2011). Retinoblastoma-independent regulation of cell proliferation and senescence by the p53-p21 axis in lamin A/C-depleted cells. *Aging Cell.* 10(5): 789-797.
- Mondal, T., Rasmussen, M., Pandey, G. K., Isaksson, A., Kanduri, C. (2010). Characterization of the RNA content of chromatin. *Genome Res.* 20(7): 899-907.
- Morton, J. P., Timpson, P., Karim, S. A., Ridgway, R. A., Athineos, D., Doyle, B., Jamieson, N. B., Oien, K. A., Lowy, A. M., Brunton, V. G., et al. (2010). Mutant p53 drives metastasis and overcomes growth arrest/senescence in pancreatic cancer. *Proc Natl Acad Sci U S A.* 107(1): 246-251.
- Mravinac, B., Sullivan, L. L., Reeves, J. W., Yan, C. M., Kopf, K. S., Farr, C. J., Schueler, M. G., Sullivan, B. A. (2009). Histone modifications within the human X centromere region. *PLoS One.* 4(8): e6602.
- Murray, K. (1964). The occurrence of epsilon-n-methyl lysine in histones. *Biochemistry.* 3: 10-15.
- Nagano, T., Mitchell, J. A., Sanz, L. A., Pauler, F. M., Ferguson-Smith, A. C., Feil, R., Fraser, P. (2008). The Air noncoding RNA epigenetically silences transcription by targeting G9a to chromatin. *Science.* 322(5908): 1717-1720.
- Narita, M., Nunez, S., Heard, E., Narita, M., Lin, A. W., Hearn, S. A., Spector, D. L., Hannon, G. J., Lowe, S. W. (2003). Rb-mediated heterochromatin formation and silencing of E2F target genes during cellular senescence. *Cell.* 113(6): 703-716.
- Narita, M., Narita, M., Krizhanovskiy, V., Nunez, S., Chicas, A., Hearn, S. A., Myers, M. P., Lowe, S. W. (2006). A novel role for high-mobility group proteins in cellular senescence and heterochromatin formation. *Cell.* 126(3): 503-514.
- Narita, M., Young, A. R., Arakawa, S., Samarajiwa, S. A., Nakashima, T., Yoshida, S., Hong, S., Berry, L. S., Reichelt, S., Ferreira, M., et al. (2011). Spatial coupling of mTOR and autophagy augments secretory phenotypes. *Science.* 332(6032): 966-970.
- Nevins, J. R. (2001). The Rb/E2F pathway and cancer. *Hum Mol Genet.* 10(7): 699-703.
- Newbold, R. F., Overell, R. W. (1983). Fibroblast immortality is a prerequisite for transformation by EJ c-Ha-ras oncogene. *Nature.* 304(5927): 648-651.

- Ng, H. H., Robert, F., Young, R. A., Struhl, K. (2003). Targeted recruitment of Set1 histone methylase by elongating Pol II provides a localized mark and memory of recent transcriptional activity. *Mol Cell*. 11(3): 709-719.
- Nichols, W. W., Murphy, D. G., Cristofalo, V. J., Toji, L. H., Greene, A. E., Dwight, S. A. (1977). Characterization of a new human diploid cell strain, IMR-90. *Science* 196(4285): 60-63.
- Nishimura, E. K., Granter, S. R., Fisher, D. E. (2005). Mechanisms of hair graying: incomplete melanocyte stem cell maintenance in the niche. *Science*. 307(5710): 720-724.
- Nishino, Y., Eltsov, M., Joti, Y., Ito, K., Takata, H., Takahashi, Y., Hihara, S., Frangakis, A. S., Imamoto, N., Ishikawa, T., et al. (2012). Human mitotic chromosomes consist predominantly of irregularly folded nucleosome fibres without a 30-nm chromatin structure. *EMBO J*. 31(7): 1644-1653.
- Ogryzko, V. V., Hirai, T. H., Russanova, V. R., Barbie, D. A., Howard, B. H. (1996). Human fibroblast commitment to a senescence-like state in response to histone deacetylase inhibitors is cell cycle dependent. *Mol Cell Biol*. 16(9): 5210-5218.
- Ohm, J. E., McGarvey, K. M., Yu, X., Cheng, L., Schuebel, K. E., Cope, L., Mohammad, H. P., Chen, W., Daniel, V. C., Yu, W., et al. (2007). A stem cell-like chromatin pattern may predispose tumor suppressor genes to DNA hypermethylation and heritable silencing. *Nat Genet*. 39(2): 237-242.
- Ohtani, N., Zebedee, Z., Huot, T. J., Stinson, J. A., Sugimoto, M., Ohashi, Y., Sharrocks, A. D., Peters, G., Hara, E. (2001). Opposing effects of Ets and Id proteins on p16INK4a expression during cellular senescence. *Nature*. 409(6823): 1067-1070.
- Orjalo, A. V., Bhaumik, D., Gengler, B. K., Scott, G. K., Campisi, J. (2009). Cell surface-bound IL-1alpha is an upstream regulator of the senescence-associated IL-6/IL-8 cytokine network. *Proc Natl Acad Sci U S A*. 106(40): 17031-17036.
- Osley, M. A. (1991). The regulation of histone synthesis in the cell cycle. *Annu. Rev. Biochem.* 60: 827-861.
- O'Sullivan, R. J., Kubicek, S., Schreiber, S. L., Karlseder, J. (2010). Reduced histone biosynthesis and chromatin changes arising from a damage signal at telomeres. *Nat Struct Mol Biol*. 17(10): 1218-1225.
- Owen, D. J., Ornaghi, P., Yang, J. C., Lowe, N., Evans, P. R., Ballario, P., Neuhaus, D., Filetici, P., Travers, A. A. (2000). The structural basis for the recognition of acetylated histone H4 by the bromodomain of histone acetyltransferase gcn5p. *EMBO J*. 19(22): 6141-6149.

- Ozboyaci, M., Gursoy, A., Erman, B., Keskin, O. (2011). Molecular recognition of H3/H4 histone tails by the tudor domains of JMJD2A: a comparative molecular dynamics simulations study. *PLoS One*. 6(3): e14765.
- Ozsolak, F., Song, J. S., Liu, X. S., Fisher, D. E. (2007). High-throughput mapping of the chromatin structure of human promoters. *Nat Biotechnol*. 25(2): 244-248.
- Packer, L., Fuehr, K. (1977). Low oxygen concentration extends the lifespan of cultured human diploid cells. *Nature*. 267(5610): 423-425.
- Page-McCaw, A., Ewald, A. J., Werb, Z. (2007). Matrix metalloproteinases and the regulation of tissue remodelling. *Nat Rev Mol Cell Biol*. 8(3): 221-233.
- Paik, W. K., Kim, S. (1967). epsilon-N-dimethyllysine in histones. *Biochem. Biophys. Res. Commun*. 27(4): 479-483.
- Palmer, D. K., O'Day, K., Wener, M. H., Andrews, B. S., Margolis, R. L. (1987). A 17-kD centromere protein (CENP-A) copurifies with nucleosome core particles and with histones. *J Cell Biol*. 104(4): 805-815.
- Pandey, R. R., Mondal, T., Mohammad, F., Enroth, S., Redrup, L., Komorowski, J., Nagano, T., Mancini-Dinardo, D., Kanduri, C. (2008). Kcnq1ot1 antisense noncoding RNA mediates lineage-specific transcriptional silencing through chromatin-level regulation. *Mol Cell*. 32(2): 232-246.
- Pang, J. H., Chen, K. Y. (1994). Global change of gene expression at late G1/S boundary may occur in human IMR-90 diploid fibroblasts during senescence. *J Cell Physiol*. 160(3): 531-538.
- Panning, B., Jaenisch, R. (1998). RNA and the epigenetic regulation of X chromosome inactivation. *Cell*. 93(3): 305-308.
- Paradis, V., Youssef, N., Dargère, D., Bâ, N., Bonvoust, F., Deschatrette, J., Bedossa, P. (2001). Replicative senescence in normal liver, chronic hepatitis C, and hepatocellular carcinomas. *Hum Pathol*. 32(3): 327-332.
- Parrinello, S., Samper, E., Krtolica, A., Goldstein, J., Melov, S., Campisi, J. (2003). Oxygen sensitivity severely limits the replicative lifespan of murine fibroblasts. *Nat Cell Biol*. 5(8): 741-747.
- Pasini, D., Bracken, A. P., Jensen, M. R., Lazzerini Denchi, E., Helin, K. (2004). Suz12 is essential for mouse development and for EZH2 histone methyltransferase activity. *EMBO J*. 23(20): 4061-4071.
- Pauler, F. M., Sloane, M. A., Huang, R., Regha, K., Koerner, M. V., Tamir, I., Sommer, A., Aszodi, A., Jenuwein, T., Barlow, D. P. (2009). H3K27me3 forms BLOCs over silent genes and intergenic regions and specifies a histone banding pattern on a mouse autosomal chromosome. *Genome Res*. 19(2): 221-233.

- Paull, T. T., Rogakou, E. P., Yamazaki, V., Kirchgessner, C. U., Gellert, M., Bonner, W. M. (2000). A critical role for histone H2AX in recruitment of repair factors to nuclear foci after DNA damage. *Curr Biol.* 10(15): 886-895.
- Pearson, M., Carbone, R., Sebastiani, C., Cioce, M., Fagioli, M., Saito, S., Higashimoto, Y., Appella, E., Minucci, S., Pandolfi, P. P., et al. (2000). PML regulates p53 acetylation and premature senescence induced by oncogenic Ras. *Nature.* 406(6792): 207-210.
- Pehrson, J. R., Fried, V. A. (1992). MacroH2A, a core histone containing a large nonhistone region. *Science.* 257(5075): 1398-1400.
- Pekovic, V., Gibbs-Seymour, I., Markiewicz, E., Alzoghaibi, F., Benham, A. M., Edwards, R., Wenhert, M., von Zglinicki, T., Hutchison, C. J. (2011). Conserved cysteine residues in the mammalian lamin A tail are essential for cellular responses to ROS generation. *Aging Cell.* 10(6): 1067-1079.
- Penny, G. D., Kay, G. F., Sheardown, S. A., Rastan, S., Brockdorff, N. (1996). Requirement for Xist in X chromosome inactivation. *Nature.* 379(6561): 131-137.
- Peric-Hupkes, D., Meuleman, W., Pagie, L., Bruggeman, S. W., Solovei, I., Brugman, W., Gräf, S., Flicek, P., Kerkhoven, R. M., van Lohuizen, M., et al. (2010). Molecular maps of the reorganization of genome-nuclear lamina interactions during differentiation. *Mol Cell.* 38(4): 603-613.
- Pesavento, J. J., Yang, H., Kelleher, N. L., Mizzen, C. A. (2008). Certain and progressive methylation of histone H4 at lysine 20 during the cell cycle. *Mol Cell Biol.* 28(1): 468-486.
- Pfau, R., Tzatsos, A., Kampranis, S. C., Serebrennikova, O. B., Bear, S. E., Tsiichlis, P. N. (2008). Members of a family of JmjC domain-containing oncoproteins immortalize embryonic fibroblasts via a JmjC domain-dependent process. *Proc Natl Acad Sci U S A.* 105(6): 1907-1912.
- Phalke, S., Nickel, O., Walluscheck, D., Hortig, F., Onorati, M. C., Reuter, G. (2009). Retrotransposon silencing and telomere integrity in somatic cells of *Drosophila* depends on the cytosine-5 methyltransferase DNMT2. *Nat Genet.* 2009 41(6): 696-702.
- Pickersgill, H., Kalverda, B., de Wit, E., Talhout, W., Fornerod, M., van Steensel, B. (2006). Characterization of the *Drosophila melanogaster* genome at the nuclear lamina. *Nat Genet.* 38(9): 1005-1014.
- Place, R. F., Noonan, E. J., Giardina, C. (2005). HDACs and the senescent phenotype of WI-38 cells. *BMC Cell Biol.* 6: 37.

- Pogribny, I. P., Ross, S. A., Tryndyak, V. P., Pogribna, M., Poirier, L. A., Karpinets, T. V. (2006). Histone H3 lysine 9 and H4 lysine 20 trimethylation and the expression of Suv4-20h2 and Suv-39h1 histone methyltransferases in hepatocarcinogenesis induced by methyl deficiency in rats. *Carcinogenesis* 27: 1180–1186.
- Pollock, P. M., Harper, U. L., Hansen, K. S., Yudt, L. M., Stark, M., Robbins, C. M., Moses, T. Y., Hostetter, G., Wagner, U., Kakareka, J., et al. (2003). High frequency of BRAF mutations in nevi. *Nat Genet.* 33(1): 19-20.
- Popescu, N., Zimonjic, D., Hatch, C., Bonner, W. (1994). Chromosomal mapping of the human histone gene H2AZ to 4q24 by fluorescence in situ hybridization. *Genomics.* 20(2): 333-335.
- Ragnauth, C. D., Warren, D. T., Liu, Y., McNair, R., Tajsic, T., Figg, N., Shroff, R., Skepper, J., Shanahan, C. M. (2010). Prelamin A acts to accelerate smooth muscle cell senescence and is a novel biomarker of human vascular aging. *Circulation.* 121(20): 2200-2210.
- Rayasam, G. V., Wendling, O., Angrand, P. O., Mark, M., Niederreither, K., Song, L., Lerouge, T., Hager, G. L., Chambon, P., Losson, R. (2003). NSD1 is essential for early post-implantation development and has a catalytically active SET domain. *EMBO J.* 22(12): 3153-3163.
- Regha, K., Sloane, M. A., Huang, R., Pauler, F. M., Warczok, K. E., Melikant, B., Radolf, M., Martens, J. H., Schotta, G., Jenuwein, T., et al. (2007). Active and repressive chromatin are interspersed without spreading in an imprinted gene cluster in the mammalian genome. *Mol Cell.* 27(3): 353-366.
- Richards, E. J., Elgin, S. C. (2002). Epigenetic codes for heterochromatin formation and silencing: rounding up the usual suspects. *Cell.* 108(4): 489-500.
- Richmond, T. J., Finch, J. T., Rushton, B., Rhodes, D., Klug, A. (1984). Structure of the nucleosomes core particle at 7 Å resolution. *Nature.* 311(5986): 532-537.
- Rinn, J. L., Kertesz, M., Wang, J. K., Squazzo, S. L., Xu, X., Bruggmann, S. A., Goodnough, L. H., Helms, J. A., Farnham, P. J., Segal, E., et al. (2007). Functional demarcation of active and silent chromatin domains in human HOX loci by noncoding RNAs. *Cell.* 129(7): 1311-1323.
- Roberson, R. S., Kussick, S. J., Vallieres, E., Chen, S. Y., Wu, D. Y. (2005). Escape from therapy-induced accelerated cellular senescence in p53-null lung cancer cells and in human lung cancers. *Cancer Res.* 65(7): 2795-2803.
- Robinson, M. D., Oshlack, A. (2010). A scaling normalization method for differential expression analysis of RNA-seq data. *Genome Biol.* 11(3): R25.
- Rodier, F., Coppé, J. P., Patil, C. K., Hoeijmakers, W. A., Muñoz, D. P., Raza, S. R., Freund, A., Campeau, E., Davalos, A. R., Campisi, J. (2009). Persistent DNA

damage signalling triggers senescence-associated inflammatory cytokine secretion. *Nat Cell Biol.* 11(8): 973-979.

- Rodríguez-Campos, A., Azorín, F. (2007). RNA is an integral component of chromatin that contributes to its structural organization. *PLoS One.* 2(11): e1182.
- Routh, A., Sandin, S., Rhodes, D. (2008). Nucleosome repeat length and linker histone stoichiometry determine chromatin fiber structure. *Proc Natl Acad Sci U S A.* 105(26): 8872-8877.
- Rudolph, K. L., Chang, S., Lee, H. W., Blasco, M., Gottlieb, G. J., Greider, C., DePinho, R. A. (1999). Longevity, stress response, and cancer in aging telomerase-deficient mice. *Cell.* 96(5): 701-712.
- Ryazanov, A. G., Nefsky, B. S. (2002). Protein turnover plays a key role in aging. *Mech Ageing Dev.* 123(2-3): 207-213.
- Sage, J., Mulligan, G. J., Attardi, L. D., Miller, A., Chen, S., Williams, B., Theodorou, E., Jacks, T. (2000). Targeted disruption of the three Rb-related genes leads to loss of G(1) control and immortalization. *Genes Dev.* 14(23): 3037-3050.
- Saito, H., Hammond, A. T., Moses, R. E. (1995). The effect of low oxygen tension on the in vitro-replicative life span of human diploid fibroblast cells and their transformed derivatives. *Exp Cell Res.* 217(2): 272-279.
- Sanders, S. L., Portoso, M., Mata, J., Bähler, J., Allshire, R. C., Kouzarides, T. (2004). Methylation of histone H4 lysine 20 controls recruitment of Crb2 to sites of DNA damage. *Cell.* 119(5): 603-614.
- Sanders, S. L., Arida, A. R., Phan, F. P. (2010). Requirement for the phospho-H2AX binding module of Crb2 in double-strand break targeting and checkpoint activation. *Mol Cell Biol.* 30(19): 4722-4731.
- Santisteban, M. S., Kalashnikova, T., Smith, M. M. (2000). Histone H2A.Z regulates transcription and is partially redundant with nucleosome remodeling complexes. *Cell.* 103(3): 411-422.
- Santos-Rosa, H., Schneider, R., Bannister, A. J., Sherriff, J., Bernstein, B. E., Emre, N. C., Schreiber, S. L., Mellor, J., Kouzarides, T. (2002). Active genes are trimethylated at K4 of histone H3. *Nature.* 419(6905): 407-411.
- Sarg, B., Koutzamani, E., Helliger, W., Rundquist, I., Lindner, H. H. (2002). Postsynthetic trimethylation of histone H4 at lysine 20 in mammalian tissues is associated with aging. *J Biol Chem.* 277(42): 39195-39201.
- Sarg, B., Chwatal, S., Talasz, H., Lindner, H. H. (2009). Testis-specific linker histone H1t is multiply phosphorylated during spermatogenesis. Identification of phosphorylation sites. *J Biol Chem.* 284(6): 3610-3618.

- Sarkisian, C. J., Keister, B. A., Stairs, D. B., Boxer, R. B., Moody, S. E., Chodosh, L. A. (2007). Dose-dependent oncogene-induced senescence in vivo and its evasion during mammary tumorigenesis. *Nat Cell Biol.* 9(5): 493-505.
- Saxena, A., Carninci, P. (2011). Long non-coding RNA modifies chromatin: epigenetic silencing by long non-coding RNAs. *Bioessays.* 33(11): 830-839.
- Schellenberg, A., Lin, Q., Schüler, H., Koch, C. M., Joussen, S., Denecke, B., Walenda, G., Pallua, N., Suschek, C. V., Zenke, M., et al. (2011). Replicative senescence of mesenchymal stem cells causes DNA-methylation changes which correlate with repressive histone marks. *Aging (Albany NY).* 3(9): 873-888.
- Schlesinger, Y., Straussman, R., Keshet, I., Farkash, S., Hecht, M., Zimmerman, J., Eden, E., Yakhini, Z., Ben-Shushan, E., Reubinoff, B. E., et al. (2007). Polycomb-mediated methylation on Lys27 of histone H3 pre-marks genes for de novo methylation in cancer. *Nat Genet.* 39(2): 232-236.
- Schneider, A. C., Heukamp, L. C., Rogenhofer, S., Fechner, G., Bastian, P. J., von Ruecker, A., Müller, S. C., Ellinger, J. (2011). Global histone H4K20 trimethylation predicts cancer-specific survival in patients with muscle-invasive bladder cancer. *BJU Int.* 108(8 Pt 2): E290-6.
- Schones, D. E., Cui, K., Cuddapah, S., Roh, T. Y., Barski, A., Wang, Z., Wei, G., Zhao, K. (2008). Dynamic regulation of nucleosome positioning in the human genome. *Cell.* 132(5): 887-898.
- Schotta, G., Lachner, M., Sarma, K., Ebert, A., Sengupta, R., Reuter, G., Reinberg, D., Jenuwein, T. (2004). A silencing pathway to induce H3-K9 and H4-K20 trimethylation at constitutive heterochromatin. *Genes Dev.* 18(11): 1251-1262.
- Schotta, G., Sengupta, R., Kubicek, S., Malin, S., Kauer, M., Callén, E., Celeste, A., Pagani, M., Opravil, S., De La Rosa-Velazquez, I. A., et al. (2008). A chromatin-wide transition to H4K20 monomethylation impairs genome integrity and programmed DNA rearrangements in the mouse. *Genes Dev.* 22(15): 2048-2061.
- Schulz, W. A., Elo, J. P., Florl, A. R., Pennanen, S., Santourlidis, S., Engers, R., Buchardt, M., Seifert, H. H., Visakorpi, T. (2002). Genomewide DNA hypomethylation is associated with alterations on chromosome 8 in prostate carcinoma. *Genes Chromosomes Cancer.* 35(1): 58-65.
- Schuster-Böckler, B., Lehner, B. (2012). Chromatin organization is a major influence on regional mutation rates in human cancer cells. *Nature.* 488(7412): 504-507.
- Sedelnikova, O. A., Horikawa, I., Zimonjic, D. B., Popescu, N. C., Bonner, W. M., Barrett, J. C. (2004). Senescing human cells and ageing mice accumulate

- DNA lesions with unrepairable double-strand breaks. *Nat Cell Biol.* 6(2): 168-170.
- Segal, E., Fondufe-Mittendorf, Y., Chen, L., Thåström, A., Field, Y., Moore, I. K., Wang, J. P., Widom, J. (2006). A genomic code for nucleosome positioning. *Nature.* 442(7104): 772-778.
- Sekinger, E. A., Moqtaderi, Z., Struhl, K. (2005). Intrinsic histone-DNA interactions and low nucleosome density are important for preferential accessibility of promoter regions in yeast. *Mol Cell.* 18(6): 735-748.
- Serrano, M., Hannon, G. J., Beach, D. (1993). A new regulatory motif in cell-cycle control causing specific inhibition of cyclin D/CDK4. *Nature.* 366(6456): 704-707.
- Serrano, M., Lin, A. W., McCurrach, M. E., Beach, D., Lowe, S. W. (1997). Oncogenic ras provokes premature cell senescence associated with accumulation of p53 and p16INK4a. *Cell.* 88(5): 593-602.
- Shannon, M., Hamilton, A. T., Gordon, L., Branscomb, E., Stubbs, L. (2003). Differential expansion of zinc-finger transcription factor loci in homologous human and mouse gene clusters. *Genome Res.* 13(6A): 1097-1110.
- Sharif, J., Muto, M., Takebayashi, S., Suetake, I., Iwamatsu, A., Endo, T. A., Shinga, J., Mizutani-Koseki, Y., Toyoda, T., Okamura, K., et al. (2007). The SRA protein Np95 mediates epigenetic inheritance by recruiting Dnmt1 to methylated DNA. *Nature.* 450(7171): 908-912.
- Sharma, S., Kelly, T. K., Jones, P. A. (2010). Epigenetics in cancer. *Carcinogenesis.* 31(1): 27-36.
- Sharp, A. J., Stathaki, E., Migliavacca, E., Brahmachary, M., Montgomery, S. B., Dupre, Y., Antonarakis, S. E. (2011). DNA methylation profiles of human active and inactive X chromosomes. *Genome Res.* 21(10): 1592-1600.
- Shay, J. W., Wright, W. E., Werbin, H. (1991). Defining the molecular mechanisms of human cell immortalization. *Biochim Biophys Acta.* 1072(1): 1-7.
- Shay, J. W., Wright, W. E. (2005). Senescence and immortalization: role of telomeres and telomerase. *Carcinogenesis.* 26(5): 867-874.
- Shelton, D. N., Chang, E., Whittier, P. S., Choi, D., Funk, W. D. (1999). Microarray analysis of replicative senescence. *Curr Biol.* 9(17): 939-945.
- Sherr, C. J., Roberts, J. M. (1999). CDK inhibitors: positive and negative regulators of G1-phase progression. *Genes Dev.* 13(12): 1501-1512.
- Sherr, C. J., DePinho, R. A. (2000). Cellular senescence: mitotic clock or culture shock? *Cell.* 102(4): 407-410.

- Shi, Y., Lan, F., Matson, C., Mulligan, P., Whetstine, J. R., Cole, P. A., Casero, R. A., Shi, Y. (2004). Histone demethylation mediated by the nuclear amine oxidase homolog LSD1. *Cell*. 119(7): 941-953.
- Shimi, T., Pflieger, K., Kojima, S., Pack, C. G., Solovei, I., Goldman, A. E., Adam, S. A., Shumaker, D. K., Kinjo, M., Cremer, T., et al. (2008). The A- and B-type nuclear lamin networks: microdomains involved in chromatin organization and transcription. *Genes Dev*. 22(24): 3409-3421.
- Shimi, T., Butin-Israeli, V., Adam, S. A., Hamanaka, R. B., Goldman, A. E., Lucas, C. A., Shumaker, D. K., Kosak, S. T., Chandel, N. S., Goldman, R. D. (2011). The role of nuclear lamin B1 in cell proliferation and senescence. *Genes Dev*. 25(24): 2579-2593.
- Shumaker, D. K., Dechat, T., Kohlmaier, A., Adam, S. A., Bozovsky, M. R., Erdos, M. R., Eriksson, M., Goldman, A. E., Khuon, S., Collins, F. S., et al. (2006). Mutant nuclear lamin A leads to progressive alterations of epigenetic control in premature aging. *Proc Natl Acad Sci U S A*. 103(23): 8703-8708.
- Simpson, R. T. (1978). Structure of the chromatosome, a chromatin particle containing 160 base pairs of DNA and all the histones. *Biochemistry*. 17(25): 5524-5531.
- Sleutels, F., Zwart, R., Barlow, D. P. (2002). The non-coding Air RNA is required for silencing autosomal imprinted genes. *Nature*. 415(6873): 810-813.
- Smogorzewska, A., van Steensel, B., Bianchi, A., Oelmann, S., Schaefer, M. R., Schnapp, G., de Lange, T. (2000). Control of human telomere length by TRF1 and TRF2. *Mol Cell Biol*. 20(5): 1659-1668.
- Souza, P. P., Völkel, P., Trinel, D., Vandamme, J., Rosnoblet, C., Hélot, L., Angrand, P. O. (2009). The histone methyltransferase SUV420H2 and Heterochromatin Proteins HP1 interact but show different dynamic behaviours. *BMC Cell Biol*. 10: 41-56.
- Spann, T. P., Moir, R. D., Goldman, A. E., Stick, R., Goldman, R. D. (1997). Disruption of nuclear lamin organization alters the distribution of replication factors and inhibits DNA synthesis. *J Cell Biol*. 136(6): 1201-1212.
- Spann, T. P., Goldman, A. E., Wang, C., Huang, S., Goldman, R. D. (2002). Alteration of nuclear lamin organization inhibits RNA polymerase II-dependent transcription. *J Cell Biol*. 156(4): 603-608.
- Squier, T. C. (2001). Oxidative stress and protein aggregation during biological aging. *Exp Gerontol*. 36(9): 1539-1550.
- Stein, G. S., Lian, J. B., Gerstenfeld, L. G., Shalhoub, V., Aronow, M., Owen, T., Markose, E. (1989). The onset and progression of osteoblast differentiation is functionally related to cellular proliferation. *Connect Tissue Res*. 20(1-4): 3-13.

- Stender, J. D., Pascual, G., Liu, W., Kaikkonen, M. U., Do, K., Spann, N. J., Boutros, M., Perrimon, N., Rosenfeld, M. G., Glass, C. K. (2012). Control of Proinflammatory Gene Programs by Regulated Trimethylation and Demethylation of Histone H4K20. *Mol Cell*. 48(1): 28-38.
- Stiff, T., O'Driscoll, M., Rief, N., Iwabuchi, K., Löbrich, M., Jeggo, P. A. (2004). ATM and DNA-PK function redundantly to phosphorylate H2AX after exposure to ionizing radiation. *Cancer Res*. 64(7): 2390-2396.
- Strichman-Almashanu, L. Z., Lee, R. S., Onyango, P. O., Perlman, E., Flam, F., Frieman, M. B., Feinberg, A. P. (2002). A genome-wide screen for normally methylated human CpG islands that can identify novel imprinted genes. *Genome Res*. 12(4): 543-554.
- Subramanian, A., Tamayo, P., Mootha, V. K., Mukherjee, S., Ebert, B. L., Gillette, M. A., Paulovich, A., Pomeroy, S. L., Golub, T. R., Lander, E. S., Mesirov, J. P. (2005). Gene set enrichment analysis: a knowledge-based approach for interpreting genome-wide expression profiles. *Proc Natl Acad Sci U S A*. 102(43): 15545-15550.
- Tachiwana, H., Kagawa, W., Osakabe, A., Kawaguchi, K., Shiga, T., Hayashi-Takanaka, Y., Kimura, H., Kurumizaka, H. (2010). Structural basis of instability of the nucleosome containing a testis-specific histone variant, human H3T. *Proc Natl Acad Sci U S A*. 107(23): 10454-10459.
- Tagami, H., Ray-Gallet, D., Almouzni, G., Nakatani, Y. (2004). Histone H3.1 and H3.3 complexes mediate nucleosome assembly pathways dependent or independent of DNA synthesis. *Cell*. 116(1): 51-61.
- Taimen, P., Pflieger, K., Shimi, T., Möller, D., Ben-Harush, K., Erdos, M. R., Adam, S. A., Herrmann, H., Medalia, O., Collins, F. S., et al. (2009). A progeria mutation reveals functions for lamin A in nuclear assembly, architecture, and chromosome organization. *Proc Natl Acad Sci U S A*. 106(49): 20788-20793.
- Tang, C. W., Maya-Mendoza, A., Martin, C., Zeng, K., Chen, S., Feret, D., Wilson, S. A., Jackson, D. A. (2008). The integrity of a lamin-B1-dependent nucleoskeleton is a fundamental determinant of RNA synthesis in human cells. *J Cell Sci*. 121(Pt 7): 1014-1024.
- Tatton-Brown, K., Rahman, N. (2007). Sotos syndrome. *Eur J Hum Genet*. 15(3): 264-271.
- Taverna, S. D., Li, H., Ruthenburg, A. J., Allis, C. D., Patel, D. J. (2007). How chromatin-binding modules interpret histone modifications: lessons from professional pocket pickers. *Nat Struct Mol Biol*. 14(11): 1025-1040.
- Taylor, R. C., Cullen, S. P., Martin, S. J. (2008). Apoptosis: controlled demolition at the cellular level. *Nat Rev Mol Cell Biol*. 9(3): 231-241.

- te Poele, R. H., Okorokov, A. L., Jardine, L., Cummings, J., Joel, S. P. (2002). DNA damage is able to induce senescence in tumor cells in vitro and in vivo. *Cancer Res.* 62(6): 1876-83.
- Toussaint, O., Medrano, E. E., von Zglinicki, T. (2000). Cellular and molecular mechanisms of stress-induced premature senescence (SIPS) of human diploid fibroblasts and melanocytes. *Exp Gerontol.* 35(8): 927-945.
- Treangen, T. J., Salzberg, S. L. (2012). Repetitive DNA and next-generation sequencing: computational challenges and solutions. *Nat Rev Genet.* 13(1): 36-46.
- Tryndyak, V. P., Kovalchuk, O., Pogribny, I.P. (2006). Loss of DNA methylation and histone H4 lysine 20 trimethylation in human breast cancer cells is associated with aberrant expression of DNA methyltransferase 1, Suv4-20h2 histone methyltransferase and methyl-binding proteins. *Cancer Biol Ther* 5: 65–70.
- Tsai, M. C., Manor, O., Wan, Y., Mosammaparast, N., Wang, J. K., Lan, F., Shi, Y., Segal, E., Chang, H. Y. (2010). Long noncoding RNA as modular scaffold of histone modification complexes. *Science.* 329(5992): 689-693.
- Tsang, L. W., Hu, N., Underhill, D. A. (2010). Comparative analyses of SUV420H1 isoforms and SUV420H2 reveal differences in their cellular localization and effects on myogenic differentiation. *PLoS One.* 5(12): e14447.
- Tsukada, Y., Fang, J., Erdjument-Bromage, H., Warren, M. E., Borchers, C. H., Tempst, P., Zhang, Y. (2006). Histone demethylation by a family of JmjC domain-containing proteins. *Nature.* 439(7078): 811-816.
- Tzatsos, A., Pfau, R., Kampranis, S. C., Tsiichlis, P. N. (2009). Ndy1/KDM2B immortalizes mouse embryonic fibroblasts by repressing the Ink4a/Arf locus. *Proc Natl Acad Sci U S A.* 106(8): 2641-2646.
- Uitto, J. (2002). Searching for clues to premature aging. *Trends Mol Med.* 8(4): 155-157.
- Vakoc, C. R., Sachdeva, M. M., Wang, H., Blobel, G. A. (2006). Profile of histone lysine methylation across transcribed mammalian chromatin. *Mol Cell Biol.* 26(24): 9185-9195.
- Van Den Broeck, A., Brambilla, E., Moro-Sibilot, D., Lantuejoul, S., Brambilla, C., Eymin, B., Khochbin, S., Gazzeri, S. (2008). Loss of histone H4K20 trimethylation occurs in preneoplasia and influences prognosis of non-small cell lung cancer. *Clin Cancer Res.* 14(22): 7237-7245.
- Venter, J. C., Adams, M. D., Myers, E. W., Li, P. W., Mural, R. J., Sutton, G. G., Smith, H. O., Yandell, M., Evans, C. A., Holt, R. A., et al. (2001). The sequence of the human genome. *Science.* 291(5507): 1304-1351.

- Ventura, A., Kirsch, D. G., McLaughlin, M. E., Tuveson, D. A., Grimm, J., Lintault, L., Newman, J., Reczek, E. E., Weissleder, R., Jacks, T. (2007). Restoration of p53 function leads to tumour regression in vivo. *Nature*. 445(7128): 661-665.
- Vermeulen, M., Eberl, H. C., Matarese, F., Marks, H., Denissov, S., Butter, F., Lee, K. K., Olsen, J. V., Hyman, A. A., Stunnenberg, H. G., et al. (2010). Quantitative interaction proteomics and genome-wide profiling of epigenetic histone marks and their readers. *Cell*. 142(6): 967-980.
- Vizioli, M. G., Possik, P. A., Tarantino, E., Meissl, K., Borrello, M. G., Miranda, C., Anania, M. C., Pagliardini, S., Seregini, E., Pierotti, M. A., et al. (2011). Evidence of oncogene-induced senescence in thyroid carcinogenesis. *Endocr Relat Cancer*. 18(6): 743-757.
- Vogel, M. J., Guelen, L., de Wit, E., Peric-Hupkes, D., Lodén, M., Talhout, W., Feenstra, M., Abbas, B., Classen, A. K., van Steensel, B. (2006). Human heterochromatin proteins form large domains containing KRAB-ZNF genes. *Genome Res*. 16(12): 1493-1504.
- von Zglinicki, T., Saretzki, G., Döcke, W., Lotze, C. (1995). Mild hyperoxia shortens telomeres and inhibits proliferation of fibroblasts: a model for senescence? *Exp Cell Res*. 220(1): 186-193.
- Wajapeyee, N., Serra, R. W., Zhu, X., Mahalingam, M., Green, M. R. (2008). Oncogenic BRAF induces senescence and apoptosis through pathways mediated by the secreted protein IGFBP7. *Cell*. 132(3): 363-374.
- Wakeman, T. P., Wang, Q., Feng, J., Wang, X. F. (2012). Bat3 facilitates H3K79 dimethylation by DOT1L and promotes DNA damage-induced 53BP1 foci at G1/G2 cell-cycle phases. *EMBO J*. 31(9): 2169-2181.
- Wang, Z., Zang, C., Rosenfeld, J. A., Schones, D. E., Barski, A., Cuddapah, S., Cui, K., Roh, T. Y., Peng, W., Zhang, M. Q., et al. (2008). Combinatorial patterns of histone acetylations and methylations in the human genome. *Nat Genet*. 40(7): 897-903.
- Wang, C., Jurk, D., Maddick, M., Nelson, G., Martin-Ruiz, C., von Zglinicki, T. (2009). DNA damage response and cellular senescence in tissues of aging mice. *Aging Cell*. 8(3): 311-323.
- Wei, S., Wei, W., Sedivy, J. M. (1999). Expression of catalytically active telomerase does not prevent premature senescence caused by overexpression of oncogenic Ha-Ras in normal human fibroblasts. *Cancer Res*. 59(7): 1539-1543.
- Whetstine, J. R., Nottke, A., Lan, F., Huarte, M., Smolikov, S., Chen, Z., Spooner, E., Li, E., Zhang, G., Colaiacovo, M., et al. (2006). Reversal of histone lysine

- trimethylation by the JMJD2 family of histone demethylases. *Cell*. 125(3): 467-481.
- Williams, S. K., Tyler, J. K. (2007). Transcriptional regulation by chromatin disassembly and reassembly. *Curr Opin Genet Dev*. 17(2): 88-93.
- Wilson, V. L., Jones, P. A. (1983). DNA methylation decreases in aging but not in immortal cells. *Science*. 220(4601): 1055-1057.
- Wolyniec, K., Wotton, S., Kilbey, A., Jenkins, A., Terry, A., Peters, G., Stocking, C., Cameron, E., Neil, J. C. (2009). RUNX1 and its fusion oncoprotein derivative, RUNX1-ETO, induce senescence-like growth arrest independently of replicative stress. *Oncogene*. 28(27): 2502-2512.
- Wong, N., Lam, W. C., Lai, P. B., Pang, E., Lau, W. Y., Johnson, P. J. (2001). Hypomethylation of chromosome 1 heterochromatin DNA correlates with q-arm copy gain in human hepatocellular carcinoma. *Am J Pathol*. 159(2): 465-471.
- Wysocka, J. (2006). Identifying novel proteins recognizing histone modifications using peptide pull-down assay. *Methods*. 40(4): 339-343.
- Xue, W., Zender, L., Miething, C., Dickins, R. A., Hernando, E., Krizhanovsky, V., Cordon-Cardo, C., Lowe, S. W. (2007). Senescence and tumour clearance is triggered by p53 restoration in murine liver carcinomas. *Nature*. 445(7128): 656-660.
- Yang, G., Rosen, D. G., Zhang, Z., Bast, R. C. Jr., Mills, G. B., Colacino, J. A., Mercado-Uribe, I., Liu, J. (2006). The chemokine growth-regulated oncogene 1 (Gro-1) links RAS signaling to the senescence of stromal fibroblasts and ovarian tumorigenesis. *Proc Natl Acad Sci U S A*. 103(44): 16472-16477.
- Yang, H., Pesavento, J. J., Starnes, T. W., Cryderman, D. E., Wallrath, L. L., Kelleher, N. L., Mizzen, C. A. (2008). Preferential dimethylation of histone H4 lysine 20 by Suv4-20. *J Biol Chem*. 283(18): 12085-12092.
- Yang, Z., Klionsky, D. J. (2010). Eaten alive: a history of macroautophagy. *Nat Cell Biol*. 12(9): 814-822.
- Ye, X., Zerlanko, B., Zhang, R., Somaiah, N., Lipinski, M., Salomoni, P., Adams, P. D. (2007a). Definition of pRB- and p53-dependent and -independent steps in HIRA/ASF1a-mediated formation of senescence-associated heterochromatin foci. *Mol Cell Biol*. 27(7): 2452-2465.
- Ye, X., Zerlanko, B., Kennedy, A., Banumathy, G., Zhang, R., Adams, P. D. (2007b). Downregulation of Wnt signaling is a trigger for formation of facultative heterochromatin and onset of cell senescence in primary human cells. *Mol Cell*. 27(2): 183-196.

- Yen, P. H., Patel, P., Chinault, A. C., Mohandas, T., Shapiro, L. J. (1984). Differential methylation of hypoxanthine phosphoribosyltransferase genes on active and inactive human X chromosomes. *Proc Natl Acad Sci U S A.* 81(6): 1759-1763.
- Yeo, E. J., Hwang, Y. C., Kang, C. M., Kim, I. H., Kim, D. I., Parka, J. S., Choy, H. E., Park, W. Y., Park, S. C. (2000). Senescence-like changes induced by hydroxyurea in human diploid fibroblasts. *Exp Gerontol.* 35(5): 553-571.
- Yoon, I. K., Kim, H. K., Kim, Y. K., Song, I. H., Kim, W., Kim, S., Baek, S. H., Kim, J. H., Kim, J. R. (2004). Exploration of replicative senescence-associated genes in human dermal fibroblasts by cDNA microarray technology. *Exp Gerontol.* 39(9): 1369-1378.
- Yotova, I. Y., Vlatkovic, I. M., Pauler, F. M., Warczok, K. E., Ambros, P. F., Oshimura, M., Theussl, H. C., Gessler, M., Wagner, E. F., Barlow, D. P. (2008). Identification of the human homolog of the imprinted mouse Air non-coding RNA. *Genomics.* 92(6): 464-473.
- Young, A. P., Schlisio, S., Minamishima, Y. A., Zhang, Q., Li, L., Grisanzio, C., Signoretti, S., Kaelin, W. G. Jr. (2008). VHL loss actuates a HIF-independent senescence programme mediated by Rb and p400. *Nat Cell Biol.* 10(3): 361-369.
- Young, A. R., Narita, M., Ferreira, M., Kirschner, K., Sadaie, M., Darot, J. F., Tavaré, S., Arakawa, S., Shimizu, S., Watt, F. M., Narita, M. (2009). Autophagy mediates the mitotic senescence transition. *Genes Dev.* 23(7): 798-803.
- Yuan, G. C., Liu, Y. J., Dion, M. F., Slack, M. D., Wu, L. F., Altschuler, S. J., Rando, O. J. (2005). Genome-scale identification of nucleosome positions in *S. cerevisiae*. *Science.* 309(5734): 626-630.
- Zahradka, P., Elliot, T., Hovland, K., Larson, D. E., Saward, L. (1993). Repression of histone gene transcription in quiescent 3T6 fibroblasts. *Eur J Biochem.* 217(2): 683-690.
- Zalensky, A. O., Siino, J. S., Gineitis, A. A., Zalenskaya, I. A., Tomilin, N. V., Yau, P., Bradbury, E. M. (2002). Human testis/sperm-specific histone H2B (hTSH2B). Molecular cloning and characterization. *J Biol Chem.* 277(45): 43474-43480.
- Zang, C., Schones, D. E., Zeng, C., Cui, K., Zhao, K., Peng, W. (2009). A clustering approach for identification of enriched domains from histone modification ChIP-Seq data. *Bioinformatics.* 25(15): 1952-1958.
- Zhang, Y., Reinberg, D. (2001). Transcription regulation by histone methylation: interplay between different covalent modifications of the core histone tails. *Genes Dev.* 15(18): 2343-2360.

- Zhang, H., Pan, K. H., Cohen, S. N. (2003). Senescence-specific gene expression fingerprints reveal cell-type-dependent physical clustering of up-regulated chromosomal loci. *Proc Natl Acad Sci U S A.* 100(6): 3251-3256.
- Zhang, R., Poustovoitov, M. V., Ye, X., Santos, H. A., Chen, W., Daganzo, S. M., Erzberger, J. P., Serebriiskii, I. G., Canutescu, A. A., Dunbrack, R. L., et al. (2005). Formation of MacroH2A-containing senescence-associated heterochromatin foci and senescence driven by ASF1a and HIRA. *Dev Cell.* 8(1): 19-30.
- Zhang, R., Chen, W., Adams, P. D. (2007). Molecular dissection of formation of senescence-associated heterochromatin foci. *Mol Cell Biol.* 27(6): 2343-2358.
- Zhang, W., Ji, W., Yang, J., Yang, L., Chen, W., Zhuang, Z. (2008). Comparison of global DNA methylation profiles in replicative versus premature senescence. *Life Sci.* 83(13-14): 475-80.
- Zhao, J., Kennedy, B. K., Lawrence, B. D., Barbie, D. A., Matera, A. G., Fletcher, J. A., Harlow, E. (2000). NPAT links cyclin E-Cdk2 to the regulation of replication-dependent histone gene transcription. *Genes Dev.* 14: 2283-2297.
- Zheng, C., Hayes, J. J. (2003). Structures and interactions of the core histone tail domains. *Biopolymers.* 68(4): 539-546.
- Zheng, X., Chou, P. M., Mirkin, B. L., Rebbaa, A. (2004). Senescence-initiated reversal of drug resistance: specific role of cathepsin L. *Cancer Res.* 64(5): 1773-1780.
- Zhu, J., Woods, D., McMahon, M., Bishop, J. M. (1998). Senescence of human fibroblasts induced by oncogenic Raf. *Genes Dev.* 12(19): 2997-3007.